The Production of Temperature and Salinity Variance and Covariance: Implications for Mixing

by

Julian J Schanze

Master of Science in Oceanography, University of Southampton, U.K. (2007)

Submitted to the Department of Earth, Atmospheric, and Planetary Sciences and the Woods Hole Oceanographic Institution in Partial Fulfillment of the Requirements for the Degree of

Doctor of Philosophy in Physical Oceanography

at the

MASSACHUSETTS INSTITUTE OF TECHNOLOGY
and the
WOODS HOLE OCEANOGRAPHIC INSTITUTION

February 2013

Author .....
MIT-WHOI Joint Program in Physical Oceanography
November 29, 2012

Certified by .....
Raymond W Schmitt, Ph.D.
Senior Scientist, WHOI
Thesis Supervisor

Accepted by .....
Glenn R Flierl, Ph.D.
Professor of Oceanography, MIT
Chair, Joint Committee for Physical Oceanography

The Production of Temperature and Salinity Variance and Covariance: Implications for Mixing

by

Julian J Schanze

Submitted to the Department of Earth, Atmospheric, and Planetary Sciences
and the Woods Hole Oceanographic Institution on November 29, 2012
in Partial Fulfillment of the Requirements for the Degree of
Doctor of Philosophy in Physical Oceanography

Abstract

Large-scale thermal forcing and freshwater fluxes play an essential role in setting temperature and salinity in the ocean. A number of recent estimates of the global oceanic freshwater balance as well as the global oceanic surface net heat flux are used to investigate the effects of heat- and freshwater forcing at the ocean surface. Such forcing induces changes in both density and density-compensated temperature and salinity changes ('spice'). The ratio of the relative contributions of haline and thermal forcing in the mixed layer is maintained by large-scale surface fluxes, leading to important consequences for mixing in the ocean interior. In a stratified ocean, mixing processes can be either along lines of constant density (isopycnal) or across those lines (diapycnal). The contribution of these processes to the total mixing rate in the ocean can be estimated from the large-scale forcing by evaluating the production of thermal variance, salinity variance and temperature-salinity covariance. Here, I use new estimates of surface fluxes to evaluate these terms and combine them to generate estimates of the production of density and spice variance under the assumption of a linear equation of state. As a consequence, it is possible to estimate the relative importance of isopycnal and diapycnal mixing in the ocean. While isopycnal and diapycnal processes occur on very different length scales, I find that the surface-driven production of density and spice variance requires an approximate equipartition between isopycnal and diapycnal mixing in the ocean interior. In addition, consideration of the full nonlinear equation of state reveals that surface fluxes require an apparent buoyancy gain (expansion) of the ocean, which allows an estimate of the amount of contraction on mixing due to cabbeling in the ocean interior

Thesis Supervisor: Raymond W Schmitt, Ph.D.
Title: Senior Scientist, WHOI

Acknowledgments

The author would like to acknowledge support from the National Aeronautics and Space Administration, grant #NNX12AF59G and the National Science Foundation, grant #OCE-0647949. Helpful comments were made by anonymous reviewers for parts of the text in Chapters 3 and 5. Data preparation and conversion of some E, P and Q_{net} datasets by Xiangze Jin is appreciated. Helpful comments by Chris Garrett and Trevor McDougall about the effects of the seasonal cycle and cabbeling in general were very useful. Discussions with Oliver Sun and Andrey Shcherbina about the role of advection were helpful in completing Chapter 4.

I would like to personally thank my advisor, Raymond Schmitt, for all the help and support he has given me over the course of my time in the Joint Program. I would also like to thank the rest of my committee, Terry Joyce, Carl Wunsch and Lisan Yu for all the help and suggestions they have provided in many committee meetings and in personal talks. Furthermore, I would like to thank Carol Anne Clayson for agreeing to be the chair of my defense and making the defense of this thesis a very pleasant experience for me.

The Joint Program has been a fantastic experience for me, in large part due to the close community of students and the tireless efforts of the staff in the academic programs offices both at MIT and WHOI to improve student life – Thank You.

Lastly, but certainty not least, I would like to thank my wonderful family for all their support throughout the years and for always being there for me.

Contents

Chapter 1

Introduction and Objectives

With the advent of synoptic observations of the ocean surface as well as detailed studies of mixing in the ocean in the 1960s and 1970s (see Thorpe (2005) for a history of ocean turbulence), it became clear that turbulence is ubiquitous in the ocean. The thermal forcing at the ocean surface as well as the oceanic freshwater cycle are responsible for setting the temperature and salinity properties of water masses. Salinity changes at the ocean surface are produced by evaporation (E), precipitation (P) and riverine runoff (R) as well as the formation and melting of ice and groundwater discharge, which may be included in either P or R (e.g. Baumgartner and Reichel, 1975). The dominant driver of temperature of the ocean is the net heat flux (Q_{net})at the ocean surface, which is defined as the sum of the net shortwave radiation at the ocean surface (Q_{SW}), the net longwave radiation at the ocean surface (Q_{LW}), sensible heat flux through the ocean surface (Q_{SH}), and latent heat loss (Q_{LH}). Q_{net} (e.g. Hartmann, 1994, and references therein).

In the same time period of major mixing studies in the ocean, the concept of 'surface power integrals' was developed by Stern (1969, 1975). These integrals state that in an ocean that is in steady state, the surface variance generated by heat- and freshwater forcing must be compensated by mixing in the interior (Stern, 1975). To illustrate this concept, one may consider the heat input to the ocean: There is a strong net input of heat to the ocean at the equator, but also a significant loss at high latitudes. If there were no mixing in the ocean, the warmer regions would become ever warmer and the colder regions would perpetually cool. This is clearly not the case, as mixing in the ocean destroys the so-generated variance and – in a steady state – maintains a constant gradient. The same is true for the input of freshwater,

albeit with a more complex pattern than that of heating (Yu et al., 2008; Schanze et al., 2010).

In such a steady-state ocean, the net flux of heat and freshwater to the ocean must sum to zero (e.g. Stern, 1975, p. 209), that is:

$$\oiint_A (Q_{SW} + Q_{LW} + Q_{SH} + Q_{LH}) dA = 0 \tag{1.1}$$

$$\oiint_A (E - P - R) dA = 0 \tag{1.2}$$

While this is a good first-order approximation for the real ocean, it is not quite accurate due to a current warming of the ocean at a rate of approximately 1–3 $\mathrm{W\,m^{-2}}$ and a global sea-level rise of 2–3 $\mathrm{mm\,yr^{-1}}$ (Church and White, 2006; Domingues et al., 2008) as observed by satellite altimetry (of which approximately 1 mm is accounted for by thermal expansion, which does not directly affect E, P or R).

Joyce (1980) used this basic theory to estimate the total thermal dissipation rate in the ocean using sea surface temperature and heat-flux data that were binned in 10° latitude bands. However, no estimates of salinity, density, or spice variance production and dissipation have been published yet. Furthermore, the SST and Q_{net} estimates used by Joyce (1980) were produced before the advent of active and passive microwave satellites, which have greatly improved our understanding of both the oceanic freshwater cycle and the global ocean heat budget (Robinson, 2004).

Both freshwater- and heat-fluxes affect the water at the ocean surface by modifying temperature and salinity properties. A local net heat input will lead to the warming of the surface ocean water and a negative flux will lead to cooling, while a positive value of E-P-R will lead to a salinity increase and a negative value of E-P-R will lead to freshening of the surface ocean. These modifications of surface waters play an important role in the general circulation of the ocean, since they affect the density (Jackett et al., 2006, e.g.) and the spiciness (the density-compensated change in temperature and salinity) of seawater (Veronis, 1972; Munk, 1981; Schmitt, 1999; Huang, 2011).

There is also a direct effect of the global (re-)distribution of freshwater over the ocean through E and P alone, which induces a circulation with a strength of up to 2 Sv: the Goldsbrough circulation (Huang and Schmitt, 1993). However, the much stronger meridional overturning circulation (MOC) is also directly affected by the potential

density profile of the oceans. The strength of the MOC is thought to be ultimately 'driven' by the input of energy into the ocean by means of wind stress and tidal forces, which is dissipated by turbulent mixing in the stratified ocean (Wunsch and Ferrari, 2004). The overturning pathways are set by density fluxes at the air-sea interface (Kuhlbrodt et al., 2007). If the surface salinity patterns of the Pacific and Atlantic Oceans were reversed, the majority of deep-water formation would likely occur in the Pacific instead of the Atlantic. Consequently, it is important to understand the mean spatial patterns of oceanic freshwater fluxes (E-P-R) as well as the net heat oceanic flux (Q_{net}) and temporal deviations from this mean.

Historically, global estimates of all required quantities to estimate freshwater and heat fluxes in the ocean were based on *in-situ* observations, which caused the data density to be biased towards arcas frequented by vessels or areas with permanent moorings or weather ships. As a consequence, there were few or no measurements in remote oceanic areas such as the Southern Ocean, leading to large errors (Schmitt et al., 1989; Schmitt, 1995, e.g.). With the introduction of various satellites capable of observing some of the variables required to quantify oceanic surface thermal and saline forcing in the 1980s and 1990s (Robinson, 2004), it became possible to include these observations in generating the current state-of-the-art estimates of evaporation (Yu and Weller, 2007), precipitation (Adler et al., 2003) and thermal forcing (Zhang et al., 2004; Trenberth et al., 2009).

Chapter 3 will explore the history of estimating E-P-R and heat flux over the ocean. Currently available products are described, and an evaluation of their spatial and temporal homogeneity is performed. By means of this evaluation, the period over which they can be used with confidence to a given error is determined. Based on the selection of suitable datasets and the date range, current state-of-the art estimates of E-P-R and Q_{net} are produced. Since it is required that the integral over the ocean be in steady state for both thermal and freshwater forcing, an artificial bias is introduced to ensure the relationships $E - P - R = 0$ and $Q_{net} = 0$ are satisfied.

It has been shown that the area integral of large-scale surface freshwater (Stern, 1975) and thermal (Joyce, 1980) forcing can be directly related to the volume integral of the total freshwater and thermal dissipation, respectively. This dissipation occurs through oceanic turbulence and advection and the approach to estimate it from surface fluxes was termed 'power integrals' by Stern (1975). It will be shown in Chapter 2 that it is furthermore possible to relate the global surface density and spice forc-

ing to the total dissipation of density (diapycnal) and spice (isopycnal) variance in the ocean. By linearizing the equation of state, the relationship between the surface density and spice forcing and interior effects are explored. For this, the estimates of E-P-R and Q_{net}, which are developed in Chapter 3 will be used with results shown in Chapter 4. The shortcomings and limitations of using a linear equation of state are highlighted and estimates of density and spice variance production at the ocean surface are produced using both a linearized equation of state and the full non-linear Thermodynamic Equation of State 2010 (TEOS-10, IOC et al. (2011); McDougall (2011)). Some effects of the nonlinearities of this equation of state are explored in Chapter 5 through the example of cabbeling, which is the dominant effect.

In summary, I present here the first estimate of salinity variance production in the global ocean using modern, satellite-derived estimates of E-P-R as well as first estimates of the covariance of temperature and salinity in the form of density and spice power integrals. As I will show in Chapter 2, the density variance production at the surface must be compensated by diapycnal mixing, while the spice variance production must be compensated by isopycnal mixing. This allows the quantification of the relative importance of isopycnal and diapycnal mixing in the ocean in Chapter 4, a theoretical constraint that is not currently used in any ocean model known to the author. As such, it may prove to become a useful constraint in ocean modeling and enhance our understanding of the global ocean circulation in general.

Chapter 2

Power Integrals

In this chapter, a linearized equation of state will be used to explore the relationships between surface forcing and thermal, salinity, density and spice dissipation in the interior. Assuming a steady-state, the dissipation of each of those variables must equal their respective surface forcing (Stern, 1975). The following situation may be used as an example of this: When differential heating is applied to two points of the ocean surface, this thermal variance must vanish at the same rate at which it is applied (through the process of thermal dissipation) lest the area that is receiving a constant net heat input warms up over time (Joyce, 1980).

The basic idea of such 'power integrals' was proposed by Stern (1969, 1975) for haline variance and was used by Joyce (1980) for thermal variance. A volume-integrated dissipation relation for volumes bounded by a tracer of constant concentration was developed by Schneider and Bhatt (2000) using salinity as an exemplary tracer, but this approach differs significantly from the global power integrals proposed by Stern (1975). The dataset on which the Joyce (1980) study is based were created before relevant satellite data became available, and it is thus of interest to repeat those calculations with current datasets to refine the estimates. With the availability of such datasets, however, it seems prudent to examine not only a single component (thermal or haline), but to look at the combined effects the net heat forcing and the oceanic freshwater cycle have on the generation of density and spice variance in the global ocean. Spice is defined as orthogonal to density in temperature and salinity and an implementation by Huang (2011) is used throughout this thesis.

For the purpose of evaluating isopycnal and diapycnal dissipation rates in the ocean, the work of Stern (1969) and Joyce (1980) is used to find equivalent expressions

for density and spice variance production using both a nonlinear and a linearized equation of state. For this, a number of simplifying assumptions need to be made: By splitting all vector quantities into isopycnal and diapycnal components, a relationship will be derived which relates the production of spice variance to isopycnal mixing and the production of density variance to diapycnal mixing. This allows the quantification of isopycnal and diapycnal mixing rates subject to the assumptions made in deriving them.

2.1 Derivation of Variance-Dissipation Relations

We start from a basic conservation equation (e.g. Joyce, 1980; Schneider and Bhatt, 2000, and references therein) of potential temperature (θ), salinity (S), density (ρ) and spice (τ) in the ocean. These are, respectively:

$$\frac{\partial \theta}{\partial t} = \boldsymbol{\nabla} \cdot (\kappa_\theta \boldsymbol{\nabla} \theta - \mathbf{u}\theta) \tag{2.1}$$

$$\frac{\partial S}{\partial t} = \boldsymbol{\nabla} \cdot (\kappa_S \boldsymbol{\nabla} S - \mathbf{u}S) \tag{2.2}$$

$$\frac{\partial \rho}{\partial t} = \boldsymbol{\nabla} \cdot (\kappa_\rho \boldsymbol{\nabla} \rho - \mathbf{u}\rho) \tag{2.3}$$

$$\frac{\partial \tau}{\partial t} = \boldsymbol{\nabla} \cdot (\kappa_\tau \boldsymbol{\nabla} \tau - \mathbf{u}\tau) \tag{2.4}$$

The temporal evolution of each variable (left hand side [LHS]) is equal to the down-gradient turbulent diffusion (first term, right hand side [RHS]) and advection (second term, RHS). For this, the ocean is assumed to be incompressible, implying that $\boldsymbol{\nabla} \cdot \mathbf{u} = 0$, an assumption which will be shown to be violated due to nonlinearities in the equation of state in Chapter 5. It is assumed that all forcing occurs at the surface of the ocean and any interior effects modifying temperature or salinity, such as the heating due to friction or changes in chemical composition of the seawater due to biogeochemical processes, are either ignored or parameterized as equivalent surface fluxes.

It is possible to separate Eqs. (2.1)-(2.4) into slowly (time-means over the time period) and rapidly varying components (departures from this time-mean) in time,

denoted by $\overline{()}$ and $()'$, respectively, following Joyce (1980, and references therein). To denote spatial means, a subscript $_0$ will be used. This allows these terms to be expanded, noting that the terms $\boldsymbol{\nabla} \cdot (\mathbf{u}'\overline{\xi})$ and $\boldsymbol{\nabla} \cdot (\overline{\mathbf{u}}\xi')$ are identically zero by definition when averaged in time. ξ shall be used to denote any of the variables θ, S, ρ, τ to avoid the quadruple repetition of otherwise identical equations. With this convention, Eqs. (2.1) – (2.4) may thus be written as one generalized conservation equation:

$$\frac{\partial \xi}{\partial t} = \boldsymbol{\nabla} \cdot (\kappa_\xi \boldsymbol{\nabla} \xi - \mathbf{u}\xi) \tag{2.5}$$

which can be separated it into slowly and rapidly varying components:

$$\frac{\partial \overline{\xi}}{\partial t} + \frac{\partial \xi'}{\partial t} = \boldsymbol{\nabla} \cdot (\kappa_\xi \boldsymbol{\nabla} \overline{\xi}) + \boldsymbol{\nabla} \cdot (\kappa_\xi \boldsymbol{\nabla} \xi') - \boldsymbol{\nabla} \cdot (\overline{\mathbf{u}}\overline{\xi}) - \boldsymbol{\nabla} \cdot (\mathbf{u}'\xi') \tag{2.6}$$

When Eq. (2.6) is multiplied with $\overline{\xi}$ and ξ' and the average is taken, the following relationships are obtained, respectively:

$$\overline{\xi}\frac{\partial \overline{\xi}}{\partial t} + \overline{\xi}\frac{\partial \xi'}{\partial t} = \overline{\xi}(\boldsymbol{\nabla} \cdot \kappa_\xi \boldsymbol{\nabla} \overline{\xi}) + \overline{\xi}(\boldsymbol{\nabla} \cdot \kappa_\xi \boldsymbol{\nabla} \xi') - \overline{\xi}(\boldsymbol{\nabla} \cdot (\overline{\mathbf{u}}\overline{\xi})) - \overline{\xi} \cdot (\boldsymbol{\nabla} \cdot (\mathbf{u}'\xi')) \tag{2.7}$$

$$\xi'\frac{\partial \overline{\xi}}{\partial t} + \xi'\frac{\partial \xi'}{\partial t} = \xi'(\boldsymbol{\nabla} \cdot \kappa_\xi \boldsymbol{\nabla} \overline{\xi}) + \xi'(\boldsymbol{\nabla} \cdot \kappa_\xi \boldsymbol{\nabla} \xi') - \xi'(\boldsymbol{\nabla} \cdot (\overline{\mathbf{u}}\overline{\xi})) - \xi' \cdot (\boldsymbol{\nabla} \cdot (\mathbf{u}'\xi')) \tag{2.8}$$

It should be noted that terms with mixed $\overline{()}$ and $()'$ terms are negligible (Joyce, 1980) and that $\boldsymbol{\nabla} \cdot (\overline{\mathbf{u}}\overline{\xi})$ can be expanded to $\overline{\xi}(\boldsymbol{\nabla} \cdot \overline{\mathbf{u}}) + \overline{\mathbf{u}} \cdot (\boldsymbol{\nabla}\overline{\xi})$ where $(\boldsymbol{\nabla} \cdot \overline{\mathbf{u}})$ is identically zero in an incompressible fluid as previously stated. Furthermore, it is assumed that the dissipation of the averaged field, $\overline{\xi}(\kappa_\xi \nabla^2 \overline{\xi})$ is very small and is consequently ignored. Furthermore noting that $\overline{\xi} \cdot \frac{\partial \overline{\xi}}{\partial t} = \frac{1}{2}\frac{\partial}{\partial t}(\overline{\xi^2})$ Eqs. (2.7)-(2.8) can be simplified to, respectively:

$$(\frac{\partial}{\partial t} + \overline{\mathbf{u}} \cdot \boldsymbol{\nabla})\tfrac{1}{2}(\overline{\xi})^2 = -\overline{\xi} \cdot \boldsymbol{\nabla}\overline{(\mathbf{u}'\xi')} \tag{2.9}$$

$$(\frac{\partial}{\partial t} + \overline{\mathbf{u}} \cdot \boldsymbol{\nabla})\tfrac{1}{2}\overline{(\xi')^2} = -\overline{(\mathbf{u}'\xi')} \cdot \boldsymbol{\nabla}\overline{\xi} - \tfrac{1}{2}\chi_\xi + \boldsymbol{\nabla} \cdot \overline{[\kappa_\xi \xi' \boldsymbol{\nabla}\xi' - (\mathbf{u}'\tfrac{1}{2}(\xi')^2)]} \tag{2.10}$$

where χ_ξ is defined as

$$\chi_\xi = 2\kappa_\xi \overline{(\nabla \xi')^2} \tag{2.11}$$

By applying these simplifications, Eq. (2.6) can be written as

$$(\frac{\partial}{\partial t} + \overline{\mathbf{u}} \cdot \boldsymbol{\nabla})\overline{\xi} = -\boldsymbol{\nabla} \cdot \overline{(\mathbf{u}'\xi')} \tag{2.12}$$

The results shown in Eqs. (2.9)-(2.12) have been previously derived for salinity by Stern (1969) and for temperature by Joyce (1980).

Eq. (2.12) can be integrated, noting that flow normal to solid boundaries must vanish at the boundaries in an incompressible fluid, which means that $\mathbf{n} \cdot (\overline{\mathbf{u}} + \mathbf{u}') = \mathbf{n} \cdot \kappa_\xi \boldsymbol{\nabla} \xi' = 0$, where $\mathbf{n}$ is a vector normal to the boundary. The vertical fluxes for θ, S, ρ and τ at the surface are thus given by, respectively:

$$F_\theta = -\overline{\rho_0 c_p} \overline{w'\theta'} = Q_{net} \tag{2.13}$$

$$F_S = \overline{\rho_F} \overline{S_0} (\overline{E - P - R}) \tag{2.14}$$

$$F_\rho = \overline{w'\rho'} \tag{2.15}$$

$$F_\tau = \overline{w'\tau'} \tag{2.16}$$

where ρ_F denotes the time- and spatial mean density of freshwater as it enters the ocean, ρ_0 is the time- and spatial mean density of seawater at the surface , c_p is the time- and spatial mean specific heat capacity of seawater at the surface, and S_0 denotes the mean sea surface salinity in time in space. This follows work by Joyce (1980) for thermal forcing. The definition of the salt flux induced by E-P-R is based on a derivation by (Warren, 2009), but S_0 is used instead of S to ensure that the salt budget closes with a closed freshwater budget. This would not be the case if S were used instead of S_0, since the spatial dependence and patterns of E-P-R would induce an apparent salt flux even when using a balanced (zero mean) freshwater budget.

When the system is in steady state, the following must hold:

$$\frac{1}{\rho_0 c_p} \oiint_A (\overline{F_\theta}) dA = 0 \tag{2.17}$$

$$\frac{1}{\rho_F} \oiint_A (\overline{F_S}) dA = 0 \tag{2.18}$$

$$\oiint_A (\overline{F_\rho}) dA = 0 \tag{2.19}$$

$$\oiint_A (\overline{F_\tau}) dA = 0 \tag{2.20}$$

Eqs. (2.17)–(2.20) state that heat, freshwater, density and spice forcing sum to zero when integrated over the area of the global ocean, since otherwise the ocean could not be in steady state. As will be shown in Chapter 3, this is currently not exactly the case for either heat (due to a net warming of the global oceans) or freshwater (due to more global sea level rise than can be explained by thermal expansion alone), but the deviations from steady-state are small compared to the total values and will consequently be ignored. In the case of density and spice, this condition is only fulfilled when a linearized version of the equation of state is used, as there is a non-zero density (and hence buoyancy) and spice input to the ocean when a full, non-linear equation of state is used. While this may seem counter-intuitive at first, this process is balanced in the interior. This is discussed further in Chapter 5.

When Eqs. (2.9)-(2.12) are integrated using the divergence theorem, assuming that the self-advection term $\overline{(w'\xi')\xi'}$ and the molecular heat flux term are negligible because they are small, one obtains:

$$\frac{1}{\rho_0 c_p} \oiint_A (\overline{\theta} - \theta_0) \overline{F_\theta} dA = - \iiint_V \boldsymbol{\nabla} \overline{\theta} \cdot \overline{\mathbf{u}' \cdot \theta'} dV = \tfrac{1}{2} \iiint_V \chi_\theta dV \tag{2.21}$$

$$\frac{1}{\rho_F} \oiint_A (\overline{S} - S_0) \overline{F_S} dA = - \iiint_V \boldsymbol{\nabla} \overline{S} \cdot \overline{\mathbf{u}' \cdot S'} dV = \tfrac{1}{2} \iiint_V \chi_S dV \tag{2.22}$$

$$\oiint_A (\overline{\rho} - \rho_0) \overline{F_\rho} dA = - \iiint_V \boldsymbol{\nabla} \overline{\rho} \cdot \overline{\mathbf{u}' \cdot \rho'} dV = \tfrac{1}{2} \iiint_V \chi_\rho dV \tag{2.23}$$

$$\oiint_A ((\overline{\tau} - \tau_0) \overline{F_\tau}) dA = - \iiint_V \boldsymbol{\nabla} \overline{\tau} \cdot \overline{\mathbf{u}' \cdot \tau'} dV = \tfrac{1}{2} \iiint_V \chi_\tau dV \tag{2.24}$$

where θ_0, S_0, ρ_0 and τ_0 are spatial and temporal means of surface θ, S, ρ and τ, respectively. While the subtraction of this constant is not technically necessary, it minimizes numerical errors in the computations and prevents the artificial amplification of the implied non-conservation of density and spice fluxes. This issue is discussed further in Chapter 5. In these equations, one sees that the variance generated by surface forcing is equal to the down-gradient flux in the interior and its respective dissipation by mixing.

2.2 Variance-Dissipation Relation with a Linear Equation of State

An analysis of density and spice variance relations using the full equation of state for seawater density is not practical, since this would involve multiplying 40 terms (McDougall, 2011) with each other. While this is theoretically feasible, the insight gained by such an exercise in relating forcing and dissipation components to each other would be lost. As a consequence, a linear approximation is used here to evaluate the fundamental physics, while its primary nonlinearity that involves a cabbeling term (McDougall, 1986) is evaluated in Chapter 5.

The linearized equation of state is given by:

$$\rho = \rho_0(1 - \alpha(\theta - \theta_0) + \beta(S - S_0)) \tag{2.25}$$

where α and β are the thermal and haline coefficients, respectively, which are defined as constants, but depend on the θ and S reference values (θ_0 and S_0, respectively). They are defined as:

$$\alpha = -\frac{1}{\rho_0} \cdot \left.\frac{\partial \rho}{\partial \theta}\right|_{S,p} \tag{2.26}$$

$$\beta = \frac{1}{\rho_0} \cdot \left.\frac{\partial \rho}{\partial S}\right|_{\theta,p} \tag{2.27}$$

In equation (2.25), the density is referenced to a salinity and density reference (ρ_0) with a linear expansion around this point based on the thermal coefficient (2nd term, RHS) and haline coefficient (3rd term, RHS) of seawater. Since an increase in temperature yields an expansion, the density is reduced as water is heated, making

the thermal expansion term negative. When salinity is increased, the density also increases. This is true from most seawater, but it should be noted that while increasing the salinity of water always increases its density, in water that is very fresh the thermal expansion coefficient may in fact change sign, as is the case with freshwater which has its greatest possible density at $\approx 4\,^{\circ}\mathrm{C}$. For this reason, I will refer to the coefficients α and β as 'thermal coefficient' and 'haline coefficient'.

Similarly, for spice (Veronis, 1972; Schmitt, 1999; Huang, 2011), the following linear approximation is used:

$$\tau = \tau_0(1 + \alpha(\theta - \theta_0) + \beta(S - S_0)) \tag{2.28}$$

with identical definitions as for the density equation. To simplify the notation in the following derivation, θ and S are defined to be the deviation from a mean state:

$$\theta = \theta - \theta_0 \tag{2.29}$$

$$S = S - S_0 \tag{2.30}$$

Adopting this simplified notation, the linearized density and spice equations may thus be written as:

$$\rho = \rho_0(1 - \alpha\theta + \beta S) \tag{2.31}$$

$$\tau = \tau_0(1 + \alpha\theta + \beta S)) \tag{2.32}$$

The actual values of α, β, S_0 and T_0 (and hence also ρ_0 and τ_0) are computed as the spatial and temporal mean of the datasets that are presented in Chapter 3.

The difference between the full nonlinear equation of seawater and the linear approximation is illustrated in Figure 2-1 in a temperature-salinity plot, indicating lines of constant density (as color contours) and lines of constant spice (as solid contours). The curvature of lines of constant density, which leads to the effect of cabbeling (e.g. McDougall, 1986, and references therein), is absent in the linear system.

Cabbeling is the formation of a water mass that is denser than the linear combination of the formation water masses (McDougall, 1986). This becomes clear when the nonlinear density-function in Figure 2-1 is considered. If 50% of a water mass of

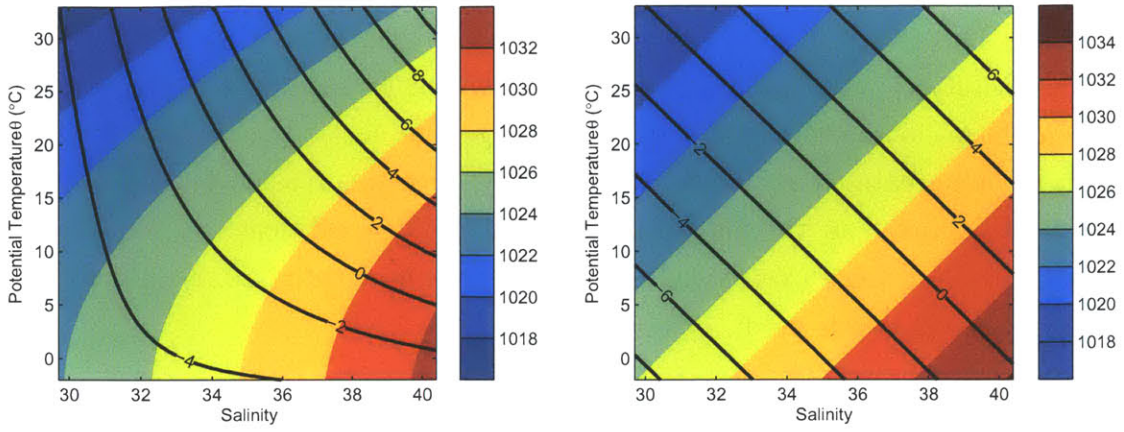

Figure 2-1: Contours of constant density (isopycnals) and constant spice are indicated by filled contours and solid lines, respectively. While the full nonlinear equation of state is used to produce the left panel, the linear approximations (Eqs. 2.31, 2.32) are shown in right panel. The spice zero-crossing is chosen as S=35, θ=0.

$\theta = 0°, S = 30$ and 50% with $\theta = 30, S = 38$ are mixed, both of which have a density of approximately $1024\,\mathrm{kg\,m^{-3}}$, the resulting water mass has a density in excess of $1025\,\mathrm{kg\,m^{-3}}$. While this is not a realistic example, the effect is an important process in the ocean. Amongst other things it compensates for a net input of buoyancy (or loss of density) by surface forcing. That is, the larger thermal expansion coefficient at high temperatures assures that more thermal buoyancy is put into the ocean than is extracted by cooling at low temperatures. Thus, the surface integral of the density flux is non-zero, even when the global heat flux is balanced. This apparent paradox is explained by the contraction on mixing due to cabbeling. McDougall and Garrett (1992) show that we should expect convergence ($\boldsymbol{\nabla} \cdot \mathbf{u}$) to be approximately balanced by the product of the second derivative of density with respect to temperature and the dissipation. This relation is used to quantify the effects of the nonlinearity of the equation of state (McDougall, 1986; Jackett et al., 2006) in Chapter 5.

When Eq. (2.31) is evaluated in Eq. (2.23), noting that when the system is in steady state, i.e. if the net oceanic heat flux and E-P-R are in global balance, ρ_0 is a constant and hence vanishes in both the area integral (variance production) and the volume integral (variance dissipation). One thus obtains:

$$\begin{aligned}\tfrac{1}{2}\iiint_V \chi_\rho dV &= -\oiint_A [-\alpha\overline{\theta} + \beta\overline{S}] \cdot [-\alpha\overline{w'\theta'} + \beta\overline{w'S'}]dA \\ &= -\iiint_V \boldsymbol{\nabla}(-\alpha\overline{\theta} + \beta\overline{S}) \cdot \overline{\mathbf{u}' \cdot (-\alpha\theta' + \beta S')}dV\end{aligned} \tag{2.33}$$

Expanding terms, one obtains:

$$\begin{aligned}\tfrac{1}{2}\iiint_V \chi_\rho dV &= -\oiint_A [\alpha^2\overline{\theta w'\theta'} - \alpha\beta\overline{\theta w'S'} - \alpha\beta\overline{Sw'\theta'} + \beta^2\overline{Sw'S'}]dA \\ &= -\iiint_V [\alpha^2\overline{\theta'\mathbf{u}'} \cdot \boldsymbol{\nabla}\overline{\theta} - \alpha\beta\overline{S'\mathbf{u}'} \cdot \boldsymbol{\nabla}\overline{\theta} \\ &\quad -\alpha\beta\overline{\theta'\mathbf{u}'} \cdot \boldsymbol{\nabla}\overline{S} + \beta^2\overline{S'\mathbf{u}'} \cdot \boldsymbol{\nabla}\overline{S}]dV\end{aligned} \tag{2.34}$$

The RHS of Eq. (2.34) is comprised of the heat flux down the temperature gradient, the salt flux down the salt gradient, the heat flux down the salt gradient and the salt flux down the temperature gradient, respectively. When spice is evaluated using Eq. (2.32) in Eq. (2.24), one finds:

$$\begin{aligned}\tfrac{1}{2}\iiint_V \chi_\tau dV &= -\oiint_A [\alpha^2\overline{\theta w'\theta'} + \alpha\beta\overline{\theta w'S'} + \alpha\beta\overline{Sw'T'} + \beta^2\overline{Sw'S'}]dA \\ &= -\iiint_V [\alpha^2\theta'\overline{\mathbf{u}'} \cdot \boldsymbol{\nabla}\overline{\theta} + \alpha\beta\overline{S'\mathbf{u}'} \cdot \boldsymbol{\nabla}\overline{\theta} \\ &\quad +\alpha\beta\overline{\theta'\mathbf{u}'} \cdot \boldsymbol{\nabla}\overline{S} + \beta^2\overline{S'\mathbf{u}'} \cdot \boldsymbol{\nabla}\overline{S}]dV\end{aligned} \tag{2.35}$$

We then separate the three-dimensional derivative into isopycnal and diapycnal components, following McDougall (1987):

$$\boldsymbol{\nabla} = \boldsymbol{\nabla}_i + \boldsymbol{\nabla}_d \tag{2.36}$$

where the subscript i denotes isopycnal and the subscript d denotes diapycnal gradients. Moreover, the three-dimensional velocity fluctuation vector $\mathbf{u}'$ is separated into isopycnal and diapycnal components, yielding:

$$\mathbf{u}' = \mathbf{u}'_i + \mathbf{u}'_d \tag{2.37}$$

where $\mathbf{u}'_d$ will be close to w' (the vertical component of the velocity fluctuation vector) in most (but not all) parts of the ocean. Using the definitions in Eqs. (2.36)-(2.37), the balance of surface density flux forcing to down-gradient dissipation given by Eq. (2.34) then becomes:

$$\begin{aligned}
\tfrac{1}{2}\iiint_V \chi_\rho dV &= -\oiint_A [\alpha^2\overline{\theta w'\theta'} - \alpha\beta\overline{\theta w' S'} - \alpha\beta\overline{S w'\theta'} + \beta^2\overline{S w' S'}]dA \\
&= -\iiint_V [\alpha^2\overline{\theta'\mathbf{u}'_i}\cdot\boldsymbol{\nabla}_i\overline{\theta} + \alpha^2\overline{\theta'\mathbf{u}'_d}\cdot\boldsymbol{\nabla}_d\overline{\theta} - \alpha\beta\overline{S'\mathbf{u}'_i}\cdot\boldsymbol{\nabla}_i\overline{\theta} \\
&\quad -\alpha\beta\overline{S'\mathbf{u}'_d}\cdot\boldsymbol{\nabla}_d\overline{\theta} - \alpha\beta\overline{\theta'\mathbf{u}'_i}\cdot\boldsymbol{\nabla}_i\overline{S} - \alpha\beta\overline{\theta'\mathbf{u}'_d}\cdot\boldsymbol{\nabla}_d\overline{S} \\
&\quad +\beta^2\overline{S'\mathbf{u}'_i}\cdot\boldsymbol{\nabla}_i\overline{S} + \beta^2\overline{S'\mathbf{u}'_d}\cdot\boldsymbol{\nabla}_d\overline{S}]dV
\end{aligned} \tag{2.38}$$

Similarly, using these definitions, the spice equation (Eq. (2.35)) becomes:

$$\begin{aligned}
\tfrac{1}{2}\iiint_V \chi_\tau dV &= -\oiint_A [\alpha^2\overline{\theta w'\theta'} + \alpha\beta\overline{\theta w' S'} + \alpha\beta\overline{S w' T'} + \beta^2\overline{S w' S'}]dA \\
&= -\iiint_V [\alpha^2\overline{\theta'\mathbf{u}'_i}\cdot\boldsymbol{\nabla}_i\overline{\theta} + \alpha^2\overline{\theta'\mathbf{u}'_d}\cdot\boldsymbol{\nabla}_d\overline{\theta} + \alpha\beta\overline{S'\mathbf{u}'_i}\cdot\boldsymbol{\nabla}_i\overline{\theta} \\
&\quad +\alpha\beta\overline{S'\mathbf{u}'_d}\cdot\boldsymbol{\nabla}_d\overline{\theta} + \alpha\beta\overline{\theta'\mathbf{u}'_i}\cdot\boldsymbol{\nabla}_i\overline{S} + \alpha\beta\overline{\theta'\mathbf{u}'_d}\cdot\boldsymbol{\nabla}_d\overline{S} \\
&\quad +\beta^2\overline{S'\mathbf{u}'_i}\cdot\boldsymbol{\nabla}_i\overline{S} + \beta^2\overline{S'\mathbf{u}'_d}\cdot\boldsymbol{\nabla}_d\overline{S}]dV
\end{aligned} \tag{2.39}$$

re-arranging and collecting terms, Eq. (2.38) becomes:

$$\begin{aligned}
\tfrac{1}{2}\iiint_V \chi_\rho dV &= -\oiint_A [\alpha\overline{\theta}(\alpha\overline{w'\theta'} - \beta\overline{w' S'}) + \beta\overline{S}(-\alpha\overline{w'\theta'} + \beta\overline{w' S'})]dA \\
&= -\iiint_V [\alpha\boldsymbol{\nabla}_i\overline{\theta}\cdot(\alpha\overline{\theta'\mathbf{u}'_i} - \beta\overline{S'\mathbf{u}'_i}) + \alpha\boldsymbol{\nabla}_d\overline{\theta}\cdot(\alpha\overline{\theta'\mathbf{u}'_d} - \beta\overline{S'\mathbf{u}'_d}) \\
&\quad +\beta\boldsymbol{\nabla}_i\overline{S}\cdot(\beta\overline{S'\mathbf{u}'_i} - \alpha\overline{\theta'\mathbf{u}'_i}) + \beta\boldsymbol{\nabla}_d\overline{S}\cdot(\beta\overline{S'\mathbf{u}'_d} - \alpha\overline{\theta'\mathbf{u}'_d})]dV
\end{aligned} \tag{2.40}$$

Similarly, the spice variance-dissipation relation (Eq. 2.39) can be written as:

$$\begin{aligned}\tfrac{1}{2}\iiint_V \chi_\tau dV &= -\oiint_A [\alpha\overline{\theta}(\alpha\overline{w'\theta'} + \beta\overline{w'S'}) + \beta\overline{S}(\alpha\overline{w'T'} + \beta\overline{w'S'})]dA \\ &= -\iiint_V [\alpha\boldsymbol{\nabla}_i\overline{\theta}\cdot(\alpha\overline{\theta'\mathbf{u}_i'} + \beta\overline{S'\mathbf{u}_i'}) + \alpha\boldsymbol{\nabla}_d\overline{\theta}\cdot(\alpha\overline{\theta'\mathbf{u}_d'} + \beta\overline{S'\mathbf{u}_d'}) \\ &\quad +\beta\boldsymbol{\nabla}_i\overline{S}\cdot(\beta\overline{S'\mathbf{u}_i'} + \alpha\overline{\theta'\mathbf{u}_i'}) + \beta\boldsymbol{\nabla}_d\overline{S}\cdot(\beta\overline{S'\mathbf{u}_d'} + \alpha\overline{\theta'\mathbf{u}_d'})]dV\end{aligned} \tag{2.41}$$

By definition, along neutral surfaces, the decrease in density due to an increase in potential temperature is compensated by the increase in density due to increased salinity (McDougall, 1987), and so it follows that:

$$\alpha\cdot\boldsymbol{\nabla}_i\overline{\theta} = \beta\cdot\boldsymbol{\nabla}_i\overline{S} \tag{2.42}$$

so that all terms with an isopycnal gradient term in Eq. (2.40) cancel:

$$\begin{aligned}\tfrac{1}{2}\iiint_V \chi_\rho dV &= -\oiint_A [(\alpha\overline{\theta} - \beta\overline{S})(\alpha\overline{w'\theta'} - \beta\overline{w'S'})]dA \\ &= -\iiint_V [(\alpha\boldsymbol{\nabla}_d\overline{\theta} - \beta\boldsymbol{\nabla}_d\overline{S})\cdot(\alpha\overline{\theta'\mathbf{u}_d'} - \beta\overline{S'\mathbf{u}_d'})]dV\end{aligned} \tag{2.43}$$

This states the intuitive result that the surface production of density variance must be balanced by the diapycnal density flux across the density gradient in the ocean interior.

Since the gradient of spice is perpendicular to that of density, it follows that isopycnal gradients compensate similarly to Eq. (2.42). In the diapycnal direction, along lines of constant spice, the decrease in density due to an increase in temperature is compensated by the increase in density due to increased salinity so that

$$-\alpha\cdot\boldsymbol{\nabla}_d\overline{\theta} = \beta\cdot\boldsymbol{\nabla}_d\overline{S} \tag{2.44}$$

which can be used to simplify Eq. (2.41). As a consequence, all diapycnal gradients vanish so that:

$$\begin{aligned}\tfrac{1}{2}\iiint_V \chi_\tau dV &= -\oiint_A [(\alpha\overline{\theta}+\beta\overline{S})(\alpha\overline{w'\theta'}+\beta\overline{w'S'})]dA \\ &= -\iiint_V [(\alpha\boldsymbol{\nabla}_i\overline{\theta}+\beta\boldsymbol{\nabla}_i\overline{S})\cdot(\alpha\overline{\theta'\mathbf{u}_i'}+\beta\overline{S'\mathbf{u}_i'})]dV\end{aligned} \tag{2.45}$$

This equation states that spice variance is dissipated by the isopycnal flux along isopycnal surfaces. Further progress in the density and spice variance relations can be made if we cast the variables in terms of one component, here chosen to be the heat fluxes and gradients. The density variance relation can be further simplified by defining two quantities. The ratio of diapycnal thermal to saline density fluxes is called the flux ratio (γ) and is defined as (Schmitt, 1994):

$$\gamma = \frac{\alpha\cdot\overline{\mathbf{u}_d'\theta'}}{\beta\cdot\overline{\mathbf{u}_d'S'}} \tag{2.46}$$

At the ocean surface, this can be expressed in terms of the haline and thermal components of the total density flux, which may be defined as:

$$F_\rho = F_{\rho S} - F_{\rho\theta} = \rho_0(\frac{1}{\rho_F}\beta F_S - \frac{1}{c_p\rho_0}\alpha F_\theta) \tag{2.47}$$

which is combined with Eqs. (2.13) & (2.14) to give:

$$F_\rho = F_{\rho S} - F_{\rho\theta} = \left(\frac{\rho_0}{\rho_F}\beta S_0(E-P-R)\right) - \left(\frac{1}{c_p}\alpha Q_{net}\right) \tag{2.48}$$

so that at the surface the flux ratio (γ) may be written as:

$$\gamma = \frac{-F_\theta}{F_S} = \frac{-\frac{1}{c_p}\alpha Q_{net}}{\frac{\rho_0}{\rho_F}\beta S_0(E-P-R)} \tag{2.49}$$

The density ratio (R_ρ) is the ratio of the diapycnal thermal density gradient to the haline density gradient (Schmitt, 1994) and is given by:

$$R_\rho = \frac{\alpha\boldsymbol{\nabla}_d\overline{\theta}}{\beta\boldsymbol{\nabla}_d\overline{S}} \tag{2.50}$$

Using these definitions Eq. (2.43) can be re-written as:

$$\begin{aligned}\tfrac{1}{2}\iiint_V \chi_\rho dV &= -\oiint_A [(\alpha\overline{\theta} - \beta\overline{S})(\alpha\overline{w'\theta'} - \beta\overline{w'S'})]dA \\ &= -\iiint_V \left[(\alpha\boldsymbol{\nabla}_d\overline{\theta}\cdot\left(1-\frac{1}{R_\rho}\right)\cdot\alpha\overline{\theta'\mathbf{u}'_d}\cdot\left(1-\frac{1}{\gamma}\right)\right]dV\end{aligned} \tag{2.51}$$

$$\begin{aligned}\tfrac{1}{2}\iiint_V \chi_\rho dV &= -\oiint_A [(\alpha\overline{\theta} - \beta\overline{S})(\alpha\overline{w'\theta'} - \beta\overline{w'S'})]dA \\ &= -\iiint_V \left[(\alpha^2\boldsymbol{\nabla}_d\overline{\theta}\cdot(\overline{\theta'\mathbf{u}'_d})\cdot\left(\frac{R_\rho-1}{R_\rho}\right)\cdot\left(\frac{\gamma-1}{\gamma}\right)\right]dV\end{aligned} \tag{2.52}$$

The terms involving the density ratio and flux ratio in Eq. (2.52) may be interpreted in terms of turbulent and double-diffusive processes. For turbulence, we expect $\gamma = R_\rho$, as heat and salt are mixed equally well down their respective gradients. We furthermore expect double diffusion to have a flux ratio < 1 and a strong dependence on the density ratio (St. Laurent and Schmitt, 1999). These differences may provide the possibility of diagnosing the relative importance of these two processes in diapycnal mixing.

Conventional turbulence mixing with $\gamma = R_\rho$ leads to a relation:

$$\begin{aligned}\tfrac{1}{2}\iiint_V \chi_\rho dV &= -\oiint_A [(\alpha\overline{\theta} - \beta\overline{S})(\alpha\overline{w'\theta'} - \beta\overline{w'S'})]dA \\ &= -\iiint_V \left[(\alpha^2\boldsymbol{\nabla}_d\overline{\theta}\cdot(\overline{\theta'\mathbf{u}'_d})\cdot\left(\frac{R_\rho-1}{R_\rho}\right)^2\right]dV\end{aligned} \tag{2.53}$$

If we assume that much of the diapycnal dissipation occurs by turbulence in the main thermocline of the Central Waters where $R_\rho \approx 2$, then we expect the diapycnal density dissipation to be about $^1/_4$of the vertical temperature dissipation when scaled in density units.

However, there is good evidence that salt fingers are active in the $R_\rho \approx 2$ Central Waters (St. Laurent and Schmitt, 1999), so we must consider the effect of $\gamma < 1$. This changes the sign of the relation, indicating that density variance can be internally generated when double diffusion is active. This is always observed in laboratory experiments (Turner, 1979); temperature and salinity contrasts are decreased but

density contrasts are increased by the action of double diffusion.

Of course, the regions where double diffusion is dominant are limited in extent; the thermohaline staircase of the tropical North Atlantic occupies about 10 % of the area of the N. Atlantic subtropical gyre. Also, we expect that in the majority of the $R_\rho \approx 2$ Central Waters the net effective flux ratio due to a mix of salt fingers and turbulence will be about one. This means that those regions could have very little effect on the destruction of density variance, while still contributing to significant dissipation of heat and salt variance.

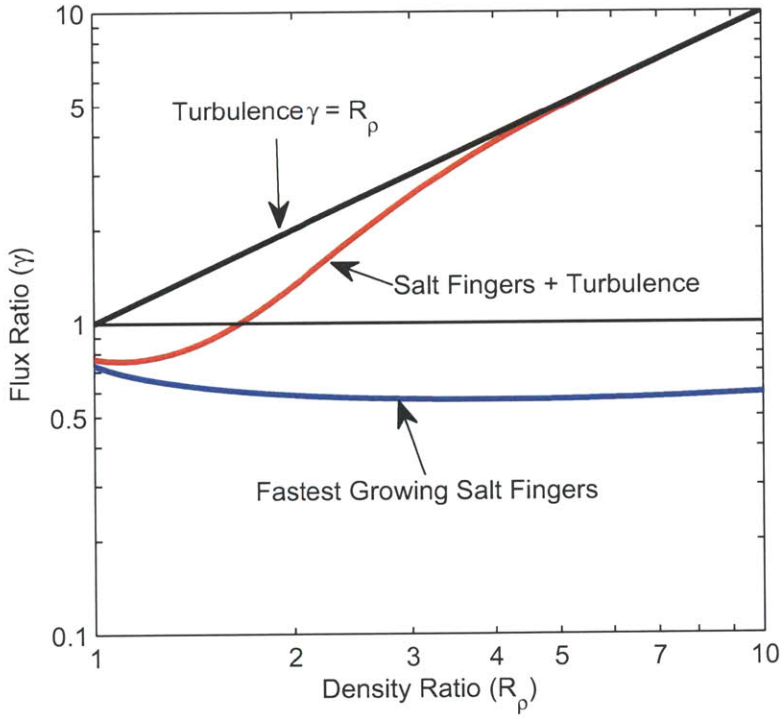

Figure 2-2: The influence of turbulence and salt fingers in producing or destroying variance for a range of flux ratios (γ) and density ratios (R_ρ). The area above 1 leads to variance destruction while the area below 1 indicates the production of density variance through salt finger fluxes. The influence of turbulence is drawn as a solid black line and salt finger effects are drawn as a solid blue line. The combined effect is indicated in red. This has a unity crossing and consequently changes from production to dissipation at R_ρ =1.66. Adapted from Zhang and Schmitt (2000) using a maximum growth model from Schmitt (1979).

Figure 2-2 shows theoretical estimates of the flux ratio γ as a function of R_ρ, as well as a speculative curve representing the fastest growing fingers and turbulence

and is adapted from Zhang and Schmitt (2000) using a maximum growth salt finger model from Schmitt (1979). This curve is inferred from the observed tendency for staircases (which can only be maintained with a counter gradient density flux) to occur only when $R_\rho < 1.66$. It is similar in shape to curves inferred by Radko (2007, 2008) in his staircase formation models.

A full census of the interior density ratio distribution, and the associated dissipation is beyond the scope of this thesis, but does provide prospects for future progress. It may be possible to infer the relative importance of turbulent and double-diffusive mixing in the global ocean, with the overall surface production of density variance providing a constraint. That is, double diffusion is tending to stratify the ocean and it will need to be compensated by a certain amount of turbulence, with the sum of the interior processes meeting the surface variance production constraint provided by Eq. (2.52).

Further, we can also write the spice variance relation in terms of heat fluxes and gradients only:

$$\begin{aligned} \tfrac{1}{2}\iiint_V \chi_\tau dV &= -\oiint_A [(\alpha\overline{\theta} + \beta\overline{S})(\alpha\overline{w'\theta'} + \beta\overline{w'S'})]dA \\ &= -\iiint_V (2\alpha\boldsymbol{\nabla}_i\overline{\theta}) \cdot (2\alpha\overline{\theta'\mathbf{u}_i'})dV \end{aligned} \tag{2.54}$$

which can be simplified to

$$\begin{aligned} \tfrac{1}{2}\iiint_V \chi_\tau dV &= -\oiint_A [(\alpha\overline{\theta} + \beta\overline{S})(\alpha\overline{w'\theta'} + \beta\overline{w'S'})]dA \\ &= -4\alpha^2 \iiint_V \boldsymbol{\nabla}_i\overline{\theta} \cdot \overline{\theta'\mathbf{u}_i'}dV \end{aligned} \tag{2.55}$$

Equations 2.52 & 2.45 have components of diapycnal (for density) and isopycnal (for spice) dissipation. The spice variance equation is thus the 'isopycnal analogue' of the density variance equation, and based on this, it will be possible to gain a first-order insight into the relative importance of isopycnal and diapycnal dissipation of thermal and haline variance. The limitations due to the approximations made in deriving this relation should not be neglected, however. These limitations include a lack of a cabbeling term in the present equations. Pressure effects and internal

heat inputs have been ignored also. However, to first order the results found can be used with the presented global estimates of Q_{net}, E-P-R, SST and SSS to gain an understanding of the relative strengths of isopycnal and diapycnal mixing.

Chapter 3

Ocean Surface Variables

In this chapter, all quantities required to evaluate the relations presented in Chapter 2 are addressed. The objective here is to find the current best-estimates of all fields, both as time-means and time-series. The required variables are sea surface temperature (SST), sea surface salinity (SSS), oceanic surface freshwater fluxes consisting of evaporation (E), precipitation (P) and riverine runoff (R) as E-P-R, the net heat flux at the sea surface (Q_{net}) as well as derived variables from these primary variables. These derived variables are computed using the Thermodynamic Equation of State 2010 (TEOS-10, IOC et al. (2011); McDougall (2011)), which consists of a set of thermodynamically self-consistent equations and computer routines.

There are a number of such estimates available, covering different time periods and in resolutions ranging from 2.5° × 2.5° to kilometer-grids. Similarly, the temporal resolution varies from a temporal mean product to 3-hourly fields. There are two basic sources of such estimates: *in-situ* observations (including remotely sensed fields) and the outputs of numerical models, such as re-analyses. The differences and relative strengths and weaknesses of these products are discussed in Section 3.1.

A homogeneity analysis of a number of E and P products indicates that since the introduction of the Special Sensor Microwave Imager (SSM/I) (Goodberlet et al., 1990) in July of 1987, the quality and quantity of available fields have been relatively homogeneous, and I thus choose the common period of 1987–2004 as the baseline for both generating time-mean fields of all variables and as the period in which the effects of seasonal variations are explored using monthly mean fields. Not all products are available from 1987: The ECCO2 state estimate (Menemenlis et al., 2008), for example, only starts in 1992. In such cases, the longest possible common period in

the 1987–2004 range (in this case, 1992–2004) is used.

Based on this analysis, a number of 'baseline' products are chosen, which will be used to produce graphical representations of the results in Chapter 4. However, the uncertainties in the covariances and error covariances between the products used in this study may result in a flawed estimate of the total error. I thus repeat all calculations with a number of different commonly available products to indicate likely upper and lower bounds on these estimates. As it is possible that there are systematic errors common to all estimates, I also perform two types of sensitivity analysis: a simple scale analysis as well as a biased offset computed with full 1° fields. This is presented in Chapter 4.8.

In addition to differences in temporal and spatial resolution between products, the spatial coverage also differs due to slightly different landmasks and different definitions of sea-ice at high latitudes. To allow an efficient computation of the values for all estimates, all fields are re-sampled to a $1° \times 1°$ resolution and a common landmask (that of ECCO2) is applied to all products. In computing the mean field in areas that have partial coverage, such as areas that are sometimes covered by sea ice, zero fluxes are assumed for nonexistent or undefined grid points. For example, if a grid point is covered by sea-ice for 10 out of 12 months but has a net heat input of $20\,\mathrm{W\,m^{-2}}$ during the remaining 2 months, I take the time-mean input to be $(20 + 20)/12 \approx 3.3\,\mathrm{W\,m^{-2}}$. The riverine runoff estimate compiled from Dai and Trenberth (2002); Dai et al. (2009) is re-sampled to the closest point defined as ocean by the common landmask, where it is added to the balance of E-P-R.

3.1 New Sources of Estimates

There are two main methods to produce a global gridded estimate of E, P or Q_{net}: the use of computational models, most commonly (re-)analyses (RA) and the use of statistical methods, such as objective analysis (OA). Both methods are heavily dependent on the input fields and data to which they are constrained (see e.g. Wunsch and Heimbach, 2007). In this section, I discuss basic properties as well as merits and problems of both types of products.

While the availability of land-based measurements is limited both spatially and temporally, it is abundant in contrast with even sparser historical observations over the ocean. Before the advent of oceanographic satellites, ship-borne *in-situ* measure-

ments were needed to gather data. Large areas which were not frequented by vessels, such as the Southern Ocean, remained virtually unsampled. This situation would only change with the availability of various satellite sensors that allow the determination of five primary oceanic variables: sea surface temperature (SST), sea surface salinity (SSS), sea surface roughness, which to first order is a function of wind speed, U_{air}, ocean color and sea surface height (Robinson, 2004). Additionally, it is possible to gain insight into various atmospheric parameters, such as moisture content, primarily through satellite-borne active radar instruments. Such estimates also allow a basic quantification of precipitation. Radiation budgets may be measured from space, such as the total incoming shortwave radiation (Q_{SW}) or the outgoing longwave radiation (Q_{LW}), but since these are measured above the atmosphere, it is difficult to estimate these fluxes at the ocean surface (e.g. Zhang et al., 2004, and references therein).

From the primary variables it is possible to derive – by the use of empirical formulas and data assimilation models – evaporation, sensible and latent heat flux fields as well as precipitation over the ocean on a near-global scale with good temporal and spatial resolution. The incoming shortwave and outgoing longwave fluxes require the use of radiative transfer models and cloud estimates, which are associated with large uncertainties (e.g. Zhang et al., 2004, and references therein).

The advances in computer technology in the last few decades have facilitated the use of computational fluid dynamics and numerical weather prediction for large coupled ocean-atmosphere data assimilation models such as those of the National Center for Environmental Prediction/National Center for Atmospheric Research (NCEP/NCAR) and the European Centre for Medium-Range Weather Forecasts (ECMWF). These RA models enable the computation of the time-evolution of a given state and seek to minimize the error between a computed state and given observations at a later time. As a consequence, it is possible to 'fill in' the gaps in regions with low data density based on our physical understanding of the system and parameterizations of governing processes which are too complex to model directly. However, even basic physical constraints such as a closure of the global water cycle is frequently violated in re-analysis models, making them physically inconsistent (e.g. Quartly et al., 2007; Yu et al., 2008). The input fields used to constrain such models are not limited to *in-situ* data, but generally include remotely sensed satellite estimates, such as SST, U_{air} and remotely sensed atmospheric fields. The outputs of such models are in widespread use today. Such models include the NCEP/NCAR Global Reanal-

ysis Project 1 (Kistler et al., 2001), hereafter NCEP-1, available from 1948–present, the NCEP/NCAR Global Reanalysis Project 2 (Kanamitsu et al., 2002), hereafter NCEP-2, which is constrained to satellite data for the entirety of the analysis period (1979–present), the Modern Era Retrospective-Analysis for Research and Applications (Bosilovich et al., 2006), hereafter MERRA (1979–present), the ECMWF Re-Analysis 40 (Uppala et al., 2005), hereafter ERA-40, which is available 1957–2002, as well as follow-on projects of the ECMWF, such as the ERA-Interim product (Simmons et al., 2007).

The other method to produce a regularly spaced global estimate of a given variable is objective analysis, which is a statistical model for gridding irregularly spaced data based on de-correlation time- and space-scales. It is also used to combine regularly gridded datasets or products with different error estimates. Using weightings based on the error estimates provided by each of input fields, it is possible to produce an objectively analyzed product (e.g. Yu and Weller, 2007; Yu et al., 2008, and references therein). The OA of data is based on a statistical rather than a physical model. Consequently, unlike a re-analysis, its purpose is not to predict the time-evolution of the system, but to find the optimal solution of an objective function. Since the objective function is weighted proportionally to the error covariance of the input data, more weight is given to data with lower error estimates (Yu et al., 2008). The homogeneity of objectively analyzed products is thus highly dependent on the quality and quantity of the input data.

The properties of both types of estimates are evaluated in the next sections by analyzing the homogeneity and closure of two OA based E products, five RA based E products, three OA based P products and four RA based P products (see Table 3.1). A homogeneity analysis of OAFlux Q_{net} is used to assess the similarities in homogeneity E and Q_{net} and the closure of 9 Q_{net} products is analyzed. Brief literature reviews of inter-comparisons of global E and P estimates are used to assess the overall suitability of the products to produce a global multi-decadal estimate of oceanic freshwater- and heat fluxes. Since the variables needed to estimate oceanic surface heat fluxes are very similar to those used in E estimates, the time-period identified as homogeneous for E and P is used for Q_net also. Due to the necessity of balancing the estimates to have a zero net global flux, the imbalances found in 9 Q_{net} products are also discussed. The sensitivity of these estimates to systematic bias towards the poles or equator is addressed analytically and through a simple sensitivity analysis in Chapter 4.8.

3.1.1 New Evaporation Estimates

For a robust estimate of evaporation using the bulk flux formula (Fairall et al., 2003), the SST, the surface wind speed at 10 m, the specific humidity and the temperature of the air overlying the sea surface at 2 m must be known. Of these four variables, two are readily observable from satellites. SST can be inferred from measuring the infrared- and microwave-emissivity of the sea surface, while wind speed can be determined from scattering, attenuation or variability of an active radar signal from a satellite (e.g. Robinson, 2004, and references therein). It is also possible to determine the atmospheric moisture content and hence surface humidity with active radar sensors (Schulz et al., 1993; Chou et al., 1995, 2003), though such estimates are not in widespread use. While observations of atmospheric temperatures are in principle possible from satellite platforms, measurements sufficiently near the sea surface ($\approx$ 2 m) are not possible or are indistinguishable from SST (Divakarla et al., 2006). Consequently, this quantity is commonly derived from *in-situ* measurements or from re-analysis models (Yu et al., 2008).

To understand historical data limitations, one must consider the temporal evolution of data availability. This time-line is summarized in Table 3.2. While high-resolution SST data became available as early as 1978, and continuously available from 1982 onwards, the accuracy of observations from the Advanced Very High Resolution Radiometer (AVHRR) was significantly improved with a match-up database to buoy measurements which started in 1985 (Smith et al., 1996). The Defense Meteorological Satellite Program's (DMSP) first Special Sensor Microwave Imager (SSM/I) instrument was operational in July 1987 and has been continued by follow-on missions (e.g. Robinson, 2004, and references therein). This sensor has brought about several enhancements for variables used in both evaporation and precipitation estimates. For evaporation, SSM/I was the first satellite to provide estimates of sea surface roughness, and consequently a global picture of wind speeds (Goodberlet et al., 1990) as well as specific surface humidity from column water vapor estimates (Chou et al., 2003).

3.1.2 New Precipitation Estimates

Due to its ability to determine water vapor content, the SSM/I mission made it possible to estimate precipitation based on attenuation of high-frequency radar due

to volume scattering of precipitation, particularly those of freezing ice crystals at high altitudes. Information on the vertical humidity structure of the air can be inferred by the differential attenuation of four radar bands ranging from $19.35 - 85.5\,\mathrm{GHz}$ (Spencer et al., 1989). The lower frequencies are dominated by precipitation above the freezing level, and from this the type of precipitation can be estimated (Spencer et al., 1989). Since rainfall is transient and localized, it is necessary to maximize the temporal sampling. While the re-visit interval of approximately 1 day is temporally inferior to a long term *in-situ* precipitation measuring station, the spatial coverage, particularly over the ocean, is vastly superior.

Since a strong correlation exists between the height and temperature of the top of tropical clouds and precipitation, it is possible to use infrared measurements from geostationary satellites to provide the necessary temporal coverage for precipitation estimates (e.g. Adler et al., 2003, and references therein). However, such observations are spatially limited to the area over which the satellite is positioned, and the empirical relationship between cloud-height and cloud-top temperature and the resulting precipitation is influenced by other parameters, with estimation uncertainties increasing towards higher latitudes. For this reason, precipitation estimates are superior in tropical and sub-tropical regions compared to poor spatial and temporal coverage in polar and sub-polar regions.

More recent satellite data sources, such as the Tropical Rainfall Measuring Mission (TRMM) are able to provide even better estimates of precipitation due to dedicated on-board precipitation radar instruments. TRMM data have only been available since November 1997, and as a result, the length of the record is short compared to other satellite observations. The spatial sampling is also concentrated on tropical and subtropical latitudes due to the satellite's orbital inclination of 35°, restricting even swath observations to a maximum latitude of $\pm 40°$.

3.1.3 New Heatflux Estimates

As for evaporation and precipitation, the introduction of oceanographic satellites has made it possible to estimate heat fluxes at much higher spatial and temporal resolutions than before. While some of the quantities needed are not directly obtainable from satellites, they can be taken from data assimilation models ingesting other types of data, such as sea surface temperature, wind speeds and radiation budgets above

the atmosphere (Robinson, 2004; Yu et al., 2008).

Evaporation is directly related to latent heat, one of the four primary heat flux components needed to produce the net oceanic surface heat flux, Q_{net}. This is comprised of the sum of incoming shortwave radiation (Q_{SW}), longwave radiation (generally outgoing, Q_{LW}), the sensible heat flux (Q_{SH}) and the latent heat flux (Q_{LH}). The latent heat flux is given by the rate of evaporation and the enthalpy of evaporation (Fairall et al., 2003; Yu et al., 2008). As such, the analysis of homogeneity of evaporation directly relates to Q_{LH}. The sensible heat flux is dependent on the temperature gradient between the sea surface and the air above it. Since both SST and air temperature are quantities needed in the computation of Q_{LH} and hence E, an analysis of E is likely to be representative for Q_{SH} also.

Some of the biggest errors (L. Yu, pers. comm.) currently associated with estimates of Q_{net} are associated with the Q_{SW} and Q_{LW} radiation budget. These estimates require knowledge about the radiative transfer and reflection of energy from clouds and gases in the atmosphere. Since there are a number of products currently available, I choose to compare 8 different Q_{net} estimates (of which 3 are based on OAFlux Q_{LH} and Q_{SH}, but using different Q_{SW}-Q_{LW} budgets) to establish a range of results. It should be noted that it is not implied that the 'true' value is necessarily bounded by the 8 estimates, let alone that it should fall in the 'middle' of these estimates, as there may be systematic biases common to all products. To address these issues, the latitudinal sensitivity of Q_{net} estimates to this analysis is investigated in Chapter 4.8.

3.1.4 Re-analysis Models

In data re-analysis, a data assimilation model is utilized for processing past observations to generate a constrained short-term forecast and to find state-estimates at given time-steps. It is the aim of a re-analysis model to simulate physical processes, and as such the models are based on governing physical equations (such as the primitive equations for the ocean and the atmosphere) as well as parameterizations for important physical processes. In the case of NCEP-1, these parameterizations include: "convection, large-scale precipitation, shallow convection, gravity wave drag, radiation with diurnal cycle and interaction with clouds, boundary layer physics, an interactive surface hydrology and vertical and horizontal diffusion processes" (Kistler

et al., 2001). The NCEP-1 assimilation system utilizes a global spectral atmospheric model with 28 vertical levels and an equivalent horizontal resolution of 209 km. While other models use different geometries, parameterizations and sources of constraining data, the concept of re-analysis of data is the same amongst all such products.

Since the underlying model does not change over time, one might expect the output of such models to be virtually homogeneous, even if the data are insufficient to constrain the model to great accuracy. However, climatological discontinuities due to the introduction of satellite data have been identified in the NCEP-1 reanalysis (Sturaro, 2003) as well as in ERA-40(Sterl, 2004). Sturaro (2003) concludes that this is due to the changing density of data to constrain the assimilation model, based on comparisons with observations and a simple bulk flux algorithm for evaporation utilizing sea surface temperature (SST) records. The homogeneity of a re-analysis model is thus not guaranteed but, akin to an OA Model, strongly dependent on the homogeneity of the input data.

3.1.5 The Sampling Problem

The basic components of the hydrological cycle are precipitation, evaporation, transpiration, riverine runoff, groundwater seeps, and ice fluxes. Precipitation occurs globally over the land, the ocean and the cryosphere, and is defined as any product of condensation, with the most common forms being rain and snow. Evaporation occurs globally also, but is significantly reduced in the cryosphere, where sublimation of ice is the dominant mechanism. On land, evaporation from soil and transpiration from plants may be combined to give evapotranspiration. Riverine discharge (R) into the ocean is the second most important freshwater input after oceanic precipitation. Groundwater seeps are sometimes included in the total R, but inputs from the cryosphere, such as the breaking away of icebergs from permanent ice-shelves on and around Greenland and Antarctica are usually accounted for separately (Dai et al., 2009, and references therein).

Measurements of precipitation and evaporation over land have been collected for multiple centuries (e.g. New et al., 2001; Roderick and Farquhar, 2002, respectively). Early measurements consisted of rainfall gauges which were little more than buckets to measure precipitation. Evaporation was traditionally measured by gauging the decrease in fluid level in water-filled pans. Over time, these systems were improved

to account for shortcomings, such as the loss of water due to splashing caused by the momentum of heavy raindrops. A classification system of the required accuracy was introduced to standardize measurements of evaporation and precipitation over land (Brutsaert, 1982), but for social and political reasons, observations were, and still are, inhomogeneous in both space and time. A high data density is available for most of Europe, the United States, Australia and some parts of Asia (particularly India), while large parts of Africa, continental South America, some regions of Asia and northern North America remain comparatively sparsely sampled (New et al., 2001). Additionally, the availability of *in-situ* data can be delayed by several years to multiple decades due to political conflicts or a lack of reciprocal data exchange between agencies.

The sampling density of Q_{net} is even more limited than that of either E or P, since there are very few measurements of all required fluxes (Yu et al., 2008), particularly over the ocean. Moreover, there are very few historic measurements as measuring the fluxes directly requires the use of advanced radiometers which only became accurate enough within the last few decades. As such, there is a large reliance on computer modeling and the use of parameterization of effects such as clouds (e.g. Zhang et al., 2004, and references therein).

3.2 The Global Ocean Freshwater Cycle

The freshwater cycle is a crucial part of the Earth's climate system and provides one of the most important resources to support human life. Freshwater is transported between and stored in oceans, land, the atmosphere and the cryosphere. While the total amount of water on Earth has remained virtually constant over human timescales, the relative distribution of that total mass between the four reservoirs has been influenced by past climate states, such as glacial cycles. The terrestrial freshwater cycle has been investigated more extensively than its oceanic counterpart, largely due to a greater availability of data over land.

The oceans account for 71% of the Earth's surface area (Hartmann, 1994), and 86% of evaporation (E) and 78% of precipitation (P) occur over the ocean (Baumgartner and Reichel, 1975; Adler et al., 2003). From the apparent imbalance of E-P over the ocean, it is clear that the terrestrial and the oceanic components are closely interconnected. To gain an understanding of the complete hydrological cycle and its

effects on global climate dynamics, it is thus imperative that the oceanic component be understood and quantified. To understand whether local changes might represent trends or natural variability, it is necessary to accurately quantify this cycle on timescales ranging from months to decades.

One of the most comprehensive studies of the world water balance, the results of which are still in wide-spread use today, was conducted by Baumgartner and Reichel (1975). Since this study, which was based solely on *in-situ* measurements, satellites have provided a near-synoptic picture of some of the variables required to quantify the hydrological cycle. With more than 30 years of new data and a number of new data products and estimates available (e.g. Quartly et al., 2007; Yu et al., 2008, and references therein), the following questions arise: Has our understanding of precipitation, evaporation and freshwater discharge into the ocean improved? Does the oceanic water budget close between evaporation, precipitation and runoff? Is it possible to determine trends in the hydrological cycle with the present data? To answer these questions, a careful analysis of presently available products along with their temporal and spatial homogeneity is required.

In Section 3.1, I described how E and P observations have benefited from technological advances in the last 30 years, including remote sensing technology and modern computer systems. In Section 3.2.2, I describe seven E and seven P estimates and review recent inter-comparisons. I analyze each product for inhomogeneities and produce a table of the mean global balance between each of the products in Section 3.2.6. In Section 3.2.7, based on a review of inter-comparisons, I present a combination of the Global Precipitation Climatology Project (GPCP) and the Objectively Analyzed Ocean-Atmosphere Fluxes (OAFlux) product as well as riverine runoff (Dai and Trenberth, 2002; Dai et al., 2009) and compare it to other recent estimates.

3.2.1 Defining Oceanic Freshwater Fluxes

Riverine inflow accounts for approximately 10% of the total freshwater input to the ocean (Dai and Trenberth, 2002). The spatial distribution of these inputs can be difficult to deal with, since some large rivers – such as the Amazon – form large deltas which span hundreds of kilometers of coastline and have multiple inflows into the ocean. One can thus attempt to define every point of inflow to the ocean, or specify the total outflow of all parts of the delta at the dominant outflow point. Since

this research is focused on basin-scale and global balances, the dominant outflow point is used as specified in Dai and Trenberth (2002) and Dai et al. (2009). While this approach is appropriate for the purpose of producing a global balance, it is important to consider the effects of riverine discharge plumes and the resulting mixing with the surrounding saltwater when studying regional effects or local buoyancy forcing.

Another source of freshwater to the ocean originates from the cryosphere. It is a common misconception that melting sea-ice causes a change in sea surface height to the ocean. Any ice which floats in the ocean displaces the same volume of water in its frozen state as if it were completely melted. This is not true for grounded ice, the weight of which is supported by land. The calving of a previously grounded ice sheet into the ocean as an iceberg thus constitutes a net freshwater influx (Shepherd and Wingham, 2007). Therefore, precipitation over sea-ice can be treated as precipitation over open water for purposes of creating a long-term freshwater budget. Clearly, the presence of sea-ice needs to be considered more carefully for short-term fluctuations, as freshwater might be stored in sea-ice and icebergs rather than mixing with the surrounding water. Moreover, the formation of sea-ice induces a salt flux to the ocean, which is quantified in Section 3.7.

Not all freshwater fluxes in the ocean occur in the form of fresh water. While all E, P and R can be taken to have zero salinity, the exchange of freshwater between ocean basins occurs within volume transports that are generally on the order of 10-100 times larger than the freshwater transports associated therewith. One can thus discuss the flux of freshwater by separating seawater into liquid ('freshwater') and solids remaining during complete evaporation ('salt') by weight, as was done by Wijffels et al. (1992). Alternatively one may define freshwater anomaly flux relative to a reference salinity.

3.2.2 Global Evaporation and Precipitation Products

In this section, I describe seven global E and seven global P products that are in common use today and review some inter-comparison to assess their quality. Current estimates of R and ice-fluxes into the ocean are also discussed.

The assessment of the quality of both E and P global products is difficult, as it strongly depends on the desired application, since products have different strengths and weaknesses in different areas (Quartly et al., 2007). If trends are to be identified,

the homogeneity, as well as the temporal and spatial coverage of the product are important factors. A state-of-the art data assimilation system is required to maximize the amount of temporal and spatial information available (Yu and Weller, 2007; Adler et al., 2003). For robust estimates of E, P and their variabilities, a product needs to span periodic events such as the El Niño Southern Oscillation (ENSO), which produce significant changes to both E and P patterns (Curtis, 2008). Consequently, the time span provided by a product should be significantly longer than a decade. At this point, it needs to be noted that natural variability occurs on all time- and space-scales, and it is not implied that trends longer than such inter-decadal events are not attributable to natural variability. This further complicates the identification of trends in such products.

To preserve data homogeneity, a trade-off between the incorporated and the available data must be made – in the case of the Global Precipitation Climatology Project (GPCP) (Adler et al., 2003), this trade-off results in the exclusion of TRMM data in the most recent (version 2.1) product due to the relatively short availability and the inhomogeneities that would otherwise occur. For this reason, TRMM data are not used in any long-term merged P product known to the author at the time of writing. Similar concessions must be made for E estimates, in which microwave observations from sensors such as the Advanced Microwave Scanning Radiometer-E (AMSR-E) are not included due to their ability to sense SST below cloud cover. While SST data under clouds may be able to improve estimates of E, the inclusion would introduce a discontinuity by changing the systematic bias that is generated by sensing SST by infrared satellites only (Yu et al., 2008).

Since not all data are ingested into the respective products, it is possible to use such independent data for validation purposes. Buoy *in-situ* observations for evaporation and TRMM observations for precipitation have been used in inter-comparisons of E (Josey, 2001; Yu et al., 2008) and P (Yin et al., 2004; Quartly et al., 2007). However, if a product uses all available data or is corrected to agree with *in-situ* or other independent data, an inter-comparison may not be possible. Such is the case with the corrected version of the Common Ocean-ice Reference Experiments 2 (CORE.2) product (Large and Yeager, 2009). Some products span periods of more than 40 years, and as a result are expected to have temporal inhomogeneities due to changes in sensors during this time. To determine if inhomogeneities can be identified in such products, a homogeneity analysis is performed in Section 3.2.6 on all products

discussed here to identify significant changes in data composition.

3.2.3 Evaporation Data Sets and Inter-Comparisons

The Objectively Analyzed Air-Sea Heat Flux (OAFlux) product (Yu and Weller, 2007; Yu et al., 2008) is constructed from an objective synthesis of remotely sensed satellite data and atmospheric re-analysis fields from the ERA-40, NCEP-1 and NCEP-2 re-analysis models to generate a state-of-the-art estimate of climatological fields relevant to air-sea fluxes. The methodology governing the objective analysis is the Gauss-Markov theorem (Yu et al., 2008). The Gauss-Markov theorem states that when unimodal data are combined in a linear fashion, the linear least squares estimator is the best linear unbiased estimator. The error in each input data source is thus reduced to produce an estimate that has the minimum variance. While re-analysis estimates are used for quantities which are not directly observable from other sensors, OAFlux is not a re-analysis in itself. Fields that use satellite data include SST and surface wind speed at 10 m above the sea surface as well as wave height and cloud cover. Surface air temperature and relative humidity relative to 2 m above the surface are based solely on re-analysis products. Based on these fields, it is possible to estimate evaporation rates over the ocean using the Coupled Ocean–Atmosphere Response Experiment (COARE) Bulk Algorithm (Fairall et al., 1996, 2003).

The CORE.2 product provides fields of air-sea fluxes, which, like OAFlux, are derived from bulk formulas. Atmospheric fields from multiple sources and an optimally interpolated merged SST product are input to the bulk flux formula to produce outputs at monthly resolution between 1948–2006. The atmospheric inputs are based on the NCEP re-analyses, while radiation data, P and sea-ice concentration are satellite-derived (Large and Yeager, 2009). The CORE.2 product is available from NCAR (2010) and uses corrections to agree with satellite and *in-situ* measurements that are too short in duration or too regional in coverage to be used to constrain fields directly. While an uncorrected version also exists, this does not include E fields. I thus restrict my discussion of CORE.2 to the corrected fields.

A further OA E product is the National Oceanography Centre – Southampton Ocean–Atmosphere Heat, Momentum and Freshwater Flux Atlas (NOCS) (Josey et al., 1998) which is based on the Comprehensive Ocean-Atmosphere Data Set (COADS) (Woodruff et al., 1987) with additional *in-situ* observations. Since COADS

does not include any satellite derived data, this product is affected by strong spatial biases due to the preferential sampling of areas often frequented by vessels (such as the North Atlantic), but since no transition between *in-situ* to satellite sampling is present, the homogeneity is good. Due to the issues of spatial biasing and insufficient global coverage, I do not consider *in-situ*-only products in the comparisons.

The most commonly used re-analysis products are the NCEP-1 (Kistler et al., 2001), NCEP-2 (Kanamitsu et al., 2002) and ERA-40 (Uppala et al., 2005) re-analyses, as well as several follow-on products, such as MERRA (Bosilovich et al., 2006) and ERA-Interim. Some strengths and weaknesses of these estimations have already been discussed in Sections 3.1–3.1.4 All of the aforementioned products include evaporation and precipitation fields. While NCEP-1 spans a time period from 1947-2001, NCEP-2 was designed to be more spatially and temporally homogeneous (Kanamitsu et al., 2002) and consequently only starts with the availability of SST data in 1979, and ERA-Interim only begins in 1989 (Simmons et al., 2007). The ERA-40 re-analysis spans the time 1957–2001 (Uppala et al., 2005) and is thus affected by a change of input data from solely ship- and buoy-based observations to the inclusion of satellite data in the 1970s and 1980s. It should be noted that it is not the primary purpose of any re-analysis to estimate E, P or a freshwater budget, but rather to produce estimates of a number of fields (Wunsch and Heimbach, 2007).

A number of buoys, such as the Prediction and Research Moored Array in the Atlantic (PIRATA) and the Tropical Atmosphere Ocean (TAO) project can be used to estimate errors in latent heat fluxes provided by all evaporation products and can thus be used to find the data product which most closely resembles the *in-situ* data. In a direct comparison of independent buoy-derived fluxes with NCEP-1 and ECMWF re-analysis fields and the NOCS flux fields (Josey, 2001), the mean errors between *in-situ*, NCEP-1, ECMWF and the NOCS fluxes, the lowest mean error was found for the NOCS product. However, it should be noted that all five buoys used in this comparison were located in the Northeast Atlantic, an area with a high coverage of ship-borne observations, and that the time-scale of observations extended for only two years from 1991-1993.

A similar comparison between *in-situ* measurements and E products was conducted by Yu et al. (2008) using a total of 107 observations of various lengths. All measurements were taken between 1988–2006, meaning that satellite data were available for the duration of comparisons. The OAFlux product exhibits the lowest errors

in all flux estimates compared to NCEP-1, NCEP-2 and ERA-40. While the observations span the Indian, Atlantic and Pacific Ocean, the locations of the observations are predominantly in equatorial and sub-tropical regions, with only four observations outside the $\pm 40°$ latitude band. It thus appears that the OA estimates (NOCS, OAFlux) have the best agreement with independent measurements.

In an inter-comparison of different satellite-based and RA latent heat products in the South China Sea by Zeng et al. (2009), the TRMM Microwave Imager (TMI) and OAFlux products were found to be more closely correlated to *in-situ* data and to exhibit less systematic error than the ERA-Interim, and NCEP-2 re-analyses and the COADS estimate. The TMI data are not considered here, since the duration of available data (1997–date) is too short.

3.2.4 Precipitation Products and Inter-Comparisons

A multitude of different precipitation products and climatologies are available today, offering different temporal and spatial coverage. In recent years, high-resolution satellite precipitation estimates with resolutions that are finer than or equal to 0.25° and have temporal resolutions on the order of 3 hours have become available (see Sapiano and Arkin (2009) for an overview of such estimates). The data input of these estimates is based on a variety of satellite sensors, and does not produce a global coverage due to the high temporal and spatial resolution. Since many of the sensors used for input data were only launched in 2002 and subsequent years, the usable duration of such estimates is insufficient for the purposes of estimating a multi-decadal picture of the oceanic freshwater cycle. Only products spanning significantly more than one decade will be considered.

As with evaporation estimates, both re-analyses and objective analyses exist. All re-analyses that were considered for E also provide fields for P; these include NCEP-1, NCEP-2, ERA-40 and MERRA. Also considered were the objectively analyzed merged gauge and satellite-derived CORE.2, CPC Merged Analysis of Precipitation (CMAP see Xie and Arkin (1997) for details) and the Global Precipitation Climatology Project (GPCP) products. A re-analysis should be self-consistent and the layman might thus expect the budget E-P-R to close. However, since the underlying prediction models are generally forward-integrating (and thus have no information of the future), closure is not guaranteed (Wunsch and Heimbach, 2007) and is in fact

violated for the freshwater cycle in all examined re-analyses. When the global balance of all investigated products is computed (Table 3.1), ERA-40 was found to add a net flux of approximately 2.41 Sv ($1\,\mathrm{Sv} = 10^6\,\mathrm{m^3 s^{-1}}$) to the ocean.

Given that the global E is $\approx 13\,\mathrm{Sv}$, this imbalance is approximately 20% of global E and clearly not physically possible, since it would imply a global sea-level rise of $0.21\,\mathrm{m\,yr^{-1}}$. Based on this alone, the ERA-40 product can be rejected for analysis of the global oceanic freshwater cycle.

Table 3.1: Global annual (P+R)-E balances between precipitation products (rows) and evaporation products (columns) in Sv ($10^6\,\mathrm{m^3 s^{-1}}$) for major objectively analyzed and re-analyzed products. Positive imbalances indicate an apparent excess input of freshwater to the ocean, while negative values indicate net water loss. Flux data are averaged between 1987–2006 or the longest common available period within 1987–2006. The combined river discharge ($\approx 1.25\,\mathrm{Sv}$) from Dai and Trenberth (2002) and Dai et al. (2009) has been added to all precipitation products. Such balances are sensitive to the land-mask used, so a common land-mask was used for these estimates.

E / P+R	OAFlux	NCEP1	NCEP2	ERA40	ERA-I	CORE2	MERRA
GPCP	+0.46	-0.41	-2.24	-1.00	-1.15	-0.69	+0.22
NCEP1	+1.05	+0.18	-1.65	-0.45	-0.54	-0.11	+0.81
NCEP2	+3.28	+2.42	+0.59	+1.65	+1.70	+2.13	+3.05
ERA40	+3.87	+3.04	+1.30	+2.41	+2.70	+2.70	+3.61
CMAP	+0.90	+0.03	-1.80	-0.53	-0.71	-0.26	+0.66
CORE2	+1.01	+0.15	-1.69	-0.45	-0.60	-0.14	+0.78
MERRA	+0.47	-0.40	-2.23	-1.30	-1.14	-0.69	+0.23

It has been shown in comparisons with independent measurements (Quartly et al., 2007) that GPCP showed a significantly higher correlation to the *in-situ* observations than fields provided by NCEP-1, NCEP-2 and ERA-40. Quartly et al. (2007) conclude that GPCP, although by no means perfect, represents the current best-estimate, even though increasing errors at high latitudes are a known problem of this product. This is caused by using an empirical correlation between cloud-top temperatures and precipitation, which is a good approximation in low latitudes, but degrades towards the poles (Adler et al., 2003; Yin et al., 2004). Comparisons of CMAP and GPCP found an over reliance on atoll and island data by CMAP (Yin et al., 2004), leading to unreasonable spatial distributions of P over the ocean. At the moment GPCP can

be regarded as the state-of-the art long-timescale P product for use over the global ocean and will thus be used for purposes of this research.

All data analysis was performed with the GPCP version 2.0 estimate. GPCP released an updated version 2.1 in July 2009. Changes to the Global Precipitation Climatology Center (GPCC) gauge analysis have increased net P estimates from gauges, resulting in higher estimates over the ocean in the pre-SSM/I era and higher land-based values overall. Since only the oceanic component of GPCP in the SSM/I era is considered here, no significant changes are expected between version 2.0 and 2.1 for the present estimate.

3.2.5 Other Sources of Freshwater to the Ocean

One of the first comprehensive datasets of river gauge data and the resulting runoff from those fields was completed by Baumgartner and Reichel (1975). Measuring the outflow of a river into the ocean is a non-trivial problem, since it is often impossible to gauge the flow at the river-mouth. This is particularly true in river deltas, in which hundreds of outflows might be present, and it would be impractical to gauge every one. Therefore, gauging stations farther inland (sometimes up to hundreds or even thousands of kilometers) are used to estimate river flows. It is also possible to use the catchment area (the total land area that drains precipitation to a given river) for each river system and utilize P, E and evapotranspiration products to estimate the total riverine discharge based on the conservation of water. However, this approach leads to the quality of the precipitation data determining the quality of the discharge data (Fekete et al., 2004). It is thus preferable to use gauging stations wherever and whenever possible. Such an approach has been taken by Dai and Trenberth (2002) in an updated global quantification of the world's rivers. This work was updated in 2009 (Dai et al., 2009) and includes previously unavailable data from gauging stations around the world.

While Dai and Trenberth (2002) provided discharges as averages for each month of the year with no information on inter-annual changes (i.e. all available data years in which the month January was available were merged to give a 'typical' January), inter-annual variability in riverine discharge was included by Dai et al. (2009). The standard deviation of the inter-annual variability, however, is found to be only 11% of that of the annual variability, indicating that the annual cycle has greater variability

(Trenberth et al., 2007). The annual variability is predominantly caused by the accumulation and melting of snow and ice in the Northern Hemisphere, which contains significantly more land area than the Southern Hemisphere, particularly at temperate latitudes.

I have thus combined the mean seasonal information found in Dai and Trenberth (2002) with the inter-annual variability in Dai et al. (2009) to produce a monthly estimate of R which was used for all subsequent analyses. This combined estimate has an arithmetic mean of 1.18 Sv, which is identical to the arithmetic mean of only the seasonal data from Dai and Trenberth (2002).

The Antarctic iceberg flux was estimated at $2300\,\mathrm{km^3yr^{-1}}$, equivalent to 0.073 Sv by Vaughan et al. (1999). In a literature review, Monaghan et al. (2006) compare studies that use precipitation data and the total mass balance and find Antarctic ice-exports ranging from 1475 to $2331\,\mathrm{km^3yr^{-1}}$ or 0.047 to 0.074 Sv. The relatively large range of estimates is caused by the uncertainties in the precipitation measurements and the surface mass balance over Antarctica (Shepherd and Wingham, 2007).

Similar mass balance calculations have been performed for Greenland by Box et al. (2006) who found a total average meltwater/iceberg runoff of $373\,\mathrm{km^3yr^{-1}}$ or 0.012 Sv. To simplify the freshwater budget to E-P-R, the iceberg/meltwater discharges from both Antarctica and Greenland were included in the total riverine runoff to augment the mean annual riverine discharge of 1.18 Sv (Dai and Trenberth, 2002) by the mean of the available iceberg/meltwater observations for Antarctica and Greenland (0.06 and 0.01 Sv, respectively) to a total value of 1.25 Sv.

Between 1993 and 2006, a sea-level rise of approximately $2.4 \pm 1\,\mathrm{mm\,yr^{-1}}$, which would be equivalent to a net influx of 0.03 Sv, was observed from satellite altimetry (Domingues et al., 2008). However, thermal expansion accounts for approximately $1\,\mathrm{mm\,yr^{-1}}$ of this, reducing this change below 0.02 Sv. In comparison with the error estimates of E, P and R, which sum to approximately 1.8 Sv, this is insignificant.

3.2.6 Evaluation of Homogeneity of E and P Products

The homogeneity of the data has to be considered carefully for the purposes of this study. By visual inspection of a time-series alone it becomes apparent that more spatial and temporal resolution is present in the data after 1987. To quantify these changes, an empirical orthogonal function (EOF) analysis was performed. The tran-

sitions can be illustrated by identifying changes in the time series associated with the loading patterns (see Figures 3-1 & 3-2). The absolute value of the normalized amplitude of the associated time series is color-coded and all series are plotted above each other, beginning at the top with the leading mode (the mode explaining the most variability and containing the highest energy). The normalization ensures that all associated time-series have identical variances. While this allows the changes to be readily compared on the same scale, it should not be forgotten that lower-numbered modes are the most energetic and explain more variability than higher-numbered ones.

If a change in high-resolution information (be it increased spatial or temporal detail) is present, the intermediate modes (those explaining less variability, but not those at the level of noise) are expected to increase. When the interpolation problem is more constrained by data, the amplitude of the highest modes, equivalent to noise in the data, is expected to decrease. This is seen in modes greater than 270 for OAFlux evaporation (of a total of 348 modes, see Figure 3-1) and modes greater than 400 in the case of GPCP precipitation (out of 588 modes, see Figure 3-2). The sum of the explained variability of modes 270–348 is 1% for GPCP and 0.6% for modes 400–588 in the case of OAFlux.

Since this analysis is performed on monthly fields, the output is smoothed using a two-dimensional Gaussian filter with half power points of 12 and 40, corresponding to 12 months in time [x-direction] and 40 modes [y-direction]. This filter is necessary to visualize inter-annual variability that would otherwise not be visible due to seasonal fluctuations in the associated time series. For OAFlux E, this analysis is shown in Figure 3-1. A first transition is evident in 1982 and after 1985 and a further change occurs in 1987, corresponding to the years in which verified SST from the AVHRR mission and wind speed from SSM/I became available, respectively (see Table 3.2 and Yu et al. (2008) for a full documentation of ingested data). After 1987, changes are evident in the lowest (most energetic) modes around 1997 and 1998 (an El Niño event) as well as 2000 and 2001 (La Niña). These changes are likely caused by wind speeds and SST changes associated with ENSO. All changes that are evident after 1987 are thus attributable to natural variability. The period of 1987–2006 is sufficiently long to observe events on the time-scale of ENSO but provides sufficient homogeneity for the purposes of this research.

Identical analyses have been performed for all other E products, and discontinu-

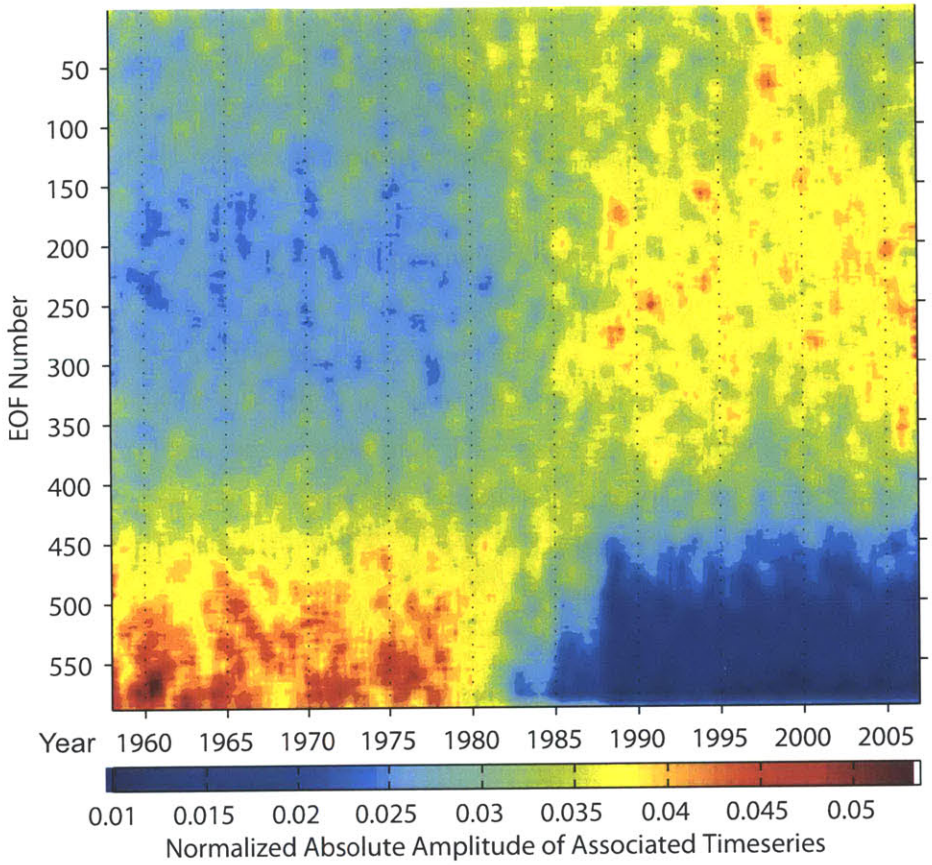

Figure 3-1: Filtered results of empirical orthogonal function (EOF) analysis of the OAFlux evaporation estimate. The magnitude of all associated time series (color-coded) is plotted with respect to time and the number of the EOF. Changes in the EOF modes 50–550 clearly indicate a strong change in data composition around 1982 and 1987, coinciding with the availability of sea-surface temperature data in 1982 and 1985 as well as SSM/I data in 1987. Natural variability associated with El Niño is evident around 1997–1998.

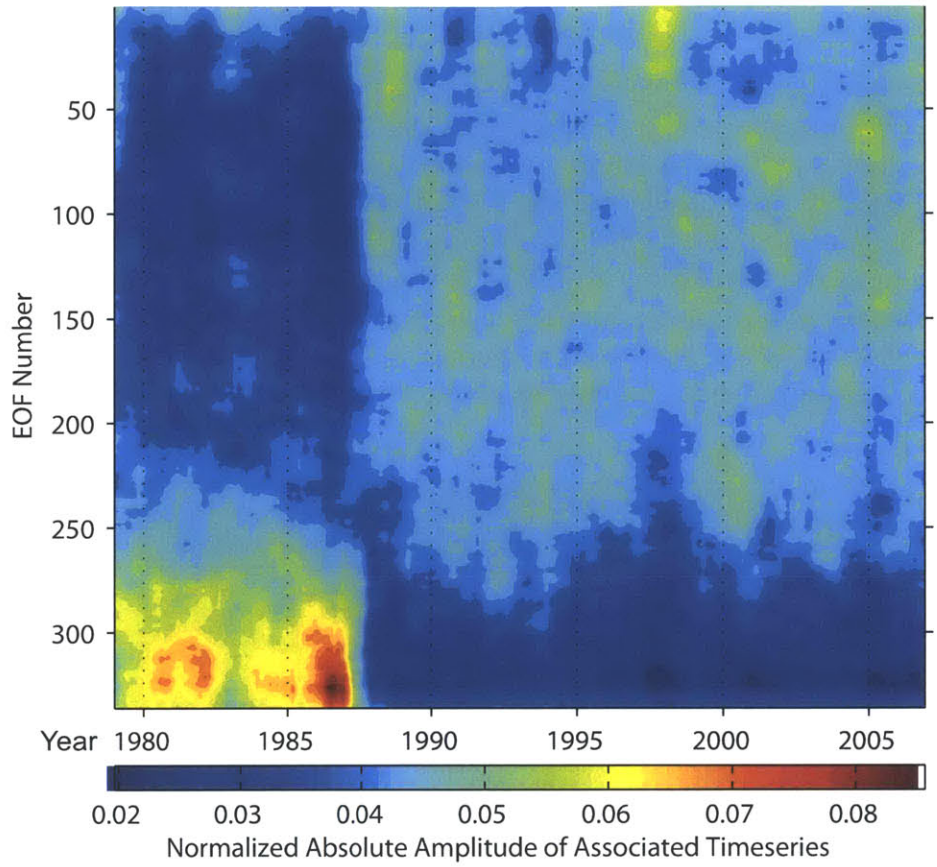

Figure 3-2: Filtered results of empirical orthogonal function (EOF) analysis of the GPCP precipitation estimate. The magnitude of all associated time series (color-coded) is plotted with respect to time and the number of the EOF. Changes in the EOF modes 50-340 clearly indicate a strong change in data composition around 1987, coinciding with the beginning of SSM/I data. Natural variability associated with El Niño is evident around 1997–1998.

Table 3.2: Dates of first continuous availability of data sources. *In-situ* measurements prior to 1948 are not considered. Only commonly used satellite missions which enhanced the data quality significantly are listed. New sources are only listed if they provide a potential significant advantage in the future. † - These data sources are not commonly used in order to preserve data homogeneity. ‡ - Even though AVHRR was first launched in 1978 and was fully operational from 1981 onwards, sufficient buoy data to constrain the data are only available after 1985.

Data	Variable	Source	Available
E	*all*	*in-situ* and NWP	1948
	T_{sea}	AVHRR	1985 ‡
		AMSR-E†	2002
	U_{air}	SSM/I	1987
		QuikSCAT	1999
	T_{air}	*in-situ*/NWP only	1948
	q_{air}	SSM/I	1987
		AIRS†	1999
P	P_{total}	*in-situ* and NWP	1948
		OPI	1979
		GPI	1986
		SSM/I	1987
		TOVS	1987
		TRMM-TMI†	1997

ities corresponding to the change of input datasets as shown in Table 3.2 were identified in all products that provide fields before 1987, including re-analyses. A more thorough homogeneity analysis of re-analyses has been performed by Sterl (2004) for ERA-40 and Sturaro (2003) for NCEP-1/2. These find a similar inhomogeneities and a near-homogeneous period starting with the introduction of SSM/I in July 1987.

To evaluate the homogeneity of P products, the same analysis technique as described for E was used. This is shown for GPCP in Figure 3-2. The discontinuity caused by the introduction of SSM/I data in 1987 thus revealed is well documented (e.g. Adler et al., 2003; Yin et al., 2004) and precludes the use of the product as a continuous time-series before 1987 without great caution. As in the case of E, re-analyses are not free of discontinuities either, since the input data constrain the model change over time. Using the same homogeneity analysis, discontinuities similar to those of GPCP were identified in NCEP-1, NCEP-2 and ERA-40 P data (results not shown). The homogeneity analysis of CORE.2 P (not shown) exhibits a sharp discontinuity at 1979 (the beginning of the Outgoing Longwave Radiation (OLR) Precipitation Index (OPI) mission, see Table 3.2) and nearly identical results to GPCP for the remaining period with an additional inhomogeneity in 2002. All transition events correspond to the change of data sources, particularly the inclusion of satellite observations.

3.2.7 Evaporation-Precipitation over the Ocean

Based on the identified near-homogeneous period of 1987–2006, global balances of E, P and R can be constructed for all products shown in Table 3.1. It becomes evident that none of the estimates close the oceanic freshwater balance completely, but some even exceed the error bounds provided by the product, such as ERA-40. The estimates agreeing most closely with independent *in-situ* observations, OAFlux E and GPCP P exhibit an imbalance of +0.46 Sv.

The error estimation in E, P and R products is difficult. In GPCP and OAFlux, a number of data based on *in-situ* and remotely sensed measurements are combined in an objective analysis. Not all data ingested provide reliable error estimates in the first place, but it is also unclear to what extent the estimates are correlated with each other temporally and spatially. While it is possible to arrive at an error estimate for each point using statistical methods, more detailed information about de-correlation space- and time scales would be needed for a full error propagation to produce global

errors of E, P or R. It is possible that systematic errors play an important role, which might bias low an error analysis not taking this into account. It is unlikely that either E or P follow a normal distribution, rendering conventional statistical methods more difficult, still. Due to these constraints, the 'best case scenario' of decreasing the error by a factor of $\sqrt{N}$, where N is the number of observations, is clearly not realistic. A 'worst-case scenario' might be to average the error provided for each data point, which would result in error estimates of approximately 30% for P (Adler et al., 2003) and 10% for E (Yu et al., 2008), due to the different error handling in each product.

It is unlikely that E and P are currently known to an accuracy greater than 5% due to the systematic spatial and temporal under-sampling. A value of approximately 5-10% also emerges from comparisons with independent *in-situ* observations (e.g. Quartly et al., 2007; Yu et al., 2008). Based on these numbers, we assume an error of approximately 10% for both P and E. The annual mean precipitation into the ocean averaged over 19 years (1987–2006) is thus estimated at 12.2 ± 1.2 Sv, the evaporative loss is estimated at 13.0 ± 1.3 Sv, and the total freshwater influx is estimated at 1.25 ± 0.1 Sv. The system is in near steady state, as is shown by the thermal-expansion corrected sea-level rise of 0.02 ± 0.01 Sv as estimated by satellite altimetry (Domingues et al., 2008). The net imbalance is found to be 0.5 ± 1.8 Sv. This means that the OAFlux-GPCP-R budget closes within the provided error estimates. The time-evolution of the balance is illustrated in Figure 3-3.

3.2.8 The Global Picture

The global mean E-P pattern based on OAFlux E and GPCP P between 1987–2006 is shown in Figure 3-4. It is evident that the sub-tropical gyres and western boundary currents of the Atlantic, Pacific and Indian oceans are all regions of net E. The inter-tropical convergence zone (ITCZ) as well as high latitudes ($> 40°$) are regions of net P. While both Atlantic subtropical gyres are net evaporative, the Pacific subtropical gyres – particularly the southern gyre – show an East–West transition with increased E near the eastern boundaries. The mean salinity of the Atlantic is greater than that of the Pacific (e.g. Durack and Wijffels, 2010, and references therein). This is likely caused by moisture transport from the Atlantic to the Pacific over Central America (Weyl, 1968). Since E is a function of the relative humidity of the air overlying the water (Fairall et al., 2003), the air becomes saturated in humidity and E decreases

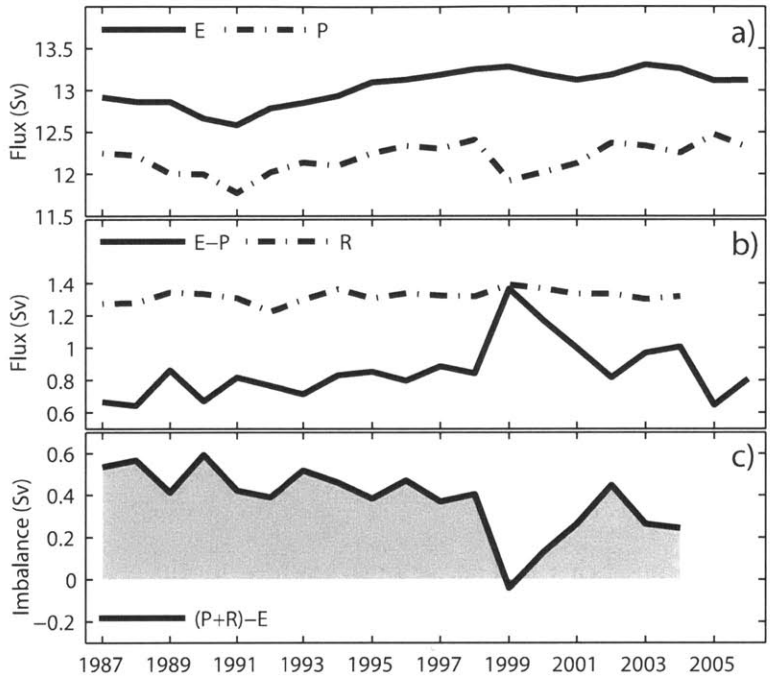

Figure 3-3: Global oceanic freshwater balance: a) Mean annual OAFlux evaporation (E) from OAFlux (solid black line) and mean annual precipitation (P) from GPCP (dashed black line) from 1987–2006. b) E-P for the same period (solid black line) from OAFlux and GPCP and global runoff (R, dashed black line, see text) from 1987–2004. c) Imbalance between (P+R)-E (solid black line). Positive regions (shaded in light gray) indicate a net influx to the ocean while negative regions (shaded in dark gray) indicate a net freshwater loss. All units are in Sv ($1\,\mathrm{Sv} = 1 \times 10^6\,\mathrm{m^3\,s^{-1}}$). A mean imbalance of 0.46 Sv (influx) is evident between data sources. The maximum imbalance of 0.59 Sv is found in in 1990 while the only negative value (-0.04 Sv) occurs in 1999.

as the overlying air is driven westward by the trade winds. From Figure 3-4, it is evident that the Atlantic is a net evaporative basin while the Pacific is neither strongly precipitative nor evaporative.

Strong seasonal patterns are present in the monthly data that were analyzed, which are not represented by the time-mean shown in Figure 3-4. To illustrate these temporal and spatial changes, a mean-removed area-corrected empirical orthogonal function (EOF) analysis, which was also used to analyze the homogeneity of the data, was re-run for the period of 1987–2006. The leading three modes (EOF1–3) are plotted in Figure 3-5. The associated time-series of the leading mode (EOF1) shows a near-sinusoidal annual pattern. This mode accounts for 29.4% of the total variability. The loading pattern (normalized to $-1...1$ $\mathrm{m\,yr^{-1}}$) shows a significant annual meridional shift of the ITCZ by 5–10 ° in both the Atlantic and the Pacific Oceans. The eastern boundary currents are clearly evident, with the Gulf Stream and the Kuroshio Current having negative E-P values (net freshwater addition) in the Northern Hemisphere summer and positive values (net freshwater loss) in winter. This cycle corresponds to the monsoon regions in the Indian and Pacific Oceans, which have the same sign as the eastern boundary currents in the Northern Hemisphere.

The associated time-series of the second leading mode (EOF2, explaining 9.2% of the total variability) also shows a clear annual signal. However, a phase lag of approximately 2-3 months compared to the leading mode is present and a significant change in the El Niño winter of 1997–1998 is evident. All major eastern boundary currents are visible as positive signatures in the Northern Hemisphere and negative areas in the Southern Hemisphere. The sign is thus reversed from the leading mode. The annual meridional ITCZ shift is evident in this mode with the same sign as the leading mode.

The third leading mode (EOF3, explaining 5.3% of the total variability) has a predominantly biannual associated time-series. The loading pattern is largely congruent with changes in E and P that would be expected to occur in an El Niño year, namely increased evaporation in the high sea-surface temperature area in the Central Pacific and enhanced precipitation in the area of the Western Pacific and the Indonesian Throughflow (Curtis, 2008). A strong peak in the associated time-series is evident in 1997–1998, corresponding to the strongest positive ENSO signal. The associated time series of EOF3 is strongly correlated to the Multivariate ENSO Index (MEI) and the loading pattern is similar to that of SST used in the creation of the MEI

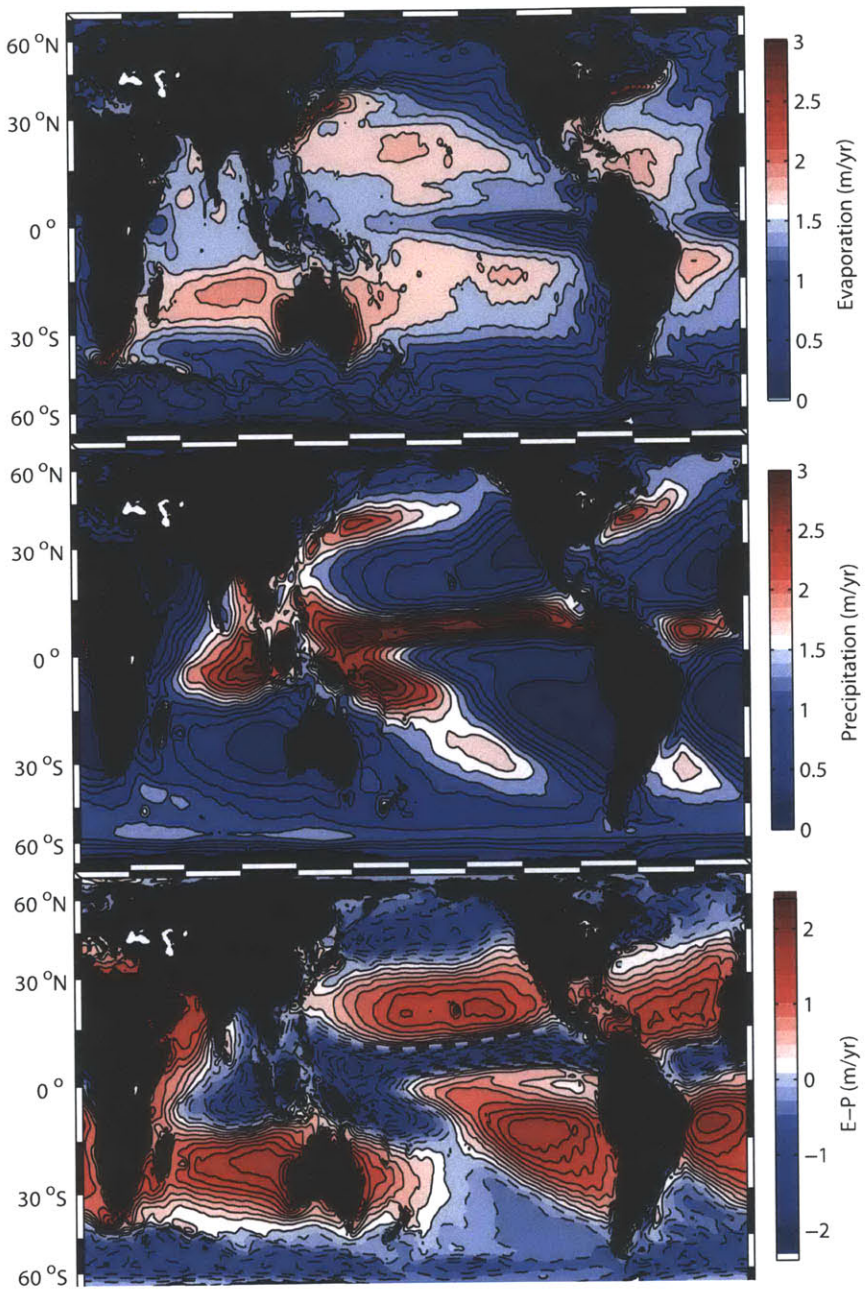

Figure 3-4: Global annual average E (top), P (middle) and E-P (bottom) maps for 1987–2006. All subtropical ocean gyres and subtropical marginal seas are dominated by excess E, while the regions of the ITCZ and the Indonesian Throughflow as well as most temperate and subtropical latitudes are dominated by excess P. The maximum imbalance (most water lost) of $2.2\,\mathrm{m\,yr^{-1}}$ occurs in the Red Sea, while the minimum (most water gained) of $2.6\,\mathrm{m\,yr^{-1}}$ occurs near the Colombian Pacific coast in the ITCZ.

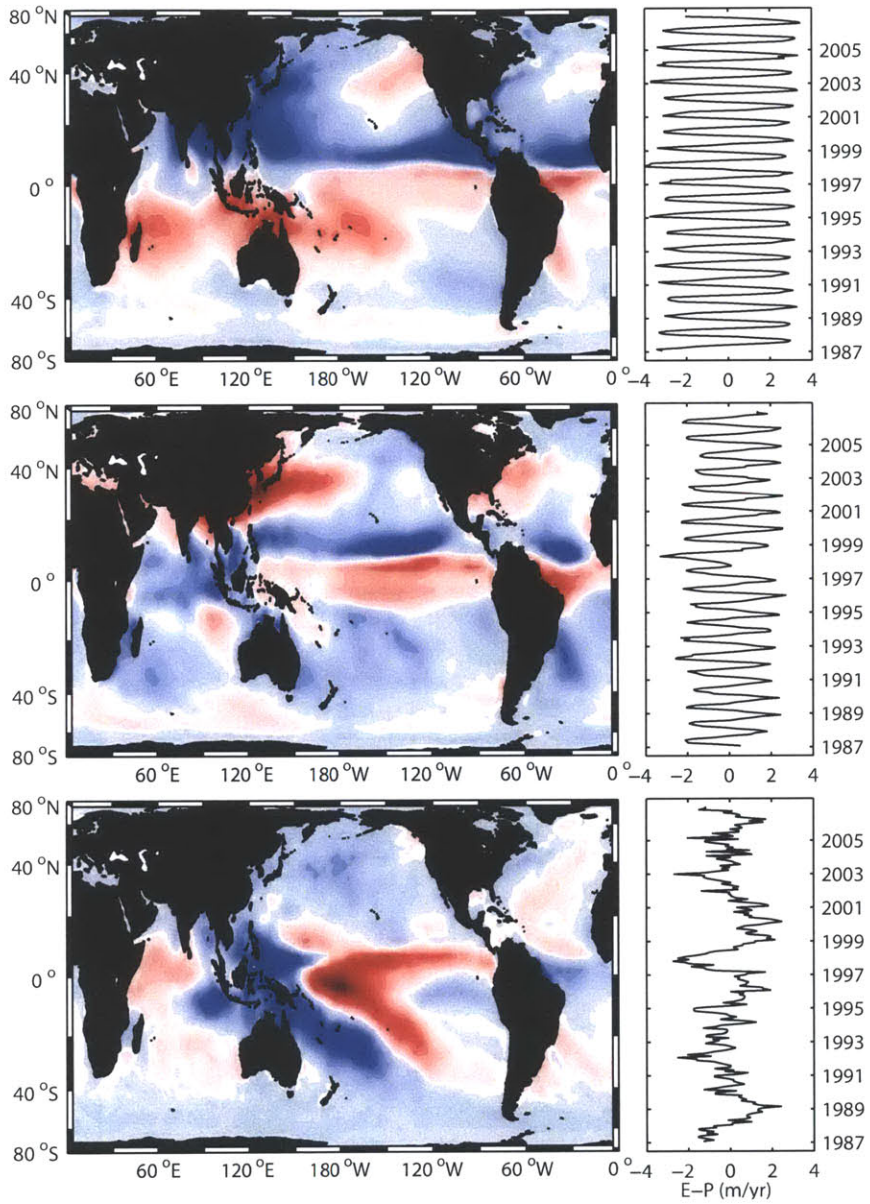

Figure 3-5: Results of area-corrected empirical orthogonal function (EOF) analysis of E-P-R estimate. a) Leading EOF Mode (EOF1) explaining 29.4% of total variability. b) EOF2, explaining 9.2% of total variability. c) EOF3, explaining 5.3% of total variability. Both EOF1 and EOF2 exhibit a 12-month seasonal pattern in the associated time series with changes in 1997-1998 for EOF2. The seasonal ITCZ shift from its off-equator position to the near-equatorial position is evident in both modes. EOF3 shows changes in the spatial distribution of E-P in the Central and West Pacific. The associated time-series is dominated by the 1997–1998 El Niño event.

(Wolter and Timlin, 1993).

3.2.9 Changes from Previous Estimates

A significant increase in both spatial and temporal resolution has been achieved since estimates of oceanic E-P by Baumgartner and Reichel (1975) (hereafter BR75) and improved North Atlantic estimates by Schmitt et al. (1989) (hereafter SBD89). The positive signature of the Kuroshio Current was almost completely lacking in BR75 and is now clearly present. While the shape and magnitude of the South-Pacific subtropical gyre closely resemble those in BR75, the transition from net evaporative to net precipitative in the southern Indian Ocean occurs at lower latitudes than in BR75. Furthermore, BR75 showed most of the ocean adjacent to northeastern Australia to be negative (net precipitative), which is now identified as positive; particularly the area of the East Australian Current which was indicated as neutral in BR75 is shown as strongly evaporative in Figure 3-4. The negative sign in the Southern Ocean remains unchanged between BR75 and my estimate, but the magnitude is generally increased between $50 - 60°$ S.

Compared to SBD89, the Atlantic is estimated to be more precipitative in subpolar latitudes, moving the line of neutral E-P to lower latitudes in general. While the Gulf Stream is present as a positive signal in my estimate, it is not as positive as in SBD89, and even becomes negative South of the Gulf Stream in an area that was previously estimated to have a net freshwater loss of approximately $0.8\,\mathrm{myr}^{-1}$. The magnitude of E-P in the subtropical gyre agrees well with estimates in SBD89, however. There is a closer agreement with modern satellite-based and re-analysis products, which I will discuss by integrating the total E-P-R fluxes.

3.2.10 Derived Freshwater Transports between Ocean Basins

From the estimates of E-P-R, it is possible to estimate freshwater transports between ocean basins by integrating E-P-R meridionally over each basin. This approach was used by Wijffels et al. (1992), hereafter W92, using data from BR75 and SBD89, by Dai and Trenberth (2003), hereafter DT03, using ECMWF data, by Talley (2008), hereafter T08, using the NCEP-1 re-analysis and by Large and Yeager (2009), hereafter LY09, using the CORE.2 product.

This integration is performed with the presented global E-P-R estimate based on

OAFlux and GPCP data from 1987–2006 (Figure 3-6). As a constant of integration, the flux through Bering Strait is based on an estimates by Woodgate and Aagaard (2005), who estimate that the total time-mean (saltwater) flux is 0.8 Sv (1 Sv = $10^6\,\mathrm{m^3 s^{-1}}$) from the Pacific into the Arctic Ocean. I assume that the density of the water transported is $\approx 1025\,\mathrm{kg\,m^{-3}}$, which is equivalent to a mass transport of $0.82 \times 10^9\,\mathrm{kg\,s^{-1}}$, which can be separated into salt transport ($\approx 3.5\%$ of the total) and freshwater transport (96.5%). I thus estimate a net water transport of 0.79 Sv. It should be noted that there are significant uncertainties in these estimates and that there is a large seasonal and inter-annual variability in the transport through Bering Strait (Woodgate and Aagaard, 2005).

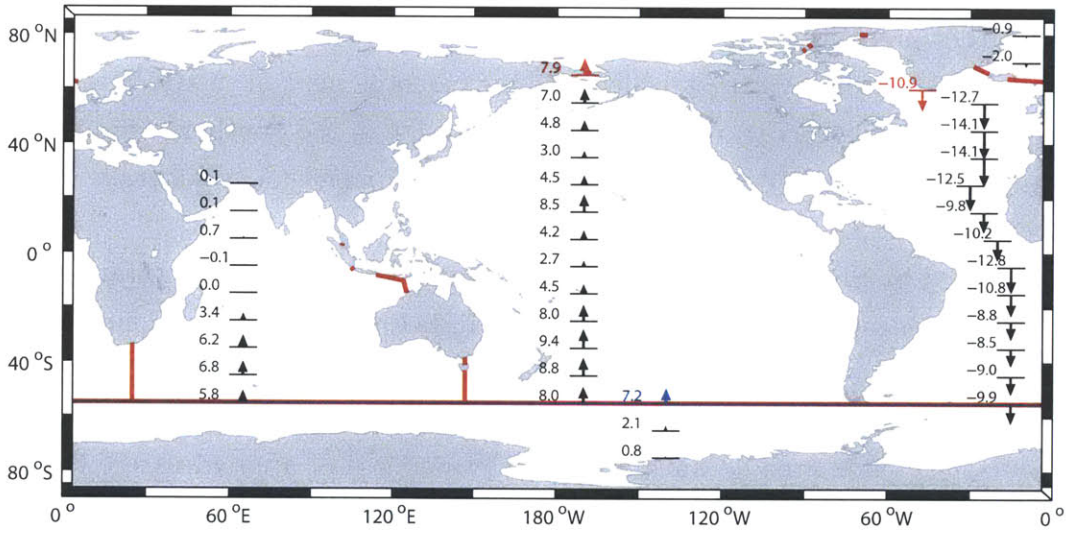

Figure 3-6: North-South integrated basin freshwater balance in $10^5\,\mathrm{m^3 s^{-1}}$ (0.1 Sv), showing mean E-P-R integrals between 1987 and 2004. Added integration constants are indicated in red. All northward fluxes are positive, while southward fluxes are negative. A freshwater flow of 0.79 Sv through the Bering Strait is used to constrain the system. The resulting Arctic flux of 1.02 Sv is added to the northern boundary of the Atlantic (with no specified pathway). Iceberg freshwater inputs of 0.01 Sv and 0.06 Sv for Greenland and Antarctica, respectively, are added at the poles. The Southern Ocean is integrated from South to North and produces a net northward freshwater transport of 0.72 Sv into the Atlantic, Pacific and Indian basins at 55°. This is in contrast with the North-South integration of the other basins, which requires a northward flux of 0.39 Sv for the system to close. The total error of 0.33 Sv at 55 °S cannot be constrained to a specific basin.

While the Bering Strait represents the only connection between the Pacific and the Arctic Ocean, there are multiple connections between the Arctic and the Atlantic Ocean. As a consequence there is no standard definition of boundaries. The following boundaries are used for this estimate: Robeson Channel (between the Northern Territories of Canada and Greenland), Parry Channel, Denmark Strait and the shortest possible straight line between Iceland and Norway. For simplicity, the boundary of the Southern Ocean is taken as 55°, close to Cape Horn. The boundary to the Indian Ocean is defined at 25° W, and the transition between the Indian Ocean and the Pacific is defined along Tasmania and the Indonesian Throughflow. These definitions are indicated geographically in Figure 3-6.

The Arctic Ocean is a net precipitative region and the combined E-P and riverine influx increase the value of 0.79 Sv through the Bering Strait by 0.3 Sv to 1.09 Sv when it reaches the Atlantic Ocean. As previously stated, the Atlantic is a net evaporative basin, and 0.1 Sv is lost. This includes the strongly net evaporative Mediterranean Sea. It should be noted that when the Atlantic Ocean is further separated from its high-latitude marginal seas (such as the Labrador Sea and the Hudson Bay), the basin becomes more evaporative, which is indicated by the maximum southward transport of 1.41 Sv at 45° N. The Southern Ocean, akin to the Arctic Ocean, is an area dominated by P and as a consequence adds 0.72 Sv of freshwater to the other oceans (indicated by a blue arrow). The Indian Ocean is strongly evaporative, leading to a net loss of 0.58 Sv of water. It is clear that the numbers at 55° S cannot add up to 0, since the balance of E-P-R is not fully closed, but has an imbalance of 0.33 Sv. This number differs slightly from the estimates in Table 3.1 due to the integration period being shorter and the application of a slightly different land mask.

The boundaries chosen for this integration are somewhat different from previous estimates (W92, DT03) in that the boundaries between the Indian, the Pacific (both 35° S) and the Atlantic (45° S) to the Southern Ocean are moved to 55° S. The estimates by T08 and LY09 use different boundary definitions altogether.

Nonetheless, significant changes from other estimates are evident. Compared to W92, who found a strongly evaporative Atlantic and a strongly precipitative Pacific, the Atlantic is found to be less net evaporative and the Pacific to be neither evaporative nor precipitative. Consequently, the difference between the Atlantic and Pacific is not as pronounced. While my estimates of the strong evaporative role of the Indian Ocean are comparable to those found by W92, DT03 found the excess E to be

less than either this estimate or the W92 estimate. Compared to W92, the Southern Ocean is much more precipitative in both this and the DT03 estimates.

The most recent publications (T08 and LY09) used in this comparison agree well with my estimates of the Pacific and indicate only a marginally net precipitative state. However, the Southern Ocean in T08 is significantly less precipitative than in my estimate, but is similar to LY09. The Indian Ocean is significantly more evaporative in this estimate than in T08 and slightly more evaporative than in LY09.

3.3 Net Heat Fluxes into the Ocean

A similar situation to the 'sampling problem' of E and P fluxes is true for oceanic heat flux data. Heat fluxes over the ocean are composed of four basic budgets: Incoming shortwave radiation (Q_{SW}), longwave radiation (Q_{LW}), sensible heat fluxes (Q_{SH}) and the latent heat loss due to evaporation (Q_{LH}). While Q_{SW} is positive (a net heat input to the ocean) in almost all circumstances, while Q_{LH} is almost always negative (a net heat loss) since the evaporation (the cause of latent heat loss) occurs at the air-sea interface while condensation (the reverse process and a net source of heat) occurs in the atmosphere and not at the surface of the ocean. Q_{SH} Q_{LW} may have either sign, depending on the region, but are negative when integrated over the global ocean (Yu et al., 2008). In the case of Q_{SH}, the sign is determined by the temperature gradient between the surface ocean and the overlying atmosphere (if the ocean is warmer, there will be a sensible heat flux from the ocean to the atmosphere), while Q_{LW} depends predominantly on the cloud cover. Integrating over the area of the oceans, a picture emerges in which the net shortwave (ultraviolet, visible and near-infrared) radiation (Q_{SW}) is balanced by the net longwave (Q_{LW}), sensible (Q_{SH}), and latent (Q_{LH}) heat fluxes (Yu et al., 2008)

The relationship between the amount of E and Q_{LH} is dependent on the temperature at which the phase transition from the liquid phase to the gaseous phase occurs. However, the relationship is linear to first order, so that with a suitable scaling factor the OAFlux E field is comparable to the OAFlux Q_{LH} field. Since sea-surface temperature (SST) is one of the input variables of E, the exact value of Q_{LH} can be calculated from E and vice versa (Hartmann, 1994; Fairall et al., 2003).

While it is possible to measure incoming shortwave radiation (Q_{SW}) from satellite platforms, the incoming radiation at the orbit of the satellite is not equivalent to the

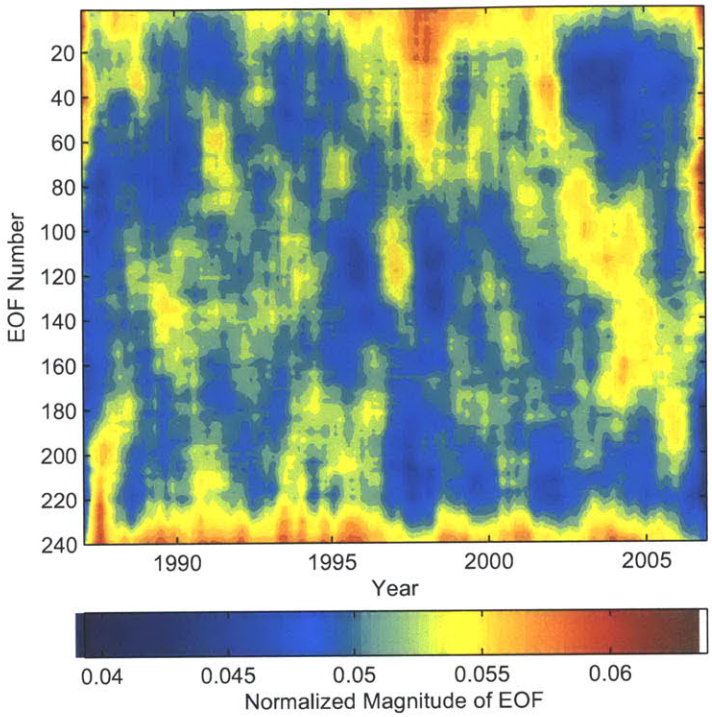

Figure 3-7: Filtered results of principal component analysis (PCA) of the OAFlux/ISCCP Q_{net} estimate. The magnitude of all PCAs (color-coded) is plotted with respect to time and the number of the PCA. In this analysis, no significant changes in patterns are observable between 1987 and 2006. An ENSO signal is evident between 1997–1998.

radiation actually reaching the surface of the Earth (Zhang et al., 2004). To parameterize the transfer of radiative energy from the top of the atmosphere to the surface, knowledge of clouds, water vapor and a humidity profile are required. These may be inferred from satellite observations using infrared, microwave and visible measurements (Zhang et al., 2004). The International Satellite Cloud Climatology Project (ISCCP, (Zhang et al., 2004)) is currently regarded as one of the most advanced quantifications of this kind, and are used by a number of Q_{net} estimates. . These estimates of Q_{SW} and Q_{LW} have been combined by Yu et al. (2008) with Q_{LH} and Q_{SH} to form the OAFlux Q_{net} estimate. Q_{SH} is based on a parameterization using SST, air temperature and the wind speed at $10m$ above sea level, all of which are also input variables for E (Fairall et al., 2003). Yu et al. (2008) thus provide a full estimate of Q_{net}. The homogeneity of this estimate is evaluated as before for E and P.

While this analysis shows no changes in the PCA analysis (Figure 3-7), the monthly mean radiation (Figure 3-8) exhibits changes around 2002, which can be linked to the introduction to a new set of SST data in the ISCCP product (Zhang et al., 2004).

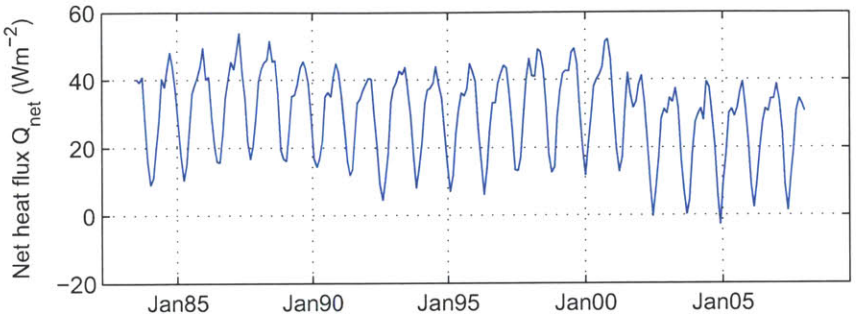

Figure 3-8: Globally integrated net radiative budget (Q_{net}) between 1987–2006. Inter-annual changes are evident before 2002, with an abrupt downward shift of the mean by approximately $10Wm^{-2}$ in 2002 due to the introduction of a different SST product. A net imbalance of $29Wm^{-2}$ is evident in the data, which is corrected to close the budget (see text).

These results indicate that the period 2002–2006 can be used with confidence, while caution should be observed when using the full duration of 1987–2006. However, a time-series of 4 years is insufficient to detect changes due to inter-annual and inter-decadal variabilities such as the El Niño Southern Oscillation (ENSO) or the North Atlantic Oscillation (NAO). Consequently, the full duration of 1987–2006 will be used with the caveat that some inhomogeneities might be present in the data. This issue will be revisited and addressed in Chapter 4.8.

Figure 3-8 indicates a net influx of heat ($29Wm^{-2}$) into the ocean, thus exceeding a flux of realistic anthropogenic ocean warming (estimated as approximately $1Wm^{-2}$ by Hansen et al. (2005)) by a factor of 30. Since a balancing of the freshwater cycle required an increase of E by 3%, Q_{LH} is re-calculated using the corrected E estimate. While this correction reduces the global imbalance to $27Wm^{-2}$, this still exceeds any realistic estimate of the current net heat imbalance. This error can be attributed to large uncertainties particularly in Q_{LW} (Zhang et al., 2004). To close the balance, the global imbalance is subtracted (taking into account the area variations caused by the usage of a $1° \times 1°$ grid) from the balance to reach a steady-state of $\iint_A Q_{net} dA = 0$.

Table 3.3: Comparison of Q_{net} imbalances of the eight evaluated products in $\mathrm{W\,m^{-2}}$. All datasets exhibit a positive heat flux (net heat is added to the ocean). Since ECCO2 is an ocean model, all surface fluxes are adjusted to match ocean observations.

Q_{net} product	Imbalance ($\mathrm{W\,m^{-2}}$)
OAFlux (ISCCP)	29
OAFlux (CERES)	24
OAFlux (SRB)	32
ERA-Interim	10
MERRA	17
ECCO2	2.3
NOCS v.2	20
J-OFURO2	24

3.4 The Global Picture of Thermal and Freshwater Forcing

In the previous sections the process of determining the current state-of-the-art of estimating the oceanic freshwater cycle and the oceanic heat budget have been discussed. Based on this work, two estimates were generated: One is the global balance of E-P-R, in which E has been artificially biased high by 3% to close the freshwater budget, fulfilling the condition that $\oiint_A (E - P - R)dA = 0$. The bias introduced to this estimation is within the error margins provided by the individual products and is based on the assumption that current E datasets do not resolve extreme events and small-scale features, such as narrow boundary currents, sufficiently. The global annual average of E-P is shown in Figure 3-4.

It is evident that the sub-tropical gyres and western boundary currents of the Atlantic, Pacific and Indian oceans are all regions of net E, while the inter-tropical convergence zone (ITCZ) as well as high latitudes ($> 40°$) are regions of net P. While the whole of the Atlantic subtropical gyres are net evaporative, the Pacific subtropical gyres – particularly the southern gyre – are predominantly net evaporative near the eastern boundaries. Since E is a function of the relative humidity of the air overlying the water (Hartmann, 1994), the air becomes saturated in humidity and E decreases as the overlying air is driven westward by the trade winds. From Figure 3-4 it is

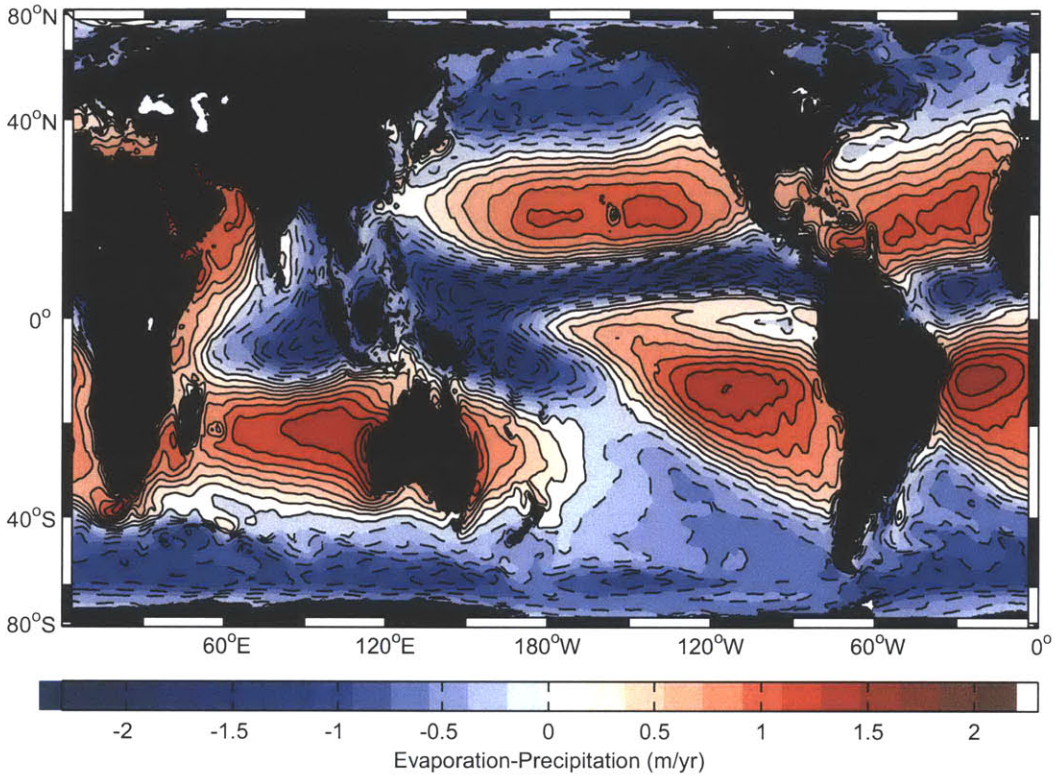

Figure 3-9: Global annual average E-P map for 1987-2006 based on OAFlux E and GPCP P with increased E to artificially balance the freshwater budget. All subtropical ocean gyres and subtropical marginal seas are dominated by excess E, while the regions of the ITCZ and the Indonesian Throughflow as well as most temperate and subtropical latitudes are dominated by excess P. The maximum imbalance of $2.2\,\mathrm{m\,yr^{-1}}$ occurs in the Red Sea, while the minimum of $-2.6\,\mathrm{m\,yr^{-1}}$ occurs near the Columbian Pacific coast in the ITCZ. Seasonal ice-cover is averaged over the ice-free period (see text).

also evident that the Atlantic is a net evaporative basin while the Pacific is net-precipitative.

The other estimate generated here is Q_{net}, which was corrected to be consistent with the increased E fields used in the E-P-R estimate. After subtracting a global imbalance of $29 W m^{-2}$, which is likely caused by errors in the incoming Q_{LW} data (L. Yu, *pers. comm.*), this estimate fulfills the condition that $\oiint_A Q_{net} dA = 0$. Figure 3-10 shows that the ITCZ and upwelling zones along the eastern boundaries of all

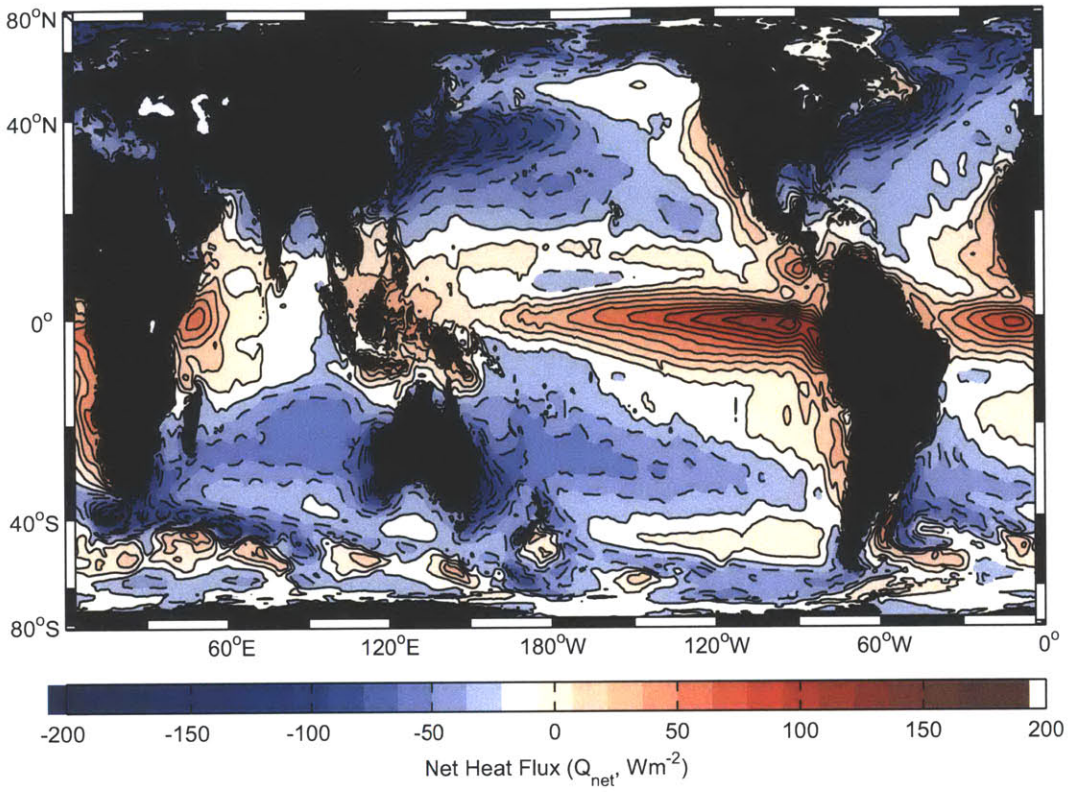

Figure 3-10: Global annual average Q_{net} map for 1987-2006 based on OAFlux Q_{LH}, Q_{SH} with increased Q_{LH} to match a 3% increase in E (see text) and ISCCP Q_{SW} and Q_{LW}. Q_{net} has been biased low by $27.26\,\mathrm{W\,m^{-2}}$ to ensure that there is no net integrated heat input to the ocean. The ITCZ as well as coastal upwelling zones along the eastern boundaries of the Atlantic, Pacific and Indian Ocean (with the exception of Australia) are regions of high heat input, while western boundary currents such as the Gulf Stream, the Kuroshio, the Agulhas, the East Australian and the Brazil current are strong sinks of heat.

three ocean basins – with the exception of the Australian coast – are areas of net heat input, while the western boundary current – the Gulf Stream, the Kuroshio, the Agulhas, the East Australian and the Brazil current – as well as some parts of the Antarctic Circumpolar current are areas of net heat loss. The Australian west coast is the only exception to the general pattern of heat loss along western boundaries and heat gain along eastern boundaries. This is caused by the Leeuwin current system which transports warm water polewards (Cresswell and Peterson, 1993). The Southern Ocean shows regions of both net heat loss and gain, closely associated with

the path of the Antarctic Circumpolar Current.

While the subtraction of a constant to artificially balance the Q_{net} estimate may seem like a primitive way to achieve the necessary conditions, there are too few *in-situ* observations to attribute such a large error to a specific area. For this reason, a sensitivity analysis is performed in Chapter 4.8 which investigates the sensitivity of variance production to equator-pole biases.

3.5 Sea Surface Salinity

Sea surface salinity (SSS) is taken from the MetOffice EN3 v3a product (Ingleby and Huddleston, 2007) and is available at a resolution of $1° \times 1°$ at monthly intervals. A global map of this is plotted in Figure 3-11. While there are new SSS estimates available through satellite remote sensing, these fields do not yet provide a significant improvement in the time-mean over *in-situ* based measurements and are thus far too short in duration to be useful in the analysis of inter-annual variability.

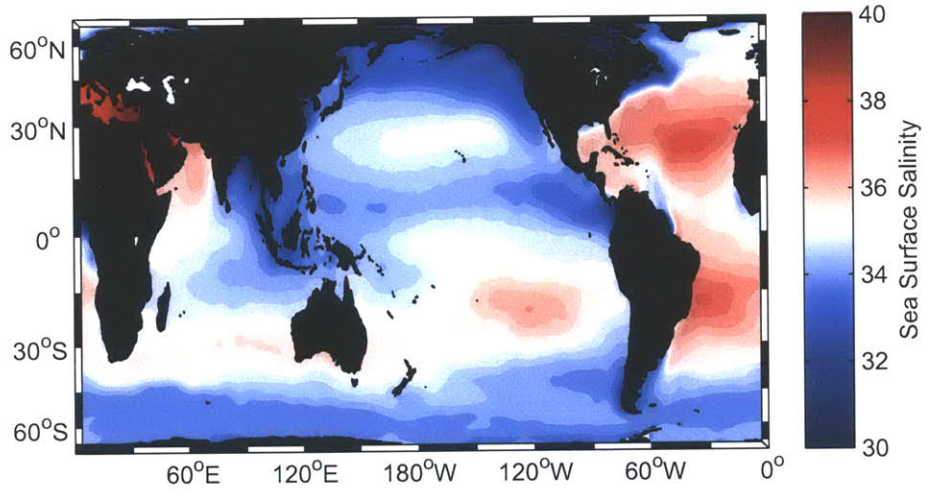

Figure 3-11: Mean Sea Surface Salinity (SSS) - MetOffice EN3 v2a 1987-2004 time-mean. The Atlantic is significantly saltier than the Pacific Ocean. The Mediterranean and Red Sea are the saltiest regions, while the Arctic Ocean is the freshest basin. The subtropical gyres are clearly visible and similar in shape to the pattern of E-P. The Amazon river plume is visible as a negative signature in the equatorial region around 60 ° W.

While the Atlantic is significantly saltier than the Pacific, the patterns of subtropical gyres are similar in shape and location to the pattern of E-P in presented in Figure 3-4. The Mediterranean and Red Sea are significantly saltier than any ocean basin, while the Arctic Ocean is the freshest area due to a large excess of precipitation and runoff. Coastal upwelling regions are visible along the West African coast as well as the North- and South American coast. The Amazon river discharge plume originates in the equatorial region around 60 °W and extends to approximately 60 °W, 10 °N. The Gulf Stream is clearly evident as a strong salinity gradient, with high salinities to the south and lower salinities to the north of it.

3.6 Sea Surface Temperature

Sea surface temperature (SST) is taken from the MetOffice EN3 products (Ingleby and Huddleston, 2007) and is available at a resolution of $1° \times 1°$. The map of the temporal mean of monthly data for the period 1987–2004 is shown in Figure 3-12. SST is one of the best-constrained estimates of all quantities used here since the introduction of oceanographic satellites. It is possible to remotely sense SST from infrared and passive microwave satellites with an accuracy of $\approx$ 0.3–1 °C (e.g. Robinson, 2004, and references therein). As a result, the choice of SST product is not critical for the purposes of this thesis, as the estimated errors associated with both freshwater- and heat-fluxes over the ocean far exceed the estimated errors of modern SST products.

While there may be more accurate SST products, The EN3 v2a product is chosen here since it is a three-dimensional product with 42 depth levels, providing consistent estimates of temperature and salinity in the interior ocean. This is used in Chapter 5 and allows the use of a single product for SST, SSS, interior temperature and salinity.

A clear meridional temperature gradient is evident in all ocean basins, modified by western boundary currents, which advect heat polewards. The equatorial upwelling regions, particularly the Pacific cold tongue, and coastal upwelling regions cause negative anomalies in this field. The warming of the Eastern North Atlantic through the North Atlantic current is evident as a positive anomaly relative to the meridional temperature gradient.

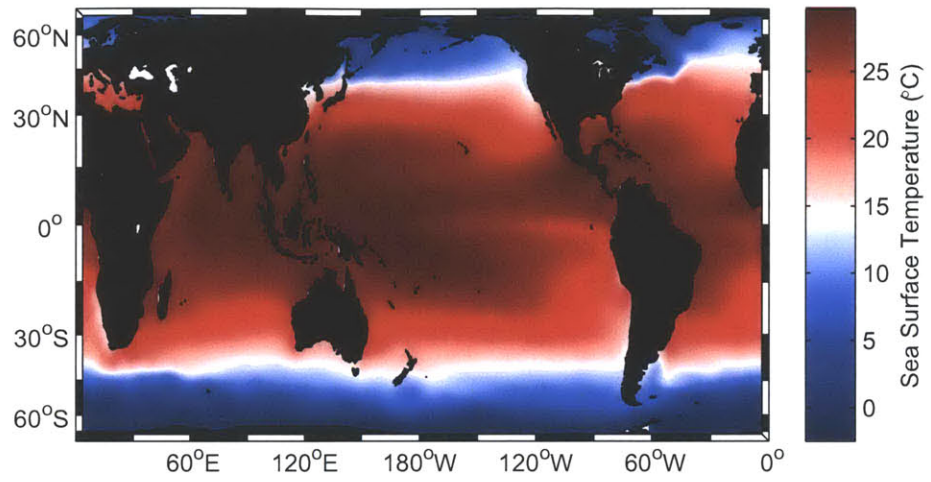

Figure 3-12: Sea Surface Temperature (SST) - MetOffice EN3 v2a 1987-2004 time-mean. A strong meridional gradient is modified by upwelling regions and western boundary currents.

3.7 Other Sources of Heat and Salt to the Ocean

While it seems likely that solar heating and heat loss through longwave, shortwave, sensible and latent heat fluxes are the dominant drivers of temperature variance generation in the ocean, there are other sources of heat to the ocean that are included in the total budget. These sources may be fluxes to the interior ocean (such as bottom fluxes) or may not be included in current estimates of surface fluxes.

3.7.1 Geothermal Heating of the Ocean

Kadko et al. (1995, and references therein) estimate the total heat flux through the oceanic crust as 8.6×10^{12} W. To include these fluxes in a calculation that uses only surface fluxes, a grid point at the surface is chosen that has temperature and salinity values closely matching those of the abyssal ocean.

Using the time-mean of the EN3 product (Ingleby and Huddleston, 2007) for both temperature and salinity, the mean values of conservative temperature (CT) and absolute salinity (SA) (McDougall, 2011) below 3000 m are found to be 2.91 °C and 34.71, respectively. This depth range is chosen because more than half of the

ocean is deeper than 3000 m (Amante et al., 2009) and most of the hydrothermal activity and heat fluxes occurs in these depths (Kadko et al., 1995, and references therein). This corresponds to a potential density of $\rho = 1027.58\,\mathrm{kg\,m^{-3}}$ with spice (Huang, 2011) of $\tau = -3.10\,\mathrm{kg\,m^{-3}}$. The grid point most closely matching these values is 74 °N, 11 °W, which is slightly northeast of Iceland. At this point, the time-mean of potential density is $\rho = 1027.60\,\mathrm{kg\,m^{-3}}$, spice is $\tau = -3.1\,\mathrm{kg\,m^{-3}}$, temperature is 3.04 °C, and the salinity is 34.69.

This particular grid point has an area of $4.74 \times 10^9\,\mathrm{m^2}$, which means the additional net heat input that is added only to this point in T-S space is given by:

$$\frac{8.6 \times 10^{12}}{4.74 \times 10^9} = 182\mathrm{W\,m^{-2}} \tag{3.1}$$

This heat is added before the artificial balancing of the global surface heat budget, since the required steady-state assumption necessitates all added heat to be removed through surface cooling. As will be shown in Chapter 4, the contribution of this heating term to the total thermal, haline, density and spice variance production is less than 0.02 %. While this makes this heat flux negligible for the purposes of this study, it should be noted that this heat is not added to the surface of the ocean, but rather directly to the deep ocean. It thus directly contributes a non-trivial amount of energy ($\approx 0.05 \times 10^{12}$ W) required to maintain the general circulation of the oceans (Wunsch and Ferrari, 2004).

There are also chemical inputs and sinks, such as for magnesium (Kadko et al., 1995), due to hydrothermal and mantle fluxes: As the water is convected through the ocean floor, minerals are dissolved and others react with rocks such as basalt at high temperature, thus affecting the salinity. When converted to buoyancy forcing, a crude estimate based on the numbers presented in Kadko et al. (1995) indicates that expressed as a buoyancy flux, this effect is at least 2 orders of magnitude smaller than that of geothermal heat forcing. As a consequence, this effect is not included in the calculations presented in Chapter 4.

3.7.2 Frictional Heating

There are additional heating terms through internal friction of mixing, with the dominant energy sources being winds and tides (Wunsch and Ferrari, 2004). These contribute approximately an estimated 23.5 TW (2.35×10^{13} W) to the interior ocean

(Wunsch and Ferrari, 2004, Fig. 5), which is equivalent to a global mean surface heat flux of approximately $0.06\,\mathrm{W\,m^{-2}}$. This term is ignored in this study as the errors in the products used are several orders of magnitude greater than this additional source term. Since the spatial distribution of the dissipation is not very well constrained (Wunsch and Ferrari, 2004), one may be tempted to add a uniform flux to the ocean surface to account for this effect. However, due to the steady-state assumption, this additional flux term would be removed in the process of zero-balancing the surface forcing, rendering this approach pointless.

3.7.3 · Sea-Ice Formation and Brine Rejection

When sea-ice freezes, brine-rejection occurs due to the crystalline structure of salt, which differs from that of ice (e.g. Midttun, 1985, and references therein). As a result, sea-ice is much fresher than seawater and in the process of freezing forms brine channels, which add salty brine to the water below the formation region. Depending on the circumstances of formation of sea-ice, the resulting ice may have a salinity of approximately 10 (Midttun, 1985). Assuming the formation and melting of sea-ice occurs in the same location (which may not be the case if the ice is advected by wind or currents), the equivalent surface freshwater and salt forcing would cancel. In the case of a seasonal cycle, however, there is an addition and removal of salt in the Arctic Ocean as well as in the Southern Ocean around Antarctica.

To quantify this effect, I use data from a modeling study by Gordon et al. (2000), which suggests an annual sea-ice volume cycle with a mean annual minimum of $10 \times 10^{12}\,\mathrm{m^3}$ and a mean annual maximum of $35 \times 10^{12}\,\mathrm{m^3}$. The salinity changes from an average high-latitude ocean surface value of ≈ 34 to ≈ 10 in the ice, thus inducing a total salinity change of ≈ 24. In the Southern Ocean, the annual cycle causes the sea ice volume to fluctuate between $7 \times 10^{12}\,\mathrm{m^3}$ and $27 \times 10^{12}\,\mathrm{m^3}$. This means that the total annual flux is approximately $25 \times 10^{12}\,\mathrm{m^3}$ in the Arctic Ocean and approximately $20 \times 10^{12}\,\mathrm{m^3}$ in the Southern Ocean, which is equivalent to annual salt fluxes of

$$24 \cdot 25 \times 10^{12}\,\mathrm{m^3} \cdot 1000\,\mathrm{kg\,m^{-3}} \cdot \frac{1008\,\mathrm{kg\,m^{-3}}}{1027\,\mathrm{kg\,m^{-3}}} = 5.9 \times 10^{14}\,\mathrm{kg} \tag{3.2}$$

$$24 \cdot 20 \times 10^{12}\,\mathrm{m^3} \cdot 1000\,\mathrm{kg\,m^{-3}} \cdot \frac{1008\,\mathrm{kg\,m^{-3}}}{1027\,\mathrm{kg\,m^{-3}}} = 4.7 \times 10^{14}\,\mathrm{kg} \tag{3.3}$$

in the Arctic (Eq. 3.2) and the Antarctic (Eq. 3.3). By making the (rather crude) assumption that the formation of the ice occurs in approximately 3 months and the melting also occurs in 3 months, it is possible to convert this to a more meaningful rate, namely to $2.25 \times 10^8\,\mathrm{kg\,s^{-1}}$ and $1.8 \times 10^8\,\mathrm{kg\,s^{-1}}$, respectively. To preserve consistency, these fluxes are added as two point sources to respective grid point that is at the highest latitude but flagged as continuously sea-ice free in all datasets. In this computation, I assume that the brine formation in the Arctic occurs in December, January and February (DJF) and that melting occurs in June, July and August (JJA). In the Southern Ocean, the opposite is assumed, namely that formation occurs in JJA and melting occurs in DJF.

As will be shown in Chapter 4, the inclusion of this flux increases the seasonal density variance generation by $\approx 2\,\%$ while the effects on spice variance are smaller, causing a decrease of $\approx -0.4\,\%$. Even though these terms are more than one order of magnitude smaller than the combined estimated errors of the datasets, they are included in all calculations in 4 to include effects of the seasonal cycle.

3.8 Derived Data

From the SST and SSS datasets discussed in Sections 3.6 & 3.5, density and the thermal and haline coefficients (α and β, respectively) are calculated using the Thermodynamic Equation of Seawater 2010 (TEOS-10 (McDougall, 2011)).

3.8.1 Sea Surface Density

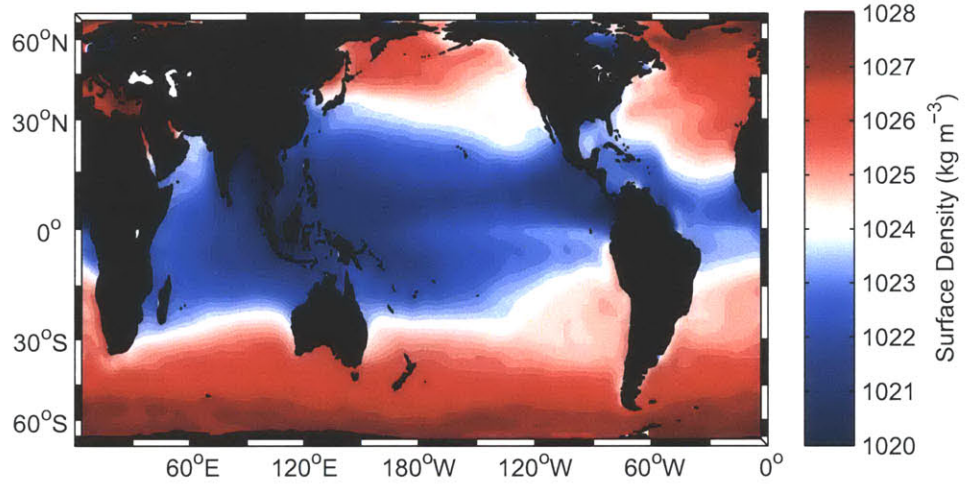

Figure 3-13: Sea surface density ρ computed using TEOS-10 from EN3 v2a SSS and SST data. The highest densities are found in regions associated with deep water formation, such as the Nordic Seas and parts of the Southern Ocean. The lowest densities are found around the equator, particularly in areas that have a net excess of precipitation.

The sea surface density ρ is shown in Figure 3-13. The highest densities occur in regions that are associated with deep water formation, such as the Seas around Greenland, Iceland and Norway as well as parts of the Southern Ocean. The lowest densities are found around the equator, as the product of the global temperature gradient ($\Delta\theta \approx 30\,^{\circ}\mathrm{C}$) with thermal coefficient (α) is greater than the product of the salinity gradient ($\Delta S \approx 10$) with the haline coefficient (β). Surface density minima are found in the ITCZ, the northern Indian Ocean and the Indonesian Throughflow.

3.8.2 Sea Surface Spice

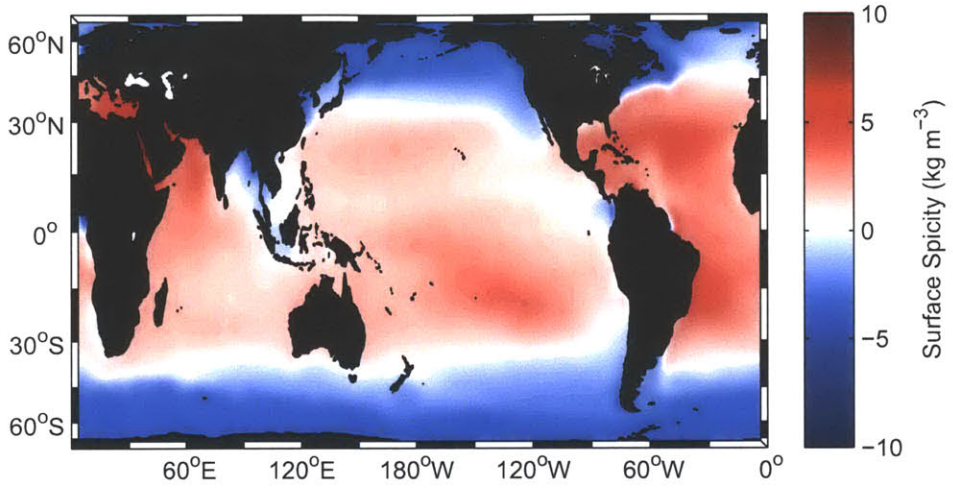

Figure 3-14: Sea surface spiciness computed from EN3 v2s SSS and SST using a spice equation by Huang (2011). The Atlantic is spicier than the Pacific due to its higher surface salinity. Waters at high latitude are the least spicy, as they tend to be cold and fresh.

Sea surface spice is so named because a region that is hot and salty is 'spicy', while a region that is fresh and cold has negative spiciness ('bland'). Spice is defined to be perpendicular to lines of equal density in *theta*-S, so a movement along lines of equal density would be equivalent to the greatest gradient in spice (Veronis, 1972; Huang, 2011). Similarly, moving along lines of equal spice maximizes the change in density. The global surface spiciness was computed using a vectorized version of the spice equation provided by Huang (2011).

The result is plotted in Figure 3-14. While the distribution of spiciness largely follows the picture evident in SST (Figure 3-12), the effects of the ITCZ are clearly visible as a negative spice signature. The Atlantic Ocean is also more spicy than the Pacific due to its higher SSS.

3.8.3 Thermal and Haline Coefficients

The TEOS-10 equations (McDougall, 2011) are used to compute the thermal and haline coefficients α and β. While α is largely a function of temperature, there are also salinity effects on α. While one may assume that β should be dominated by salinity in the global ocean, the influence of temperature is greater than that of salinity over typical oceanic gradients. By determining α and β for each grid point (and for each time step in the case of monthly data), it becomes possible to compute the nonlinear density and spice fluxes into the ocean, which will be shown in Chapter 4.

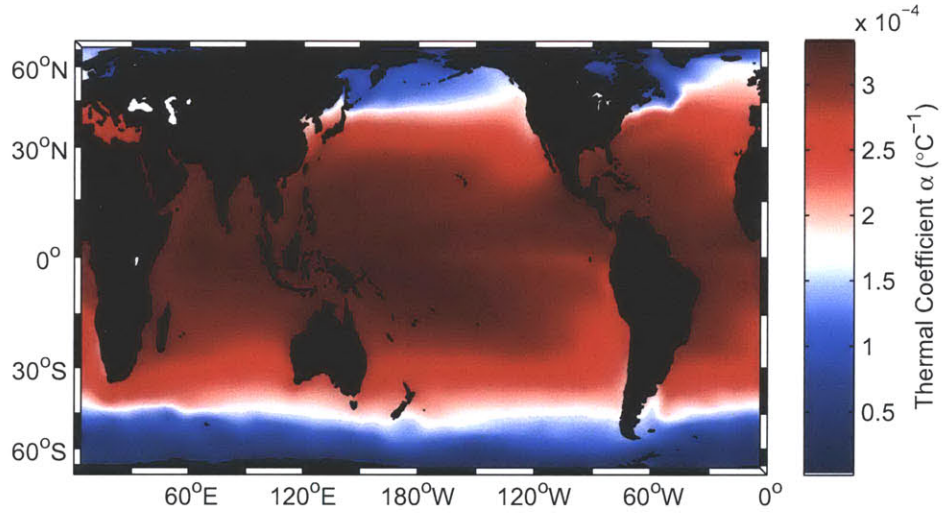

Figure 3-15: Thermal coefficient of expansion or contraction α for the surface ocean calculated using TEOS-10 equations with EN3 v2a SSS and SST datasets. The patterns largely follow those discussed for SST, as α is largely a function of temperature.

As discussed in Chapter 2, Eqs. (2.26 & 2.27), α and β are defined as:

$$\alpha = -\frac{1}{\rho_0} \cdot \left.\frac{\partial \rho}{\partial \theta}\right|_{S,p} \tag{3.4}$$

$$\beta = \frac{1}{\rho_0} \cdot \left.\frac{\partial \rho}{\partial S}\right|_{\theta,p} \tag{3.5}$$

The global distribution of α is plotted in Figure 3-15. The patterns very closely

follow those of sea surface temperature (Figure 3-12) with identical features.

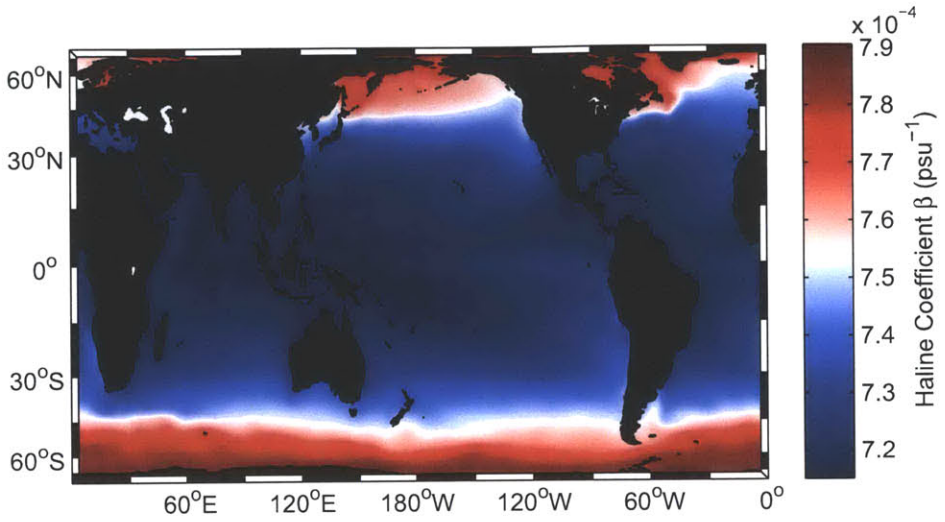

Figure 3-16: Haline coefficient β computed using TEOS-10 routines with EN3 v2a SSS and SST data. The distribution largely follows the inverse of SST. The range of values of β at the ocean surface is significantly smaller than that of α.

The global results of β are shown in Figure 3-16, the features of which are largely an inverse of α and hence SST. β increases with decreasing temperature and thus the highest values are found in high latitudes. It should be noted that while α changes from a minimum of approximately $0.1\,^{\circ}\mathrm{C}^{-1}$ to $3.3 \times 10^{-4}\,^{\circ}\mathrm{C}^{-1}$, the changes in β are much smaller, ranging merely from $7.15 \times 10^{-4}\,\mathrm{psu}^{-1}$ to $7.85\,\mathrm{psu}^{-1}$ at the surface of the global ocean. As a result, the apparent negative density flux into the ocean and the compensation through cabbeling in the interior, which is discussed in Chapter 5, is largely driven by thermal forcing.

Chapter 4

Variance Estimates

With the estimates discussed in Chapter 3 it is now possible to evaluate the 'power integrals' (Stern, 1969, 1975) that were derived in Chapter 2. In this chapter, I estimate thermal, haline, density, and spice variance production and thus the required dissipation through mixing that is required to maintain a gradient in steady-state. While the production and dissipation of thermal variance in the ocean has already been evaluated by Joyce (1980), I repeat this process with a number of satellite-derived estimates.

While the combination of OAFlux evaporation (E) (Yu et al., 2008), GPCP precipitation (P) (Adler et al., 2003) and Dai and Trenberth (2002); Dai et al. (2009) riverine runoff (R) as well as OAFlux net heat flux (Q_{net}) is used as the 'baseline' for all computations, 7 other Q_{net} estimates and 5 other E-P-R estimates are used in later sections to provide a range of values and to illustrate the range of results. While some of these products produce markedly different results than others, it should be noted that this does not imply that this is an absolute upper and lower bound on the estimates, as systematic errors that are common to all products may produce estimates that are outside the range of estimates provided here. It is also not implied that all products are equally credible, as was described in Chapter 3. In comparisons with independent data, the *in-situ* Q_{net} and E-P-R products (OAFlux, NOCS v.2 and J-OFURO2) consistently produce lower errors than re-analysis based products.

The use of surface power integrals assumes that all fluxes occur at the surface and do not account for internal sources of variance generation. In Chapter 2 the relationship between the flux ratio γ and R_ρ in Eq. (2.53) may produce a net generation of density variance at low values of R_ρ. This was illustrated in Figure 2-2.

4.1 Heat, Freshwater, Density, and Spice Fluxes in the Ocean

In Chapter 2 it has become clear that the patterns of surface freshwater and thermal forcing are important in evaluating the production and dissipation of variance. For the purpose of evaluating fluxes relative to θ, S, ρ and τ, the time means of surface forcings have been computed for the period of 1987–2004 in Chapter 3. These are then used in $\theta - S$ space to examine the relative distributions and the gradients associated with them. Both density and spice are also contoured on all diagrams. This is a graphic representation of basis of power integrals: High tracer concentrations tend to occur in areas of positive fluxes (and vice versa). This implies a down-gradient flux, which is driven by mixing in the ocean.

4.1.1 Heat Fluxes

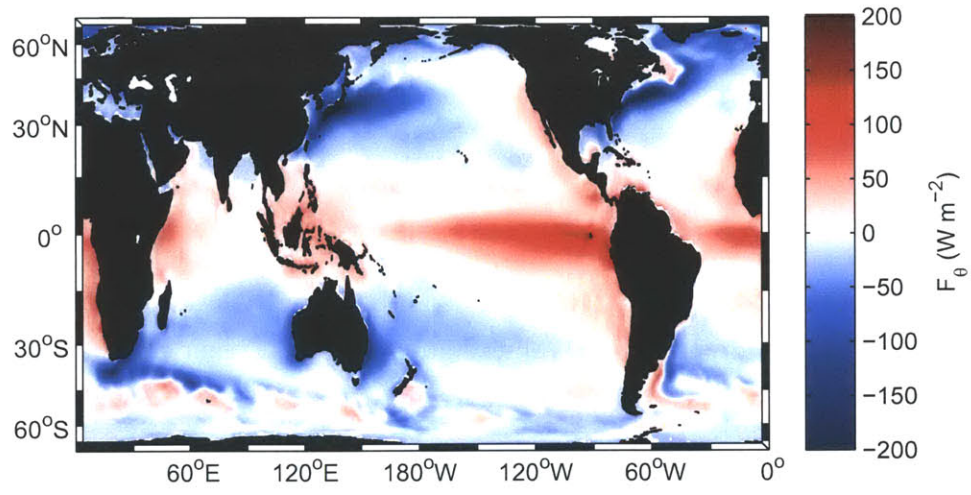

Figure 4-1: Surface heat flux F_θ W m^{-2}. The main gradient is meridional between equators and poles. This pattern is modified by heat entering the ocean in tropical regions and along areas of coastal upwelling, such as the West Coast of Africa. Strong heat losses are also evident over all Western Boundary Currents.

The global pattern of the heat flux is plotted in Figure 4-1. As is noted in Chapter 2, Eq. (2.13), this is simply Q_{net}. The dominant gradient is meridional, with heat entering the ocean in tropical latitudes, particularly along the equator, and heat loss

occurring mainly polewards of 30°. This pattern is modified by additional heat gain along coastal upwelling regions, such as the West Coasts of North America, South America and Africa. Strong heat losses are evident in all Western Boundary Currents.

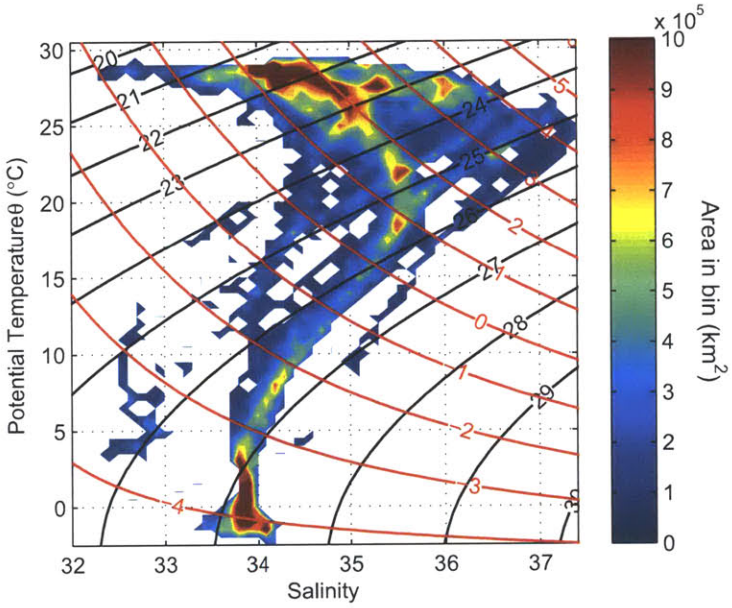

Figure 4-2: Total surface area (km^2) for each potential temperature and salinity bin. The bin separation is 0.1 in salinity and 0.5 °C in potential temperature.

To illustrate the distribution of data in $\theta - S$ space, the data were binned using a division of 0.1 for S and 0.5 for θ. The total surface area of each bin is shown in Figure 4-2, with all bins which sum to less than $5 \times 10^4\,\mathrm{km}^2$ having been removed. From this, it is evident that large areas of the global ocean have very similar surface θ and S characteristics. The broadest peak occurs around $\theta \approx 28\,^\circ\mathrm{C}$, $S \approx 34.7$, caused by relatively fresh but warm waters in the inter-tropical convergence zone (ITCZ). High values of surface area per bin are found at high salinity and somewhat lower θ. This continues towards the sub-polar gyres and finally into the Arctic and Antarctic waters where a second peak of $\theta = 0°C, S = 33.8$ is found.

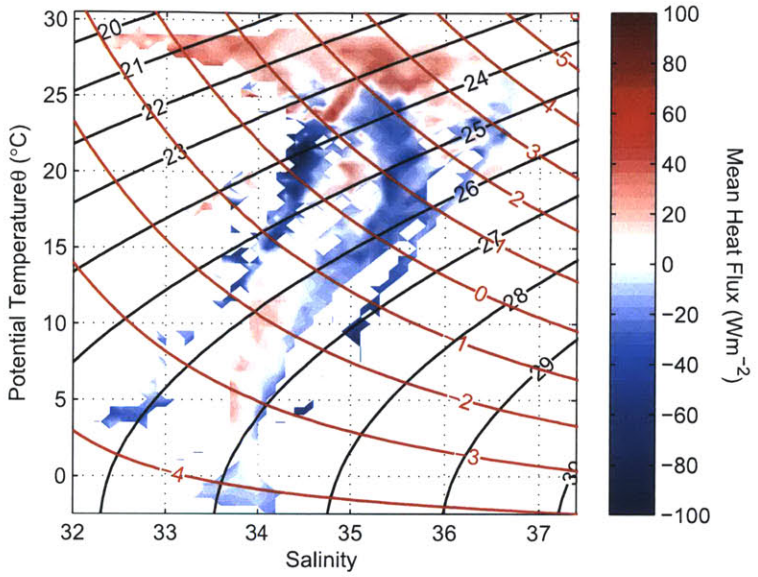

Figure 4-3: Corrected mean heat flux (Wm^{-2}) for each potential temperature and salinity bin. The bin separation is 0.1 in salinity and 0.5 °C in potential temperature.

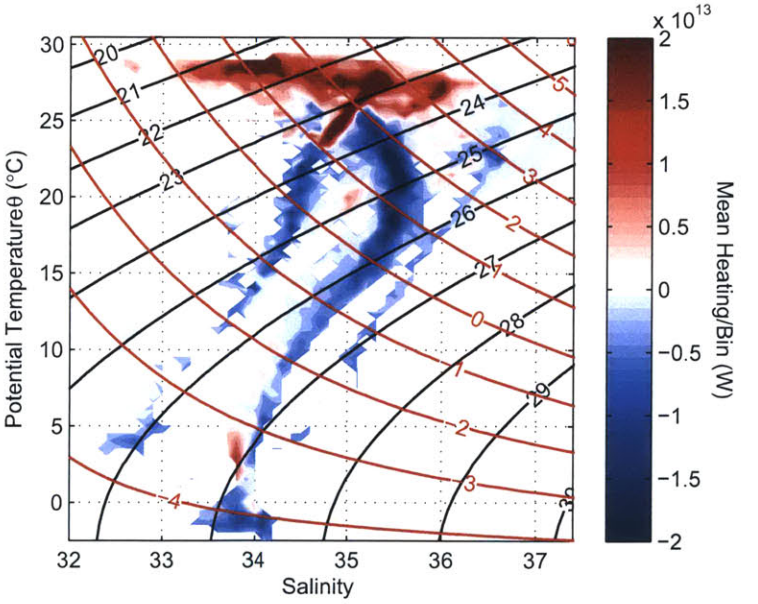

Figure 4-4: Total heat flux (W) for each potential temperature and salinity bin. The bin separation is 0.1 in salinity and 0.5 °C in potential temperature.

In the same manner as for the total area, the net heat flux can be plotted in $\theta - S$ space. This is shown in Figure 4-3. Heat loss occurs in the subtropical gyres where E is dominant, while heat is gained in the ITCZ as well as regions of boundary currents such as the Gulf Stream, Kuroshio, Agulhas and East Australian Current.

It should be noted that three distinct transition lines are evident: the most saline transition from high to low temperatures is associated with the North Atlantic Ocean, while the central and lower salinity tracks are representative of values in the Pacific and Indian Ocean. When the heat flux is multiplied by the area of each bin, the total flux in each bin is obtained. This is plotted in Figure 4-4 and illustrates that the surface properties of the basins tend to be rather homogeneous.

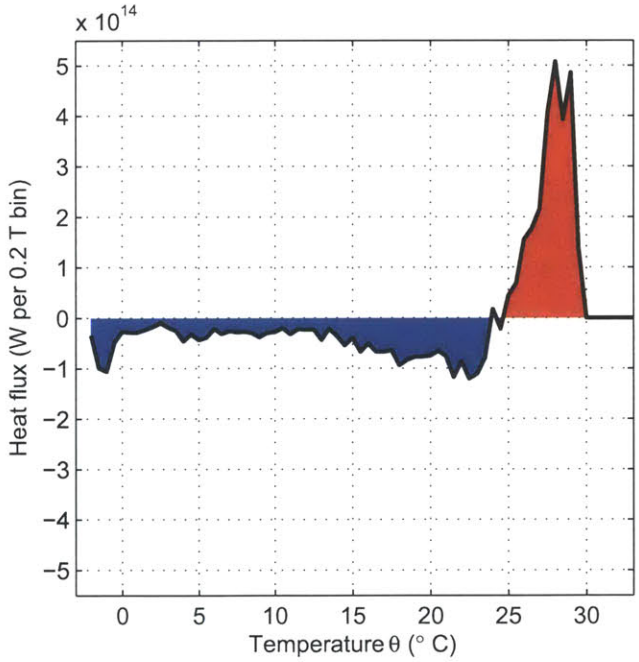

Figure 4-5: Heat flux Q_{net} ($\mathrm{W\,m^{-2}}$) for each potential temperature bin. The bin separation is 0.1 °C. There is a clear separation of heat input at high sea surface temperatures and heat loss at low sea surface temperatures.

Figure 4-4 shows the absolute heat flux in each bin, i.e. the total area multiplied by the mean value of Q_{net} corresponding to each bin. It is evident that there are strong gradients between positive heat fluxes in the ITCZ and strong negative fluxes in the subtropical gyres. While most of the temperate ocean ($10 < \theta < 22$ °C) exhibits negative heat fluxes, a significant heat input associated with the Southern

Ocean is evident at low temperatures. This suggests surface production of thermal variance in the tropics and subtropics, but a more complex picture emerges in the Southern Ocean, where the datasets surprisingly indicate there is significant buoyancy gain. This is likely associated with wind driven upwelling of deep waters south of the Antarctic Circumpolar Current (Toggweiler and Samuels, 1995; Karsten and Marshall, 2002)

The fluxes in each bin as shown in Figure 4-4 may be summed along lines of constant temperature to illustrate the down-gradient flux. This is plotted in Figure 4-5. A strong net heat gain is evident above a temperature of 25 °C, with heat losses occurring over a greater range of temperatures from -2 °C to 25 °C.

4.1.2 Freshwater and Salt Fluxes

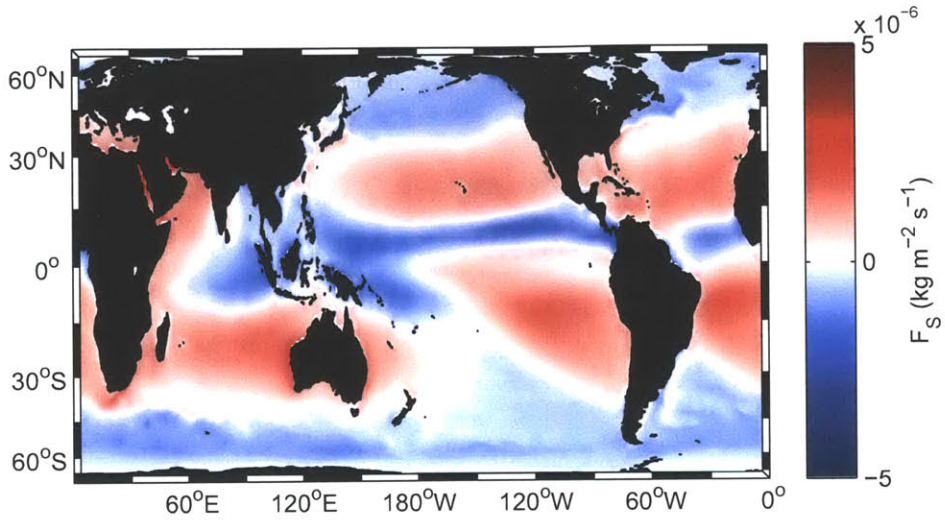

Figure 4-6: Surface salt flux $\overline{F_S}$ ($\mathrm{kg\,m^{-2}\,s^{-1}}$). It should be noted that salt fluxes are not 'true fluxes' in the sense that the salt is not actually moved, but rather concentrated or diluted at the surface due to E, P and R. A negative salt flux is evident in the ITCZ as well as high latitudes, while sub-tropical gyres show a strong positive salt flux into the ocean, caused by net excess evaporation.

The general distribution of the salt flux is plotted in Figure 4-6. The definition of this flux follows work by Schmitt et al. (1989); Warren (2009). While the surface salt flux is a theoretical flux in the sense that salt does not actually enter or leave the ocean, it is an equivalent flux caused by dilution (net P or R) or concentration (net E) of surface waters. The ITCZ has a strong negative salt flux due to excess precipitation leading to the dilution of surface waters with freshwater, while the net evaporative sub-tropical gyres exhibit a strong positive salt flux.

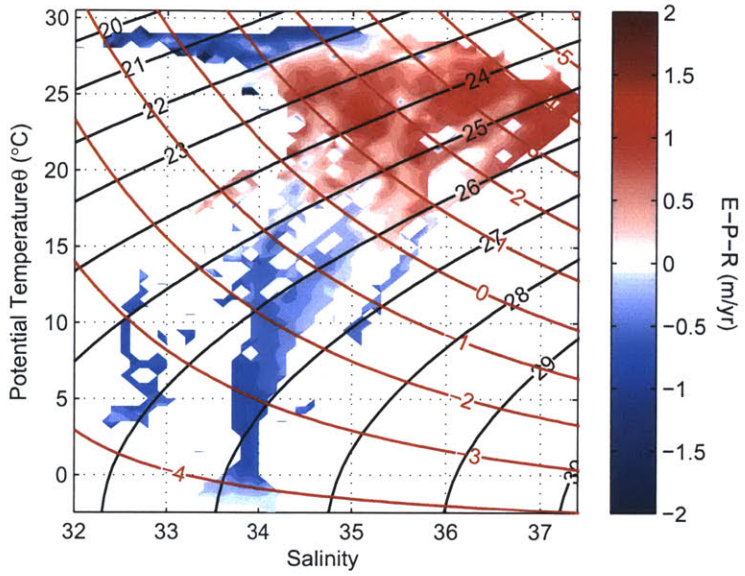

Figure 4-7: Balanced time-mean surface freshwater (E-P-R) flux ($\mathrm{m\,yr^{-1}}$) for each bin. The bin separation is 0.1 in salinity and 0.5 °C in potential temperature.

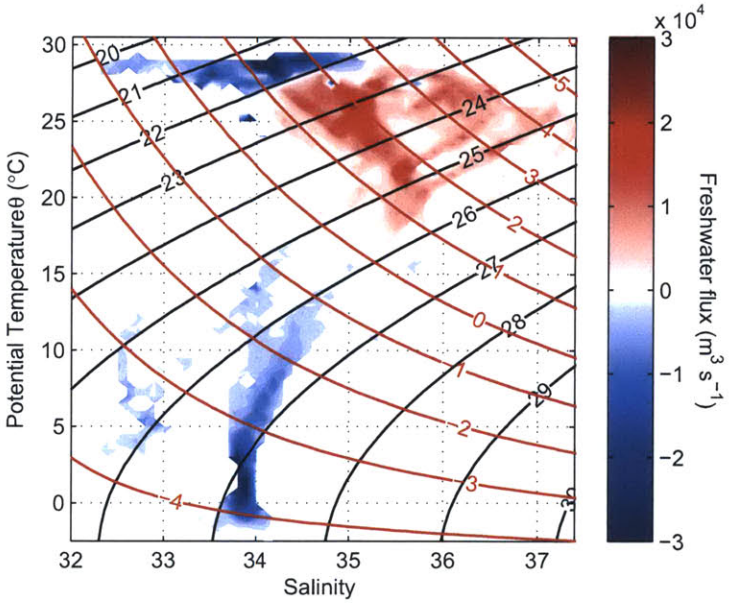

Figure 4-8: Total balanced freshwater flux at the surface ($\mathrm{m^3\,s^{-1}}$) for each potential temperature and salinity bin. The bin separation is 0.1 in salinity and 0.5 °C in potential temperature.

The approach of using a θ-S diagram may also be used for haline forcing. When freshwater forcing is examined (Figure 4-7), a strong freshwater input is evident in cold (high latitude) regions as well as the ITCZ, which characterized by the highest temperatures and low salinities. Strong net evaporation dominates the subtropical gyres, which are marked by the highest salinities and temperatures around 25 °C. The western boundary currents represent the branches of positive E-P-R extending into relatively low (15 °C) temperatures.

As for temperature, these fluxes are multiplied with the total area in each bin (Figure 4-2) to illustrate the sum of freshwater fluxes occurring over the global ocean. This is shown in Figure 4-8. The separation between basins is evident here with most precipitation occurring in the ITCZ, as well as at high latitudes at temperatures below 10 °C.

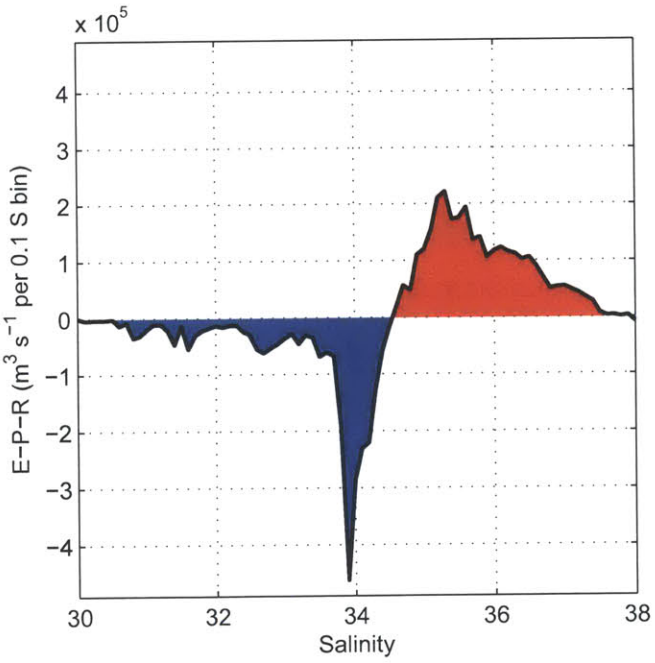

Figure 4-9: Freshwater flux ($m^3 s^{-1}$) for each 0.1 salinity bin. There is a clear separation of salinity input at high sea surface salinity values and salinity loss at low values of salinity.

The absolute freshwater flux (Figure 4-8) shows three distinct patterns. The sub-tropical gyre salinity maximum region and the sub-tropical marginal seas (Mediterranean, Red Sea) incur a strong freshwater loss, while fresher regions in both high

latitudes and the ITCZ show strong gains of freshwater. This clearly shows the generation of salinity variance. When Figure 4-8 is summed along lines of constant salinity, Figure 4-9 is obtained.

The down-gradient flux evident in Figure 4-9 is different from the temperature down-gradient flux in that the strongest negative freshwater fluxes (regions of high precipitation and riverine runoff) have the strongest amplitude. The inflow of the Amazon River largely coincides with the ITCZ around a salinity of 34.

4.1.3 Density Fluxes

To compute density fluxes, I use Q_{net} and E-P-R estimates with the definition of density flux from Chapter 2, Eq. (2.15). The density flux F_ρ is computed using the TEOS-10 equation of state (McDougall, 2011) in two steps: The equivalent nonlinear thermal and haline forcing components at the surface are computed and are then combined to give either density or spice surface fluxes. The density forcing was defined in Chapter 2, Eq. (2.47) as:

$$F_\rho = F_{\rho S} - F_{\rho\theta} = \rho_0(\frac{1}{\rho_F}\beta F_S - \frac{1}{c_p\rho_0}\alpha F_\theta) \tag{4.1}$$

and spice flux may be similarly defined:

$$F_\tau = F_{\rho S} + F_{\rho\theta} = \rho_0(\frac{1}{\rho_F}\beta F_S + \frac{1}{c_p\rho_0}\alpha F_\theta) \tag{4.2}$$

As is evident from Eqs. (4.1 & 4.12), the difference is a simple sign reversal of the thermal forcing components of the density flux, which follows from the definition of spice (Veronis, 1972; Schmitt, 1999; Huang, 2011). The thermal component is plotted in Figure 4-10 while the haline component is mapped in Figure 4-11.

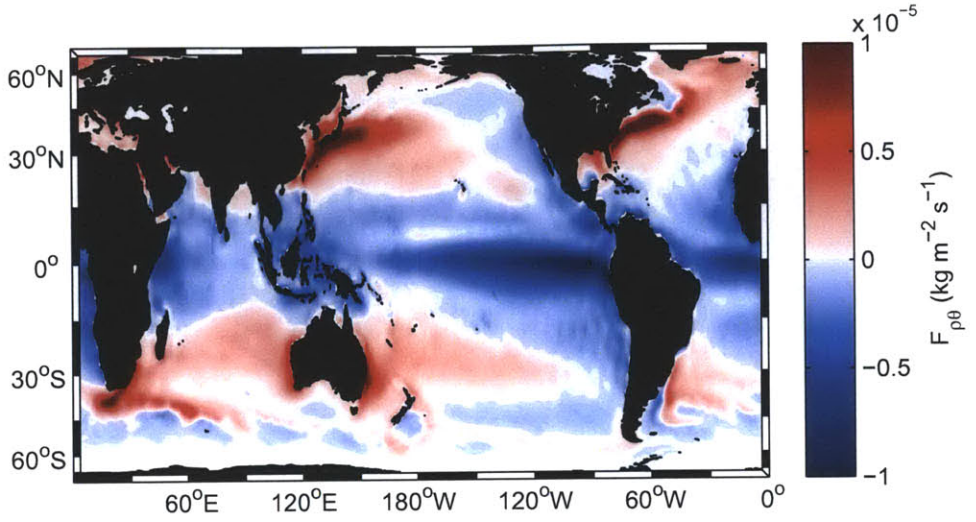

Figure 4-10: Thermal component of the surface density flux $\overline{F_{\rho\theta}}$ ($\mathrm{kg\,m^{-2}\,s^{-1}}$). This is the density flux caused only by the heat flux $\overline{F_{\theta}}$ into the ocean.

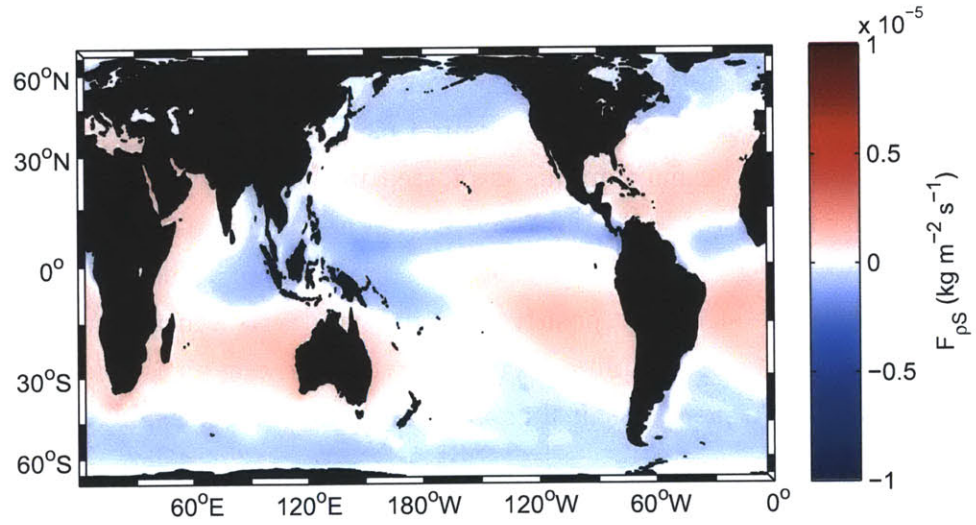

Figure 4-11: Haline component of the surface density flux $\overline{F_{\rho S}}$ ($\mathrm{kg\,m^{-2}\,s^{-1}}$). This combines the effects of heat- and salt-fluxes into the surface ocean. Strong densification (a positive density input) is evident in western boundary currents, while freshening and warming combine in the ITCZ to cause a significant negative density flux.

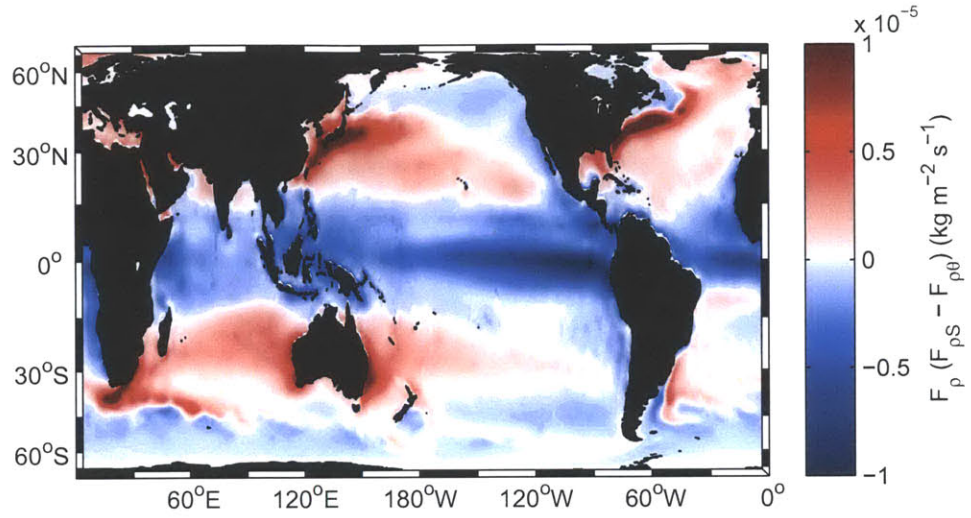

Figure 4-12: Surface density flux $\overline{F_\rho}$ ($\mathrm{kg\,m^{-2}\,s^{-1}}$). This combines the effects of heat- and salt-fluxes into the surface ocean. Strong densification (a positive density input) is evident in western boundary currents, while freshening and warming combine in the ITCZ to cause a significant negative density flux.

Using the Q_{net} and E-P-R estimates with definition of density flux from Chapter 2, Eq. (2.15, the density flux F_ρ is computed using the TEOS-10 equation of state (McDougall, 2011). The map of this is plotted in Figure 4-12 and shows a strong negative density flux in the ITCZ due to both a net heat input and excess precipitation causing both warming and freshening of the surface ocean. The western boundary currents produce the strongest positive density input: As warm water is advected polewards, evaporation and cooling occur since the overlying air is colder than at the origin. This leads to a positive salt flux as well as a negative heat flux, both of which contribute to densification.

It is also possible to repeat the flux visualization in θ-S space. Since contours of equal density based on the TEOS-10 equation of state (McDougall, 2011) are drawn in addition to the θ and S grid, it is possible to evaluate the fluxes along lines of equal density.

The fluxes for each bin are shown in Figure 4-13. While this may appear similar to the heat flux at first glance, there are significant differences, particularly at high temperatures, where the flux is negative. The flux is negative in the ITCZ due to heating and freshening of the surface waters, while the subtropical gyres are generally

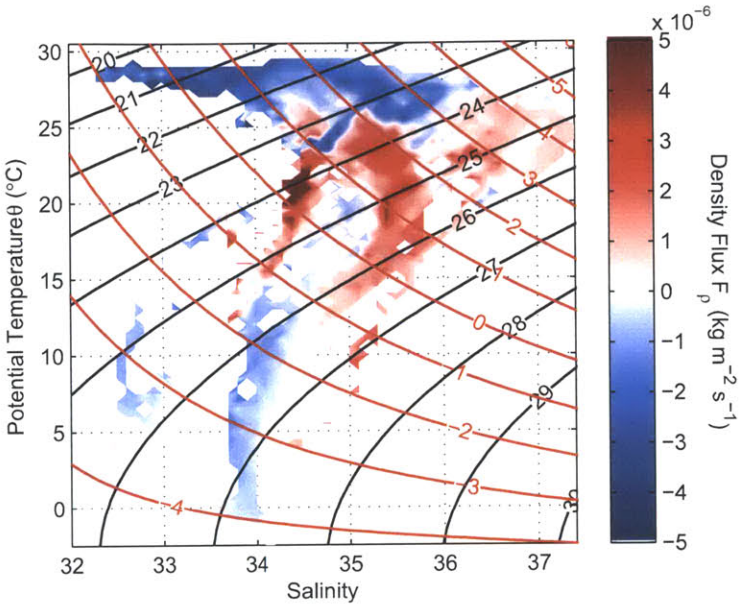

Figure 4-13: (Nonlinear) time-mean surface density flux $\overline{F_\rho}$ ($\mathrm{kg\,m^{-2}}$) for each potential temperature and salinity bin. The bin separation is 0.1 in salinity and 0.5 °C in potential temperature.

positive. The western boundary currents exhibit the strongest positive (densification) flux. As relatively warm water is moved northwards in these currents, extreme heat losses occur, which lead to both evaporation and cooling.

When the density flux F_ρ is multiplied by the area for each bin as before for temperature and salinity, the absolute density flux is obtained. This is shown in Figure 4-14. Here, the influence of the western boundary currents is barely evident, as these are relatively small areas compared to subtropical gyres and the ITCZ. The summation along lines of equal density is done using the full TEOS-10 equation of state, thus summing along the (curved) lines of density. The results of this integration are shown in Figure 4-15.

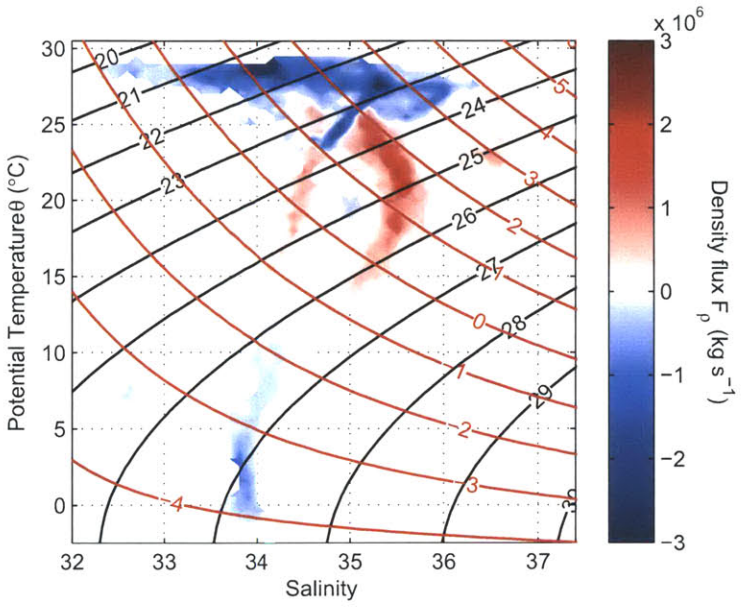

Figure 4-14: Absolute time-mean density flux $\overline{F_\rho}$ ($\mathrm{kg\,s^{-1}}$) for each bin. The bin separation is 0.1 in salinity and 0.5 °C in potential temperature.

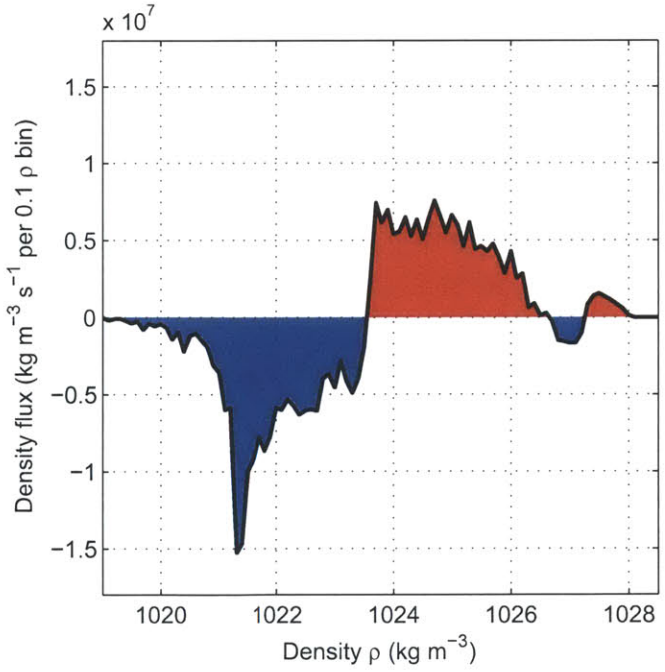

Figure 4-15: Sum of density fluxes $\overline{F_\rho}$ ($\mathrm{kg\,s^{-1}}$) for each density bin. The bin separation is 0.1 $\mathrm{kg\,m^{-3}}$ in density space. There is a clear separation of density input at high sea surface density values and density loss at low values of density, with the exception of a negative flux around 1027 $\mathrm{kg\,m^{-3}}$.

The density flux is more complicated than either the net heat or freshwater flux alone, since there is more than one zero-crossing: The fresh but cold water at high latitudes, particularly in the Southern Ocean, is denser than the majority of salty and warm water in the subtropical gyres. However, it is still subject to a negative density flux by precipitation. Aside from this, the general pattern of tracer input at high values and loss at low values persists. It is evident in Figure 4-15 that the mean of this graph is negative, that is, there is a net density loss. This apparent inconsistency (which is actually balanced in the interior ocean) is discussed in detail in Chapter 5.

4.1.4 Spice Fluxes

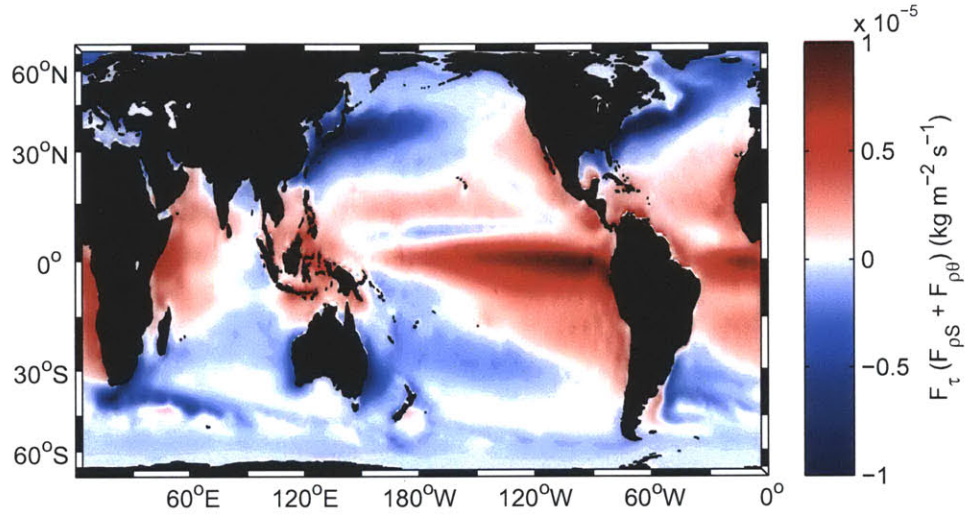

Figure 4-16: Surface spice flux $\overline{F_\tau}$ ($\mathrm{kg\,m^{-2}\,s^{-1}}$). This combines the effects of heat- and salt-fluxes into the surface ocean. The strongest positive spice fluxes occur near the equator as well as in coastal upwelling regions. Western boundary currents are strongly negative, while the ITCZ is almost compensated between heating (positive spice flux) and freshening (negative spice flux).

As with the density flux, spice fluxes are computed from the 'baseline' E-P-R and Q_{net} estimates using Eq. (2.16) and the TEOS-10 equation of state (McDougall, 2011), with the difference being a simple sign reversal of the thermal component of the flux as pointed out in Eq. (4.1). A global map of spice flux is shown in Figure 4-16. The strongest positive fluxes are found near the equator and in coastal upwelling regions, particularly along the West African coast. Very little spice flux occurs in the ITCZ due to competing effects of freshening and warming, which cause negative and positive spice fluxes, respectively. The cooling and freshening in high latitudes also causes a negative spice flux.

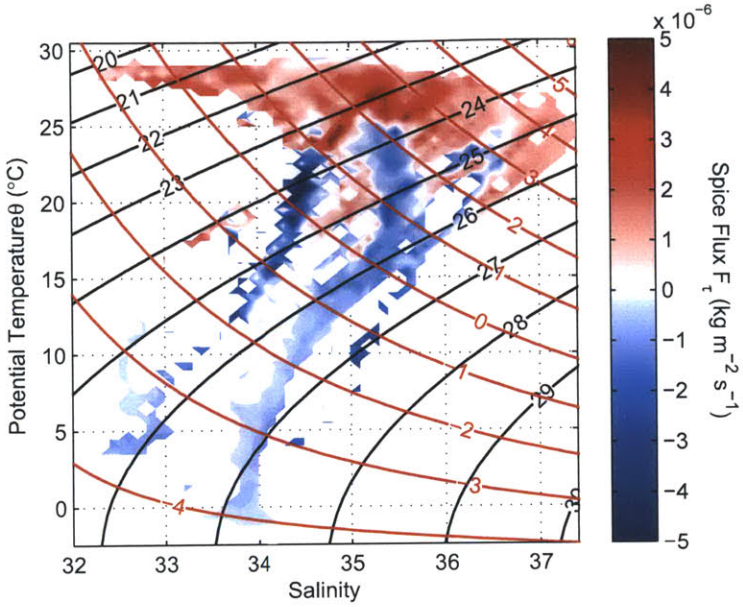

Figure 4-17: Nonlinear time-mean spice flux $\overline{F_\tau}$ ($\mathrm{kg\,m^{-2}\,s^{-1}}$) for each bin. The bin separation is 0.1 in salinity and 0.5 °C in potential temperature.

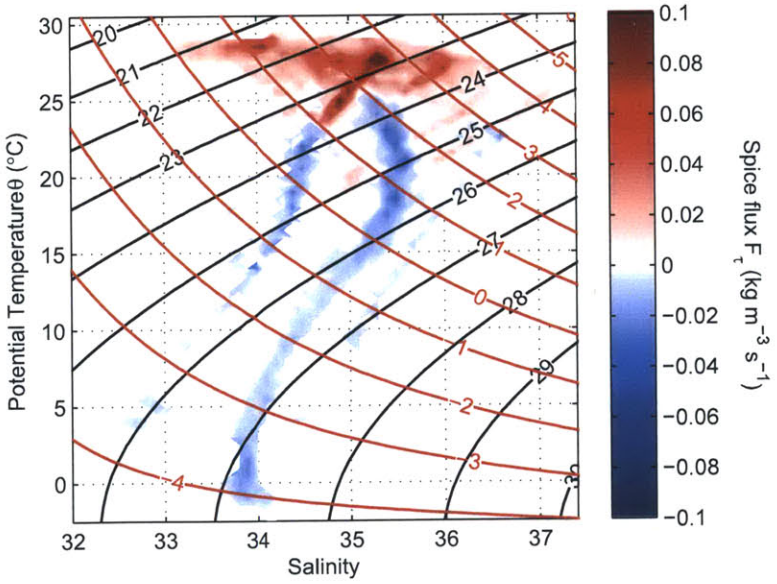

Figure 4-18: Absolute time-mean spice flux $\overline{F_\tau}$ ($\mathrm{kg\,s^{-1}}$) for each bin. The bin separation is 0.1 in salinity and 0.5 °C in potential temperature.

To visualize spice fluxes in θ-S space, lines of constant spice are computed using vectorized routines provided by Huang (2011); these are indicated in all θ-S figures. The spice flux in θ-S space is shown in Figure 4-17.

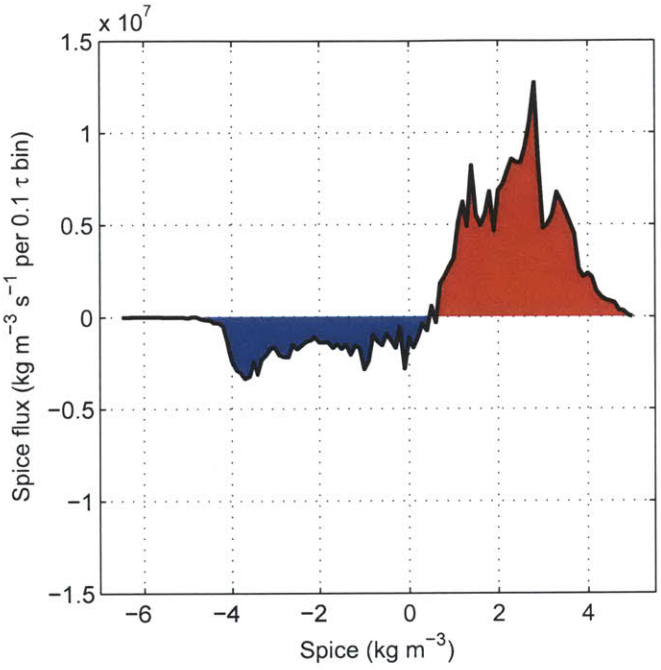

Figure 4-19: Total time-mean spice flux $\overline{F_\tau}$ ($\mathrm{kg\,s^{-1}}$) for each spice bin. The bin separation is $0.1\,\mathrm{kg\,m^{-3}}$ in spice space. There is a clear separation of spice input at high spice values and spice loss at low values of spice. As for the nonlinear density flux, the area under the curve does not add to zero (see text).

Spice input is dominant at high temperatures, including the ITCZ, while virtually all spice fluxes at temperatures below 20 °C are negative. The strong cooling in regions of western boundary currents leads to strong negative fluxes around 20 °C and a salinity of 34. As before, I produce the total time-mean spice flux for each bin by multiplication with the area of each bin. This is shown in Figure 4-18.

The equatorial regions, subtropical gyres and coastal upwelling zones are clearly the dominant areas of spice input to the ocean, since this combines net heating and net evaporation (which would be competing effects for density) while temperate and high latitudes are the main sinks due to net cooling and precipitation. When Figure 4-18 is integrated along lines of constant spice, the total spice flux may be plotted in spice space (Figure 4-19).

The spice flux is positive in regions of high spice and negative in regions of low spice, with the highest inputs occurring around a spice value of $3\,\mathrm{kg\,m^{-3}}$. As with the nonlinear density flux F_ρ, the area under the F_τ curve in Figure 4-19 does not integrate to zero. Rather, there is a net spice input to the ocean, which must be destroyed by 'spice-cabbeling', that is, de-spicification upon mixing.

For example, if one were to mix 2 water masses at the ocean surface, with one water mass having S=37 and θ=30 °C and the other having S=33 and θ=0 °C, they would have spiciness values of $5.34\,\mathrm{kg\,m^{-3}}$ and $-4.04\,\mathrm{kg\,m^{-3}}$, respectively. If spice were a linear quantity, the mixing of equal parts of these water masses would thus result in a spiciness of $0.65\,\mathrm{kg\,m^{-3}}$, but it is really $-0.40\,\mathrm{kg\,m^{-3}}$. While this is an interesting concept, it seems to be inconsequential to the ocean circulation and θ-S properties of the world oceans and thus, unlike cabbeling, is not addressed further in this thesis.

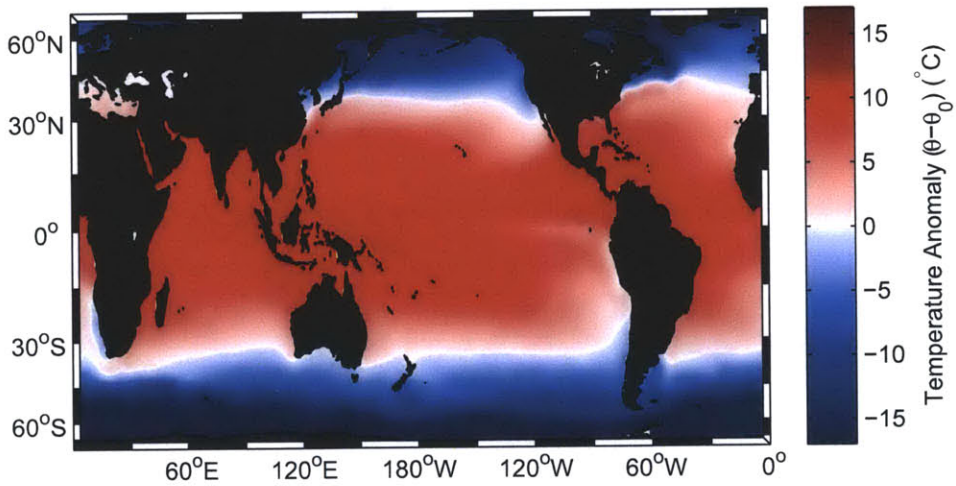

Figure 4-20: Sea surface temperature anomaly $(\bar{\theta} - \theta_0)$ (°C). Positive variance is generated when positive areas in this map are multiplied with positive areas in the heat flux (F_θ) field.

As was discussed in Chapter 2, tracer anomalies are used to produce estimates of temperature, salinity and spice variance. In the case of density variance generation this means instead of using ρ at the surface, which has values ranging from 1020 – $1030\,\mathrm{kg\,m^{-3}}$, I subtract the spatial and temporal mean from all fields, thus giving

$\bar{\rho} - \rho_0$. The same is done for temperature, salinity, and spice as $\bar{\theta} - \theta_0$, $\overline{S} - S_0$, and $\bar{\tau} - \tau_0$, respectively. Due to the definition of spiciness by Huang (2011) as a departure from a mean value, the anomaly field is virtually identical to the computed field of τ, with differences being caused only by the use of different SST and SSS datasets. The anomaly for θ relative to the spatial and temporal mean of θ_0 =18.31 °C is plotted in Figure 4-20.

Regions that are shaded in red have a positive anomaly, while regions that are shaded in blue have a negative anomaly. Since this field is multiplied with the temperature flux as shown in Eq. (2.22), areas that are shaded in white do not contribute to the generation of variance. The change from positive to negative values is generally located around 30–40 ° latitude and is modified by features discussed in Section 3.5.

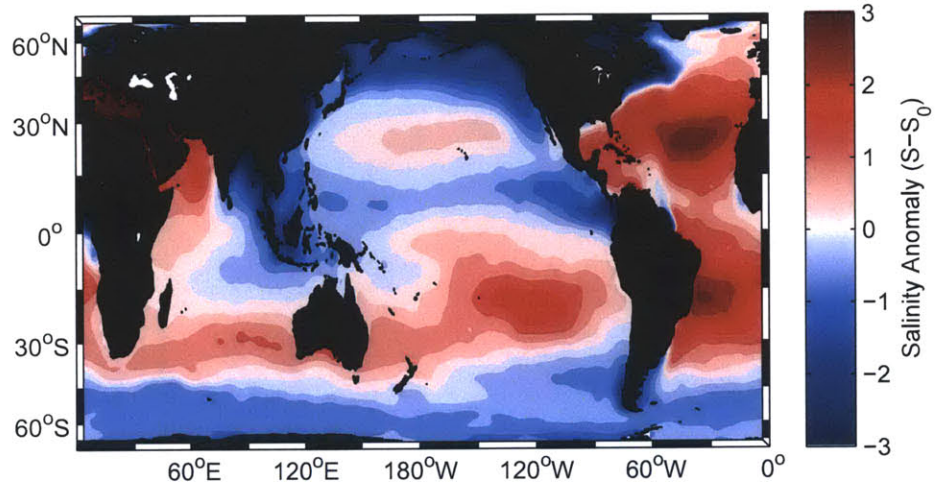

Figure 4-21: Sea surface salinity anomaly ($\bar{S} - S_0$). Positive variance is generated when positive areas in this map are multiplied with positive areas in the salt flux ($\overline{F_S}$) field.

As for temperature, the anomaly field for sea surface salinity $\overline{S} - S_0$ is computed and graphed in Figure 4-21. The mean absolute sea surface salinity (McDougall, 2011) was found to be S_A =34.71. Most of the Atlantic Ocean is characterized by a positive anomaly (shaded in red), while the Southern Ocean, ITCZ and the Northern Pacific are strongly negative (shaded in blue). As with temperature, regions that are shaded in white do not contribute significantly to salinity variance production. The

gradients of salinity anomaly are not clearly aligned in a meridional direction, as is the case for temperature anomaly. There are significant zonal gradients, particularly in areas modified by ocean currents as well as gradients between ocean basins. It will be shown in Section 4.3 that this plays an important role when zonal averages are used in the computation of salinity variance generation.

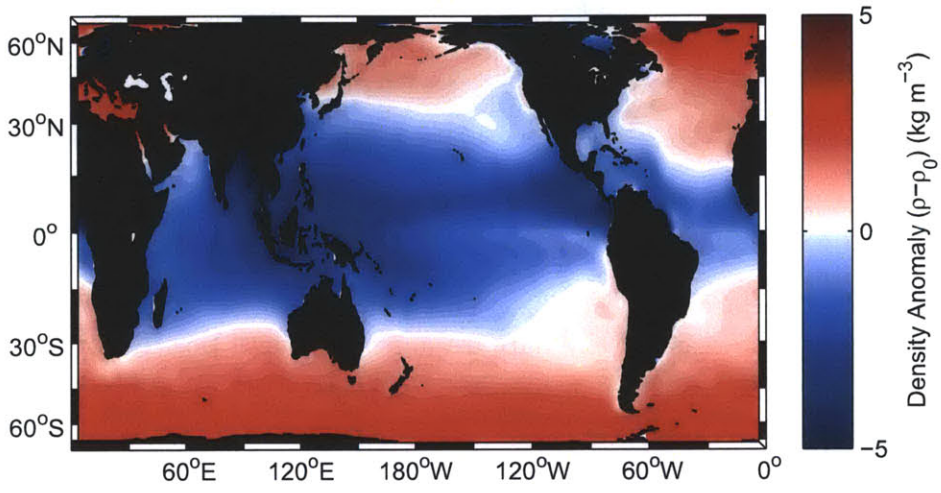

Figure 4-22: Sea surface density anomaly ($\bar{\rho} - \rho_0$). Positive variance is generated when positive areas in this map are multiplied with positive areas in the density flux ($\overline{F_\rho}$) field.

The density anomaly $\bar{\rho} - \rho_0$ is plotted in Figure 4-22 using the same conventions as for temperature and salinity: Areas which are shaded in red indicate regions of positive anomalies, while blue areas indicate negative anomalies and white regions are insignificant in the generation of density variance. The spatial and temporal mean density is ρ_0 =1024.35 kg m^{-3}. The patterns found are identical to those discussed in more detail in Section 3.8.1. It should be noted that the gradients are not aligned as meridionally as is the case for temperature anomaly. As a result, the use of latitudinal bands, as was done for temperature variance production and dissipation by Joyce (1980) does not necessarily lead to an increase in density variance production. This is discussed further in Section 4.4 for its effect on density variance production, while Section4.6 describes the influence of advection in the ocean.

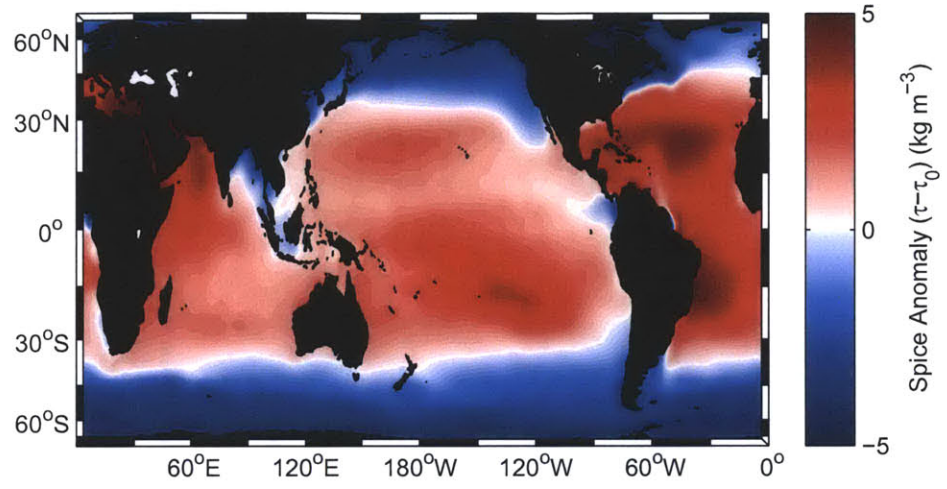

Figure 4-23: Sea surface spice anomaly $(\overline{\tau} - \tau_0)$ $(\mathrm{kg\,m^{-3}})$. Positive variance is generated when positive areas in this map are multiplied with positive areas in the salt flux $(\overline{F_\tau})$ field.

A map of spice anomaly $\overline{\tau} - \tau_0$ is shown in Figure 4-23 using the same colormap and scale as for density anomaly with reds indicating positive anomalies, blues indicating negative anomalies and white areas indicating regions that are insignificant in the generation of spice variance. The spatial and temporal mean spiciness is $\tau_0 = 0.05\,\mathrm{kg\,m^{-3}}$, and only differs from zero due to the usage of a different SST and SSS product than that used in the definition of the spice equations by Huang (2011). The patterns found are identical to those discussed in more detail in Section 3.8.2. As for density, the gradients are more meridional than those of SSS, but less so than those found for SST.

The calculation of the generation of thermal, haline, density and spice variance in the ocean is done by multiplying these anomaly fields with the respective tracer flux. The total generated variance is proportional to the area integral of these two quantities, as was shown in Section 2.1 and will be shown individually in the following sections.

4.2 Thermal Variance

As has been derived in Chapter 2, Eq. (2.21) may be combined with Eq. (2.13) to give:

$$\frac{1}{\rho_0 c_{p0}} \iint_A (\overline{Q_{net}\theta}) dA = -\iiint_V \nabla\bar{\theta} \cdot \overline{\mathbf{u}' \cdot \theta'} dV = \tfrac{1}{2} \iiint_V \chi_\theta dV \tag{4.3}$$

$$\chi_\theta = 2\kappa_\theta \nabla^2 \theta' \tag{4.4}$$

This states that the area integral of the thermal variance production at the surface and the destruction of thermal variance in the interior through down-gradient mixing must compensate and are equal to half the thermal dissipation rate in the ocean interior.

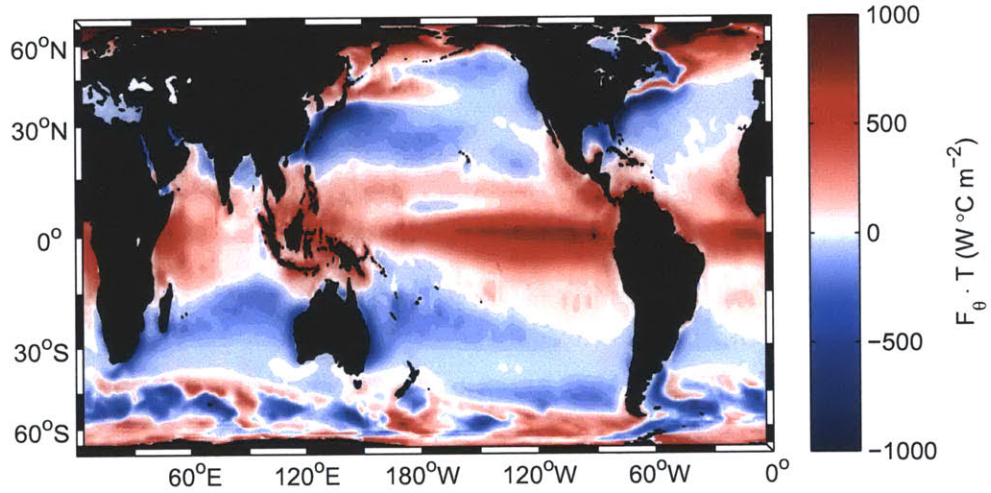

Figure 4-24: Global estimate of $\overline{F_\theta} \cdot (\bar{\theta} - \theta_0)$ ($\mathrm{W\,^\circ C\,m^{-2}}$) using OAFlux 3.0 Q_{net} and EN3 SST. A strong positive variance generation occurs in the ITCZ and at high latitudes while the subtropical gyres and western boundary currents are largely negative. The area integral of this figure is $100\,\mathrm{W\,^\circ C\,m^{-2}}$.

While the dissipation rate χ_θ is a handy number to compare to *in-situ* observations, such as microstructure profiler data (e.g. Nash and Moum, 1999, and references therein), a mixing scale height is required to relate the two quantities (Joyce, 1980). It would be possible to assume uniform mixing occurs in the ocean, in which case

the scale height would be the mean depth of the ocean, but it is likely that more dissipation occurs in the permanent thermocline than in the abyssal ocean (with the exception of ridges (e.g. Polzin et al., 1997)).

Assuming a layer of depth H in which the surface thermal forcing is dissipated, the variance generation caused by surface forcing $Q_{net}\theta$ can thus be directly related to the dissipation:

$$\chi_\theta H = 2\frac{\overline{Q_{net}\theta}}{\rho_0 c_{p0}} \tag{4.5}$$

Using estimates of Q_{net} and θ binned in 10° latitude bands and assuming a scale height of H =600 m, Joyce (1980) used this relationship to estimate the area integral of $\overline{Q_{net}\theta}$ as 130 W °C m^{-2} and the implied thermal dissipation rate as $\chi_\theta = 1 \times 10^{-7}$ °C^2 s^{-1}.

Evaluating Eq. (4.3) using the OAFlux Q_{net} and EN3 SST products described in Chapter 3, the thermal variance production in the ocean is found. This is shown in Figure 4-24 and may be thought of as the graphical representation of the RHS of Eq. (4.3). The area integral of this map is the total production term, $\overline{\theta Q_{net}}$. The time-mean of the OAFlux Q_{net} product and the EN3 SST estimate implies a generation term of $\overline{Q_{net}\theta}$=100 W °C m^{-2}.

This term is used in Eq. (4.5) to calculate $\chi_\theta H$, which is estimated as 5.0×10^{-5} °C^2 m s^{-1} from OAFlux Q_{net} and EN3 ocean surface products. The results of the use of other estimates of Q_{net} are shown in Figure 4-25.

The implied variance dissipation, that is, the RHS of Eq. (4.3), is also numerically evaluated using a scale height of H =600 m as in Joyce (1980). The results of χ_θ range from 4.7×10^{-8} °C^2 s^{-1} – 1.4×10^{7} °C^2 s^{-1}. This is shown graphically for all 8 evaluated products in Figure 4-26. The tabulated values are included in Table A.4. The estimates are relatively close, albeit mostly lower, to the value of $\chi_\theta = 1 \times 10^{-7}$ °C^2 s^{-1} found by Joyce (1980).

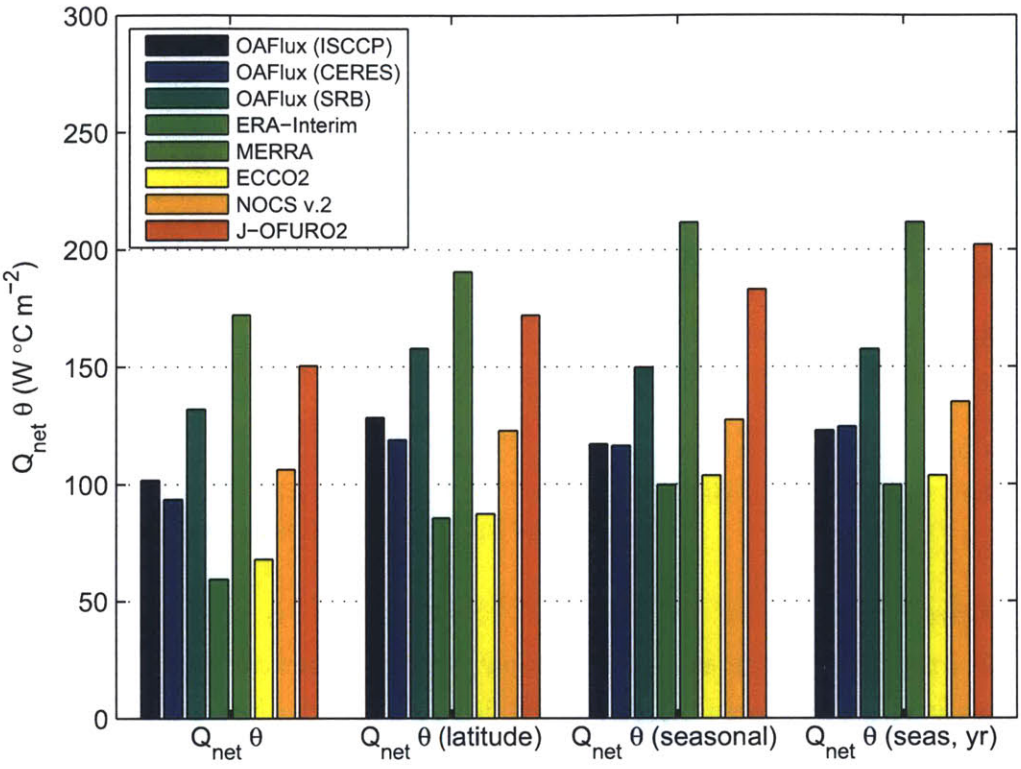

Figure 4-25: Global area integrals of $\overline{Q_{net}\theta}$ (W °C m^{-2}) using 8 different Q_{net} estimates and EN3 SST using the 1° resolution time-mean fields (left-hand set of bars), 10° latitude bands as in Joyce (1980) (second set of bars) and allowing for the effects of the seasonal cycle using monthly data (third set of bars). The right-hand set of bars also uses monthly fields, but balances the global oceanic heat budget in each given year to minimize effects of inter-annual variability.

To allow a better comparison to the estimates by Joyce (1980), I repeat his calculation using 10° latitude bands. The estimates are shown in Figure 4-26 as the second set of bars and tabulated in Table A.5. While these results are slightly higher, the increase varies between datasets owing to the different spatial structures and resulting increase in correlation between Q_{net} and SST, an effect that is described in more detail in Section 4.6. While the estimates exhibit a considerable spread of approximately 7×10^{-8} to 1.5×10^{-7}, the results from *in-situ* products compare well to those estimated by Joyce (1980), given the uncertainties in the measurements which will be explored in greater detail in Section 4.8.

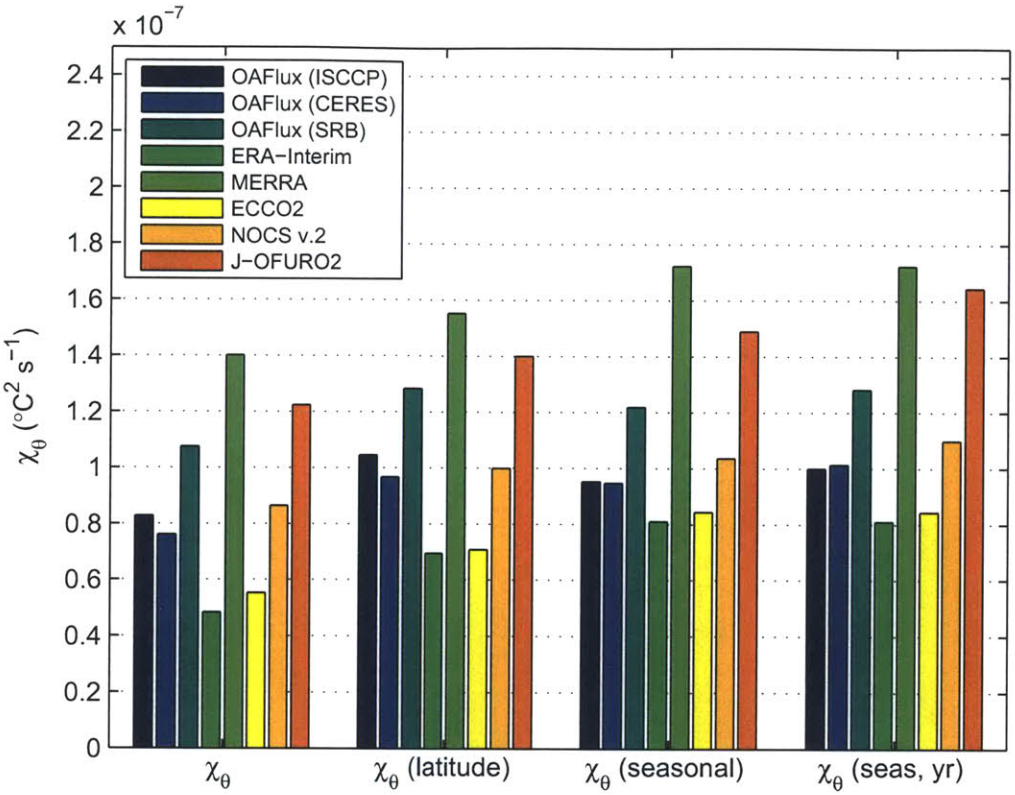

Figure 4-26: Estimates of implied global temperature variance dissipation χ_θ ($^\circ\mathrm{C}^2\,\mathrm{s}^{-1}$) using eight different Q_{net} products and EN3 SST using 1° resolution time-mean fields (left-hand group of bars), 10° latitude bands as in Joyce (1980) (second group of bars), allowing for the effects of the seasonal cycle using monthly 1° resolution fields (third group of bars) and allowing for seasonal effects, but zero-biasing the flux on a year-to-year basis (right-hand group of bars).

With the aforementioned set of Q_{net} products and SST from EN3 v2a, it is possible to evaluate the area integral over time, that is, to include seasonal and inter-annual effects. For this purpose, I use monthly fields from 1987–2004 (unless stated otherwise). As may be expected, the inclusion of the seasonal cycle increases the overall variance generation and hence the implied dissipation rates. The increases range from approximately 10 % to 75 % depending on the Q_{net} product used. The greatest increases are seen in products which implied the lowest thermal variance dissipation in the time–mean state, thus reducing the spread of the results. These results are graphically represented in the third group of bars in Figure 4-26 and are also tabulated in

Table A.6.

While this increase represents a real variance production, it should be noted that not all of it has to be dissipated in the ocean interior. In the case of the seasonal cycle, local warming and cooling of the mixed layer (and possibly a deepening of the thermocline) may occur. While some of the seasonal cycle is likely dissipated internally as with the time-mean state, the fraction of local heat cycling is unknown. These results should thus be interpreted with caution.

So far, all products were balanced to a net-zero mean area integral of Q_{net}, as discussed in Chapter 2. This balancing consists of subtracting the spatial and temporal mean value from each grid point of the estimate and may not be the best way to adjust the global fluxes to zero. If there are time-mean changes in the net zero balance, as may be caused by a change in the data composition ingested into a particular product, this could lead to a spurious inter-annual generation term in the seasonal and inter-annual averages. Such changes in the time mean may occur through changes in the data constraining a model or analysis (e.g. Sterl, 2004, and references therein).

As a result, the removal of the mean is repeated for each year, thus causing Q_{net} averaged globally and temporally between each given January and December to have a net-zero mean area integral. The mean value of χ_θ is then computed. Both are shown in Figure 4-26 with only subtly different values. The results from this computation are tabulated in Table A.7. The changes to the time-mean balanced results are small with variations not exceeding 2 %.

The result of this by-year bias adjustment is a slightly (<10 %) enhanced thermal variance production for most products. Other methods of adjusting the bias to achieve a net zero–mean Q_{net} field are discussed in Section 4.8.

Not all results from the products compared in the above Figure 4-26 are equally credible, as has been discussed in Chapter 3. Re-analysis models are generally designed as forecast models that have been adapted for data assimilation purposes. As such, a number of physical constraints, such as the closure of the global water cycle and the closure of the global heat budget, are violated. In *in-situ* comparisons with independent measurements, satellite-derived products using objective analysis (OA) tend to have the best agreement (Quartly et al., 2007; Yu et al., 2008). These OA products are OAFlux, NOCS v.2 and J-OFURO2 (see Chapter 3 for a more detailed description). It may thus not come as a surprise that re-analyses produce both the lowest (ERA-Interim) and highest (MERRA) estimates of thermal variance pro-

duction in the global ocean. While ECCO2 is a completely different approach that assimilates ocean data, it is forced with re-analysis products at the surface which are adjusted to match ocean observations. As the constraining ocean observations are relatively sparse, the amount of thermal variance destruction is largely prescribed by diffusivity parameters inherent to the ocean model. As such, ECCO2 is presented here mainly for purposes of comparison rather than to estimate thermal variance destruction in the ocean interior.

While it does not seem plausible to produce a formal error estimate due to unknown error co-variances and possible systematic errors in all underlying estimates of variables, it does appear likely that the obtained results are robust to a factor of approximately 2, as will be shown in more detail in Chapter 4.8.

4.3 Salinity Variance

As for temperature, the relationship between surface forcing, down-gradient flux and internal dissipation of salinity variance was derived in Chapter 2, Eq. (2.22). When this is combined with Eq. (2.14) one obtains:

$$\frac{1}{\rho_F} \oiint_A \rho_F S_0 (\overline{E-P-R})(\bar{S}-S_0) dA = -\iiint_V \nabla \bar{S} \cdot \overline{\mathbf{u}' \cdot S'} dV = \tfrac{1}{2} \iiint_V \chi_S dV \quad (4.6)$$

This states that the area integral of the salinity variance production at the surface and the interior salt flux down the salt gradient must compensate and are equal to half the salinity dissipation rate in the ocean interior. This relationship is used to produce estimates of χ_S.

As with temperature, by assuming a layer of depth H in which the surface salinity forcing is uniformly dissipated, the surface forcing $\frac{1}{\rho_F} S_0 (\overline{E-P-R})(\bar{S}-S_0)$ can thus be directly related to the dissipation:

$$\chi_S H = 2 S_0 \frac{1}{\rho_F} (\overline{E-P-R})(\bar{S}-S_0) \quad (4.7)$$

Evaluating Eq. (4.6) using the Schanze et al. (2010) E-P-R estimate and EN3 v2a SSS product described in Chapter 3, the salinity variance production (RHS of Eq. (4.6)) in the ocean is calculated and shown in Figure 4-27. The area integral of

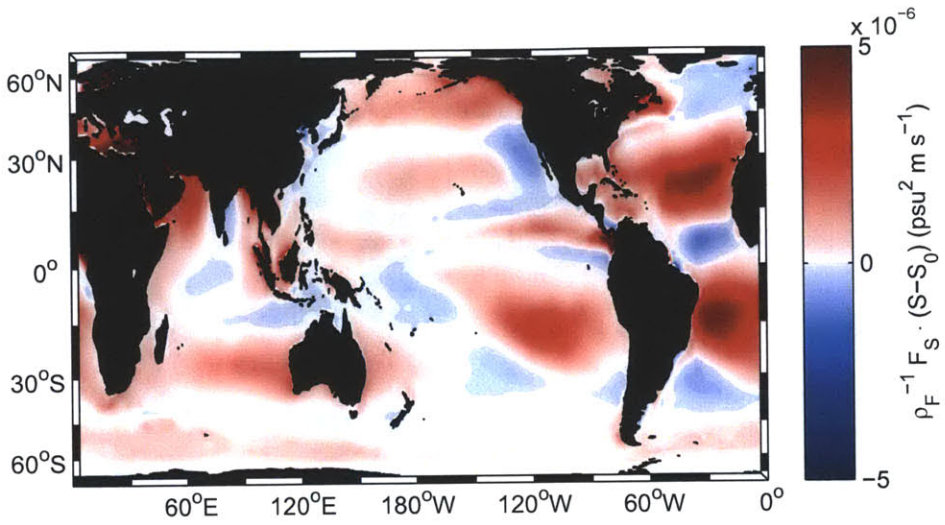

Figure 4-27: Global estimates of salinity variance generation $\frac{1}{\rho_F}\overline{F_S}(\bar{S} - S_0)$ ($\mathrm{psu}^2\,\mathrm{m\,s}^{-1}$) using Schanze et al. (2010) E-P-R and EN3 SSS. A strong positive salinity variance generation is evident the subtropical gyres and at high latitudes, while the ITCZ and temperate latitudes are largely negative. The area integral of this figure is $100\,\mathrm{psu}^2\,\mathrm{m\,s}^{-1}$.

this is graphically shown for six E-P-R estimates in the left-hand group of columns in Figure 4-28. It is also tabulated in Table A.8.

The use of 10° latitude bands is motivated by the same procedure for thermal variance production and the work by Joyce (1980), which also used 10° latitude bands. As is evident in Figure 4-27, the latitudinal gradient is less dominant in E-P-R and SSS than it is in the case of Q_{net} and SST. The results of this calculation are shown graphically in the second group of columns of Figure 4-28. These results are tabulated in Table A.9.

As for temperature, I evaluate this integral over time to include seasonal and inter-annual effects. The inclusion of the seasonal cycle increases the overall salinity variance generation and hence the implied dissipation rates as was the case for thermal variance production and dissipation. The increases range between approximately 10 % and 20 % depending on the products used. These increases are lower than the temperature equivalent, which indicates that the global oceanic seasonal cycle of Q_{net} may have a stronger amplitude than that of E-P-R. These results are tabulated in Table A.14.

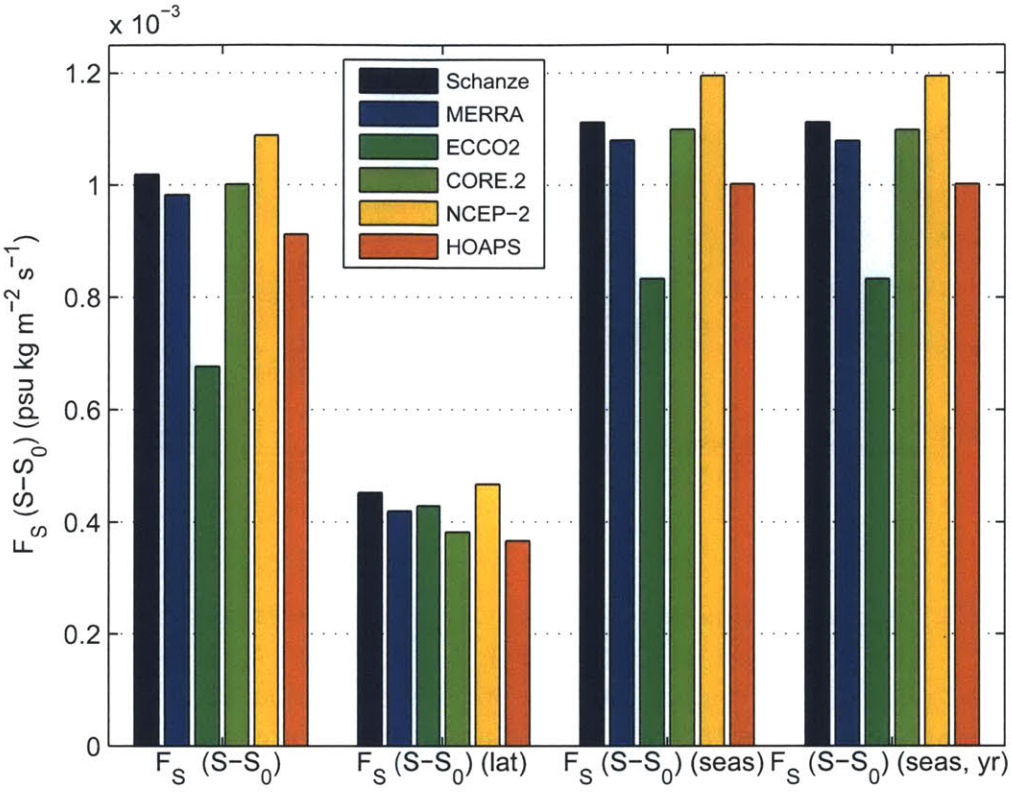

Figure 4-28: Global estimates of salinity variance generation $\overline{F_S}(\overline{S} - S_0)$ ($\mathrm{psu}^2\,\mathrm{m\,s}^{-1}$) using various E-P-R products and EN3 SSS. The left hand group of columns uses the time-mean of the products indicated in the legend. The second group of columns uses 10° latitude bands, the third group uses monthly fields to include seasonal and inter-annual effects. The right hand group of columns also uses monthly fields, but balances the global integral to zero for each given year. It is clear that the use of latitude bands decreases the salinity variance generation, as the pattern is not dominated by a meridional gradient as with thermal variance generation. The estimates using monthly fields show increases for all products. The by-year balanced monthly field estimate is virtually indistinguishable from the time-mean balanced estimate.

The surface production term $\overline{F_S}(\bar{S} - S_0)$ ($\mathrm{psu\,kg\,m}^{-2}\,\mathrm{s}^{-1}$) is evaluated for 6 different E-P-R estimates and tabulated in Table A.8. The estimates are similar for all products except for ECCO2, which uses spreading functions for rivers and thus differs significantly from the other estimates using riverine runoff by Dai and Trenberth (2002); Dai et al. (2009) as described in Schanze et al. (2010). It should be noted

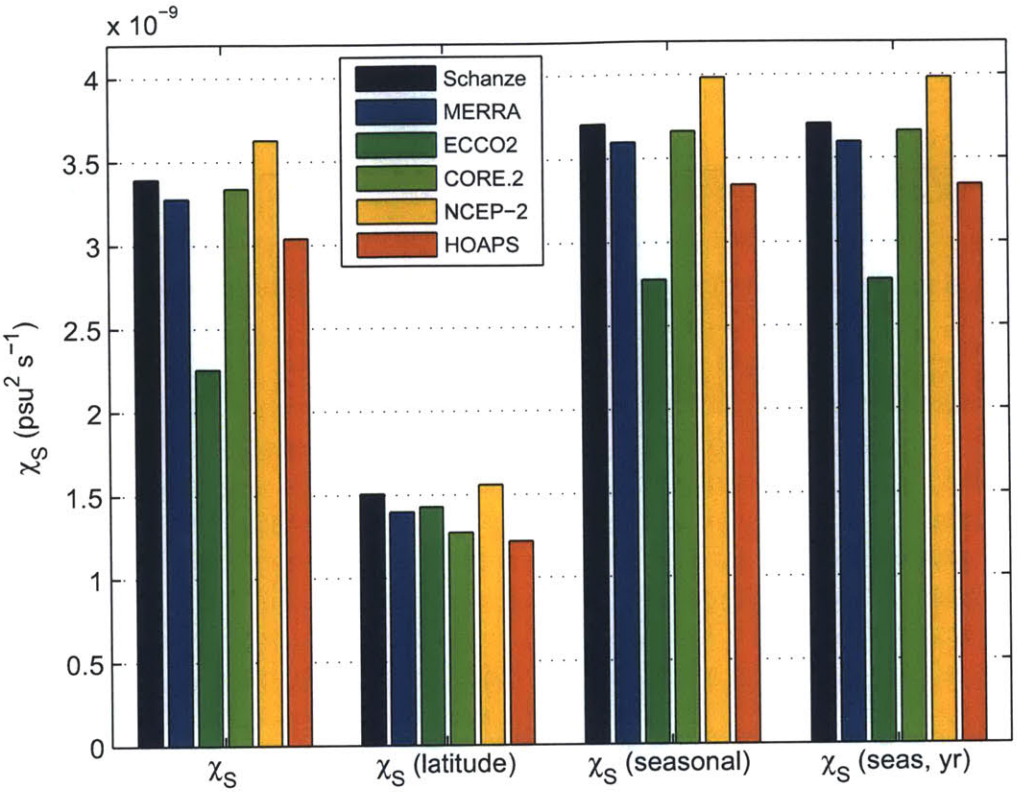

Figure 4-29: Global estimates of salinity variance dissipation $\chi_S \frac{1}{\rho_F} \overline{F_S}(\bar{S} - S_0)$ ($\mathrm{psu}^2\,\mathrm{m\,s}^{-1}$) using various E-P-R products and EN3 SSS. The left hand group of columns uses the time-mean of the products indicated in the legend. The second group of columns uses 10° latitude bands, the third group uses monthly fields to include seasonal and inter-annual effects. The right hand group of columns also uses monthly fields, but balances the global integral to zero for each given year. It is clear that the use of latitude bands decreases the implied salinity variance dissipation as is the case for the generation. The estimates using monthly fields show increases for all products. The by-year balanced monthly field estimate is virtually indistinguishable from the time-mean balanced estimate.

that due to the different units, this cannot be directly compared to the temperature variance generation. To compare those terms, $F_{\rho\theta}$ and $F_{\rho S}$ may be used instead of F_θ and F_S. This is discussed in Section 6.4.

The implied variance dissipation, that is, the RHS of Eq. (4.6), is also numerically evaluated using a scale height of H =600 m as before for temperature. The results of

χ_S range from $2.3 \times 10^{-9}\,\mathrm{psu^2\,s^{-1}} - 3.4 \times 10^{-9}\,\mathrm{psu^2\,s^{-1}}$. These are tabulated for all 4 datasets in Table A.12.

While some of the variance generated likely cancels in time, fluctuations in the freshwater cycle tend to be on longer time-scales than those of the heat budget, which are largely seasonal. Some of the increase seen here may thus be real variance generation. However, it is not possible to quantify this without additional information about the structure of salinity variance dissipation in the interior ocean. The same caveat as for temperature is thus valid here: The addition of the seasonal cycle may be seen as an upper bound as some of the variance is likely dissipated locally.

4.4 Density Variance

Spice- and density variance generation may be computed either using a full (nonlinear) equation of state, such as the TEOS-10 (McDougall, 2011) routines or using a linearized equation of state as discussed in Chapter 2, Eqs. (2.25–2.28). The main difference between a linear and a non-linear estimate is caused by changes in α at the sea surface, caused by a strong dependence on temperature. This was shown in Chapter 3, Figure 3-15. While all computed values of surface α shown there are positive, α may even become negative at very low temperatures and salinities. β also changes with temperature and salinity, but over a significantly smaller range.

These dependencies lead to a flux imbalance: Heat is largely added at low latitudes, where α is high, but is primarily removed in high latitudes, where α is low. This leads to a negative density flux, or a positive buoyancy flux. It was shown that this flux is compensated by cabbeling in the ocean interior (e.g. McDougall and Garrett, 1992) and its magnitude, distribution and implications are explored in more detail in Chapter 5.

The equation governing the production and dissipation of density variance was derived in Chapter 2:

$$\oiint_A (\overline{\rho} - \rho_0)\overline{F_\rho} dA = -\iiint_V \nabla\overline{\rho} \cdot \overline{\mathbf{u}' \cdot \rho'} dV = \tfrac{1}{2} \iiint_V \chi_\rho dV \tag{4.8}$$

As with temperature and salinity, it is possible to directly relate the surface forcing to the dissipation term by assuming a layer of depth H in which the variance is dissipated:

$$\chi_\rho H = 2\overline{F_\rho}(\bar{\rho} - \rho_0) \tag{4.9}$$

Using Eq. (4.8), I compute both linear and non-linear density fluxes and separate these fluxes into the relative contribution from thermal and the haline fluxes, following Schmitt et al. (1989), but using the definitions derived in Chapter 2. The linear density variance generation into the ocean is mapped in Figure 4-30. A strong variance generation is evident along the equator, where light water loses density. A negative flux is evident only in subtropical latitudes and the Southern Ocean as well as the Kuroshio Current. The errors associated with the linearization (the leading effect being that α is constant) are significant (in excess of 200 %) in high latitudes where

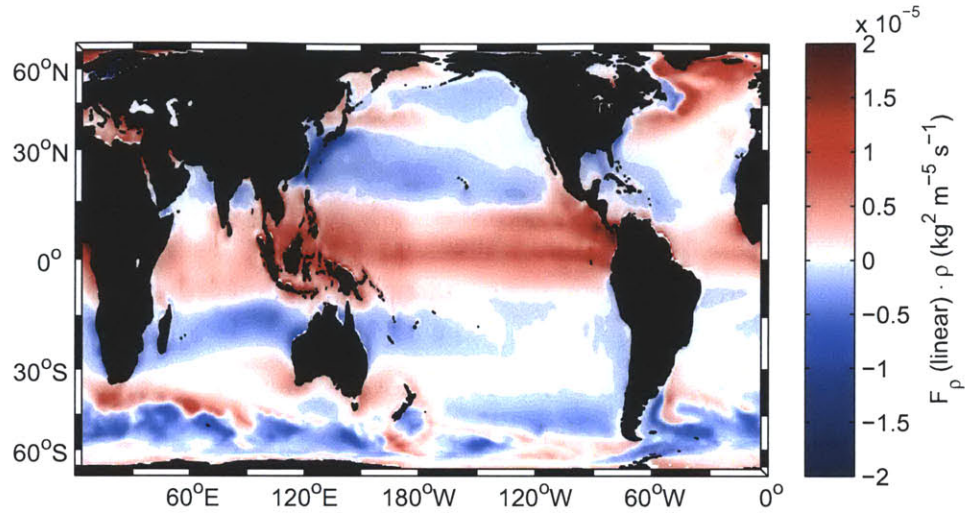

Figure 4-30: Global estimate of linear density variance generation $\overline{F_{\rho(linear)}}(\bar{\rho} - \rho_0)$ $((\mathrm{kg/m^3})^2/\mathrm{m^2/s.}$) using Schanze et al. (2010) E-P-R and EN3 SSS.

α should be very small.

The implied linear density variance dissipation $\chi_{\rho linear}$ as computed from the area integral of Figure 4-30 is tabulated in Table A.22. While ECCO2 and ERA-Interim provide the lowest estimates, MERRA and J-OFURO2 provide the highest estimates. These results are also shown graphically in Figure 4-31.

The linearization of density and spice fluxes provides a useful foundation for understanding the roles of heat fluxes and freshwater fluxes for the generation of density and spice variance, as was discussed in Chapter 2. However, the nonlinearities are significant, particularly at high and low latitudes. The density variance generation is thus evaluated using the full TEOS-10 equation of state at each grid-point of the estimate. The result of this is shown graphically in Figure 4-31.

While the equatorial regions remain the dominant input of density variance, the values are increased by the higher than average α in low latitudes. Conversely, the reduction of α at high latitudes dampens the signals in these areas. As a result, the Southern Ocean no longer appears as a significant source term. The area integral of this is computed for a number of Q_{net} and E-P-R estimates, which is shown graphically in Figure 4-32. Black bars in this figure indicate the range of results caused by different E-P-R estimates. The results are also tabulated in Tables A.16 through A.20. When

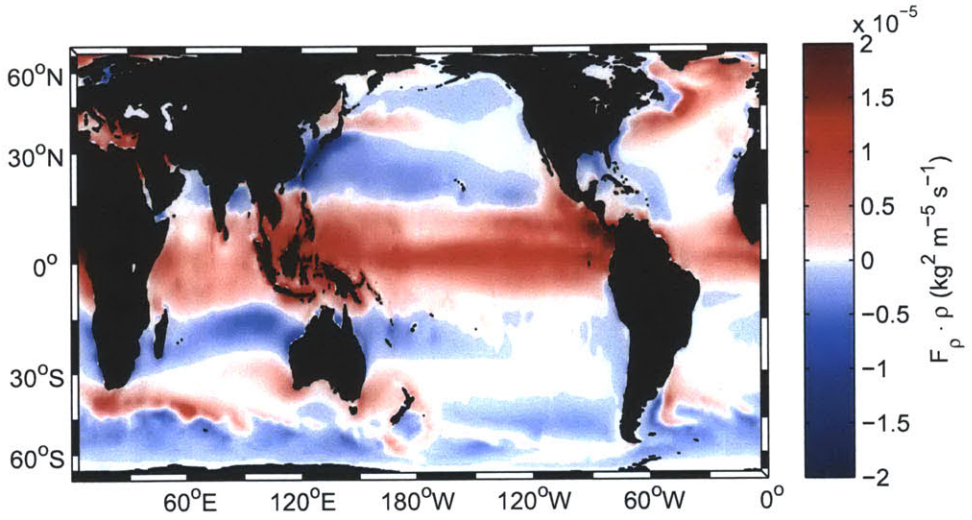

Figure 4-31: Global estimate of nonlinear density variance generation $\overline{F_\rho}(\bar{\rho} - \rho_0)$ $((\mathrm{kg/m^3})^2/\mathrm{m^2/s})$ using OAFlux Q_{net}, Schanze et al. (2010) E-P-R and EN3 v2a SST and SSS.

10° latitude bands are used, the estimates change by $-20\,\%$ to $15\,\%$ depending on the Q_{net} and E-P-R products used. This result is caused by a combination of an increase of the correlation between Q_{net} with SST (leading to increased estimates) competing with a reduction in correlation for E-P-R and SSS, which cause a decrease of the estimates. The importance of advective effects on these estimates are discussed further in Section 4.6.

As with thermal and haline variance generation, there is an increase when monthly fields are used instead of time-mean fields. Depending on the Q_{net} and E-P-R products used, this increase ranges from approximately $25\,\%$ to $65\,\%$. The results of this calculation are tabulated in Table A.19. A similar result is found when the monthly fields are balanced on a year-by-year basis rather than subtracting a time-mean to ensure an annual closure of the global water cycle and heat budget. This is tabulated in Table A.20.

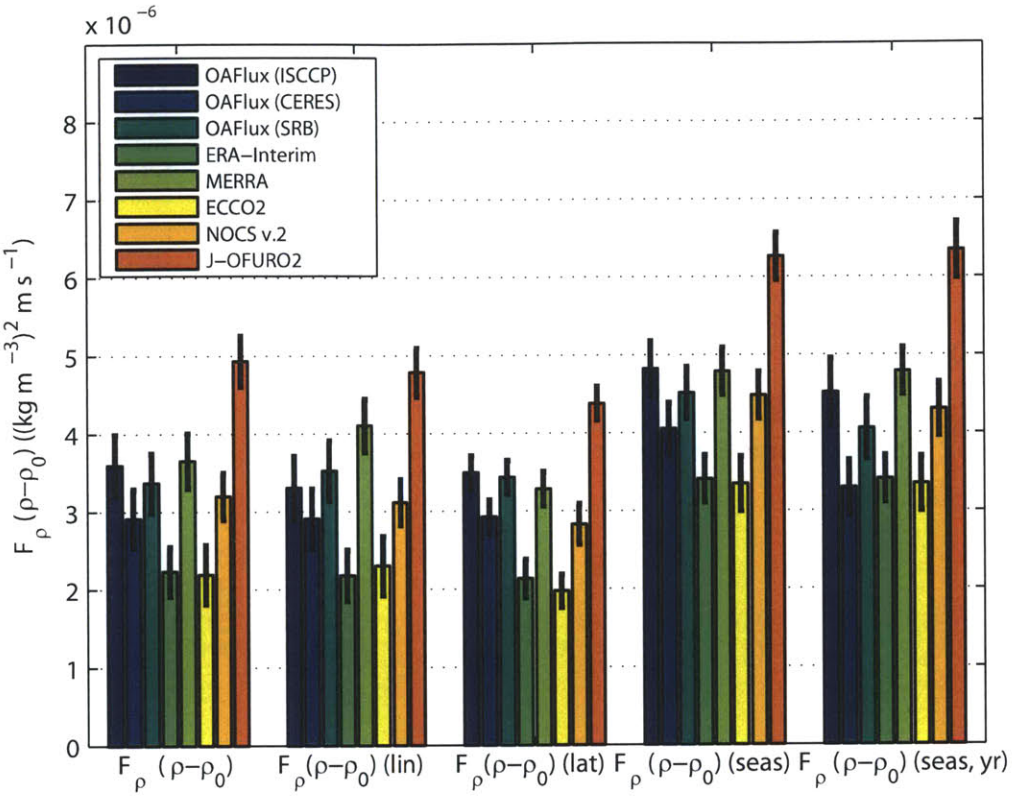

Figure 4-32: Global estimates of density variance production $F_\rho(\bar{\rho} - \rho_0)$ $((\mathrm{kg/m^3})^2/\mathrm{m^2/s})$ using 8 different Q_{net} products as well as 6 different E-P-R products (the spread of which is indicated by black bars) with EN3 v2a SST and SSS. The left-hand group of bars is the nonlinear estimate of density variance production, while the second group of bars is the linearized production estimate. The use of 10° latitude bands is shown in the middle group of bars, while the fourth group of bars shows the results of the use of monthly fields to include the effects of inter-annual variability and the seasonal cycle. The right-hand group of bars indicates the use of monthly fields that have been balanced to zero-mean annual flux (see text).

The resulting implied density variance dissipation estimates χ_ρ for a number of Q_{net} and E-P-R products are shown graphically in Figure 4-32, with error bars indicating the range produced by the six different E-P-R products. The results are also tabulated in Tables A.21 through A.25 using a scale height of H =600 m, as for temperature and salinity. These estimates range from $3 \times 10^{-9}\,(\mathrm{kg/m^3})^2/\mathrm{s}$ to $9 \times 10^{-9}\,(\mathrm{kg/m^3})^2/\mathrm{s}$ for the nonlinear estimate of χ_ρ.

When 10° latitude bands are used, the estimates are changed by −15 % to 15 % depending on the Q_{net} and E-P-R products used. The results of this are tabulated in Table A.23 and shown graphically in the middle group of bars in Figure 4-33. Upon inclusion of the seasonal cycle in the computations by using monthly fields and evaluating the flux using the TEOS-10 equations at each point in both time and space, the implied density variance dissipation increases by approximately 60 %, depending on the dataset used.

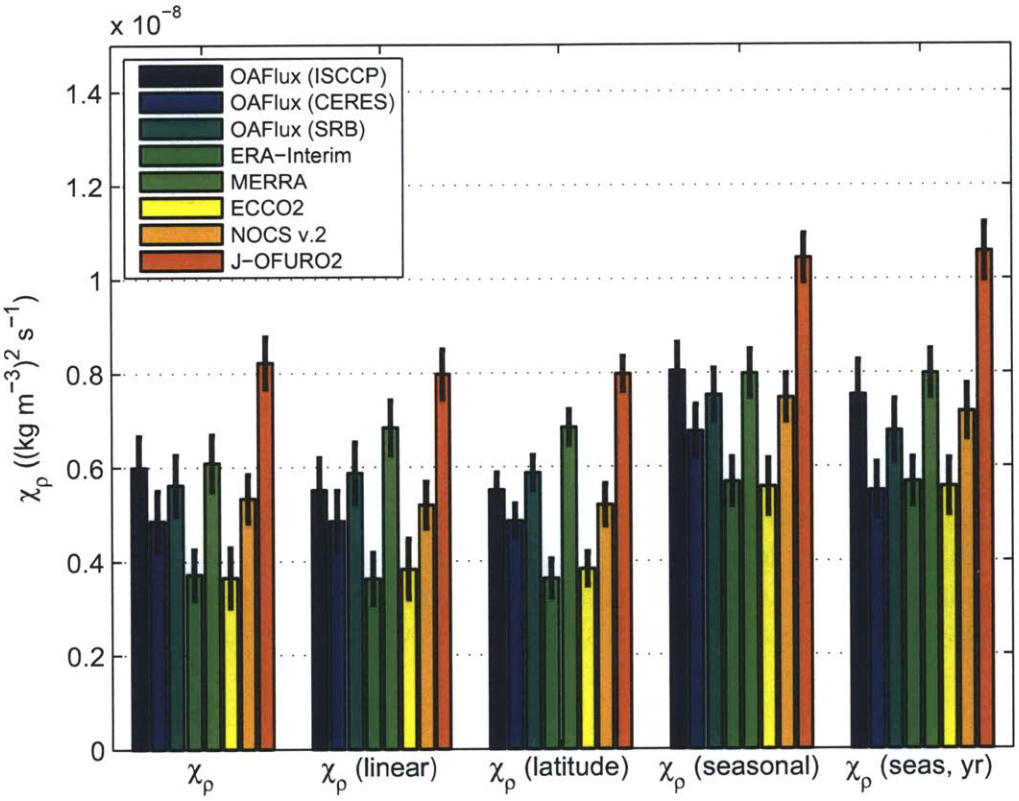

Figure 4-33: Global estimates of density dissipation χ_ρ $((\mathrm{kg/m^3})^2\mathrm{m/s})$ using 8 different Q_{net} products as well as 6 different E-P-R products (the spread of which is indicated by black bars) with EN3 v2a SST and SSS. The left-hand group of bars is the nonlinear estimate of χ_ρ, while the second group of bars is the linearized dissipation estimate. The use of 10° latitude bands is shown in the middle group of bars, while the fourth group of bars shows the results of the use of monthly fields to include the effects of inter-annual variability and the seasonal cycle. The right-hand group of bars indicates the use of monthly fields that have been balanced to zero-mean annual flux (see text).

This is tabulated in Table A.24 and shown in the fourth group of bars. As for the temperature variance generation, it is likely that some of the density variance thus generated is dissipated locally and in the surface layer rather than being dissipated through a down-gradient flux. As such, these estimates should be used with care. The use of annual balancing, that is, the balancing to zero-mean annual Q_{net} and E-P-R causes only moderate changes in the estimate compared to the time-mean balanced seasonal estimate. The results of this are shown in the left-hand group of bars in Figure 4-33 and tabulated in Table A.25.

4.5 Spice Variance

As with the density variance production, it is possible to evaluate spice variance production using either a linearized equation of state with constant α and β coefficients or using the full TEOS-10 equation of state. The governing equation as derived in Chapter 2 is given by:

$$\oiint_A((\bar{\tau}-\tau_0)\overline{F_\tau})dA = -\iiint_V \nabla\bar{\tau}\cdot\overline{\mathbf{u}'\cdot\tau'}dV = \tfrac{1}{2}\iiint_V \chi_\tau dV \tag{4.10}$$

As with temperature, salinity and density, the surface generation of spice variance is thus compensated by a dissipation of spice variance down the spice gradient. As for the other three variables, it is possible to directly relate the surface forcing to the dissipation term by assuming a scale height of depth H in which the variance is dissipated:

$$\chi_\tau H = 2\overline{F_\tau}(\bar{\tau}-\tau_0) \tag{4.11}$$

A map of linear spice variance generation $\overline{F_\tau}(linear)(\bar{\tau}-\tau_0)$ is plotted in Figure 4-34.

While there is a significant generation of spice variance in the tropical ocean, there is variance destruction in regions of high precipitation, such as the ITCZ in the Pacific. This is caused by the freshening of relatively warm (and hence spicy) water. The high latitudes are also a significant source due to the freshening and cooling of less spicy water, leading to a net positive spice variance generation. The implied dissipation is given by the area integral of Figure 4-34.

As discussed in the case of density variance generation, the linearization leads to significant errors due to α being a constant. I thus repeat the calculations using the full TEOS-10 equation of state to compute all coefficients at each point. The results are mapped in Figure 4-35.

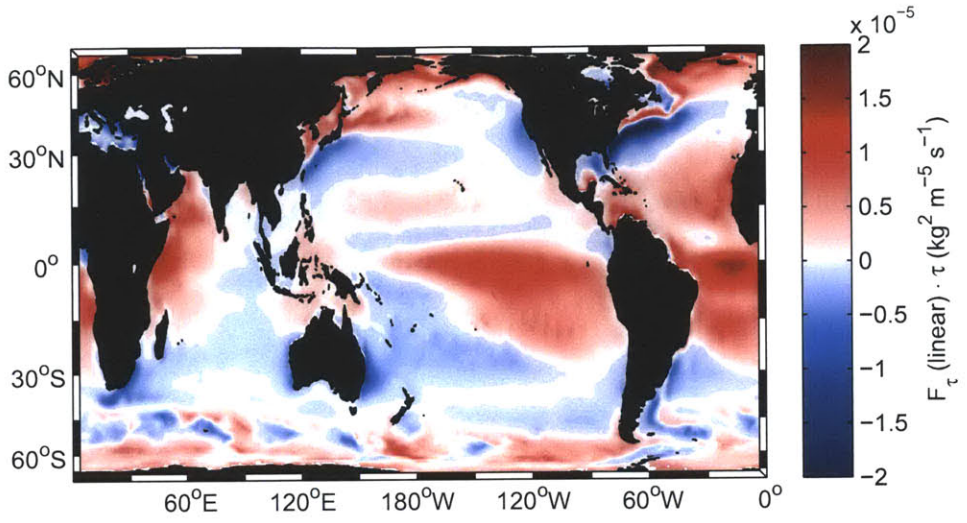

Figure 4-34: Global estimate of linear spice variance generation $\overline{F_\tau}(linear)(\bar{\tau} - \tau_0)$ $((\mathrm{kg/m^3})^2/\mathrm{m^2/s})$ using OAFlux v3 Q_{net}, Schanze et al. (2010) E-P-R and EN3 v2a SST and SSS. Spice variance generation occurs in most subtropical gyres, while variance is destroyed in western boundary currents and parts of the ITCZ.

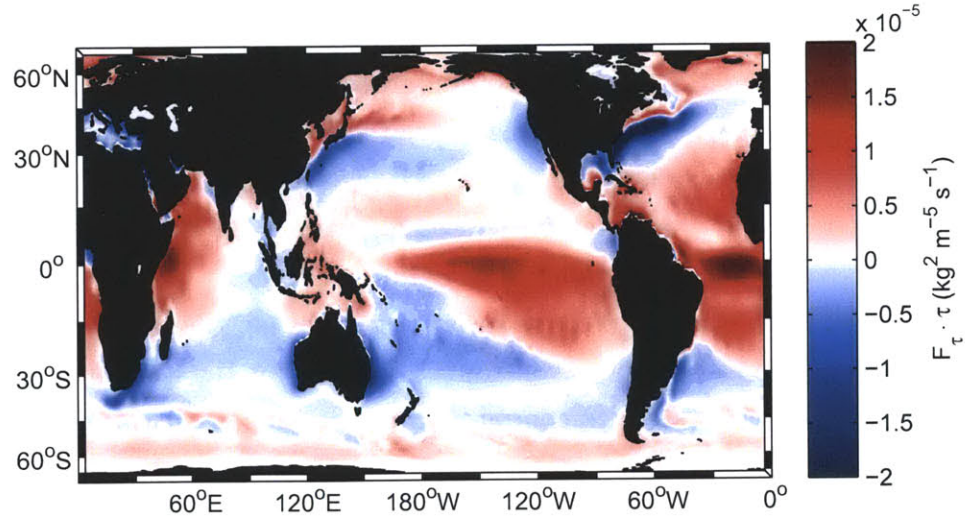

Figure 4-35: Global estimate of nonlinear spice variance generation $\overline{F_\tau}(\bar{\tau} - \tau_0)$ $((\mathrm{kg/m^3})^2/\mathrm{m^2/s})$ using OAFlux v3 Q_{net}, Schanze et al. (2010) E-P-R and EN3 v2a SST and SSS. Compared to the linear case, the generation in subtropical latitudes and near the equator is amplified while the generation in high latitudes is muted.

The influence of low-latitude areas in the generation of spice variance is enhanced, while the influence of high latitudes is muted, as was the case for the production of density variance. The subtropical gyres and equatorial regions are the strongest inputs, while western boundary currents are the most significant sinks: As spicy water is transported polewards, it loses spiciness due to cooling.

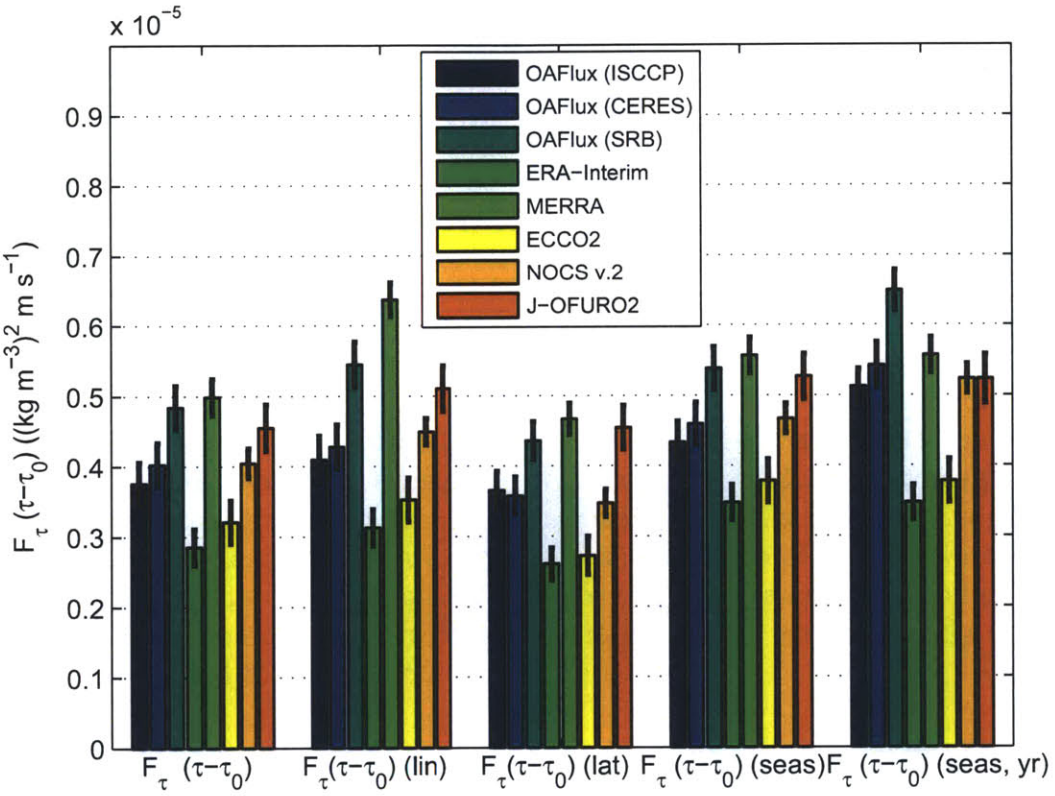

Figure 4-36: Global estimates of spice variance production $F_\tau(\bar{\tau} - \tau_0)$ $((\mathrm{kg/m^3})^2\mathrm{m/s})$ using 8 different Q_{net} products as well as 6 different E-P-R products (the spread of which is indicated by black bars) used with EN3 v2a SST and SSS. The left-hand group of bars is the nonlinear estimate of spice variance production, while the second group of bars is the linearized production estimate. The use of 10° latitude bands is shown in the middle group of bars, while the fourth group of bars shows the results of the use of monthly fields to include the effects of inter-annual variability and the seasonal cycle. The right-hand group of bars indicates the use of monthly fields that have been balanced to zero-mean annual flux (see text).

When this map is integrated, estimates of the nonlinear spice variance production

are obtained. These are shown in Table A.26, whereas the linear results are shown in Table A.27.

For an unscaled comparison with $\chi_\rho H$ estimates, the results of $\chi_\tau H$ are shown graphically in Figure 4-36. Corresponding numeric values are provided in Tables A.26 through A.30.

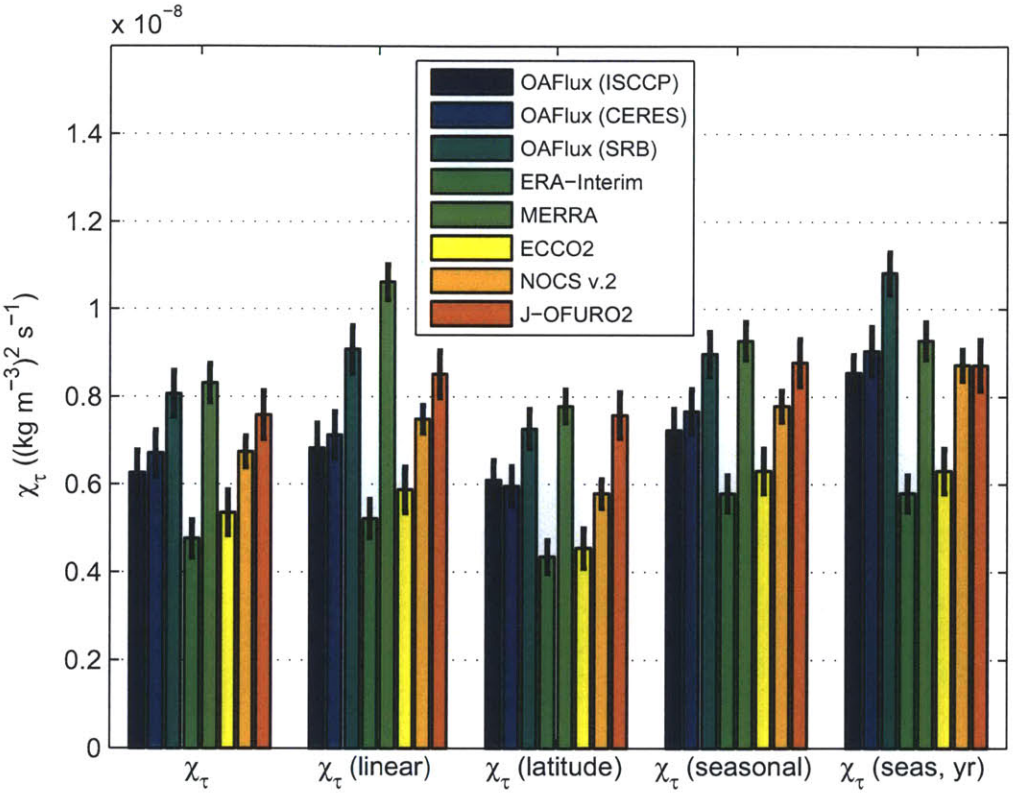

Figure 4-37: Global estimates of spice dissipation χ_τ $((\mathrm{kg/m^3})^2\mathrm{m/s})$ using 8 different Q_{net} products as well as 6 different E-P-R products (the spread of which is indicated by black bars) in combination with EN3 v2a SST and SSS. The left-hand group of bars is the nonlinear estimate of χ_τ, while the second group of bars is the linearized dissipation estimate. The use of 10° latitude bands is shown in the middle group of bars, while the fourth group of bars shows the results of the use of monthly fields to include the effects of inter-annual variability and the seasonal cycle. The right-hand group of bars indicates the use of monthly fields that have been balanced to zero-mean annual flux.

Perhaps surprisingly, the range of estimates is smaller than that of density variance

production, with results of χ_τ ranging from 4.7×10^{-9} $(\mathrm{kg/m^3})^2/\mathrm{s}$ to 9×10^{-9} $(\mathrm{kg/m^3})^2/\mathrm{s}$. The magnitude of the estimates, however, is comparable to that of density variance dissipation, albeit slightly higher for most products.

To facilitate a comparison with χ_ρ, a scale height of H =600 m was used as for the estimates of χ_θ χ_S and χ_ρ. The results of this are shown graphically in Figure 4-37. They are also tabulated for the nonlinear estimates in Table A.31, for the linear estimates in Table A.32 and for the 10° latitude band estimates in Table A.33.

When the seasonal cycle is included, all estimates increase by approximately 10–20 %, which is comparable to the increase seen in the case of salinity variance generation, but lower than that of thermal variance generation or density variance generation. The matrix of $\chi_{\tau(seasonal)}$ results is provided in Table A.34 Nevertheless, the same caveat as for the other seasonal variance generation estimate applies to this: The additional spice variance generated by the seasonal cycle may be partly compensated locally and this estimate should thus be treated with care.

No significant changes in the estimates occur when the balancing is done by-year rather than using the time-mean of 1987–2004. The results are shown graphically in the right-hand group of bars in Figure 4-37 and are tabulated in Table A.35.

4.6 The Role of Advection

In evaluating the power integrals, it has become evident that the use of latitudinal bands increases the estimates of thermal variance generation and hence the implied thermal dissipation. However, the use of latitudinal averaging leads to a decrease in haline variance generation and implied salinity variance dissipation. This leads to two major issues that need to be addressed: The role of advective transports in the ocean and the resulting quadrature between Q_{net} and SST. To illustrate this effect, I will show three hypothetical configurations of Q_{net} and SST in the North Atlantic.

In the absence of clouds or other reflective layers, the amount of incoming solar radiation at the Earth's surface depends on the angle of incidence of sun (Hartmann, 1994). Consequently, the highest insolation occurs in low latitudes while high latitudes tend to have less insolation. To first order, this sets up a gradient of Q_{net} that is largely meridional, with some notable exceptions, such as Western Boundary Currents, which carry heat polewards and are subject to significant surface heat losses (e.g. Yu et al., 2008, and references therein). As is evident in the map of thermal variance production and destruction shown earlier in this Chapter (Figure 4-24), these act as destruction terms of thermal variance. It is thus a legitimate question to ask how much thermal dissipation occurs due to large-scale time-mean advection and how much dissipation occurs due to other mixing processes, such as mesoscale turbulence. It should be noted that in all cases the effects of the atmosphere on the ocean, such as a latitudinal dependence of wind speed or atmospheric advection and heat transport, are ignored.

4.6.1 No Advection

In the absence of advective transports, the gradients of SST and Q_{net} in the ocean should be purely meridional. That is, the input to the ocean from incoming shortwave radiation (Q_{SW}) has a meridional gradient due to the variation of inclination to the sun. As this would set up a meridional SST gradient, the heat loss to the atmosphere through latent heat loss (Q_{LH}), sensible heat loss (Q_{SH}) and outgoing longwave radiation (Q_{LW}) would also be meridional. This is illustrated in Figure 4-38 using values of Q_{net} and SST that are loosely based on the actual meridional gradient, but vary linearly with latitude.

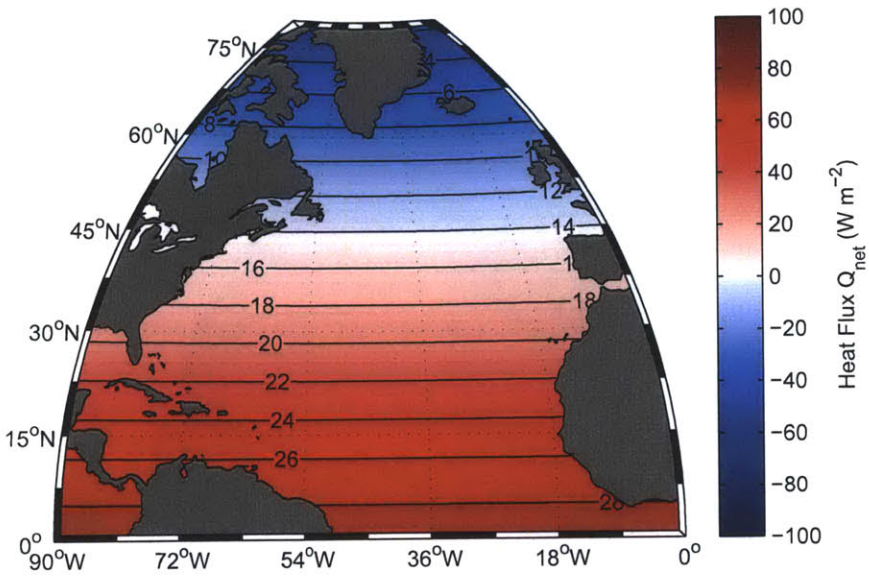

Figure 4-38: Idealized map of Q_{net} and SST in the North Atlantic in absence of advection in either the ocean or the atmosphere. Q_{net} (W m^{-2}) is shaded in colors while SST (°C is contoured using black lines. The values used are loosely based on the actual meridional gradient in the North Atlantic, but are shown for illustration purposes only. The perfect correlation between Q_{net} and SST produce a maximum thermal variance generation compared to advective cases.

In this case, there is a perfect correlation between Q_{net} and SST, leading to the maximum production of thermal variance and thus implying the greatest thermal dissipation in the ocean interior. When latitude bands are used, the gradients of Q_{net} and SST are not linear as will be shown in Figure 5-2. Nevertheless, the correlation between Q_{net} and SST is increased compared to the estimate using $1° \times 1°$ resolution, leading to an increase in the estimated thermal variance production. Conversely, for haline variance production, the correlation between SSS and E-P-R is decreased by using zonal averaging. The estimates of haline variance generation are thus lower. It should be noted that in this illustration, Q_{net} would not sum to zero due to the change in area with latitude.

4.6.2 Pure Advection

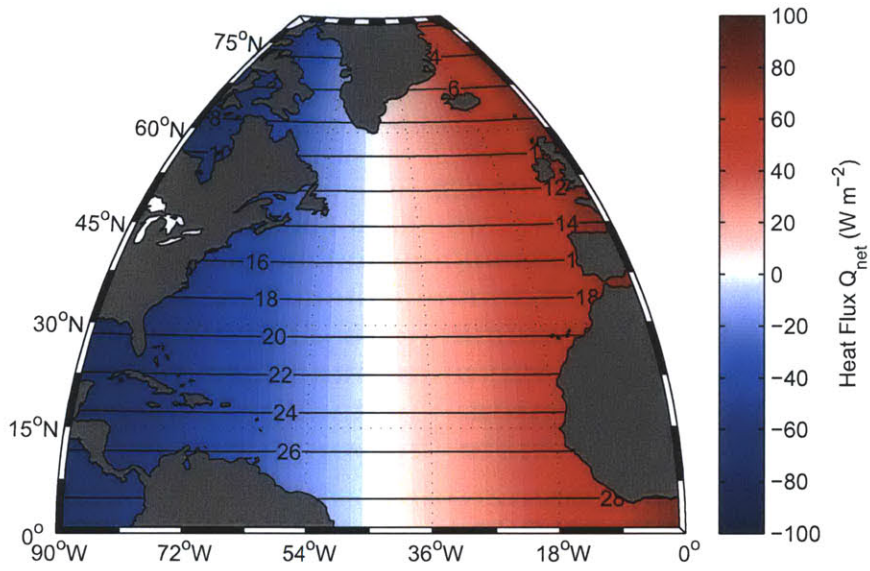

Figure 4-39: Idealized map of Q_{net} and SST in the North Atlantic for purely advective laminar large-scale surface currents. Q_{net} (W m^{-2}) is shaded in colors while SST (°C) is contoured using black lines. The values shown here are for illustration purposes only. The perfect quadrature between Q_{net} and SST produce a zero net thermal variance generation in the thermal power integral.

If all dissipation of thermal variance were due to basin-scale advection, the picture would look radically different from what was shown in Figure 4-38. Consider a turntable with a heating element at one side (the 'equator') and a cooling element on the other (the 'pole') which heats a solid platter with negligible thermal conductivity. This would be a suitable analogue for a purely advective ocean. Assuming a perfectly laminar and circular large-scale surface circulation, the resulting ocean may look akin to the picture shown in Figure 4-39.

The gradients of SST in the ocean should be purely zonal, while Q_{net} in the ocean should be meridional to first order, albeit modifications of Q_{LH}, Q_{SH} and Q_{LW} would occur as a result of the SST, which are ignored here. As a result, the thermal power integral would be zero, as Q_{net} and SST are in perfect quadrature.

4.6.3 Advection and Mixing in the Ocean

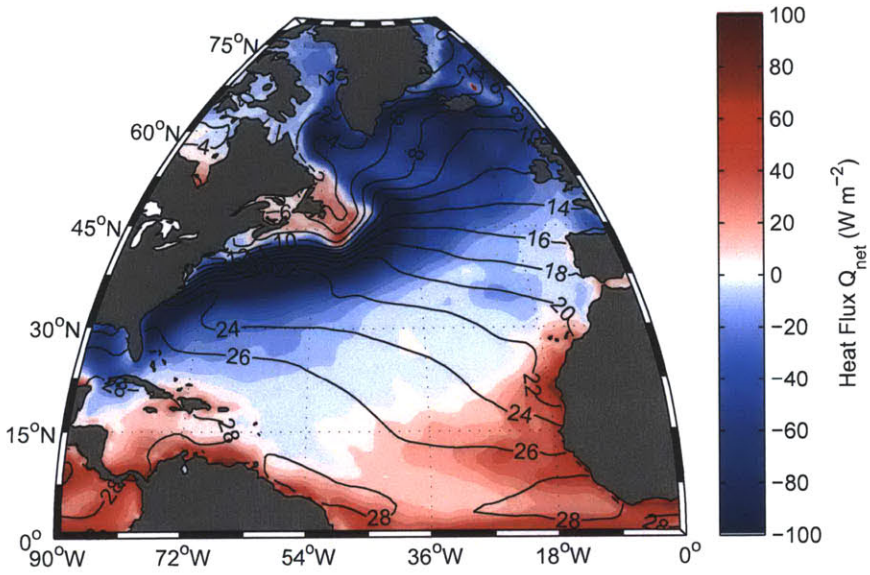

Figure 4-40: Time mean (1987–2004) of adjusted OAFlux Q_{net} and EN3 v2a SST in the North Atlantic. Q_{net} (W m^{-2}) is shaded in colors while SST (°C) is contoured using black lines. While a significant heat loss is evident in the Gulf Stream, the primary gradient of both Q_{net} and SST is meridional.

The question thus arises which of these two representations are closer to the ocean as represented by the estimates of Q_{net} and SST presented in Chapter 3. The time-mean between 1987–2004 of both these variables is plotted in Figure 4-40 using identical color scales to those in Figures 4-38 and 4-39,

In this map, the Gulf Stream is the cause of heat losses in excess of 100 W m^{-2}, leading to a non-monotonous Q_{net} dependence on latitude. The meridional gradient is nonetheless significantly stronger than the zonal gradient. This causes the lines of equal Q_{net} to be slanted in an east-northeast direction. SST is slanted in a west-southwest direction. The two fields are thus clearly not in complete quadrature, but nevertheless modified by advection. To generate a similar result using linear gradients, the ocean is assumed to be dominated by an 80 % meridional gradient in both Q_{net}

and SST with the remaining 20 % of each gradients being zonal. This is shown in Figure 4-41.

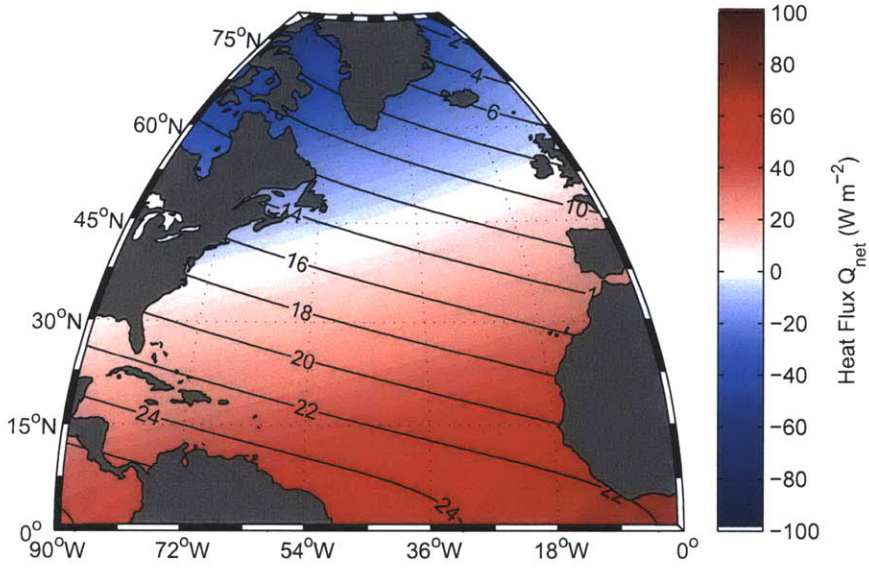

Figure 4-41: Idealized map of Q_{net} and SST in the North Atlantic using both an advective zonal gradient (20 %) and a meridional diffusive gradient (80 %). Q_{net} (W m^{-2}) is shaded in colors while SST (°C) is contoured using black lines. The values shown here are for illustration purposes only. The resulting thermal power integral is reduced compared to the purely diffusive case.

While clearly not a perfect representation of the OAFlux/EN3 v2a estimate due to the linear gradients and the resulting lack of a distinct Western Boundary Current, this illustration is representative of an ocean basin that is subject to both advective and mixing processes. In this representation, the resulting thermal power integral is reduced compared to the perfectly correlated case shown in Figure 4-38. However, it is distinctly non-zero, unlike the case of perfect quadrature shown in Figure 4-39.

All Q_{net} and SST products described in Chapter 3 and evaluated as power integrals in this chapter have significant zonal variations caused by heat transport in both the ocean and the atmosphere. As such, the effects of time-mean large-scale advection are effectively 'removed' from the estimates presented here, except for the latitude-

band averages. The changes in χ_θ between using $1° \times 1°$ and $10°$ latitudinal bands as shown in Figure 4-26 and tabulated in Tables A.4 and A.5 is approximately 20 % for most products. This is comparable to the illustration in Figure 4-41 compared to the meridional-gradient-only case.

While no claim is made as to the actual distribution of advective and mixing processes in the ocean leading to the destruction of thermal variance, these values indicate that mixing processes are likely dominant.

A global map of thermal variance production was shown in Figure 4-24. To facilitate the comparison with the previous idealized maps, these estimates are plotted for the same region of the North Atlantic in Figure 4-42.

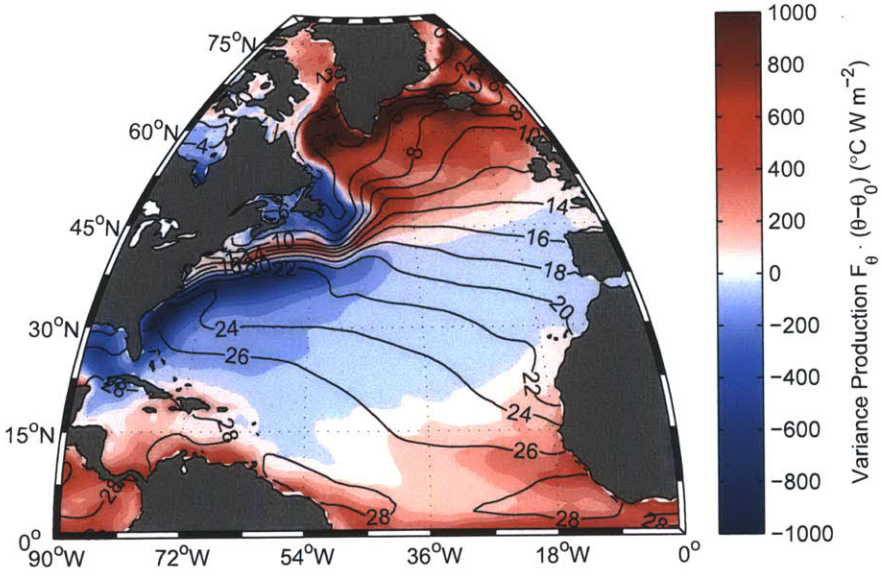

Figure 4-42: Thermal variance generation ($\overline{F_\theta} \cdot (\overline{\theta} - \theta_0)$) based on the time mean (1987–2004) of adjusted OAFlux Q_{net} and EN3 v2a SST in the North Atlantic. Variance generation (°C W m^{-2}) is shaded in colors while SST (°C) is contoured using black lines. Significant positive contributions from both high and low latitudes are evident, while the poleward advection of warm water in the Gulf Stream leads to the destruction of thermal variance.

The thermal variance generation map illustrates that thermal variance is produced

both at high and low latitudes where SST and Q_{net} are correlated. The poleward advection of warm water and consequent cooling leads to a negative correlation between SST and Q_{net}, and as a result, thermal variance is destroyed in the Gulf Stream.

4.7 Relative Influence of Heat and Salt

As was pointed out in Section 4.1.3 and Section 4.1.4, the density and spice flux may be separated into a thermal forcing component $F_{\rho\theta}$ and a haline forcing component $F_{\rho S}$:

$$F_\rho = F_{\rho S} - F_{\rho\theta} = \rho_0(\frac{1}{\rho_F}\beta F_S - \frac{1}{c_p\rho_0}\alpha F_\theta) \tag{4.12}$$

While the thermal forcing induces a negative density flux (due to warming), it induces a positive spice flux. The difference between the definitions of density and spice variance generation is thus simply the substitution of ρ for τ and the reversal of the sign in front of the thermal surface forcing:

$$F_\tau = F_{\rho S} + F_{\rho\theta} = \rho_0(\frac{1}{\rho_F}\beta F_S + \frac{1}{c_p\rho_0}\alpha F_\theta) \tag{4.13}$$

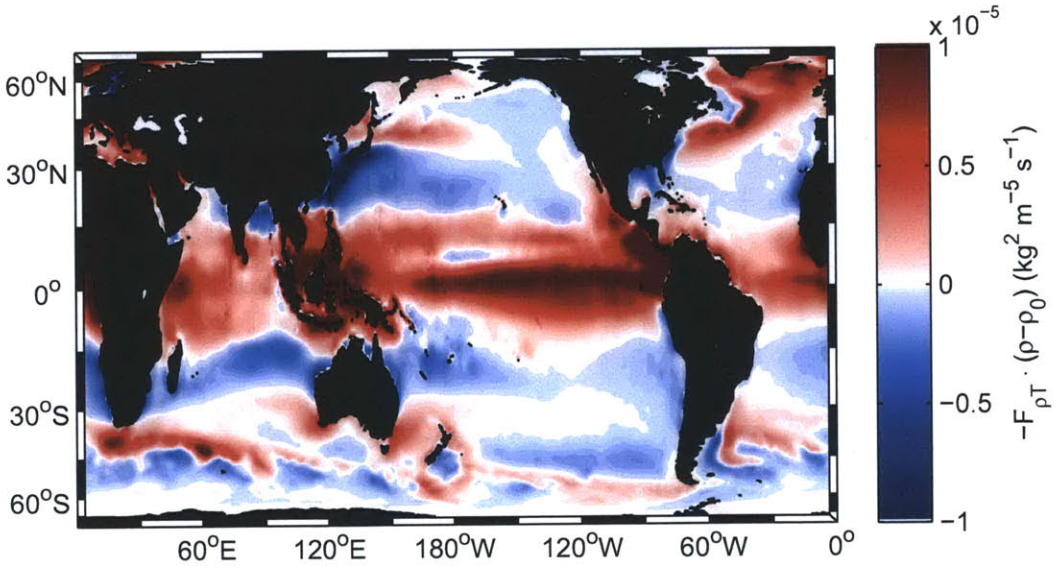

Figure 4-43: Thermal component of the time-mean density flux (negative as in density equation) $(-\overline{F_{\rho T}}\cdot(\bar{\rho}-\rho_0))$ $((\mathrm{kg/m^3})^2/\mathrm{m/s})$. Equatorial regions and the North Atlantic are major points of density variance generation while most of the destruction occurs in subtropical latitudes.

It is thus possible to compute the fields of the thermal and haline components of spice and density variance generation by substituting $F_{\rho\theta}$ and $F_{\rho S}$ for the full F_ρ and F_τ in Eq. (4.8) and Eq. (4.10), respectively. The thermal component of density variance production $(-F_{\rho T} \cdot (\rho - \rho_0))$ is shown in Figure 4-43.

It is evident in Figure 4-43 that the equatorial regions, in which relatively light water gains a significant amount of heat and thus becomes even lighter, is the biggest contributor to density variance. The densification of relatively dense water in high latitudes, such as in the North Atlantic also contributes a positive generation term. The main sinks of density variance are the subtropical parts of western boundary currents, in which relatively light water becomes denser. Large areas of all subtropical gyres are also negative due to a slight heat loss (and thus densification) of light water.

The haline component of the density variance generation $(F_{\rho S} \cdot (\rho - \rho_0))$ is plotted in Figure 4-44 using the same color-scale for comparison. It is clear that the thermal component of forcing is the dominant term in the production of density variance generation.

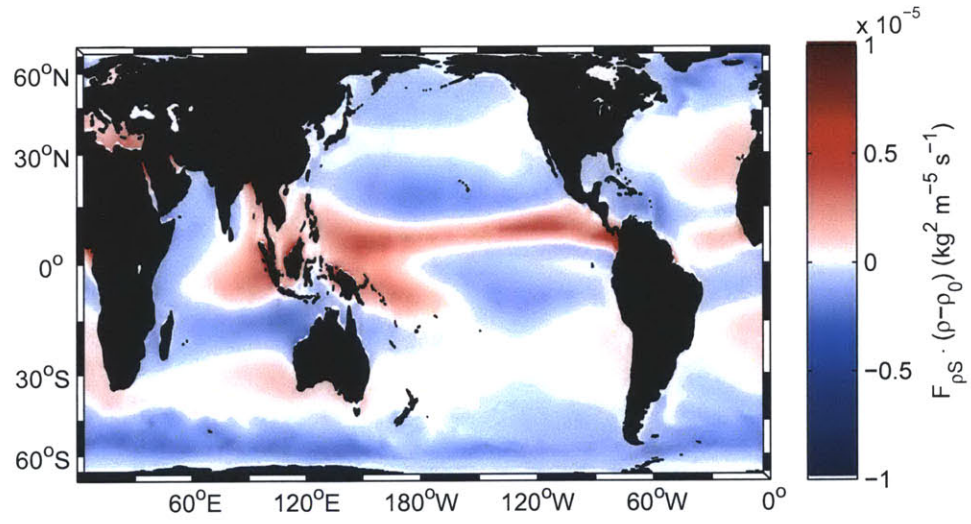

Figure 4-44: Haline component of the time-mean density flux $(\overline{F_{\rho S}} \cdot (\bar{\rho} - \rho_0))$ $((\mathrm{kg/m^3})^2/\mathrm{m/s})$. The ITCZ and Atlantic subtropical gyres are the largest generating points of density variance while high latitudes tend to be sinks.

In Figure 4-44, the dominant areas of density variance generation are the ITCZ as well as the subtropical gyres in the North Atlantic, where relatively dense water

is made denser by evaporation. Since high latitudes tend to be net precipitative, the dense water here is freshened by excess P, leading to density variance destruction.

As shown in Eq. (4.13), a decomposition into the thermal and haline components is also possible for spice variance generation. The thermal component ($F_{\rho T}(\tau - \tau_0)$) is shown in Figure 4-45.

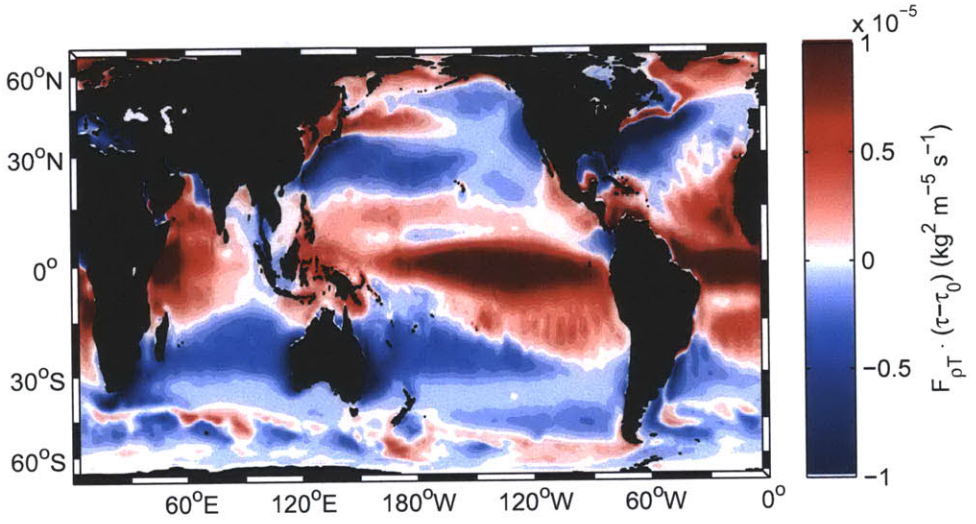

Figure 4-45: Thermal component of the time-mean spice flux ($\overline{F_{\rho T}}(\bar{\tau} - \tau_0)$) $((\mathrm{kg/m^3})^2/\mathrm{m/s})$. Spice variance is generated in equatorial regions and high latitudes and destroyed in subtropical latitudes, particularly in western boundary currents.

It is evident in Figure 4-45 that the equatorial regions are also the dominant input of spice variance. All subtropical latitudes are areas of spice variance destruction, but western boundary currents are significantly enhanced. As warm water is advected polewards, it loses spiciness in a region of relatively high spice. At high latitudes, 'bland' (low spice) water loses spice through a negative heat flux. While the patterns are generally similar to those found in the thermal component of density forcing, there are significant differences, particularly in subtropical latitudes and western boundary currents.

The haline component of spice variance generation ($F_{\tau S}(\bar{\tau} - \tau_0)$) is mapped in Figure 4-46.

The spice variance generated by the haline component (Figure 4-46) is largely positive, with destruction only in the ITCZ and roughly along a latitude band of

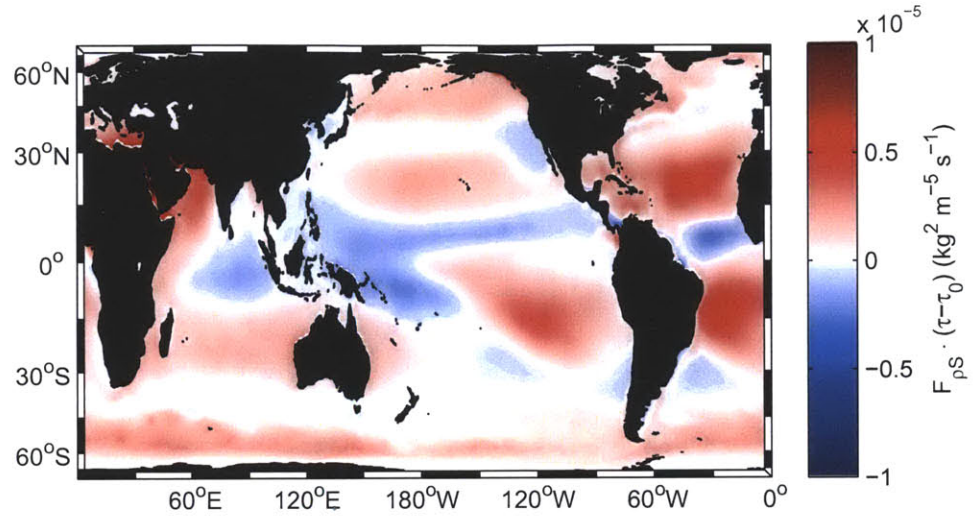

Figure 4-46: Haline component of the spice variance generation $(\overline{F_{\rho S}}(\bar{\tau} - \tau_0))$ $((\mathrm{kg/m^3})^2/\mathrm{m/s})$. Spice variance is generated in subtropical gyres and high latitudes and is destroyed in the ITCZ and in some areas in temperate latitudes.

40°. The destruction in the ITCZ is caused by very spicy water (due to its high temperature) losing spice due to precipitation. The net evaporation in the subtropical gyres is in areas of relatively high spice, as these waters tend to be warm and salty, particularly in the Atlantic Ocean. At high latitudes, 'bland' water is made even less spicy by net P, thus contributing to spice variance generation

The ratio of haline to thermal forcing, the flux ratio γ, was discussed in the derivation of the power integrals in Chapter 2. There, the importance of the ratio of the flux ratio γ to the density ratio R_ρ was discussed for the generation of salt fingers, which can generate density variance in the ocean interior. This is a commonly observed process in laboratory experiments (Turner, 1979). While a full three-dimensional evaluation of the density ratio R_ρ in the interior ocean is beyond the scope of this thesis, I present a map of the absolute value of the flux ratio $|\gamma|$ as computed from the thermal and haline components of density forcing in Figure 4-47. This is contoured using a logarithmic scale to illustrate the relative importance of the thermal to the haline component of density forcing.

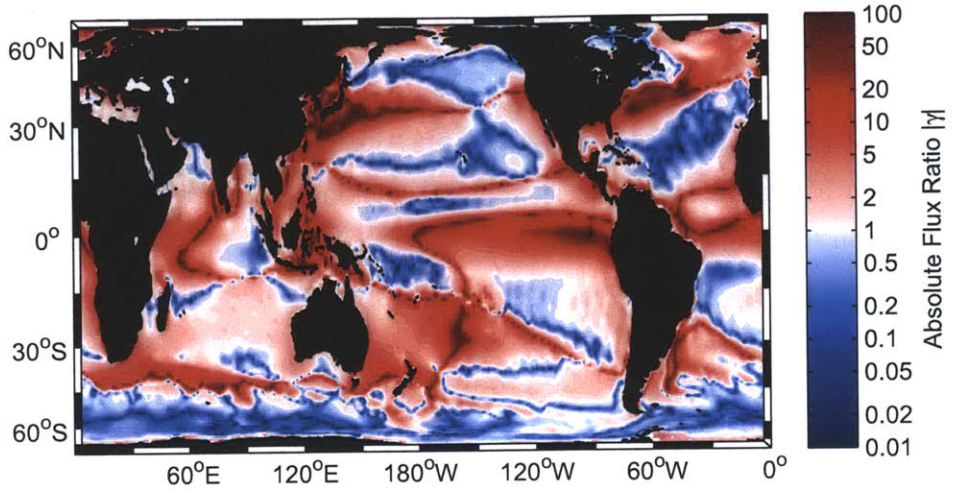

Figure 4-47: Absolute value of the flux ratio $|\gamma|$ as derived from datasets discussed in Chapter 3. A flux ratio greater than 1 means that the density flux is dominated by thermal forcing, while a flux ratio of less than 1 means a dominant haline forcing. All Western Boundary Currents are dominated by heat loss, while the ITCZ and high latitudes are dominated by precipitation and subtropical gyres are dominated by evaporation.

Numbers greater than 1 indicate that the density flux is dominated by thermal forcing. A flux ratio of less than 1 indicates a dominance of haline forcing. As was discussed in Chapter 2 and shown in Figure 2-2, low values of γ (≤ 1) are conducive to the salt finger growth (Schmitt, 1979), and there is good evidence that salt fingers are active in the $R_\rho \approx 2$ Central Waters (St. Laurent and Schmitt, 1999). The areas contoured in blue hues in Figure 4-47 are thus areas that may (depending on R_ρ) support salt finger growth and hence may lead to the internal generation of density variance.

In general, the salinity maximum regions of each of the subtropical gyres reveal a dominance of the haline component of the density flux. In contrast the "'eighteen-degree-water"' formation site (e.g. Joyce, 2012) south of the Gulf Stream is dominated by thermal density fluxes, helping to account for the deep mixed layers formed there in winter. Thus, such flux ratio maps can be connected to water mass formation sites, but a detailed regional description and analysis is beyond the scope of this thesis.

4.8 Sensitivity of Estimates

Some of the possible errors associated with the estimates of ocean variables used in the calculations of χ_θ, χ_S, χ_ρ, and χ_τ have been discussed in Chapters 3 and 4. However, I concluded that a formal error analysis may not yield a reasonable estimate of the error associated with fields such as Q_{net} or E-P-R, as there are unknown error co-variances and possible systematic errors common to all products. This also means merely using an "'ensemble mean"' of a number of products may not produce a reasonable estimate of upper and lower bounds, as these products generally ingest common input data.

While it is beyond the scope of this thesis, and may even be impossible, to fully address the issue of systematic errors, I here offer two approaches to test the robustness of the estimates presented in Chapter 4: A scale analysis of thermal variance generation, which reduces the problem to two variables (the differences in heat flux and in surface temperature between poles and equator) and also a sensitivity analysis of the full calculation using the same $1° \times 1°$ calculation presented in Chapter 4, but with a linear gradient of Q_{net} adjustment along latitudes.

In conclusion of these analyses, I will show that while the latitudinal gradient of χ_θ is the dominant component of both χ_ρ and χ_τ, the effect of $\Delta Q_{net}(equator - pole)$ is less significant on either of these two estimates than on χ_θ.

4.8.1 Scale Analysis of Thermal Variance

To simplify the case of thermal variance generation and dissipation in the ocean, various approaches may be used. Joyce (1980) chose to use 10° latitude bands for the calculation of a dissipation integral, but it is possible to reduce this problem to the simplest possible state: uniform heating in a tropical region and uniform cooling in a polar region. While this is not very realistic – amongst other issues, it would create an infinite gradient in Q_{net} – is does simplify the problem considerably.

There are a number of choices to select the area of heating and cooling, with the two most obvious being a separation into an equal forcing based on a global estimate of Q_{net} and the other being a separation into equal areas of heating and cooling.

In the case of equal forcing, I use the OAFlux 3.0 Q_{net} product (Yu et al., 2008), which is artificially balanced to integrate to zero globally, as described in Chapter 3. From this, the latitude range that most closely follows a distribution of equal heating in the equatorial region and equal cooling in the polar region is 20° latitude. The

resulting areas are defined thus:

- Polar: The ice-free ocean area between 21–90 °N and 21–90 °S. In the balanced Q_{net} estimate presented in Chapter 3 this area is subject to a mean cooling of $-16\,\mathrm{W\,m^{-2}}$ over an area (A_{pl}) of $2.3 \times 10^{14}\,\mathrm{m^2}$, totaling a heat flux of $-3.5 \times 10^{15}\,\mathrm{W}$ or $-3.5\,\mathrm{PW}$. The mean sea surface temperature (SST), denoted by θ, is taken from the EN3 v2a product (see Chapter 3 for a discussion of this product) and is 13.3 °C. The resulting SST anomaly relative to the global mean SST (θ_0) is $\theta_{pl} - \theta_0$ =−5.3 °C. The subscript $_{pl}$ shall denote variables in the polar region as defined above.

- Equatorial: The ocean area between 20 °N and 20 °S is heated with an average heat flux of Q_{eq} =25 $\mathrm{W\,m^{-2}}$ over an area (A_{eq}) of $1.4 \times 10^{14}\,\mathrm{m^2}$, totaling a net heat input of $3.5 \times 10^{15}\,\mathrm{W}$ or 3.5 PW. The mean SST as estimated in the EN3 v2a product is 27.3 °C and the resulting anomaly is $\theta_{eq} - \theta_0$ =8.7 °C. The subscript $_{eq}$ shall denote variables in the equatorial region as defined above.

As was shown in Chapter 2, the following condition must be fulfilled:

$$\frac{1}{\rho_0 c_p} \oiint_A (\overline{F_\theta}) dA = 0 \tag{4.14}$$

where the forcing term F_θ is defined in Eq. (2.13) as $F_\theta = Q_{net}$, ρ_0 is defined as the global mean sea surface density of the ocean and c_p is defined as the heat capacity of seawater, which in this scale analysis is taken as the global mean sea surface heat capacity of seawater, c_{p0}.

The relation of production and dissipation of variance was derived in Eq. (2.21) and is linearized and simplified to include only the difference in heat flux and in sea surface temperature (and the areas associated with the regions):

$$\chi_\theta = 2 \cdot \frac{[A_{eq} \cdot Q_{eq} \cdot (\theta_{eq} - \theta_0) + A_{pl} \cdot Q_{pl} \cdot (\theta_{pl} - \theta_0)]}{H \cdot \rho_0 \cdot c_{p0} \cdot (A_{eq} + A_{pl})} \tag{4.15}$$

when substituting the above values for each variable, assuming a scale height of H =600 m for dissipation in the thermocline, the following is obtained:

$$\chi_\theta = 2 \cdot \frac{[1.4 \times 10^{14}\,\mathrm{m^2} \cdot 25\,\mathrm{W\,m^{-2}} \cdot 8.7\,^\circ\mathrm{C} + 2.3 \times 10^{14}\,\mathrm{m^2} \cdot (-16\,\mathrm{W\,m^{-2}}) \cdot (-5.3\,^\circ\mathrm{C})]}{600\,\mathrm{m} \cdot 1024\,\mathrm{kg\,m^{-3}} \cdot 3998\,\mathrm{J\,^\circ C^{-1}\,kg^{-1}} \cdot 3.7 \times 10^{14}\,\mathrm{m^2}} \tag{4.16}$$

so that, noting that the definition of 1 W is 1 J s^{-1}, Eq (4.16) can be evaluated:

$$\chi_\theta = 1.1 \times 10^{-7}\,^\circ\mathrm{C}^2\,\mathrm{s}^{-1} \tag{4.17}$$

It should be noted that this estimate, despite being calculated with values of the 'baseline' estimate of OAFlux Q_{net} and EN3 v2a SST is higher than the estimate using fields at 1° × 1° resolution, and even exceeds the estimate of using 10° latitudinal bands as in Joyce (1980). This is due to the improved correlation between SST and Q_{net} caused by integrating over a larger area here, an effect that was already discussed by Joyce (1980) and shown in Chapter 4.

The errors associated with SST are at least one order of magnitude smaller than those found in Q_{net} (Yu and Weller, 2007; Yu et al., 2008; Ingleby and Huddleston, 2007), and the remaining variables, such as ρ_0, c_{p0} and ocean area sizes are even less sensitive: the variations of sea surface density as computed with TEOS-10 (McDougall, 2011) are less than 3 % in the global ocean, which is further reduced by integrating over the global ocean. c_p changes by less than 5 % over the entire range of salinities and temperatures found at the surface of the ocean, which implies much lower errors in the global mean. By using the error estimate provided with the EN3 v2a product (Ingleby and Huddleston, 2007), it is possible to propagate the upper and lower bounds of temperature and salinity through the calculations. The resulting change to the overall estimate of variance generation for density and spice variance is on the order of 1 % and thus deemed insignificant compared to the error estimates of the surface flux products. However, it is possible that changes in SSS and SST on small time- and space-scales, such as diurnal changes, may lead to greater errors than those estimated for the EN3 v2a product.

The estimate of χ_θ depends linearly on the choice of the scale height, H, but since the scale height is applied to all estimates, it does not affect the production term of thermal variance, but only the strength and distribution of the implied thermal dissipation in the interior. The area of the ice-free ocean changes by less than 5 % depending on the landmask used.

The dominant variables influencing χ_θ under the assumptions of area distribution between poles and equator are thus clearly Q_{eq} and Q_{pl}. It should be noted that when Q_{eq} is increased, Q_{pl} must be decreased by a factor of A_{eq}/A_{pl}, which is approximately 0.61 in the given case.

This means that if Q_{eq} is increased by 10 W m^{-2}, Q_{pl} must be decreased by

6.1 W m^{-2}. Conversely, a decrease of heat input in the equatorial region would necessitate a 61 % increase of heat input in the polar region.

The result of adjusting Q_{eq} is shown graphically in Figure 4-48. The point of no adjustment (and thus the result obtained in Eq. (4.17) is indicated as a blue circle, while the equivalent result of using the full fields of all variables is shown by a red circle. As is evident from Eq. (4.15), this is a linear relationship, which, by definition, is zero when $\Delta Q_{eq} = 0$, at which point Q_{eq}=Q_{pl}.

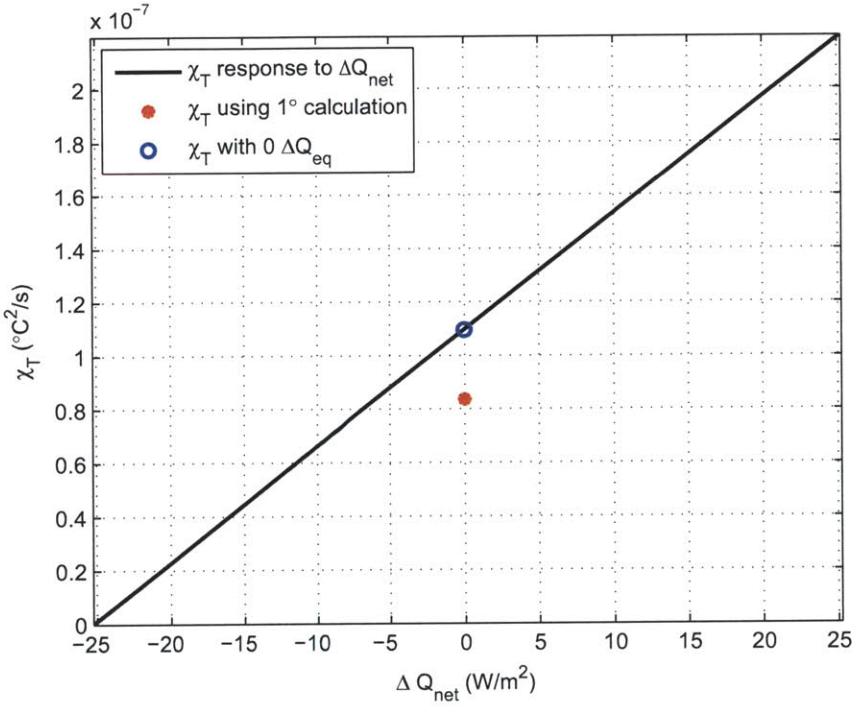

Figure 4-48: Simple scale relationship of χ_θ with changing Q_{eq}. The equatorial region is defined to be the global ocean between 20 ° S and 20 ° N, while the polar region is the remaining ice-free ocean north and south of 20°. The relationship is linear with a zero crossing at $\Delta Q_{net} = -Q_{eq}$ =−25 W m^{-2}.

This implies that unless one asserts that the Polar Regions receive net heat and the equatorial regions are subject to a net heat loss, the dissipation must always be a positive number. There is no conceivable way to reverse the sign without violating the second law of thermodynamics or changing the global distribution of sea surface temperature. While the latter is conceivable to some extent, the basic properties of the Earth's orientation to the sun dictate that there is a higher input of short-wave radiation at the equator than there is at the poles (Hartmann, 1994). This makes a

full reversal of the temperature gradient physically implausible.

While the adjustment of the cut-off latitude changes the sensitivity of the system to changes in ΔQ_{eq}, the linear relationship and the zero-crossing at $Q_{eq} = Q_{pl}$ remain. As a result, a repetition of this analysis with different limits would be futile.

4.8.2 Sensitivity of Thermal Variance Production

While the effect of the latitudinal gradient, which appears as the dominant term in all evaluated Q_{net} products, has been addressed in the previous section, the question of the effect of the regional patterns of Q_{net} remains. I have shown in Chapter 4 that using 10° latitude bands as in Joyce (1980) increases the global integral of thermal variance production for all eight evaluated Q_{net} products. It is then clear that the linearized case of the previous section is an upper limit of the time-mean production of thermal variance and that there is an effect of decreasing thermal variance production with the inclusion of zonal structure. This is due to the effects of advection, such as in western boundary currents, as is evidenced in Figure 4-24 in which areas of poleward advection (cooling) of warm water act as a strong destruction term for thermal variance. There are no advective effects in an ocean that has homogeneous SST and Q_{net} properties in an equatorial band and in a polar band.

To evaluate the sensitivity in the case of a more realistic picture of the ocean, which includes advection, the Q_{net} estimate is artificially biased with an linear offset from equator to pole. That is, a value is added to each grid point which is zero at 90° and increases linearly with latitude towards the equator. After this biasing, the residual spatial mean is subtracted to ensure a steady state as prescribed in Eq. (4.14). This biasing varied between $-20\,\mathrm{W\,m^{-2}}$ and $20\,\mathrm{W\,m^{-2}}$ and the results are shown in Figure 4-49.

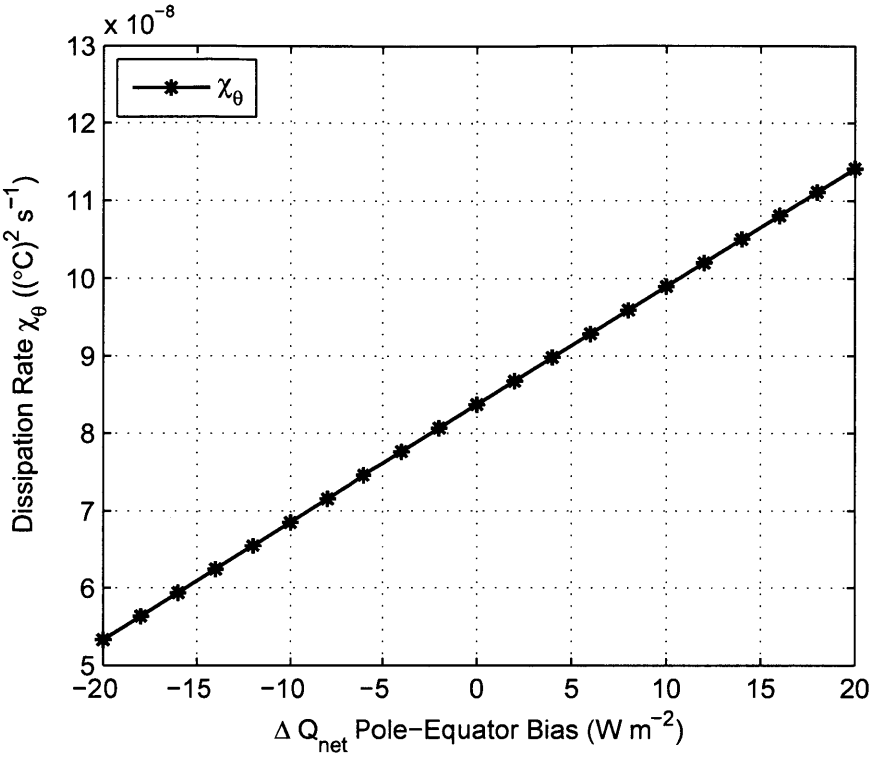

Figure 4-49: Sensitivity of χ_θ to a linear Q_{net} bias between 90° latitude and the equator. Positive values indicate the additional difference in forcing (in $\mathrm{W\,m^{-2}}$ between the poles and the equator. Negative values indicate that the additional difference results in greater Q_{net} at the poles and a reduced Q_{net} at the equator. The relationship is linear.

It is evident that the sensitivity is linear. This was verified by a linear regression analysis (not shown here). This shows that even with more complex patterns, the basic finding of the scale analysis holds: χ_θ is directly proportional to the difference in Q_{net} between poles and equator (ΔQ_{net}). While the gradient between poles and equator is certainly the first-order term in the production of thermal variance, the same is not true for salinity variance and the implied salinity variance dissipation χ_S. Since E-P-R is a complex pattern with no clearly dominant meridional or zonal gradient, a sensitivity analysis as was performed for χ_θ would not yield representative results. Moreover, the effects of E-P-R on χ_ρ and χ_τ are comparatively small.

4.8.3 Sensitivity of Density and Spice Variance Production

Due to the large influence of thermal variance production on both χ_ρ and χ_τ, I decided to repeat the sensitivity analysis performed for χ_θ for both of these variables. The same offset in Q_{net} is thus applied to the forcing fields that are used in the generation of χ_ρ and χ_τ. The results of this are shown in Figure 4-50.

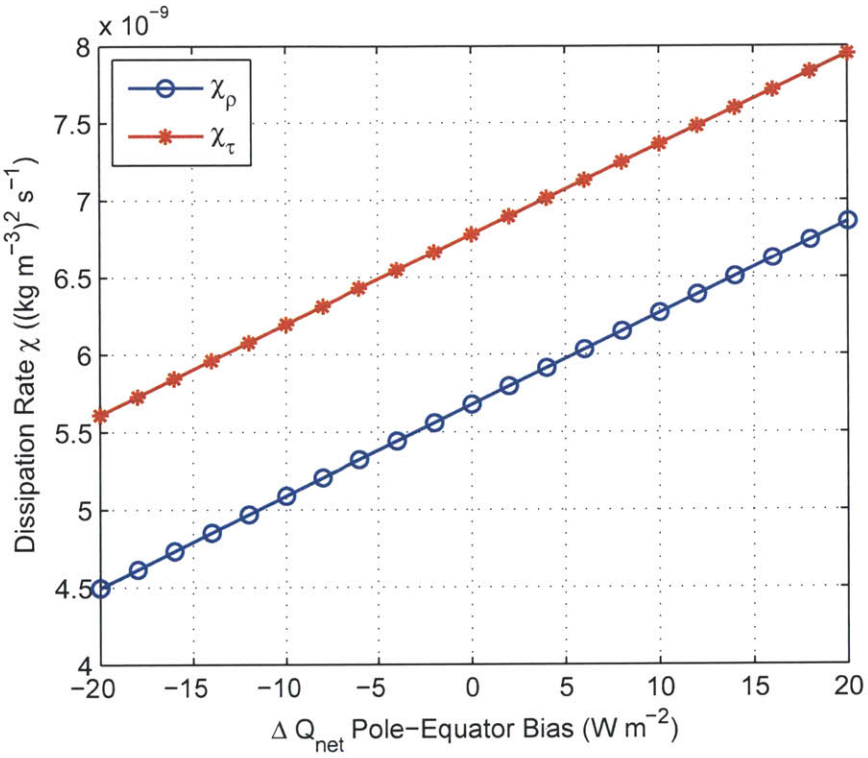

Figure 4-50: Sensitivity of χ_ρ and χ_τ to a linear Q_{net} bias between 90° latitude and the equator. Positive values indicate the additional difference in forcing (in $\mathrm{W\,m^{-2}}$ between the poles and the equator. Negative values indicate that the additional difference results in greater Q_{net} at the poles and a reduced Q_{net} at the equator. The relationship is linear in both cases, with χ_ρ being marginally more sensitive to changes in ΔQ_{net}.

It is evident that the results show a reduced sensitivity to the applied bias compared to χ_θ, that is, the absolute values of χ_ρ and χ_τ change less with the same ΔQ_{net}. The range of change for χ_θ was found to be approximately $\pm$ 50 % between ΔQ_{net}=$-20\,\mathrm{W\,m^{-2}}$ and ΔQ_{net} =$20\,\mathrm{W\,m^{-2}}$. However, the range for both χ_ρ and χ_τ is approximately 25 % for the same ΔQ_{net}.

This indicates that the results of χ_ρ and χ_τ are more robust to errors in the

meridional gradient in Q_{net} than is the estimate of χ_θ. The same procedure is repeated for χ_ρ and χ_τ using monthly fields, thus including effects of the seasonal cycle, as discussed in Chapter 4. This is shown in Figure 4-51.

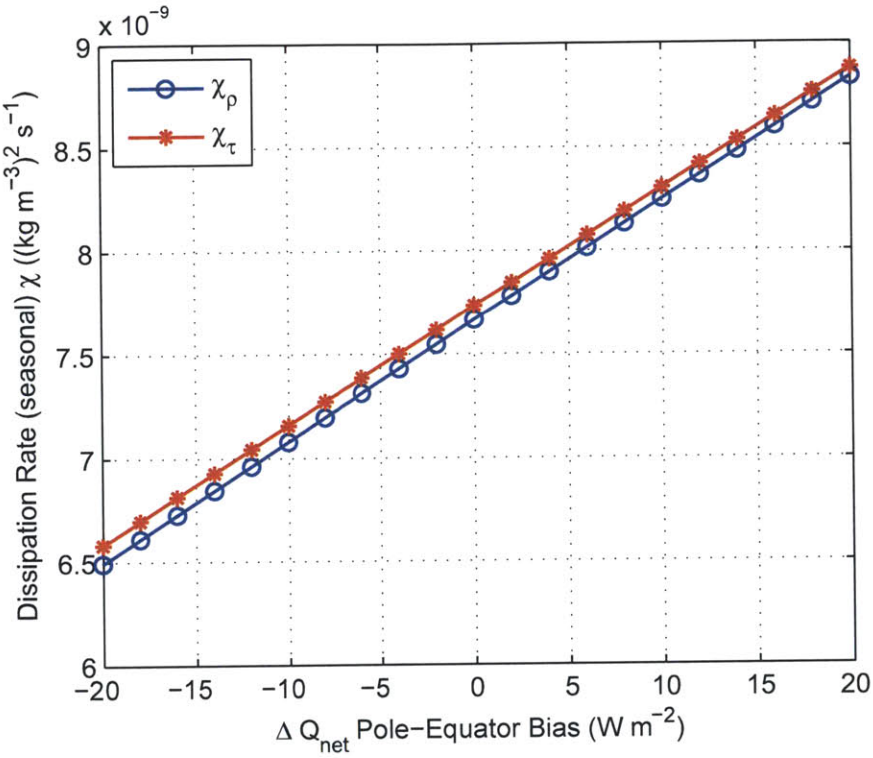

Figure 4-51: Sensitivity of χ_ρ and χ_τ to a linear Q_{net} bias between 90° latitude and the equator. Positive values indicate the additional difference in forcing (in $\mathrm{W\,m^{-2}}$ between the poles and the equator. Negative values indicate that the additional difference results in greater Q_{net} at the poles and a reduced Q_{net} at the equator. The relationship is linear in both cases. It is evident that χ_ρ is somewhat more sensitive to ΔQ_{net} than χ_θ

As was shown in the results in Chapter 4, the difference between χ_ρ and χ_τ is smaller than in the time-mean case when using the OAFlux Q_{net} product and the Schanze E-P-R estimate. It is evident that χ_ρ has a slightly higher slope than χ_τ, that is, it is slightly more sensitive to meridional changes in Q_{net}.

4.8.4 Sensitivity of Estimates to Temporal Variability

While the question of the influence of the seasonal cycle has been addressed in Chapter 4, the effects of inter-annual variability need to be examined more closely. There are also possible effects caused by changes in the composition of the data sources that are used in the estimation of Q_{net} and E-P-R, as well as SST and SSS. Such changes were discussed for both E-P-R and Q_{net} in Chapter 3. In the analysis in Section 3.3, a change in 2002 was evident for the OAFlux-ISCCP Q_{net} estimate. To address these issues, the implied thermal, salinity, density and spice dissipation are plotted for each year between 1987–2004 in Figure 4-52.

The results confirm the changes in Q_{net} identified in Chapter 3 in all but salinity dissipation. This is to be expected, as χ_S is not based on Q_{net}, except of the Q_{LH} (latent heat loss) term in Q_{net}, which is proportional to evaporation. The lack of sensitivity thus indicates that the change in Q_{net} is not caused by a change in the Q_{LH} field, a result which is congruent with the homogeneity analysis for E in Chapter 3.

Variations in χ_θ of up to $\pm$ 70 % are identified in the time period 1987–2004. While some of these variations are likely attributable to natural variability, it is unclear how much of it may be caused by changes in input data composition changes used in producing estimates of Q_{net}. To address this better, the analysis was repeated with a Q_{net} estimate which was zero-balanced for each year between 1987–2004 rather than removing a time-mean. Both balancing methods fulfill the steady state prescribed in Eq. (4.14). The results are shown in Figure 4-53. The changes in the time-mean values of χ_θ, χ_S, χ_ρ, and χ_τ caused by this difference in balancing were presented in Chapter 4 and are generally small.

While it is evident that the inter-annual variability has been reduced, a reduction in χ_θ that likely exceeds natural variability is still present after 2002. The inter-annual variability in both χ_ρ and χ_τ is reduced more strongly than that of χ_θ, which is likely due to the effect of balancing E-P-R by-year also. This can also be seen in the reduction of inter-annual variability in the estimate of χ_S.

From these results, as well as the variations between different Q_{net} and E-P-R products, it seems reasonable to assert that the estimates of χ_ρ and χ_τ are robust to a factor of at least 2. This would likely be considered a conservative estimate by most, given the significant uncertainties, particularly in estimates of Q_{net}. While products based on satellite and *in-situ* observations tend to give the best agreement

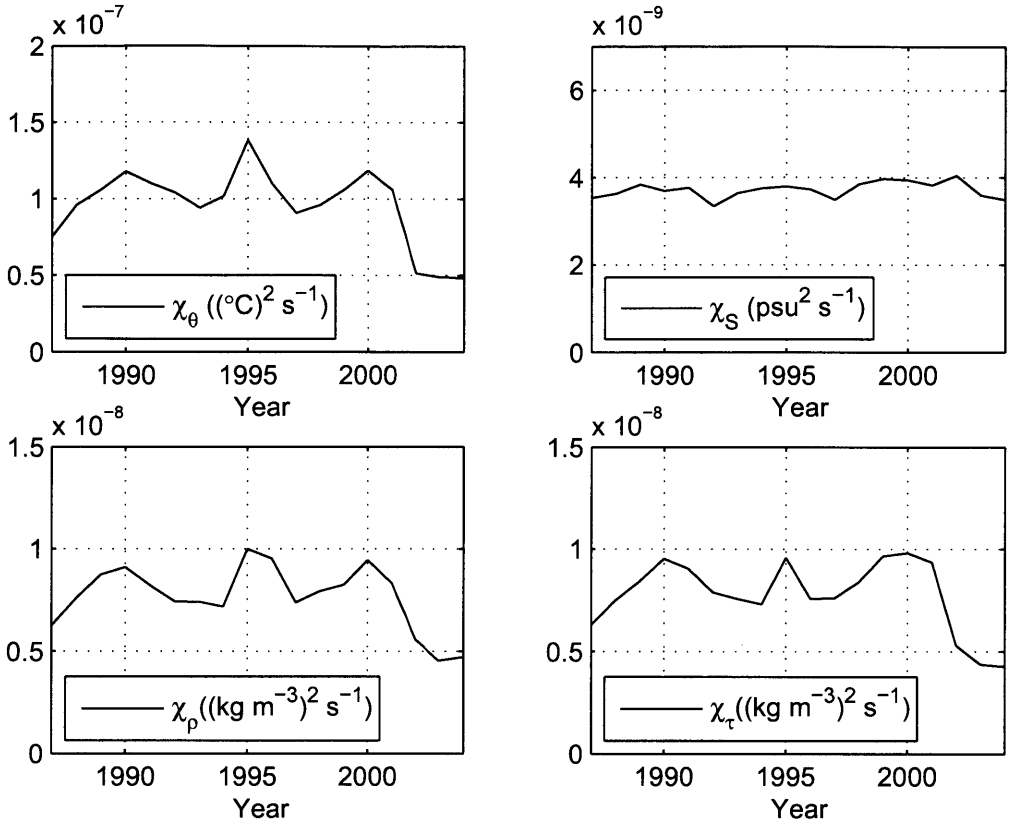

Figure 4-52: Changes in dissipation with time, based on the OAFlux Q_{net} product, the Schanze E-P-R estimate and EN3 v2a SST and SSS. The estimates were calculated for each month and averaged to produce yearly means. Thermal dissipation (χ_θ) is shown in the upper right panel, salinity dissipation (χ_S) is shown in the upper left, density dissipation (χ_ρ) is shown in the lower left, and spice dissipation (χ_τ) is shown in the lower right. A negative change after 2002 is evident in all but the salinity variance estimate.

with buoy measurements (Yu et al., 2008), they are also systematically biased by approximately 20–30 $\mathrm{W\,m^{-2}}$. From the results in this chapter, I conclude that the estimated error in these estimates is neither 10 % nor 10-fold, but likely less than 2-fold. It is thus possible to draw conclusions about the basic partition between diapycnal and isopycnal dissipation of density and spice.

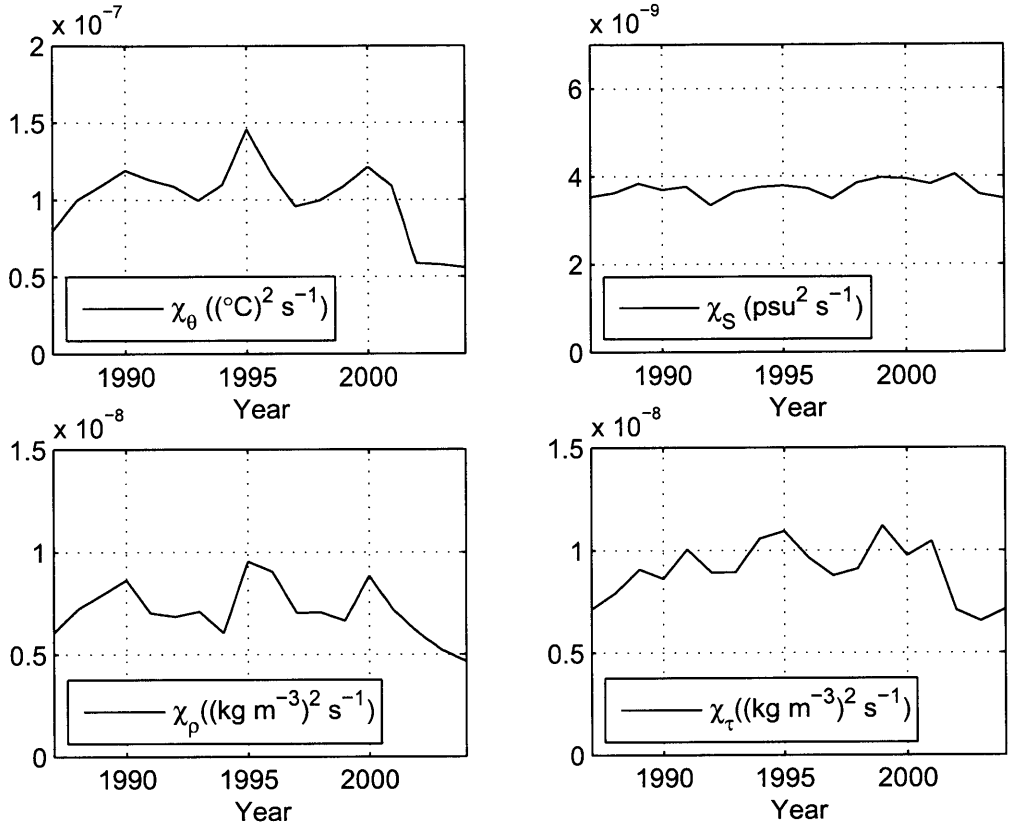

Figure 4-53: Changes in dissipation with time, based on the OAFlux Q_{net} product, the Schanze E-P-R estimate and EN3 v2a SST and SSS, and balancing the estimates for each year between 1987–2004 rather than using a time-mean balancing factor. The estimates were calculated for each month and averaged to produce yearly means. Thermal dissipation (χ_θ) is shown in the upper right panel, salinity dissipation (χ_S) is shown in the upper left, density dissipation (χ_ρ) is shown in the lower left, and spice dissipation ($\chi_\tau$is shown in the lower right. A negative change after 2002 is evident in all but the salinity variance estimate.

4.9 A Simple Diffusivity Relationship

The estimates of χ_θ, χ_S, χ_ρ and χ_τ presented in Sections 4.2 – 4.5 can be translated into horizontal and vertical diffusivities using some assumptions. For all calculations so far, I have assumed a vertical scale height of H=600 m, identical to the choice in Joyce (1980). Using the EN3 v2a product and the TEOS-10 equation of state (McDougall, 2011), I can calculate vertical gradients of potential temperature, absolute salinity and potential density in the upper 600 m and use them to estimate mean

vertical diffusivities in the ocean.

$$\kappa_Z(\theta) \approx \frac{\chi_\theta}{\left(\frac{\partial\theta}{\partial z}\right)^2} \tag{4.18}$$

$$\kappa_Z(S) \approx \frac{\chi_S}{\left(\frac{\partial S}{\partial z}\right)^2} \tag{4.19}$$

$$\kappa_Z(\rho) \approx \frac{\chi_\rho}{\left(\frac{\partial\rho}{\partial z}\right)^2} \tag{4.20}$$

Substituting the values of χ_θ, χ_S, χ_ρ as derived from OAFlux v3 Q_{net} and Schanze et al. (2010) E-P-R, and the gradients as described above into Eqs. (4.18), (4.19) and (4.20), respectively, the following values are obtained:

$$\kappa_Z(\theta) \approx \frac{6 \times 10^{-8}\,^\circ\mathrm{C}^2\,\mathrm{s}^{-1}}{9.7 \times 10^{-4}\,^\circ\mathrm{C}^2\,\mathrm{m}^{-2}} \approx 6.2 \times 10^{-5}\,\mathrm{m}^2\,\mathrm{s}^{-1} \tag{4.21}$$

$$\kappa_Z(S) \approx \frac{3.4 \times 10^{-9}\,\mathrm{psu}^2\,\mathrm{s}^{-1}}{7.4 \times 10^{-5}\,\mathrm{psu}^2\,\mathrm{m}^{-2}} \approx 4.6 \times 10^{-5}\,\mathrm{m}^2\,\mathrm{s}^{-1} \tag{4.22}$$

$$\kappa_Z(\rho) \approx \frac{5.7 \times 10^{-9}\,(\mathrm{kg/m^3})^2/\mathrm{s}}{1.1 \times 10^{-4}\,(\mathrm{kg/m^3})^2/\mathrm{m}^2} \approx 5.3 \times 10^{-5}\,\mathrm{m}^2\,\mathrm{s}^{-1} \tag{4.23}$$

These values are comparable to a factor of approximately 2 and agree relatively well with independent estimates of κ_z based on diffusion experiments or microstructure profiler data (e.g. Polzin et al., 1997; Nash and Moum, 1999; Wunsch and Ferrari, 2004; Thorpe, 2005, and references therein). While the value of κ_Z estimated here is slightly larger than values reported in these studies for the main thermocline, this estimate includes large areas of relatively low stratification (such as the Southern Ocean), which are likely regions of higher vertical diffusivities.

The typical variation of τ in the horizontal direction is on the order of $\approx 2\,\mathrm{kg\,m^{-3}}$ over L=1000 km as determined by the spice equation by Huang (2011) the EN3 v2a product (Ingleby and Huddleston, 2007) and representative spice gradients in the Atlantic, the Pacific and the Arctic ocean. The relationship between κ_H and χ_τ may thus be written as:

$$\kappa_H(\tau) \approx \frac{\chi_\tau}{\left(\frac{\partial\tau}{\partial L}\right)^2} \tag{4.24}$$

which, using the assumptions stated above, evaluates to:

$$\kappa_H(\tau) \approx \frac{6.9 \times 10^{-9}\,(\mathrm{kg/m^3})^2/\mathrm{s}}{4 \times 10^{-12}\,(\mathrm{kg/m^3})^2/\mathrm{m^2}} \approx 1.7 \times 10^3\,\mathrm{m^2\,s^{-1}} \tag{4.25}$$

This compares well with estimates by Ledwell et al. (1998), which were obtained from a tracer mixing experiment in the pycnocline. While the assumptions inherent in the calculation of these values preclude their use as 'real' estimates, it is useful to consider the relationship between diffusivities, gradients and dissipation rates in interpreting the estimates of χ_θ, χ_S, χ_ρ and χ_τ presented in this thesis. More information about the ocean interior (such as from microstructure profiler data) would be needed to calculate horizontal and vertical diffusivities in the ocean.

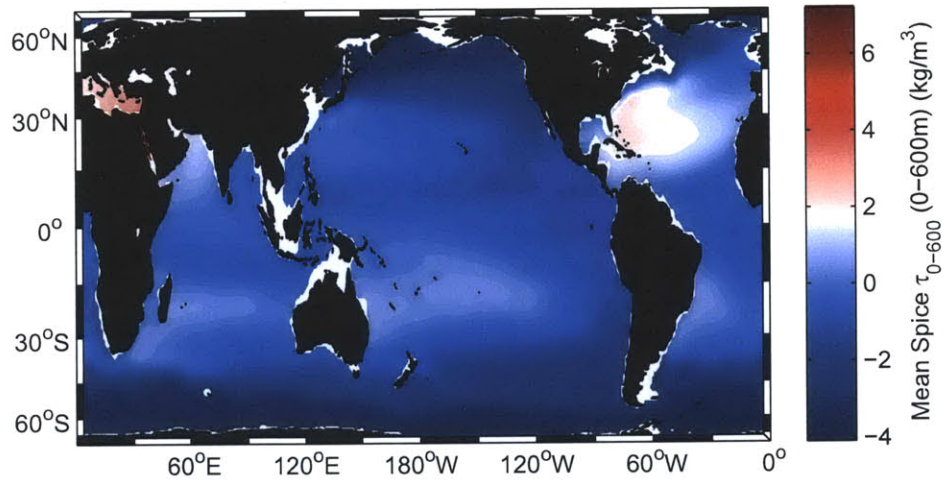

Figure 4-54: Mean spice in the top 600 m of the ocean as calculated from EN3 v2a fields. While the gradients are reduced compared to sea surface spice, the meridional and zonal gradients are still significant.

By assuming uniform spice dissipation in the upper ocean, it is possible to generate a map of horizontal diffusivities. For this purpose, I calculate the mean value of spice in the upper 600 m of the ocean. This is shown in Figure 4-54. Compared to the map of sea surface spice shown in Figure 3-14, the gradients are reduced but still significant in both the zonal and meridional direction. From this, I compute the magnitude of the horizontal gradient $|\frac{\partial \tau}{\partial L}|$ as follows:

$$|\frac{\partial \tau}{\partial L}| = \sqrt{\left(\frac{\partial \tau}{\partial x}\right)^2 + \left(\frac{\partial \tau}{\partial y}\right)^2} \tag{4.26}$$

Using Eq. (4.26) and Eq. (4.24), the implied diffusivity is then computed for each grid point:

$$\kappa_H(\tau) = \frac{\chi_\tau}{\left(\sqrt{\left(\frac{\partial \tau}{\partial x}\right)^2 + \left(\frac{\partial \tau}{\partial y}\right)^2}\right)^2} \tag{4.27}$$

The global result from the evaluation of Eq. (4.27) is mapped in Figure 4-55. Sin e is cho

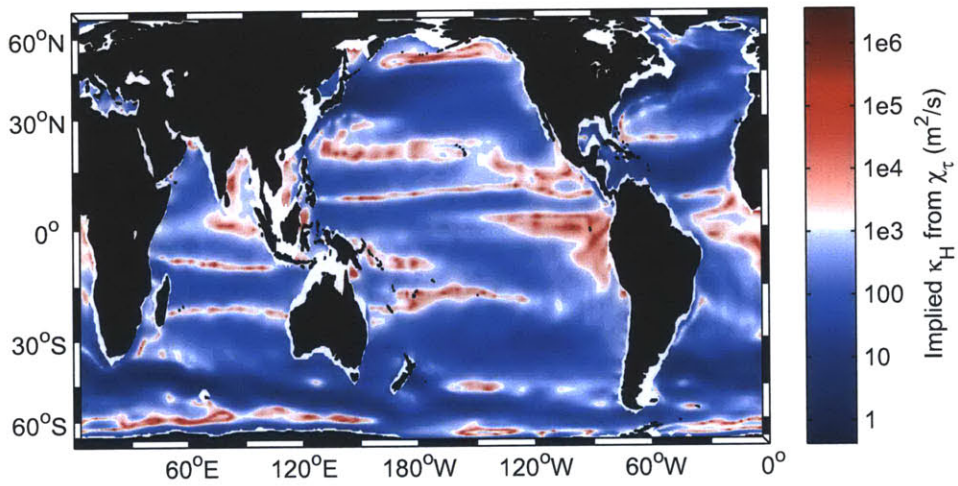

Figure 4-55: Map of implied horizontal diffusivities assuming a uniform spice dissipation of χ_τ=6.9 $\times$ 10^{-9} $(kg/m^3)^2/s$. Since the dissipation is assumed to be uniform, diffusivities must be greatest in regions of low gradients.

This map implies very large diffusivities near the equator as well as parts of the subtropical gyres, the North Pacific and the high-latitude Southern Ocean. While this is clearly not a realistic map of diffusivities, particularly in areas of very low or near-zero gradients, it may prove useful as a starting point for a more sophisticated analysis that may include estimates of local horizontal diffusivities from microstructure measurements or tracer mixing experiments.

Chapter 5

Nonlinearities and Cabbeling

The apparent density flux when using the full equation of state was pointed out in Chapter 2 and will be addressed in more detail in this chapter to illustrate some of the effects of nonlinearity. Consider an ocean with a steady state heat- and freshwater-budget: There is an apparent negative density flux due to the nonlinearity of the equation of state, which would imply that the ocean should expand with zero net forcing at the surface. That is, the ocean is generally heated in low latitudes where surface temperatures (and thermal expansion coefficients) are high, and cooled in high latitudes where surface temperatures (and expansion coefficients) are low, as was shown in Chapter 3 and was evident in density and spice flux budgets in Chapter 4. The apparent thermal density flux is negative (meaning that there is a positive buoyancy flux) even though the global heat budget is be balanced. How can this be? This question was posed by Eric B. Kraus during the 19th International Liège Colloquium on Ocean Hydrodynamics in 1987, and answered by Chris Garrett and Trevor McDougall, who were in the audience. A detailed answer was given a few years thereafter by McDougall and Garrett (1992):

> *"Does the ocean continually expand as a result [of the non-zero density flux]? No. Rather, "densification upon mixing" in the interior of the ocean can ensure that its average density does not change. "*

Further elaborations were given by Davis (1994) Zahariev and Garrett (1997), particularly in regards to the apparent non-zero density flux due to the seasonal cycle.

While both temperature and salinity contribute to cabbeling, the nonlinear contraction due to mixing of salinity is at least one order of magnitude smaller than thermal contraction (McDougall and Garrett, 1992). To first order, one may thus approximate the divergence equation (McDougall and Garrett, 1992, Eq. 23) as:

$$\boldsymbol{\nabla} \cdot \overline{\mathbf{u}} \approx -\frac{1}{2}\frac{\partial \alpha}{\partial \theta}\chi_\theta \tag{5.1}$$

where $\boldsymbol{\nabla} \cdot \overline{\mathbf{u}}$ is the divergence of the velocity field, θ is potential temperature, α is the thermal expansion coefficient $\alpha = -\frac{1}{\rho}\frac{\partial \rho}{\partial \theta}|_{S,p}$, χ_θ is the dissipation rate of the thermal variance and ρ is potential density. Overbars in all equations denote temporal averages and primes denote fluctuating components, so that $\mathbf{u} = \bar{\mathbf{u}} + \mathbf{u}'$. For typical values of $\frac{\partial \alpha}{\partial \theta}$ and the thermal dissipation rate χ_θ, McDougall and Garrett (1992) estimated the right-hand-side term of Eq. (5.1) to be on the order of $10^{-13}\,\mathrm{s}^{-1}$. While this makes it negligible for many practical applications of measuring or modeling the ocean interior, it still has potential important consequences (McDougall and Garrett, 1992; Davis, 1994), particularly for water mass transformations (Iudicone et al., 2008) and advection and diffusion (Klocker and McDougall, 2010). Some further consequences are also highlighted in Chapter 6.

The conundrum posed by Professor Kraus is readily answered by the global integral of Eq. (5.1): The apparent expansion induced by the negative density flux (and hence buoyancy input) at the surface is compensated by the contraction from the destruction of thermal variance (mixing) in the interior of the ocean. The positive relation between surface heat fluxes and the thermal expansion coefficient generates a net expansion that is compensated by contraction associated with the interior mixing (Eq. (5.1)). In this chapter, I evaluate the magnitude of the global net density flux imbalance and its implications for ocean cabbeling. I also relate these results to estimates of the global thermal dissipation rate, which were derived in Chapter 4.

The mean density equation at the surface and in steady state (meaning that $\frac{\partial \bar{\rho}}{\partial t} = 0$ and $\bar{\mathbf{u}} \cdot \boldsymbol{\nabla}\bar{\rho} = 0$) may, to a first order approximation, be adapted from McDougall and Garrett (1992, Eqs. 23 and 29) to be written as:

$$\iiint_V \boldsymbol{\nabla} \cdot \overline{[\mathbf{u}'\rho']} dA = -\bar{\rho} \iiint_V \boldsymbol{\nabla} \cdot \bar{\mathbf{u}} dV = \tfrac{1}{2}\bar{\rho} \iiint_V \left(\frac{\partial \alpha}{\partial \theta}\chi_\theta + \frac{\partial \beta}{\partial S}\chi_S \right) dV \tag{5.2}$$

where β is the haline coefficient of seawater $\beta = \frac{1}{\rho}\frac{\partial \rho}{\partial S}|_{\theta,p}$, S is sea surface salinity, and χ_S is the dissipation rate of salinity variance, which is analogous to χ_θ for temperature. Both dissipation rates have been derived in Chapter 4. Since the variation of β with S is small, only the thermal component will be considered here. Using Gauss's divergence theorem, the first-order estimate of thermal component of the density flux may then be written as:

$$\oiint_A \overline{[c_p^{-1}\alpha Q_{net}]} dA = -\bar{\rho} \iiint_V \nabla \cdot \bar{\mathbf{u}} dV = \tfrac{1}{2}\bar{\rho} \iiint_V \frac{\partial \alpha}{\partial \theta} \chi_\theta dV \tag{5.3}$$

where c_p denotes the specific heat capacity of water, which is taken as constant for thermodynamic consistency, and Q_{net} is the net radiative budget at the surface, defined as the sum of shortwave radiation (Q_{SW}), longwave radiation (Q_{LW}), sensible heat flux (Q_{SH}), and latent heat flux (Q_{LH}). This equation shows how the global areal integral of surface density flux is balanced by the volume integral of the contraction due to mixing.

With the estimates of surface ocean fluxes presented in Chapter 3, it is possible to estimate the total rate of the density flux (and thus the buoyancy flux, which is proportional but opposite to the density flux) into the global ocean. From such flux fields, the cabbeling rate in the interior can be calculated if a steady state is assumed. The surface density flux F_ρ was defined in Chapter 4, Eq. (4.1) as:

$$F_\rho = F_{\rho S} - F_{\rho\theta} = \rho_0 (\frac{1}{\rho_F}\beta F_S - \frac{1}{c_p \rho_0}\alpha F_\theta) \tag{5.4}$$

where E is the evaporation rate, P is the precipitation rate, and R is the riverine freshwater flux, as in previous Chapters. Since this equation is valid only at the ocean surface, changes in pressure and the resulting pressure term are negligible and thus ignored here. It is clear from Eq. (5.4) that left-hand-side term in Eq. (5.3) is just the thermal component of the density flux, $F_{\rho T}$.

The nonlinearities in this equation stem from the changes of α, β, where the change of α with θ is at least one order of magnitude greater than the salinity term (McDougall and Garrett, 1992). To illustrate this effect, I have plotted the relationship of α as well as its first derivative with respect to potential temperature against potential temperature in Figure 5-1. The zonal distribution of sea surface temperature (SST), α, Q_{net} and $F_{\rho T}$ are shown in Figure 5-2. The global distribution of density flux into the ocean is shown in Figure 5-3. The most obvious areas of den-

sification are the western boundary currents, particularly the Gulf Stream and the Kuroshio Current. In these currents, warm water is advected polewards, which leads to evaporation and sensible heat loss. As a result of this, the surface water is cooled, leading to densification.

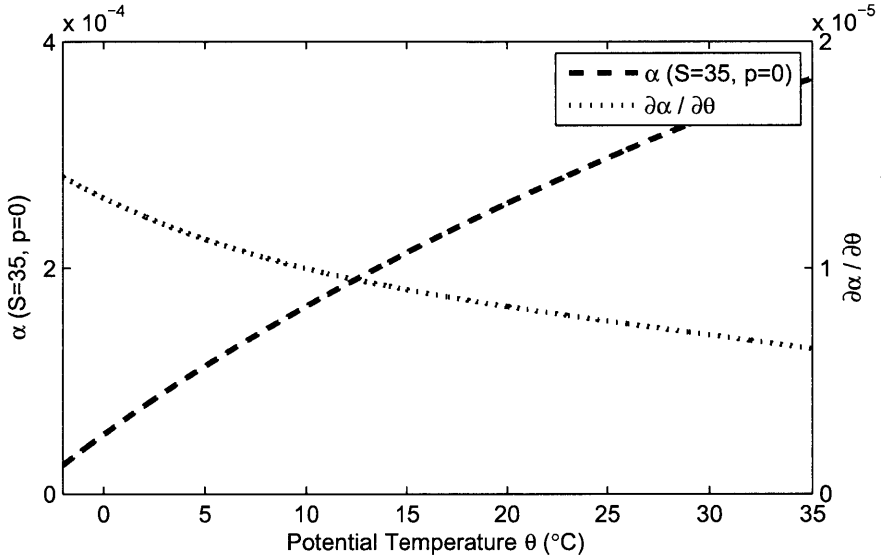

Figure 5-1: Relationship between the thermal expansion coefficient α (at $S = 35$ and $p = 0$) and potential temperature (θ), as well as the first derivative $\frac{\partial \alpha}{\partial \theta}$. It is evident that α increases significantly with increasing temperature, but the greatest changes in α occur at low temperatures.

The nonlinearities in this equation stem from the changes of α, β, where the change of α with θ is at least one order of magnitude greater than the salinity term (McDougall and Garrett, 1992). To illustrate this effect, I have plotted the relationship of α as well as its first derivative with respect to potential temperature against potential temperature in Figure 5-1. The zonal distribution of sea surface temperature (SST), α, Q_{net} and $F_{\rho T}$ are shown in Figure 5-2. The global distribution of density flux into the ocean is shown in Figure 5-3. The most obvious areas of densification are the western boundary currents, particularly the Gulf Stream and the Kuroshio Current. In these currents, warm water is advected polewards, which leads to evaporation and sensible heat loss. As a result of this, the surface water is cooled, leading to densification.

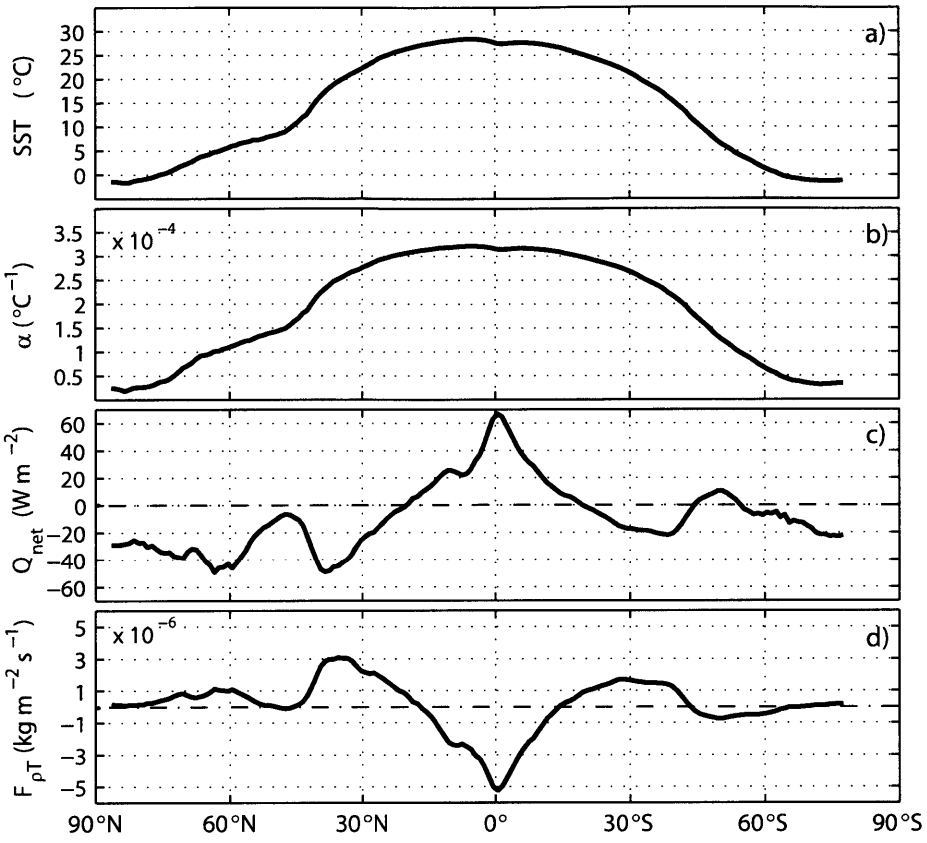

Figure 5-2: Zonal means of: a) Sea surface temperature (SST) (°C), b) The thermal coefficient α (°C^{-1}), c) Net oceanic heat flux Q_{net} into the ocean (W m^{-2}), and d) The resulting thermal component of the density flux $F_{\rho T}$ into the ocean (kg m^{-2} s^{-1}). α is largely a function of SST and thus, like SST, decreases with increasing latitude.

5.1 Global Cabbeling Rates

With the estimates presented in Chapter 3, it is possible to evaluate the global area integral of density forcing, to estimate the effects of the seasonal cycle and to estimate which areas of the ocean have the highest contraction potential due to cabbeling effects.

When Eq. (5.4) is integrated over the global ocean, a nonzero result emerges as noted by McDougall and Garrett (1992) and Zahariev and Garrett (1997), thus seemingly contradicting the density equation (Eq. (2.3)) in Chapter 2:

$$\iint_A F_\rho dA \neq 0 \tag{5.5}$$

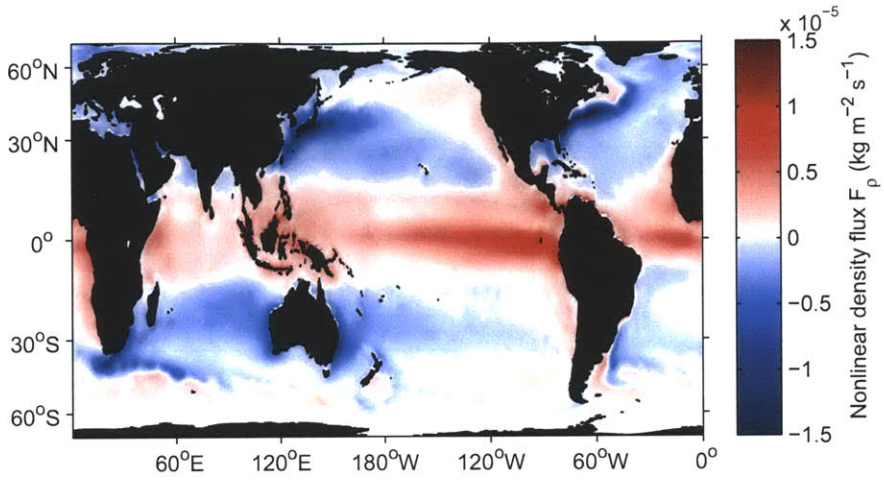

Figure 5-3: Net density flux distribution in the global ice-free ocean. All western boundary currents are areas of densification (due to cooling of relatively warm water that is advected polewards) while the polar regions and the tropics are areas of net buoyancy input due to freshening and warming of the surface waters, respectively. The area integral of this map, using temporal averages between 1987–2004 of all fields, is nonzero with a net buoyancy flux into the ocean of $-7.6 \times 10^7\,\mathrm{kg\,s^{-1}}$. This buoyancy input is equivalent to a volume flux of $74\,000\,\mathrm{m^3\,s^{-1}}$

Upon evaluation of Eq. (5.5), using the balanced OAFlux data set described in Chapter 3, I find a global imbalance of $7.6 \times 10^7\,\mathrm{kg\,s^{-1}}$, which translates to an equivalent volume flux of $74\,000\,\mathrm{m^3\,s^{-1}}$ or 0.07 Sv, which is equivalent to a global sea level rise of $6.3\,\mathrm{mm\,yr^{-1}}$ or approximately 450 % of the average discharge of the Mississippi river. This compares to observations between 1972 and 2008, in which a sea-level rise of approximately $(2.1 \pm 1.0)\,\mathrm{mm\,yr^{-1}}$ was observed from tide gauges and satellite altimetry (Church et al., 2011). The spatial distribution of density flux (F_ρ) is shown in Figure 5-3 and the zonal averages for each degree of latitude are shown in Figure 5-2.

All western boundary currents show a clear density input, which is caused by cooling (and hence densification) of relatively warm water that is advected poleward. This is also evident in the zonal averages of the heat flux into the ocean as shown in Figure 5-2.

To illustrate the relationship between the surface forcing and the dissipation in the

interior, I chose to focus on the leading terms and consequently ignore the effects of salinity and β. As Joyce (1980) has shown, the interior dissipation of thermal variance is equal to the surface integral of the product of heat flux and temperature, with an estimate of χ_θ of $1 \times 10^{-7}\,°C^2\,s^{-1}$. Upon repeating these calculations in Chapter 4, this estimate is in the range of results obtained from 9 different Q_{net} products, albeit as one of the higher estimates.

These separate estimates of buoyancy production and dissipation rates can be used as rough checks on one another. That is, I find that a volume weighted average value of $\frac{\partial\alpha}{\partial\theta}|_{S,p}$ of $9.8 \times 10^{-6}\,°C^{-2}$, as computed with the Gibbs Seawater (GSW) Oceanographic Toolbox (McDougall, 2011), which uses the TEOS-10 equation of state (IOC et al., 2011). This would correspond to a volume weighted potential temperature of 3.15 °C. I then compare this to the buoyancy input (in a steady-state ocean) of $\nabla\cdot\bar{\mathbf{u}} = 5.6 \times 10^{-14}\,s^{-1}$ or $7.6 \times 10^{-14}\,s^{-1}$ when seasonal effects are included, equivalent to a theoretical sea level rise of $6.3\,mm\,yr^{-1}$ or $8.6\,mm\,yr^{-1}$, respectively.

When scaling χ_θ to the mean depth of the ocean instead of a scale height of H =600 m as was done in Chapter 4 in order to compare it to other estimates using this scale height, I obtain a value of $\chi_{\theta full} = 1.3 \times 10^{-8}\,°C^2\,s^{-1}$. When these values are plugged into the right-hand side of Eq. (5.1), $\nabla\cdot\overline{\mathbf{u}}$ is found to be approximately $-6.4 \times 10^{-14}\,s^{-1}$. This value would be equivalent to a sea level change of $-7.2\,mm\,yr^{-1}$, which is comparable (and, as expected, opposite in sign) to the value obtained from the density input rates. Since this calculation assumes a spatially uniform dissipation of thermal variance, which may cause a high bias in this result since $\frac{\partial\alpha}{\partial\theta}|_{S,p}$ would be lower in the upper ocean where most of the dissipation occurs, I repeat this calculation, assuming that the dissipation rate is proportional to the temperature gradient $\overline{\theta}_z$ or the square of the temperature gradient $(\overline{\theta}_z)^2$. This results in $\frac{\partial\alpha}{\partial\theta}|_{S,p}$ to be $9.4 \times 10^{-6}\,°C^{-2}$ and $8.6 \times 10^{-6}\,°C^{-2}$, respectively, changing $\nabla\cdot\overline{\mathbf{u}}$ to $-6.1 \times 10^{-14}\,s^{-1}$ and $-5.6 \times 10^{-14}\,s^{-1}$, respectively. Given the uncertainties in the underlying products, these values closely match the inferred cabbeling from the density flux estimates.

Of course, the actual distribution of χ_θ as a function of temperature would have to be estimated to determine the distribution of cabbeling induced contraction in the ocean. In Section 5.4 of this chapter, I estimate where simple vertical mixing would cause the greatest contraction on mixing.

5.2 Effects of the Seasonal Cycle

So far, all calculations were performed using time-means of all parameters. There is, however, another effect that was pointed out by Zahariev and Garrett (1997): since the peak of the heat-flux roughly coincides with the seasonal temperature peak (and vice-versa), a positive buoyancy flux is introduced. The inclusion of the seasonal cycle increases the global surface buoyancy forcing by 35 % compared to the time-mean case to 101 000 $m^3\,s^{-1}$, which is equivalent to a sea level rise of 8.6 mm yr^{-1} or 600 % of the Mississippi river mean discharge. This is illustrated in Figure 5-4, in which the zonal average of the thermal component of the buoyancy flux is shown using the time-mean and using monthly data to include the effects of the seasonal cycle. There is little difference in the tropics since seasonality is suppressed, and only small differences in mid-latitude. However, the seasonal contribution is significant to the global sum.

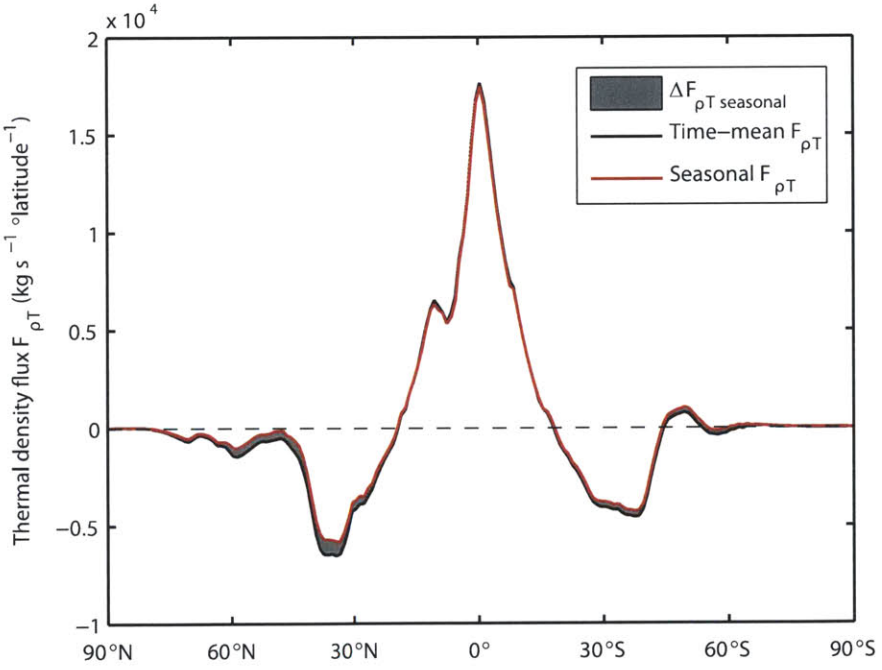

Figure 5-4: Comparison of $F_{\rho T}$ with and without seasonal effects. Seasonal effects add a further nonlinearity which increases the global area integral of buoyancy forcing by 35 %. The greatest increases can be seen between 20° and 60° due to the strong seasonal cycle in that latitude band.

It is likely that only a fraction of the seasonal input is mixed below the seasonal

thermocline and dissipated there, with most of thermal variance being destroyed by seasonal mixing in the upper ocean through entrainment of deeper water. This was shown by Zahariev and Garrett (1997). Similarly, there are also non-zero effects due to the diurnal cycle which causes the top few meters of the ocean to heat and cool. However, this is of a much smaller magnitude, since diurnal variations of SST are considerably less than seasonal ones. This is also likely dissipated within the depth of the diurnal thermocline by entrainment of deeper water and is unlikely to have any significant effect on the ocean interior.

5.3 Product Inter-Comparison

To assess the robustness of these estimates, they are repeated with the products outlined in Chapter 3 that were used in the inter-comparison of dissipation estimates in Chapter 4.

The products used are the Modern Era Retrospective-analysis for Research and Applications (MERRA) re-analysis (Bosilovich et al., 2006), which provides E, P and Q_{net}, the adjusted Common Ocean Reference Experiment v. 2 (CORE.2) re-analysis (Large and Yeager, 2009; NCAR, 2010) (E and P), the ERA-Interim re-analysis by the European Centre for Medium-Range Weather Forecasts (E,P and Q_{net}), the National Oceanography Centre Southampton Flux Dataset v2.0 (NOCS v2) (Berry and Kent, 2009) (Q_{net}), the ECCO2 ocean state estimate (Menemenlis et al., 2008) (E-P-R, Q_{net}), the Japanese ocean flux data sets with use of remote sensing observations (J-OFURO) (Kubota et al., 2002) (Q_{net}) as well as two experimental versions of OAFlux with different short-wave and long-wave (Q_{SW} and Q_{LW}) products (CERES and SRB instead of ISCCP, which is used in the currently published version) (Lisan L. Yu, *pers. comm.*). The evaluated time period of the datasets is 1987–2004, except for ECCO2, which starts in 1990 and J-OFURO2, which starts in 1988. A more detailed description of these products is given in Chapter 3.

The results of evaluating the time-mean of all products to produce buoyancy flux estimates are shown in Table 5.1, while the density flux estimates including seasonal effects are tabulated in Table 5.2. While most datasets agree with each other to within approximately 50 %, the MERRA Q_{net} product suggests more than double the density flux than the mean of the products; this is likely due to extreme heat fluxes at high latitudes. The lowest estimates are produced by the ERA-Interim and ECCO2

Q_{net} estimates. As may be expected from theory, the choice of the E-P-R dataset influences most results by less than 5 % in the time-mean case and approximately 10 % when the seasonal cycle is included.

Table 5.1: Comparison of density flux in equivalent sea level rise ($\mathrm{mm\,yr^{-1}}$) for different time-means of Q_{net} and E-P-R products

Q_{net} \ E-P-R	Schanze	MERRA	ECCO2	CORE2	NCEP2	HOAPS
OAFlux+ISCCP	7.3	7.3	7.0	7.3	7.3	7.0
OAFlux+CERES	6.8	6.7	6.7	6.7	6.7	6.6
OAFlux+SRB	9.6	9.6	9.6	9.6	9.6	9.5
ERA-Interim	4.3	4.2	4.5	4.2	4.2	4.5
MERRA	13	13	13	13	13	13
ECCO2	5.0	4.9	5.0	5.0	4.9	4.9
NOCS v.2	7.5	7.4	8.1	7.5	7.4	8.0
J-OFURO2	11	10	11	10	10	10

The results of evaluating the time-mean of all products to produce negative density flux estimates are shown in Table 5.1, while the negative density flux estimates including seasonal effects are tabulated in Table 5.2. While most products agree with each other to within less than a factor of 2, the MERRA Q_{net} product suggests more than twice the magnitude of negative density flux than the mean of the products; this is likely due to extreme heat fluxes at high latitudes. The lowest estimates are produced by the ERA-Interim and ECCO2 Q_{net} estimates. As may be expected from theory, the choice of the E-P-R product influences most results by less than 5 % in the time-mean case and approximately 10 % when the seasonal cycle is included.

5.4 Cabbeling due to Vertical Mixing

This estimate of the cabbeling rate poses the further question: If the ocean were entirely mixed through stirring, causing uniform conservative temperature (Θ) and salinity, what would the resulting drop in sea level be?

This question was addressed by Gille (2004), who found a potential sea level height decrease of 165 mm upon complete (stirring) homogenization of the upper 3000 m of the ocean. I repeat the Gille (2004) experiment with the EN3 dataset to

Table 5.2: Comparison of density flux in equivalent sea level rise ($\mathrm{mm\,yr^{-1}}$) for different of Q_{net} and E-P-R products, using monthly means for seasonal effects

Q_{net} \ E-P-R	Schanze	MERRA	ECCO2	CORE2	NCEP2	HOAPS
OAFlux+ISCCP	11	11	10	11	11	10
OAFlux+CERES	9.7	9.6	9.6	9.6	9.6	9.6
OAFlux+SRB	13	13	13	13	13	13
ERA-Interim	7.1	7.0	7.4	7.1	7.0	7.3
MERRA	15	15	16	15	15	16
ECCO2	7.5	7.4	7.5	7.5	7.4	7.4
NOCS v.2	10	10	11	10	10	11
J-OFURO2	14	14	14	14	14	14

the full available depth to illustrate the potential contraction of the water column due to vertical mixing at each point in the ocean. For the purpose of computing density (and hence density changes) at each time step, I use the TEOS-10 equation of state (IOC et al., 2011) as implemented in the GSW toolbox (McDougall, 2011) and use conservative temperature as the tracer instead of potential temperature to avoid issues of enthalpy that were pointed out by McDougall (2003). I thus allow the vertical profile at each 1° latitude and longitude to diffuse according to Eq. (5.6) with a mixing coefficient of $\kappa_z = 1 \times 10^{-4}\,\mathrm{m^2\,s^{-1}}$ over a period of 10 000 years, motivated by Davis (1994) and Gille (2004), which is virtually an end-state of turbulent mixing.

$$\frac{\partial \Theta}{\partial t} = \kappa_z \frac{\partial^2 \Theta}{\partial z^2} \tag{5.6}$$

This equation is integrated numerically and the result is shown in Figure 5-5. The greatest cabbeling potential is found in the subtropical gyres, particularly in the Pacific and Indian Oceans, but also in the North Atlantic. From this it is evident that the contraction potential is predominantly a function of the main thermocline temperature gradient and depth as well as the total ocean depth at each grid point. By calculating the area-weighted average of the vertical cabbeling contraction potential, I estimate the global sea-level drop that would result from vertical mixing as 230 mm.

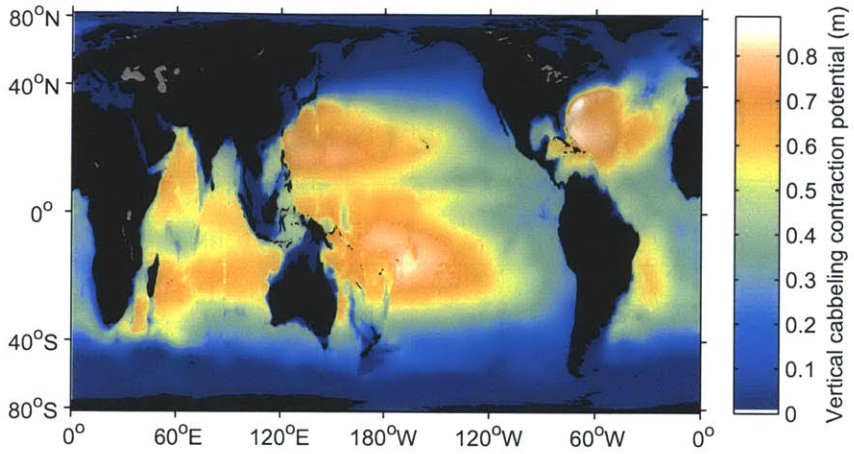

Figure 5-5: Sea level change due to complete vertical mixing after 10 000 years with a mixing coefficient of $\kappa_z = 10^{-4}\,\mathrm{m^2\,s^{-1}}$. The global mean sea-level change that would result from this is 230 mm.

5.5 Total Cabbeling Potential in the Ocean

While I find that the global mean sea level would decrease by 230 mm solely by vertical mixing as outlined in the previous section, the elimination of horizontal temperature- and salinity gradients would result in even more cabbeling. I thus homogenize all available cells of the EN3 dataset to an end state caused by turbulent mixing using the GSW toolbox (McDougall, 2011) as before. Turbulent mixing would lead to a homogenization of conservative temperature rather than *in-situ* temperature, and thus the end-state is one of uniform salinity and conservative temperature. While one may speculate about a molecular-diffusive end state, this is not considered here, as it would take millions of years of no turbulent mixing to achieve this, making this a purely fictional exercise. Further, it should be noted that the final equilibrium state of a quiet ocean would actually have a strong increase in salinity with depth as it reached diffusive balance with the gravitational field due to the baro-diffusion effect (Levenspiel and de Nevers, 1974; IOC et al., 2011). This would only happen on geological timescales (and in the absence of turbulent mixing) and is not considered as a plausible end state.

All computations are performed using the TEOS-10 equations to full precision

using the GSW toolbox (McDougall, 2011). The total cabbeling potential after full horizontal and vertical homogenization to uniform salinity and conservative temperature would cause the sea level to decrease by 300 mm. This shows that while vertical mixing in the ocean is the dominant contributor, a significant fraction ($\approx\frac{1}{4}$) of the global ocean cabbeling potential can be attributed to horizontal mixing.

Chapter 6

Discussion and Conclusions

The aim of this thesis was to estimate the relative importance of isopycnal to diapycnal mixing. While the assessment of the relative importance ultimately comes down to comparing two numbers, there were a number of obstacles to overcome in producing these estimates. The first was both a lack and a surplus of datasets: While there are many data products available to quantify the global freshwater cycle, heat fluxes and sea surface properties, it is challenging to discern their relative strengths and weaknesses and to identify a suitable time-period in which a homogeneous record is present. This task was undertaken for both the freshwater cycle and the global heat budget, and based on this analysis, a 'best estimate' was published (Schanze et al., 2010). The results of this are presented in Chapter 3 of this thesis. The basic derivation of the power integrals presented in Chapter 2 is relatively straightforward until the non-linearities in the equation of state of seawater have to be addressed. For this reason, the derivation of the isopycnal and diapycnal components was done using a linear equation of state, and some of the effects of the nonlinearities are addressed in Chapter 5. The global fluxes, variance production estimates, and dissipation estimates are then presented in Chapter 4.

6.1 Estimates of Ocean Fluxes

A new estimate of E-P-R based on state-of-the-art long-term E and P products as well as the most complete dataset for R has been assembled based on the OAFlux evaporation fields, the GPCP precipitation product and a combination of the Dai and Trenberth (2002) and Dai et al. (2009) riverine runoff for the seasonal cycle

and the inter-annual variability, respectively. These datasets were chosen out of a total of seven E datasets and seven P datasets, primarily based on a review of inter-comparisons with independent data but also based on homogeneity analyses and oceanic freshwater budget closure calculations.

Inhomogeneities were identified in all seven E and seven P datasets before 1987, attributable to the inclusion of SSM/I satellite data thereafter. A number of datasets are available long before this period, and I caution any user of such datasets to be wary of inhomogeneities caused by advent of satellites and avoid using data predating 1987 if possible. Based on these analyses, the period of 1987–2004 was identified as suitable for constructing a global climatology of E-P-R using OAFlux and GPCP. The selected datasets have been shown in inter-comparisons to outperform re-analysis estimates consistently. While OAFlux and GPCP are deemed to be amongst the state-of-the-art, it should be noted that they might not be ideally suited for every application. This estimate of E-P-R shows a significant improvement in both spatial and temporal detail from older, *in-situ*-only estimates by Baumgartner and Reichel (1975) and Schmitt et al. (1989), particularly in regions of boundary currents. The differences from modern estimates are less obvious, but still significant.

With the available time-period, the analysis of seasonal variations as well as limited insights into inter-annual variability of the global freshwater cycle become possible. This is shown by a clear presence of the El Niño Southern Oscillation, as revealed by an EOF analysis of the OAFlux/GPCP E-P estimate. The third leading EOF mode was found to be closely correlated to the Multivariate ENSO Index(MEI) and the associated loading pattern agreed well with the sea-surface temperature loading pattern that is used to produce the MEI.

Our findings support other studies (e.g. Dai and Trenberth, 2003; Talley, 2008) which found the Pacific to be less precipitative and the Atlantic to be less evaporative than previously thought (Wijffels et al., 1992). The Southern Ocean, however, is estimated to be more precipitative and the Indian Ocean more evaporative than in Wijffels et al. (1992).

The annual mean precipitation into the ocean averaged over 19 years (1987–2004) is estimated at $12.2 \pm 1.2\,\mathrm{Sv}$, the evaporative loss is estimated at $13.0 \pm 1.3\,\mathrm{Sv}$, and the total freshwater input from land is estimated at $1.25 \pm 0.1\,\mathrm{Sv}$. Since the global sea-level rise is only an insignificant departure from steady state, the net imbalance is found to be $0.5 \pm 1.8\,\mathrm{Sv}$. The system thus closes within the errors estimated for

each data set. The remaining imbalance, equivalent to 4% of oceanic evaporation, could be caused by either E or P alone or any combination of E, P and R. Evaporation might be biased low by a systematic under-sampling of small-scale and extreme events such as narrow boundary currents or extreme winds in hurricanes. With improved satellite measurements and continued *in-situ* sampling, it should be possible to further constrain the source of such errors in the future.

The analysis of 9 different Q_{net} oceanic heat flux estimates revealed an overwhelming picture of a strong positive imbalance in all conventional datasets. While the ECCO2 state estimate Menemenlis et al. (2008) is in near-balance, this is due to adjustments to the fluxes based on oceanic data. Since the objective is to estimate variance dissipation from surface fluxes, it is imperative that these estimates be independent and not based on an ocean model (in which case the density and spice variance dissipation may be diagnosed directly in the model). While some of the re-analyses provide reasonable homogeneity and global balance, the imbalances are still at least on the order of $10\,\mathrm{W\,m^{-2}}$ and *in-situ* comparisons with buoys Yu et al. (e.g. 2008, and references therein). Despite an imbalance of $29\,\mathrm{W\,m^{-2}}$, the choice for the 'baseline' Q_{net} dataset thus fell on OAFlux 3.0 (Yu et al., 2008). While it may seem crude to balance a heat flux by subtracting a constant, there are insufficient constraints to justify a more elaborate correction.

Since the error covariances between these estimates are not known, a formal error analysis of a combination of these products is virtually impossible. Instead of attempting this, I decided to instead produce all estimates using a number of datasets that are currently regarded as state-of-the-art. While this does not guarantee that the true value is bracketed by all available datasets, it gives a reasonable estimate of the discrepancies between datasets and how much they influence the estimates.

6.2 Global Power Integrals

The global power integrals (Stern, 1975) derived in Chapter 2 are based on work by Stern (1969, 1975); Joyce (1980) and Schneider and Bhatt (2000). By using a linearized equation of state, it was possible to show that surface density variance generation is related to diapycnal mixing while surface spice variance generation is related to isopycnal mixing. Furthermore, it was possible to show that the power integrals may be written in terms of the flux ratio γ and the density ratio R_ρ. In

this relation, it becomes clear that the variance dissipation equation may change sign (and become a variance production term). This is caused by double-diffusion or 'salt fingers' (Turner, 1979; Schmitt, 1979; Zhang and Schmitt, 2000) and an intensification of density gradients is routinely seen in laboratory experiments (Turner, 1979). While it may be the scope of another thesis to produce a three-dimensional estimate of R_ρ in the ocean, an estimate of γ at the sea surface made it possible to identify areas in which salt finger formation may lead to an additional variance generation in the interior.

6.3 Effects of Nonlinearities in the Ocean

The new estimates of surface buoyancy fluxes due to heat and moisture transport shown in Chapter 3 have allowed us to estimate the global integral of buoyancy forcing. Since the ocean is heated predominantly in warm areas with higher thermal expansion coefficient, and cooled in cold areas with low expansion coefficient, an addition of buoyancy (a net density loss due to expansion) is estimated. As McDougall and Garrett (1992) have suggested, this addition of buoyancy must be compensated by the interior densification on mixing due to the nonlinear equation of state (cabbeling). We show that the estimated cabbeling is consistent with expected dissipation rates for thermal variance as in Joyce (1980). We find that the mean buoyancy flux would contribute to a sea level rise of $6.3\,\mathrm{mm\,yr^{-1}}$ if uncompensated by mixing. The correspondence between surface temperature and heat flux in the seasonal cycle provides an additional 35 % of potential sea level rise (increasing it to $8.6\,\mathrm{mm\,yr^{-1}}$). These numbers correspond to volume fluxes that are 4.5 and 6 times larger than the average discharge of the Mississippi River, respectively. While the choice of the data product does influence this result significantly to within a factor of approximately 2, it is clear that significant mixing and therefore cabbeling is occurring in the ocean interior to absorb this apparent expansion of the ocean. We find that an independent estimate of the velocity divergence ($\boldsymbol{\nabla}\cdot\bar{\mathbf{u}}$) based on the dissipation of thermal variance provides a close match to our estimate of the time-mean cabbeling rate as inferred from the surface buoyancy forcing. The potential sea level change upon complete (diffusive) vertical mixing of the ocean is estimated as 230 mm. When horizontal mixing is included, the global ocean cabbeling potential is estimated for a turbulent mixing end-state as 300 mm. While this contraction will never occur in today's cli-

mate system, it demonstrates that changes in the stratification or mixing rate of the ocean may play a non-trivial role in global sea level change. Also, the question arises of whether variations in ocean mixing rates can contribute to the temporal variability observed in sea level records (Church et al., 2011).

6.4 The Relative Importance of Isopycnal and Diapycnal Mixing

While the estimate of thermal dissipation in the ocean was based on research by Joyce (1980), and salinity dissipation (albeit not in a surface integral) had been computed by Schneider and Bhatt (2000), the estimation of density and spice variance is novel to this thesis to my best knowledge. The original estimate of thermal variance dissipation χ_θ made by Joyce (1980) was $\chi_\rho = 1 \times 10^{-7}\,°\mathrm{C}^2\,\mathrm{s}^{-1}$. All estimates found using 9 different datasets of Q_{net} were lower or comparable to this original estimate, ranging from $3.4 \times 10^{-8}\,°\mathrm{C}^2\,\mathrm{s}^{-1}$ to $1 \times 10^{-7}\,°\mathrm{C}^2\,\mathrm{s}^{-1}$. When repeated in latitude bands instead of a 1×1 degree resolution, as was done by Joyce (1980), these estimates increase to $3.7 \times 10^{-8}\,°\mathrm{C}^2\,\mathrm{s}^{-1} - 1.1 \times 10^{-7}\,°\mathrm{C}^2\,\mathrm{s}^{-1}$, with 7 of 9 estimates greater than $0.6 \times 10^{-8}\,°\mathrm{C}^2\,\mathrm{s}^{-1}$.

The estimates of χ_S range from $2.3 \times 10^{-9}\,\mathrm{psu}^2\,\mathrm{s}^{-1} - 3.4 \times 10^{-9}\,\mathrm{psu}^2\,\mathrm{s}^{-1}$. Due to the different units and as these are the first such estimates, is difficult to compare these with past results. Nash and Moum (1999) used a salinity microstructure profiler and found values of approximately $7 \times 10^{-8}\,\mathrm{psu}^2\,\mathrm{s}^{-1}$ in a turbulent patch. While the value estimated by Nash and Moum (1999) is approximately 20 times more salinity variance dissipation than estimated here for the upper 600 m, this is nonetheless a conceivable number given that large areas of the ocean are less turbulent (Polzin et al., 1997).

The first estimates of χ_ρ from surface fluxes range from $3 \times 10^{-9}\,(\mathrm{kg/m^3})^2/\mathrm{s}$ to $8.2 \times 10^{-9}\,(\mathrm{kg/m^3})^2/\mathrm{s}$, while χ_τ ranges from values of $4.7 \times 10^{-9}\,(\mathrm{kg/m^3})^2/\mathrm{s}$ to $9 \times 10^{-9}\,(\mathrm{kg/m^3})^2/\mathrm{s}$. While the estimate for the spice variance production and implied dissipation is marginally higher, within the range of estimates this indicates an equipartition between spice and density variance dissipation. This also implies an equipartition between isopycnal and diapycnal mixing, albeit on very different gradients and thus length-scales. This equipartition may be an important constraint in

ocean models, in which horizontal and vertical mixing processes tend to be parameterized independently of each other.

Appendix A

Supplemental Tables

Table A.1: Comparison of estimated area integrals of $\overline{Q_{net}\theta}$ ($\mathrm{W\,^{\circ}C\,m^{-2}}$) for time-means of eight Q_{net} products

Q_{net} Product	$Q_{net}\theta$ ($\mathrm{W\,^{\circ}C\,m^{-2}}$)
OAFlux+ISCCP	100
OAFlux+CERES	94
OAFlux+SRB	130
ERA-Interim	58
MERRA	170
ECCO2	68
NOCS v.2	100
J-OFURO2	150

Table A.2: Comparison of estimated area integrals of $\overline{Q_{net}\theta}$ ($\mathrm{W\,^{\circ}C\,m^{-2}}$) using 10° latitude band averages as in Joyce (1980) with time-means of eight Q_{net} products

Q_{net} Dataset	$Q_{net}\theta$ ($\mathrm{W\,^{\circ}C\,m^{-2}}$)
OAFlux+ISCCP	130
OAFlux+CERES	120
OAFlux+SRB	160
ERA-Interim	84
MERRA	190
ECCO2	87
NOCS v.2	120
J-OFURO2	170

Table A.3: Comparison of estimated area integral of $Q_{net}\theta$ ($\mathrm{W\,^{\circ}C\,m^{-2}}$) using monthly fields to include seasonal effects as well as inter-annual effects using eight Q_{net} products.

Q_{net} Product	$Q_{net}\theta$ ($\mathrm{W\,^{\circ}C\,m^{-2}}$)
OAFlux+ISCCP	120
OAFlux+CERES	120
OAFlux+SRB	150
ERA-Interim	98
MERRA	210
ECCO2	100
NOCS v.2	120
J-OFURO2	180

Table A.4: Comparison of implied temperature variance dissipation χ_θ ($\mathrm{^{\circ}C^2\,s^{-1}}$), assuming a scale height of $H = 600$ m for time-means of eight Q_{net} products.

Q_{net} Product	χ_θ ($\mathrm{^{\circ}C^2\,s^{-1}}$)
OAFlux+ISCCP	$8.4 \cdot 10^{-8}$
OAFlux+CERES	$7.6 \cdot 10^{-8}$
OAFlux+SRB	$1.1 \cdot 10^{-7}$
ERA-Interim	$4.7 \cdot 10^{-8}$
MERRA	$1.4 \cdot 10^{-7}$
ECCO2	$5.5 \cdot 10^{-8}$
NOCS v.2	$8.4 \cdot 10^{-8}$
J-OFURO2	$1.2 \cdot 10^{-7}$

Table A.5: Comparison of implied temperature variance dissipation χ_θ ($^\circ C^2\,s^{-1}$) using 10° latitude band averages as in Joyce (1980) and assuming a scale height of $H = 600$ m for time-means of eight Q_{net} products.

Q_{net} Product	χ_θ (lat) ($^\circ C^2\,s^{-1}$)
OAFlux+ISCCP	$1.1 \cdot 10^{-7}$
OAFlux+CERES	$9.7 \cdot 10^{-8}$
OAFlux+SRB	$1.3 \cdot 10^{-7}$
ERA-Interim	$6.8 \cdot 10^{-8}$
MERRA	$1.5 \cdot 10^{-7}$
ECCO2	$7.1 \cdot 10^{-8}$
NOCS v.2	$9.8 \cdot 10^{-8}$
J-OFURO2	$1.4 \cdot 10^{-7}$

Table A.6: Comparison of estimated temperature variance dissipation χ_θ ($^\circ C^2\,s^{-1}$) for different Q_{net} products, assuming a scale height of H =600 m and using monthly data, thus including effects of the seasonal cycle and inter-annual variability.

Q_{net} Product	χ_θ (seasonal) ($^\circ C^2\,s^{-1}$)
OAFlux+ISCCP	$9.6 \cdot 10^{-8}$
OAFlux+CERES	$9.5 \cdot 10^{-8}$
OAFlux+SRB	$1.2 \cdot 10^{-7}$
ERA-Interim	$8.0 \cdot 10^{-8}$
MERRA	$1.7 \cdot 10^{-7}$
ECCO2	$8.4 \cdot 10^{-8}$
NOCS v.2	$1.0 \cdot 10^{-7}$
J-OFURO2	$1.5 \cdot 10^{-7}$

Table A.7: Comparison of estimated temperature variance dissipation χ_θ ($^\circ C^2\,s^{-1}$) for different Q_{net} products, assuming a scale height of H =600 m and using monthly data, thus including effects of the seasonal cycle and inter-annual variability. Balancing here is done separately for each year (i.e. for each 12 months). A small increase is evident for most products.

Q_{net} Product	χ_θ (seasonal, by-year) ($^\circ C^2\,s^{-1}$)
OAFlux+ISCCP	$1.0 \cdot 10^{-7}$
OAFlux+CERES	$1.0 \cdot 10^{-7}$
OAFlux+SRB	$1.3 \cdot 10^{-7}$
ERA-Interim	$8.0 \cdot 10^{-8}$
MERRA	$1.7 \cdot 10^{-7}$
ECCO2	$8.4 \cdot 10^{-8}$
NOCS v.2	$1.1 \cdot 10^{-7}$
J-OFURO2	$1.6 \cdot 10^{-7}$

Table A.8: Comparison of estimated salinity variance production $\overline{F_S}(\bar{S} - S_0)$ (psu kg m^{-2} s^{-1}) for different E-P-R products.

E-P-R Product	$\overline{F_S}(\bar{S} - S_0)$ (psu kg m^{-2} s^{-1})
Schanze	$1.0 \cdot 10^{-6}$
MERRA	$9.8 \cdot 10^{-7}$
ECCO2	$6.8 \cdot 10^{-7}$
CORE2	$1.0 \cdot 10^{-6}$
NCEP2	$1.1 \cdot 10^{-6}$
HOAPS	$9.2 \cdot 10^{-7}$

Table A.9: Comparison of estimated salinity variance production $\overline{F_S}(\bar{S} - S_0)$ ($\mathrm{psu\,kg\,m^{-2}\,s^{-1}}$) using 10° latitude band zonal means for different E-P-R products.

E-P-R Product	$\overline{F_S}(S - S_0)$ ($\mathrm{psu\,kg\,m^{-2}\,s^{-1}}$)
Schanze	$4.5 \cdot 10^{-7}$
MERRA	$4.2 \cdot 10^{-7}$
ECCO2	$4.3 \cdot 10^{-7}$
CORE2	$3.8 \cdot 10^{-7}$
NCEP2	$4.7 \cdot 10^{-7}$
HOAPS	$3.7 \cdot 10^{-7}$

Table A.10: Comparison of estimated salinity variance production $F_S(S - S_0)$ ($\mathrm{psu\,kg\,m^{-2}\,s^{-1}}$) using monthly data to include effects of the seasonal cycle and inter-annual variability.

E-P-R Product	$F_S(S - S_0)$ ($\mathrm{psu\,kg\,m^{-2}\,s^{-1}}$)
Schanze	$1.1 \cdot 10^{-6}$
MERRA	$1.1 \cdot 10^{-6}$
ECCO2	$8.3 \cdot 10^{-7}$
CORE2	$1.1 \cdot 10^{-6}$
NCEP2	$1.2 \cdot 10^{-6}$
HOAPS	$1.0 \cdot 10^{-6}$

Table A.11: Comparison of estimated salinity variance production $F_S(S - S_0)$ ($\mathrm{psu\,kg\,m^{-2}\,s^{-1}}$) using monthly data to include effects of the seasonal cycle. Remaining inter-annual global means have been removed by balancing the estimates for each individual year between 1987–2004

E-P-R Product	$F_S(S - S_0)$ ($\mathrm{psu\,kg\,m^{-2}\,s^{-1}}$)
Schanze	$1.1 \cdot 10^{-6}$
MERRA	$1.1 \cdot 10^{-6}$
ECCO2	$8.3 \cdot 10^{-7}$
CORE2	$1.1 \cdot 10^{-6}$
NCEP2	$1.2 \cdot 10^{-6}$
HOAPS	$1.0 \cdot 10^{-6}$

Table A.12: Comparison of estimated salinity variance dissipation χ_S ($\mathrm{psu}^2\,\mathrm{s}^{-1}$) for different time-means of E-P-R products using a scale height of H=600 m.

Dataset	χ_S $\mathrm{psu}^2\,\mathrm{s}^{-1}$
Schanze	$3.4 \cdot 10^{-9}$
MERRA	$3.3 \cdot 10^{-9}$
ECCO2	$2.3 \cdot 10^{-9}$
CORE2	$3.3 \cdot 10^{-9}$
NCEP2	$3.6 \cdot 10^{-9}$
HOAPS	$3.1 \cdot 10^{-9}$

Table A.13: Comparison of estimated salinity variance dissipation χ_S ($\mathrm{psu}^2\,\mathrm{s}^{-1}$) using 10° latitude bands of different time-means of E-P-R datasets using a scale height of H=600 m.

Dataset	χ_S $\mathrm{psu}^2\,\mathrm{s}^{-1}$
Schanze	$1.5 \cdot 10^{-9}$
MERRA	$1.4 \cdot 10^{-9}$
ECCO2	$1.4 \cdot 10^{-9}$
CORE2	$1.3 \cdot 10^{-9}$
NCEP2	$1.6 \cdot 10^{-9}$
HOAPS	$1.2 \cdot 10^{-9}$

Table A.14: Comparison of estimated salinity variance dissipation χ_S including seasonal effects ($\mathrm{psu}^2\,\mathrm{s}^{-1}$) for different time-means of E-P-R products using a scale height of H=600 m. Monthly fields are used instead of the time-mean to include effects of the seasonal cycle and inter-annual variability.

Dataset	χ_S $\mathrm{psu}^2\,\mathrm{s}^{-1}$ (seasonal)
Schanze	$3.7 \cdot 10^{-9}$
MERRA	$3.6 \cdot 10^{-9}$
ECCO2	$2.8 \cdot 10^{-9}$
CORE2	$3.7 \cdot 10^{-9}$
NCEP2	$4.0 \cdot 10^{-9}$
HOAPS	$3.4 \cdot 10^{-9}$

Table A.15: Comparison of estimated salinity variance dissipation χ_S including seasonal effects ($\mathrm{psu}^2\,\mathrm{s}^{-1}$) for different time-means of E-P-R products using a scale height of H=600 m. Monthly fields are used instead of the time-mean to include effects of the seasonal cycle. Balancing is done for each individual year to remove effects of inter-annual residual means.

Dataset	χ_S $\mathrm{psu}^2\,\mathrm{s}^{-1}$ (seas, yr)
Schanze	$3.7 \cdot 10^{-9}$
MERRA	$3.6 \cdot 10^{-9}$
ECCO2	$2.8 \cdot 10^{-9}$
CORE2	$3.7 \cdot 10^{-9}$
NCEP2	$4.0 \cdot 10^{-9}$
HOAPS	$3.4 \cdot 10^{-9}$

Table A.16: Comparison of estimated density variance generation $\overline{F_\rho} \cdot (\bar{\rho} - \rho_0)$ $((\mathrm{kg/m^3})^2\mathrm{m/s})$ for different time-means of Q_{net} and E-P-R products

E-P-R / Q_{net}	Schanze	MERRA	ECCO2	CORE2	NCEP2	HOAPS
OAFlux+ISCCP	$1.7{\cdot}10^{-6}$	$1.9{\cdot}10^{-6}$	$1.6{\cdot}10^{-6}$	$1.8{\cdot}10^{-6}$	$2.0{\cdot}10^{-6}$	$1.9{\cdot}10^{-6}$
OAFlux+CERES	$1.4{\cdot}10^{-6}$	$1.5{\cdot}10^{-6}$	$1.3{\cdot}10^{-6}$	$1.4{\cdot}10^{-6}$	$1.6{\cdot}10^{-6}$	$1.5{\cdot}10^{-6}$
OAFlux+SRB	$1.6{\cdot}10^{-6}$	$1.7{\cdot}10^{-6}$	$1.5{\cdot}10^{-6}$	$1.7{\cdot}10^{-6}$	$1.9{\cdot}10^{-6}$	$1.8{\cdot}10^{-6}$
ERA-Interim	$9.9{\cdot}10^{-7}$	$1.2{\cdot}10^{-6}$	$9.6{\cdot}10^{-7}$	$1.1{\cdot}10^{-6}$	$1.3{\cdot}10^{-6}$	$1.2{\cdot}10^{-6}$
MERRA	$1.7{\cdot}10^{-6}$	$1.9{\cdot}10^{-6}$	$1.6{\cdot}10^{-6}$	$1.8{\cdot}10^{-6}$	$2.0{\cdot}10^{-6}$	$1.9{\cdot}10^{-6}$
ECCO2	$9.9{\cdot}10^{-7}$	$1.2{\cdot}10^{-6}$	$9.0{\cdot}10^{-7}$	$1.1{\cdot}10^{-6}$	$1.3{\cdot}10^{-6}$	$1.2{\cdot}10^{-6}$
NOCS v.2	$1.5{\cdot}10^{-6}$	$1.6{\cdot}10^{-6}$	$1.5{\cdot}10^{-6}$	$1.6{\cdot}10^{-6}$	$1.8{\cdot}10^{-6}$	$1.7{\cdot}10^{-6}$
J-OFURO2	$2.4{\cdot}10^{-6}$	$2.5{\cdot}10^{-6}$	$2.3{\cdot}10^{-6}$	$2.4{\cdot}10^{-6}$	$2.6{\cdot}10^{-6}$	$2.5{\cdot}10^{-6}$

Table A.17: Comparison of estimated linearized density variance generation $\overline{F_\rho} \cdot (\bar{\rho} - \rho_0)$ $((\mathrm{kg/m^3})^2\mathrm{m/s})$ for different time-means of Q_{net} and E-P-R products

Q_{net} \ E-P-R	Schanze	MERRA	ECCO2	CORE2	NCEP2	HOAPS
OAFlux+ISCCP	$1.6{\cdot}10^{-6}$	$1.7{\cdot}10^{-6}$	$1.4{\cdot}10^{-6}$	$1.6{\cdot}10^{-6}$	$1.8{\cdot}10^{-6}$	$1.7{\cdot}10^{-6}$
OAFlux+CERES	$1.4{\cdot}10^{-6}$	$1.5{\cdot}10^{-6}$	$1.3{\cdot}10^{-6}$	$1.4{\cdot}10^{-6}$	$1.6{\cdot}10^{-6}$	$1.5{\cdot}10^{-6}$
OAFlux+SRB	$1.7{\cdot}10^{-6}$	$1.8{\cdot}10^{-6}$	$1.6{\cdot}10^{-6}$	$1.7{\cdot}10^{-6}$	$1.9{\cdot}10^{-6}$	$1.8{\cdot}10^{-6}$
ERA-Interim	$9.7{\cdot}10^{-7}$	$1.1{\cdot}10^{-6}$	$9.3{\cdot}10^{-7}$	$1.1{\cdot}10^{-6}$	$1.2{\cdot}10^{-6}$	$1.2{\cdot}10^{-6}$
MERRA	$1.9{\cdot}10^{-6}$	$2.1{\cdot}10^{-6}$	$1.9{\cdot}10^{-6}$	$2.0{\cdot}10^{-6}$	$2.2{\cdot}10^{-6}$	$2.1{\cdot}10^{-6}$
ECCO2	$1.0{\cdot}10^{-6}$	$1.2{\cdot}10^{-6}$	$9.5{\cdot}10^{-7}$	$1.1{\cdot}10^{-6}$	$1.3{\cdot}10^{-6}$	$1.2{\cdot}10^{-6}$
NOCS v.2	$1.4{\cdot}10^{-6}$	$1.6{\cdot}10^{-6}$	$1.4{\cdot}10^{-6}$	$1.5{\cdot}10^{-6}$	$1.7{\cdot}10^{-6}$	$1.7{\cdot}10^{-6}$
J-OFURO2	$2.3{\cdot}10^{-6}$	$2.4{\cdot}10^{-6}$	$2.2{\cdot}10^{-6}$	$2.4{\cdot}10^{-6}$	$2.6{\cdot}10^{-6}$	$2.5{\cdot}10^{-6}$

Table A.18: Comparison of estimated density variance generation $\overline{F_\rho} \cdot (\bar{\rho} - \rho_0)$ $((\mathrm{kg/m^3})^2\mathrm{m/s})$ using 10° latitude band averages for different time-means of Q_{net} and E-P-R products

Q_{net} \ E-P-R	Schanze	MERRA	ECCO2	CORE2	NCEP2	HOAPS
OAFlux+ISCCP	$1.6{\cdot}10^{-6}$	$1.8{\cdot}10^{-6}$	$1.7{\cdot}10^{-6}$	$1.7{\cdot}10^{-6}$	$1.8{\cdot}10^{-6}$	$1.8{\cdot}10^{-6}$
OAFlux+CERES	$1.4{\cdot}10^{-6}$	$1.5{\cdot}10^{-6}$	$1.4{\cdot}10^{-6}$	$1.4{\cdot}10^{-6}$	$1.6{\cdot}10^{-6}$	$1.5{\cdot}10^{-6}$
OAFlux+SRB	$1.6{\cdot}10^{-6}$	$1.7{\cdot}10^{-6}$	$1.7{\cdot}10^{-6}$	$1.7{\cdot}10^{-6}$	$1.8{\cdot}10^{-6}$	$1.8{\cdot}10^{-6}$
ERA-Interim	$9.4{\cdot}10^{-7}$	$1.1{\cdot}10^{-6}$	$1.0{\cdot}10^{-6}$	$9.9{\cdot}10^{-7}$	$1.2{\cdot}10^{-6}$	$1.2{\cdot}10^{-6}$
MERRA	$1.5{\cdot}10^{-6}$	$1.7{\cdot}10^{-6}$	$1.6{\cdot}10^{-6}$	$1.6{\cdot}10^{-6}$	$1.7{\cdot}10^{-6}$	$1.7{\cdot}10^{-6}$
ECCO2	$8.7{\cdot}10^{-7}$	$1.0{\cdot}10^{-6}$	$9.3{\cdot}10^{-7}$	$9.2{\cdot}10^{-7}$	$1.1{\cdot}10^{-6}$	$1.1{\cdot}10^{-6}$
NOCS v.2	$1.3{\cdot}10^{-6}$	$1.4{\cdot}10^{-6}$	$1.4{\cdot}10^{-6}$	$1.3{\cdot}10^{-6}$	$1.5{\cdot}10^{-6}$	$1.5{\cdot}10^{-6}$
J-OFURO2	$2.1{\cdot}10^{-6}$	$2.2{\cdot}10^{-6}$	$2.2{\cdot}10^{-6}$	$2.1{\cdot}10^{-6}$	$2.3{\cdot}10^{-6}$	$2.3{\cdot}10^{-6}$

Table A.19: Comparison of estimated density variance generation $F_\rho \cdot (\rho - \rho_0)$ $((\mathrm{kg/m^3})^2\mathrm{m/s})$ using monthly fields to include seasonal and inter-annual effects for different Q_{net} and E-P-R products

Q_{net} \ E-P-R	Schanze	MERRA	ECCO2	CORE2	NCEP2	HOAPS
OAFlux+ISCCP	$2.3{\cdot}10^{-6}$	$2.5{\cdot}10^{-6}$	$2.2{\cdot}10^{-6}$	$2.4{\cdot}10^{-6}$	$2.6{\cdot}10^{-6}$	$2.5{\cdot}10^{-6}$
OAFlux+CERES	$1.9{\cdot}10^{-6}$	$2.1{\cdot}10^{-6}$	$1.9{\cdot}10^{-6}$	$2.0{\cdot}10^{-6}$	$2.2{\cdot}10^{-6}$	$2.1{\cdot}10^{-6}$
OAFlux+SRB	$2.1{\cdot}10^{-6}$	$2.3{\cdot}10^{-6}$	$2.1{\cdot}10^{-6}$	$2.2{\cdot}10^{-6}$	$2.4{\cdot}10^{-6}$	$2.3{\cdot}10^{-6}$
ERA-Interim	$1.6{\cdot}10^{-6}$	$1.7{\cdot}10^{-6}$	$1.6{\cdot}10^{-6}$	$1.7{\cdot}10^{-6}$	$1.9{\cdot}10^{-6}$	$1.8{\cdot}10^{-6}$
MERRA	$2.3{\cdot}10^{-6}$	$2.4{\cdot}10^{-6}$	$2.3{\cdot}10^{-6}$	$2.4{\cdot}10^{-6}$	$2.6{\cdot}10^{-6}$	$2.5{\cdot}10^{-6}$
ECCO2	$1.6{\cdot}10^{-6}$	$1.7{\cdot}10^{-6}$	$1.5{\cdot}10^{-6}$	$1.7{\cdot}10^{-6}$	$1.9{\cdot}10^{-6}$	$1.7{\cdot}10^{-6}$
NOCS v.2	$2.1{\cdot}10^{-6}$	$2.3{\cdot}10^{-6}$	$2.1{\cdot}10^{-6}$	$2.2{\cdot}10^{-6}$	$2.4{\cdot}10^{-6}$	$2.3{\cdot}10^{-6}$
J-OFURO2	$3.0{\cdot}10^{-6}$	$3.2{\cdot}10^{-6}$	$3.0{\cdot}10^{-6}$	$3.1{\cdot}10^{-6}$	$3.3{\cdot}10^{-6}$	$3.2{\cdot}10^{-6}$

Table A.20: Comparison of estimated density variance generation $F_\rho \cdot (\rho - \rho_0)$ $((\mathrm{kg/m^3})^2\mathrm{m/s})$ using monthly fields that are balanced to have zero annual means of different Q_{net} and E-P-R products

Q_{net} \ E-P-R	Schanze	MERRA	ECCO2	CORE2	NCEP2	HOAPS
OAFlux+ISCCP	$2.1{\cdot}10^{-6}$	$2.3{\cdot}10^{-6}$	$2.0{\cdot}10^{-6}$	$2.2{\cdot}10^{-6}$	$2.5{\cdot}10^{-6}$	$2.3{\cdot}10^{-6}$
OAFlux+CERES	$1.5{\cdot}10^{-6}$	$1.7{\cdot}10^{-6}$	$1.6{\cdot}10^{-6}$	$1.6{\cdot}10^{-6}$	$1.8{\cdot}10^{-6}$	$1.7{\cdot}10^{-6}$
OAFlux+SRB	$1.9{\cdot}10^{-6}$	$2.1{\cdot}10^{-6}$	$1.8{\cdot}10^{-6}$	$2.0{\cdot}10^{-6}$	$2.2{\cdot}10^{-6}$	$2.1{\cdot}10^{-6}$
ERA-Interim	$1.6{\cdot}10^{-6}$	$1.7{\cdot}10^{-6}$	$1.6{\cdot}10^{-6}$	$1.7{\cdot}10^{-6}$	$1.9{\cdot}10^{-6}$	$1.8{\cdot}10^{-6}$
MERRA	$2.3{\cdot}10^{-6}$	$2.4{\cdot}10^{-6}$	$2.3{\cdot}10^{-6}$	$2.4{\cdot}10^{-6}$	$2.6{\cdot}10^{-6}$	$2.5{\cdot}10^{-6}$
ECCO2	$1.6{\cdot}10^{-6}$	$1.7{\cdot}10^{-6}$	$1.5{\cdot}10^{-6}$	$1.7{\cdot}10^{-6}$	$1.9{\cdot}10^{-6}$	$1.7{\cdot}10^{-6}$
NOCS v.2	$2.0{\cdot}10^{-6}$	$2.2{\cdot}10^{-6}$	$2.0{\cdot}10^{-6}$	$2.1{\cdot}10^{-6}$	$2.3{\cdot}10^{-6}$	$2.2{\cdot}10^{-6}$
J-OFURO2	$3.0{\cdot}10^{-6}$	$3.2{\cdot}10^{-6}$	$3.2{\cdot}10^{-6}$	$3.1{\cdot}10^{-6}$	$3.3{\cdot}10^{-6}$	$3.2{\cdot}10^{-6}$

Table A.21: Comparison of estimated density variance dissipation χ_ρ $((\mathrm{kg/m^3})^2/\mathrm{s})$ for different time-means of Q_{net} and E-P-R products

Q_{net} \ E-P-R	Schanze	MERRA	ECCO2	CORE2	NCEP2	HOAPS
OAFlux+ISCCP	$5.7{\cdot}10^{-9}$	$6.2{\cdot}10^{-9}$	$5.3{\cdot}10^{-9}$	$6.0{\cdot}10^{-9}$	$6.6{\cdot}10^{-9}$	$6.2{\cdot}10^{-9}$
OAFlux+CERES	$4.5{\cdot}10^{-9}$	$5.1{\cdot}10^{-9}$	$4.2{\cdot}10^{-9}$	$4.8{\cdot}10^{-9}$	$5.4{\cdot}10^{-9}$	$5.1{\cdot}10^{-9}$
OAFlux+SRB	$5.3{\cdot}10^{-9}$	$5.8{\cdot}10^{-9}$	$4.9{\cdot}10^{-9}$	$5.6{\cdot}10^{-9}$	$6.2{\cdot}10^{-9}$	$5.9{\cdot}10^{-9}$
ERA-Interim	$3.3{\cdot}10^{-9}$	$3.8{\cdot}10^{-9}$	$3.2{\cdot}10^{-9}$	$3.6{\cdot}10^{-9}$	$4.2{\cdot}10^{-9}$	$4.1{\cdot}10^{-9}$
MERRA	$5.7{\cdot}10^{-9}$	$6.3{\cdot}10^{-9}$	$5.5{\cdot}10^{-9}$	$6.0{\cdot}10^{-9}$	$6.6{\cdot}10^{-9}$	$6.4{\cdot}10^{-9}$
ECCO2	$3.3{\cdot}10^{-9}$	$3.9{\cdot}10^{-9}$	$3.0{\cdot}10^{-9}$	$3.6{\cdot}10^{-9}$	$4.2{\cdot}10^{-9}$	$3.9{\cdot}10^{-9}$
NOCS v.2	$4.9{\cdot}10^{-9}$	$5.5{\cdot}10^{-9}$	$4.8{\cdot}10^{-9}$	$5.2{\cdot}10^{-9}$	$5.8{\cdot}10^{-9}$	$5.8{\cdot}10^{-9}$
J-OFURO2	$7.8{\cdot}10^{-9}$	$8.4{\cdot}10^{-9}$	$7.7{\cdot}10^{-9}$	$8.1{\cdot}10^{-9}$	$8.8{\cdot}10^{-9}$	$8.5{\cdot}10^{-9}$

Table A.22: Comparison of estimated linear density variance dissipation χ_ρ $((\mathrm{kg/m^3})^2/\mathrm{s})$ for different time-means of Q_{net} and E-P-R products

Q_{net} \ E-P-R	Schanze	MERRA	ECCO2	CORE2	NCEP2	HOAPS
OAFlux+ISCCP	$5.2{\cdot}10^{-9}$	$5.7{\cdot}10^{-9}$	$4.8{\cdot}10^{-9}$	$5.5{\cdot}10^{-9}$	$6.1{\cdot}10^{-9}$	$5.7{\cdot}10^{-9}$
OAFlux+CERES	$4.5{\cdot}10^{-9}$	$5.0{\cdot}10^{-9}$	$4.2{\cdot}10^{-9}$	$4.8{\cdot}10^{-9}$	$5.4{\cdot}10^{-9}$	$5.1{\cdot}10^{-9}$
OAFlux+SRB	$5.5{\cdot}10^{-9}$	$6.1{\cdot}10^{-9}$	$5.2{\cdot}10^{-9}$	$5.8{\cdot}10^{-9}$	$6.5{\cdot}10^{-9}$	$6.1{\cdot}10^{-9}$
ERA-Interim	$3.2{\cdot}10^{-9}$	$3.8{\cdot}10^{-9}$	$3.1{\cdot}10^{-9}$	$3.5{\cdot}10^{-9}$	$4.2{\cdot}10^{-9}$	$4.0{\cdot}10^{-9}$
MERRA	$6.5{\cdot}10^{-9}$	$7.0{\cdot}10^{-9}$	$6.3{\cdot}10^{-9}$	$6.7{\cdot}10^{-9}$	$7.4{\cdot}10^{-9}$	$7.2{\cdot}10^{-9}$
ECCO2	$3.5{\cdot}10^{-9}$	$4.1{\cdot}10^{-9}$	$3.2{\cdot}10^{-9}$	$3.8{\cdot}10^{-9}$	$4.4{\cdot}10^{-9}$	$4.1{\cdot}10^{-9}$
NOCS v.2	$4.7{\cdot}10^{-9}$	$5.3{\cdot}10^{-9}$	$4.7{\cdot}10^{-9}$	$5.0{\cdot}10^{-9}$	$5.7{\cdot}10^{-9}$	$5.6{\cdot}10^{-9}$
J-OFURO2	$7.6{\cdot}10^{-9}$	$8.1{\cdot}10^{-9}$	$7.5{\cdot}10^{-9}$	$7.9{\cdot}10^{-9}$	$8.5{\cdot}10^{-9}$	$8.2{\cdot}10^{-9}$

Table A.23: Comparison of estimated density variance dissipation χ_ρ $((\mathrm{kg/m^3})^2/\mathrm{s})$ using 10° latitude bands of different time-means of Q_{net} and E-P-R products

Q_{net} \ E-P-R	Schanze	MERRA	ECCO2	CORE2	NCEP2	HOAPS
OAFlux+ISCCP	$5.5{\cdot}10^{-9}$	$5.9{\cdot}10^{-9}$	$5.7{\cdot}10^{-9}$	$5.6{\cdot}10^{-9}$	$6.2{\cdot}10^{-9}$	$6.1{\cdot}10^{-9}$
OAFlux+CERES	$4.5{\cdot}10^{-9}$	$5.0{\cdot}10^{-9}$	$4.7{\cdot}10^{-9}$	$4.7{\cdot}10^{-9}$	$5.2{\cdot}10^{-9}$	$5.2{\cdot}10^{-9}$
OAFlux+SRB	$5.4{\cdot}10^{-9}$	$5.8{\cdot}10^{-9}$	$5.6{\cdot}10^{-9}$	$5.5{\cdot}10^{-9}$	$6.1{\cdot}10^{-9}$	$6.0{\cdot}10^{-9}$
ERA-Interim	$3.1{\cdot}10^{-9}$	$3.6{\cdot}10^{-9}$	$3.5{\cdot}10^{-9}$	$3.3{\cdot}10^{-9}$	$3.8{\cdot}10^{-9}$	$3.9{\cdot}10^{-9}$
MERRA	$5.1{\cdot}10^{-9}$	$5.6{\cdot}10^{-9}$	$5.4{\cdot}10^{-9}$	$5.2{\cdot}10^{-9}$	$5.8{\cdot}10^{-9}$	$5.8{\cdot}10^{-9}$
ECCO2	$2.9{\cdot}10^{-9}$	$3.4{\cdot}10^{-9}$	$3.1{\cdot}10^{-9}$	$3.1{\cdot}10^{-9}$	$3.6{\cdot}10^{-9}$	$3.6{\cdot}10^{-9}$
NOCS v.2	$4.3{\cdot}10^{-9}$	$4.7{\cdot}10^{-9}$	$4.7{\cdot}10^{-9}$	$4.4{\cdot}10^{-9}$	$5.0{\cdot}10^{-9}$	$5.1{\cdot}10^{-9}$
J-OFURO2	$6.9{\cdot}10^{-9}$	$7.4{\cdot}10^{-9}$	$7.3{\cdot}10^{-9}$	$7.1{\cdot}10^{-9}$	$7.6{\cdot}10^{-9}$	$7.6{\cdot}10^{-9}$

Table A.24: Comparison of estimated density variance dissipation χ_ρ $((\mathrm{kg/m^3})^2/\mathrm{s})$ using monthly fields and thus including seasonal effects as well as inter-annual effects for different time-means of Q_{net} and E-P-R products

Q_{net} \ E-P-R	Schanze	MERRA	ECCO2	CORE2	NCEP2	HOAPS
OAFlux+ISCCP	$7.7{\cdot}10^{-9}$	$8.2{\cdot}10^{-9}$	$7.5{\cdot}10^{-9}$	$8.0{\cdot}10^{-9}$	$8.7{\cdot}10^{-9}$	$8.2{\cdot}10^{-9}$
OAFlux+CERES	$6.4{\cdot}10^{-9}$	$6.9{\cdot}10^{-9}$	$6.2{\cdot}10^{-9}$	$6.7{\cdot}10^{-9}$	$7.4{\cdot}10^{-9}$	$7.0{\cdot}10^{-9}$
OAFlux+SRB	$7.1{\cdot}10^{-9}$	$7.7{\cdot}10^{-9}$	$7.0{\cdot}10^{-9}$	$7.5{\cdot}10^{-9}$	$8.1{\cdot}10^{-9}$	$7.7{\cdot}10^{-9}$
ERA-Interim	$5.2{\cdot}10^{-9}$	$5.8{\cdot}10^{-9}$	$5.3{\cdot}10^{-9}$	$5.5{\cdot}10^{-9}$	$6.2{\cdot}10^{-9}$	$6.0{\cdot}10^{-9}$
MERRA	$7.5{\cdot}10^{-9}$	$8.1{\cdot}10^{-9}$	$7.6{\cdot}10^{-9}$	$7.9{\cdot}10^{-9}$	$8.5{\cdot}10^{-9}$	$8.3{\cdot}10^{-9}$
ECCO2	$5.2{\cdot}10^{-9}$	$5.8{\cdot}10^{-9}$	$5.0{\cdot}10^{-9}$	$5.5{\cdot}10^{-9}$	$6.2{\cdot}10^{-9}$	$5.7{\cdot}10^{-9}$
NOCS v.2	$7.0{\cdot}10^{-9}$	$7.5{\cdot}10^{-9}$	$7.1{\cdot}10^{-9}$	$7.3{\cdot}10^{-9}$	$8.0{\cdot}10^{-9}$	$7.8{\cdot}10^{-9}$
J-OFURO2	$1.0{\cdot}10^{-8}$	$1.1{\cdot}10^{-8}$	$1.0{\cdot}10^{-8}$	$1.0{\cdot}10^{-8}$	$1.1{\cdot}10^{-8}$	$1.1{\cdot}10^{-8}$

Table A.25: Comparison of estimated density variance dissipation χ_ρ ($(kg/m^3)^2/s$) using monthly fields to include effects of the seasonal cycle as well as inter-annual variability of Q_{net} and E-P-R products. The yearly temporal and spatial mean is removed from each individual year of the analysis rather than removing a time-mean value.

E-P-R / Q_{net}	Schanze	MERRA	ECCO2	CORE2	NCEP2	HOAPS
OAFlux+ISCCP	$7.1{\cdot}10^{-9}$	$7.8{\cdot}10^{-9}$	$6.8{\cdot}10^{-9}$	$7.5{\cdot}10^{-9}$	$8.3{\cdot}10^{-9}$	$7.6{\cdot}10^{-9}$
OAFlux+CERES	$4.9{\cdot}10^{-9}$	$5.6{\cdot}10^{-9}$	$5.4{\cdot}10^{-9}$	$5.3{\cdot}10^{-9}$	$6.1{\cdot}10^{-9}$	$5.6{\cdot}10^{-9}$
OAFlux+SRB	$6.3{\cdot}10^{-9}$	$7.0{\cdot}10^{-9}$	$6.1{\cdot}10^{-9}$	$6.7{\cdot}10^{-9}$	$7.5{\cdot}10^{-9}$	$7.0{\cdot}10^{-9}$
ERA-Interim	$5.2{\cdot}10^{-9}$	$5.8{\cdot}10^{-9}$	$5.3{\cdot}10^{-9}$	$5.5{\cdot}10^{-9}$	$6.2{\cdot}10^{-9}$	$6.0{\cdot}10^{-9}$
MERRA	$7.5{\cdot}10^{-9}$	$8.1{\cdot}10^{-9}$	$7.6{\cdot}10^{-9}$	$7.9{\cdot}10^{-9}$	$8.5{\cdot}10^{-9}$	$8.3{\cdot}10^{-9}$
ECCO2	$5.2{\cdot}10^{-9}$	$5.8{\cdot}10^{-9}$	$5.0{\cdot}10^{-9}$	$5.5{\cdot}10^{-9}$	$6.2{\cdot}10^{-9}$	$5.7{\cdot}10^{-9}$
NOCS v.2	$6.7{\cdot}10^{-9}$	$7.3{\cdot}10^{-9}$	$6.7{\cdot}10^{-9}$	$7.0{\cdot}10^{-9}$	$7.8{\cdot}10^{-9}$	$7.5{\cdot}10^{-9}$
J-OFURO2	$9.9{\cdot}10^{-9}$	$1.1{\cdot}10^{-8}$	$1.1{\cdot}10^{-8}$	$1.0{\cdot}10^{-8}$	$1.1{\cdot}10^{-8}$	$1.1{\cdot}10^{-8}$

Table A.26: Comparison of estimated global spice variance production $\overline{F_\tau} \cdot (\bar{\tau} - \tau_0)$ ($(kg/m^3)^2 m/s$) for different time-means of Q_{net} and E-P-R products

E-P-R / Q_{net}	Schanze	MERRA	ECCO2	CORE2	NCEP2	HOAPS
OAFlux+ISCCP	$2.2{\cdot}10^{-6}$	$2.0{\cdot}10^{-6}$	$1.9{\cdot}10^{-6}$	$2.1{\cdot}10^{-6}$	$2.1{\cdot}10^{-6}$	$1.9{\cdot}10^{-6}$
OAFlux+CERES	$2.3{\cdot}10^{-6}$	$2.1{\cdot}10^{-6}$	$2.0{\cdot}10^{-6}$	$2.2{\cdot}10^{-6}$	$2.2{\cdot}10^{-6}$	$2.0{\cdot}10^{-6}$
OAFlux+SRB	$2.9{\cdot}10^{-6}$	$2.7{\cdot}10^{-6}$	$2.6{\cdot}10^{-6}$	$2.8{\cdot}10^{-6}$	$2.8{\cdot}10^{-6}$	$2.6{\cdot}10^{-6}$
ERA-Interim	$1.7{\cdot}10^{-6}$	$1.5{\cdot}10^{-6}$	$1.4{\cdot}10^{-6}$	$1.6{\cdot}10^{-6}$	$1.6{\cdot}10^{-6}$	$1.5{\cdot}10^{-6}$
MERRA	$3.3{\cdot}10^{-6}$	$3.1{\cdot}10^{-6}$	$3.1{\cdot}10^{-6}$	$3.2{\cdot}10^{-6}$	$3.2{\cdot}10^{-6}$	$3.1{\cdot}10^{-6}$
ECCO2	$1.9{\cdot}10^{-6}$	$1.7{\cdot}10^{-6}$	$1.6{\cdot}10^{-6}$	$1.8{\cdot}10^{-6}$	$1.8{\cdot}10^{-6}$	$1.6{\cdot}10^{-6}$
NOCS v.2	$2.4{\cdot}10^{-6}$	$2.2{\cdot}10^{-6}$	$2.2{\cdot}10^{-6}$	$2.3{\cdot}10^{-6}$	$2.3{\cdot}10^{-6}$	$2.2{\cdot}10^{-6}$
J-OFURO2	$2.7{\cdot}10^{-6}$	$2.5{\cdot}10^{-6}$	$2.5{\cdot}10^{-6}$	$2.6{\cdot}10^{-6}$	$2.6{\cdot}10^{-6}$	$2.4{\cdot}10^{-6}$

Table A.27: Comparison of estimated global linear spice variance production $\overline{F_\tau} \cdot (\bar{\tau} - \tau_0)$ $((\mathrm{kg/m^3})^2\mathrm{m/s})$ for different time-means of Q_{net} and E-P-R products

Q_{net} \ E-P-R	Schanze	MERRA	ECCO2	CORE2	NCEP2	HOAPS
OAFlux+ISCCP	$2.2{\cdot}10^{-6}$	$2.0{\cdot}10^{-6}$	$1.9{\cdot}10^{-6}$	$2.1{\cdot}10^{-6}$	$2.1{\cdot}10^{-6}$	$1.9{\cdot}10^{-6}$
OAFlux+CERES	$2.3{\cdot}10^{-6}$	$2.1{\cdot}10^{-6}$	$2.0{\cdot}10^{-6}$	$2.2{\cdot}10^{-6}$	$2.2{\cdot}10^{-6}$	$2.0{\cdot}10^{-6}$
OAFlux+SRB	$2.9{\cdot}10^{-6}$	$2.7{\cdot}10^{-6}$	$2.6{\cdot}10^{-6}$	$2.8{\cdot}10^{-6}$	$2.8{\cdot}10^{-6}$	$2.6{\cdot}10^{-6}$
ERA-Interim	$1.7{\cdot}10^{-6}$	$1.5{\cdot}10^{-6}$	$1.4{\cdot}10^{-6}$	$1.6{\cdot}10^{-6}$	$1.6{\cdot}10^{-6}$	$1.5{\cdot}10^{-6}$
MERRA	$3.3{\cdot}10^{-6}$	$3.1{\cdot}10^{-6}$	$3.1{\cdot}10^{-6}$	$3.2{\cdot}10^{-6}$	$3.2{\cdot}10^{-6}$	$3.1{\cdot}10^{-6}$
ECCO2	$1.9{\cdot}10^{-6}$	$1.7{\cdot}10^{-6}$	$1.6{\cdot}10^{-6}$	$1.8{\cdot}10^{-6}$	$1.8{\cdot}10^{-6}$	$1.6{\cdot}10^{-6}$
NOCS v.2	$2.4{\cdot}10^{-6}$	$2.2{\cdot}10^{-6}$	$2.2{\cdot}10^{-6}$	$2.3{\cdot}10^{-6}$	$2.3{\cdot}10^{-6}$	$2.2{\cdot}10^{-6}$
J-OFURO2	$2.7{\cdot}10^{-6}$	$2.5{\cdot}10^{-6}$	$2.5{\cdot}10^{-6}$	$2.6{\cdot}10^{-6}$	$2.6{\cdot}10^{-6}$	$2.4{\cdot}10^{-6}$

Table A.28: Comparison of estimated global spice variance production $\overline{F_\tau} \cdot (\bar{\tau} - \tau_0)$ $((\mathrm{kg/m^3})^2\mathrm{m/s})$ using 10° latitude bands of different time-means of Q_{net} and E-P-R products

Q_{net} \ E-P-R	Schanze	MERRA	ECCO2	CORE2	NCEP2	HOAPS
OAFlux+ISCCP	$1.9{\cdot}10^{-6}$	$1.8{\cdot}10^{-6}$	$1.9{\cdot}10^{-6}$	$1.8{\cdot}10^{-6}$	$1.8{\cdot}10^{-6}$	$1.7{\cdot}10^{-6}$
OAFlux+CERES	$1.9{\cdot}10^{-6}$	$1.8{\cdot}10^{-6}$	$1.8{\cdot}10^{-6}$	$1.8{\cdot}10^{-6}$	$1.8{\cdot}10^{-6}$	$1.6{\cdot}10^{-6}$
OAFlux+SRB	$2.3{\cdot}10^{-6}$	$2.2{\cdot}10^{-6}$	$2.2{\cdot}10^{-6}$	$2.2{\cdot}10^{-6}$	$2.2{\cdot}10^{-6}$	$2.0{\cdot}10^{-6}$
ERA-Interim	$1.4{\cdot}10^{-6}$	$1.3{\cdot}10^{-6}$	$1.4{\cdot}10^{-6}$	$1.3{\cdot}10^{-6}$	$1.3{\cdot}10^{-6}$	$1.2{\cdot}10^{-6}$
MERRA	$2.4{\cdot}10^{-6}$	$2.3{\cdot}10^{-6}$	$2.4{\cdot}10^{-6}$	$2.3{\cdot}10^{-6}$	$2.3{\cdot}10^{-6}$	$2.2{\cdot}10^{-6}$
ECCO2	$1.5{\cdot}10^{-6}$	$1.3{\cdot}10^{-6}$	$1.4{\cdot}10^{-6}$	$1.4{\cdot}10^{-6}$	$1.4{\cdot}10^{-6}$	$1.2{\cdot}10^{-6}$
NOCS v.2	$1.8{\cdot}10^{-6}$	$1.7{\cdot}10^{-6}$	$1.8{\cdot}10^{-6}$	$1.7{\cdot}10^{-6}$	$1.7{\cdot}10^{-6}$	$1.6{\cdot}10^{-6}$
J-OFURO2	$2.4{\cdot}10^{-6}$	$2.2{\cdot}10^{-6}$	$2.4{\cdot}10^{-6}$	$2.3{\cdot}10^{-6}$	$2.3{\cdot}10^{-6}$	$2.1{\cdot}10^{-6}$

Table A.29: Comparison of estimated global spice variance production $F_\tau \cdot (\tau - \tau_0)$ ((kg/m^3)^{2}m/s) using monthly fields of different Q_{net} and E-P-R products to include seasonal and inter-annual effects

E-P-R / Q_{net}	Schanze	MERRA	ECCO2	CORE2	NCEP2	HOAPS
OAFlux+ISCCP	$2.3{\cdot}10^{-6}$	$2.2{\cdot}10^{-6}$	$2.0{\cdot}10^{-6}$	$2.2{\cdot}10^{-6}$	$2.2{\cdot}10^{-6}$	$2.1{\cdot}10^{-6}$
OAFlux+CERES	$2.5{\cdot}10^{-6}$	$2.3{\cdot}10^{-6}$	$2.2{\cdot}10^{-6}$	$2.3{\cdot}10^{-6}$	$2.4{\cdot}10^{-6}$	$2.2{\cdot}10^{-6}$
OAFlux+SRB	$2.8{\cdot}10^{-6}$	$2.7{\cdot}10^{-6}$	$2.5{\cdot}10^{-6}$	$2.7{\cdot}10^{-6}$	$2.8{\cdot}10^{-6}$	$2.6{\cdot}10^{-6}$
ERA-Interim	$1.9{\cdot}10^{-6}$	$1.7{\cdot}10^{-6}$	$1.6{\cdot}10^{-6}$	$1.8{\cdot}10^{-6}$	$1.8{\cdot}10^{-6}$	$1.7{\cdot}10^{-6}$
MERRA	$2.9{\cdot}10^{-6}$	$2.8{\cdot}10^{-6}$	$2.7{\cdot}10^{-6}$	$2.8{\cdot}10^{-6}$	$2.8{\cdot}10^{-6}$	$2.7{\cdot}10^{-6}$
ECCO2	$2.0{\cdot}10^{-6}$	$1.9{\cdot}10^{-6}$	$1.7{\cdot}10^{-6}$	$1.9{\cdot}10^{-6}$	$2.0{\cdot}10^{-6}$	$1.8{\cdot}10^{-6}$
NOCS v.2	$2.5{\cdot}10^{-6}$	$2.3{\cdot}10^{-6}$	$2.2{\cdot}10^{-6}$	$2.4{\cdot}10^{-6}$	$2.4{\cdot}10^{-6}$	$2.3{\cdot}10^{-6}$
J-OFURO2	$2.8{\cdot}10^{-6}$	$2.6{\cdot}10^{-6}$	$2.6{\cdot}10^{-6}$	$2.7{\cdot}10^{-6}$	$2.7{\cdot}10^{-6}$	$2.5{\cdot}10^{-6}$

Table A.30: Comparison of estimated global spice variance production $F_\tau \cdot (\tau - \tau_0)$ ((kg/m^3)^{2}m/s) using monthly fields of different Q_{net} and E-P-R products to include seasonal and inter-annual effects. The annual temporal and spatial mean is removed from the fields rather than removing a time-mean to produce a balanced estimate of Q_{net} and E-P-R

E-P-R / Q_{net}	Schanze	MERRA	ECCO2	CORE2	NCEP2	HOAPS
OAFlux+ISCCP	$2.7{\cdot}10^{-6}$	$2.5{\cdot}10^{-6}$	$2.6{\cdot}10^{-6}$	$2.6{\cdot}10^{-6}$	$2.6{\cdot}10^{-6}$	$2.5{\cdot}10^{-6}$
OAFlux+CERES	$2.8{\cdot}10^{-6}$	$2.6{\cdot}10^{-6}$	$2.9{\cdot}10^{-6}$	$2.7{\cdot}10^{-6}$	$2.7{\cdot}10^{-6}$	$2.5{\cdot}10^{-6}$
OAFlux+SRB	$3.4{\cdot}10^{-6}$	$3.2{\cdot}10^{-6}$	$3.2{\cdot}10^{-6}$	$3.3{\cdot}10^{-6}$	$3.3{\cdot}10^{-6}$	$3.1{\cdot}10^{-6}$
ERA-Interim	$1.9{\cdot}10^{-6}$	$1.7{\cdot}10^{-6}$	$1.6{\cdot}10^{-6}$	$1.8{\cdot}10^{-6}$	$1.8{\cdot}10^{-6}$	$1.7{\cdot}10^{-6}$
MERRA	$2.9{\cdot}10^{-6}$	$2.8{\cdot}10^{-6}$	$2.7{\cdot}10^{-6}$	$2.8{\cdot}10^{-6}$	$2.8{\cdot}10^{-6}$	$2.7{\cdot}10^{-6}$
ECCO2	$2.0{\cdot}10^{-6}$	$1.9{\cdot}10^{-6}$	$1.7{\cdot}10^{-6}$	$1.9{\cdot}10^{-6}$	$2.0{\cdot}10^{-6}$	$1.8{\cdot}10^{-6}$
NOCS v.2	$2.7{\cdot}10^{-6}$	$2.5{\cdot}10^{-6}$	$2.6{\cdot}10^{-6}$	$2.6{\cdot}10^{-6}$	$2.6{\cdot}10^{-6}$	$2.6{\cdot}10^{-6}$
J-OFURO2	$2.7{\cdot}10^{-6}$	$2.5{\cdot}10^{-6}$	$2.8{\cdot}10^{-6}$	$2.6{\cdot}10^{-6}$	$2.6{\cdot}10^{-6}$	$2.4{\cdot}10^{-6}$

Table A.31: Comparison of estimated spice variance dissipation χ_τ ((kg/m^3)^2/s) for different time-means of Q_{net} and E-P-R products

Q_{net} \ E-P-R	Schanze	MERRA	ECCO2	CORE2	NCEP2	HOAPS
OAFlux+ISCCP	$6.8{\cdot}10^{-9}$	$6.2{\cdot}10^{-9}$	$5.8{\cdot}10^{-9}$	$6.4{\cdot}10^{-9}$	$6.4{\cdot}10^{-9}$	$5.9{\cdot}10^{-9}$
OAFlux+CERES	$7.2{\cdot}10^{-9}$	$6.7{\cdot}10^{-9}$	$6.2{\cdot}10^{-9}$	$6.9{\cdot}10^{-9}$	$6.9{\cdot}10^{-9}$	$6.3{\cdot}10^{-9}$
OAFlux+SRB	$8.6{\cdot}10^{-9}$	$8.0{\cdot}10^{-9}$	$7.6{\cdot}10^{-9}$	$8.3{\cdot}10^{-9}$	$8.3{\cdot}10^{-9}$	$7.7{\cdot}10^{-9}$
ERA-Interim	$5.2{\cdot}10^{-9}$	$4.7{\cdot}10^{-9}$	$4.4{\cdot}10^{-9}$	$4.9{\cdot}10^{-9}$	$4.9{\cdot}10^{-9}$	$4.5{\cdot}10^{-9}$
MERRA	$8.8{\cdot}10^{-9}$	$8.2{\cdot}10^{-9}$	$7.9{\cdot}10^{-9}$	$8.4{\cdot}10^{-9}$	$8.4{\cdot}10^{-9}$	$8.0{\cdot}10^{-9}$
ECCO2	$5.9{\cdot}10^{-9}$	$5.3{\cdot}10^{-9}$	$4.9{\cdot}10^{-9}$	$5.5{\cdot}10^{-9}$	$5.6{\cdot}10^{-9}$	$5.0{\cdot}10^{-9}$
NOCS v.2	$7.2{\cdot}10^{-9}$	$6.6{\cdot}10^{-9}$	$6.5{\cdot}10^{-9}$	$6.8{\cdot}10^{-9}$	$6.8{\cdot}10^{-9}$	$6.6{\cdot}10^{-9}$
J-OFURO2	$8.1{\cdot}10^{-9}$	$7.5{\cdot}10^{-9}$	$7.4{\cdot}10^{-9}$	$7.8{\cdot}10^{-9}$	$7.8{\cdot}10^{-9}$	$7.0{\cdot}10^{-9}$

Table A.32: Comparison of estimated linear spice variance dissipation χ_τ ((kg/m^3)^2/s) for different time-means of Q_{net} and E-P-R products

Q_{net} \ E-P-R	Schanze	MERRA	ECCO2	CORE2	NCEP2	HOAPS
OAFlux+ISCCP	$7.4{\cdot}10^{-9}$	$6.8{\cdot}10^{-9}$	$6.2{\cdot}10^{-9}$	$7.1{\cdot}10^{-9}$	$7.0{\cdot}10^{-9}$	$6.4{\cdot}10^{-9}$
OAFlux+CERES	$7.7{\cdot}10^{-9}$	$7.1{\cdot}10^{-9}$	$6.6{\cdot}10^{-9}$	$7.3{\cdot}10^{-9}$	$7.3{\cdot}10^{-9}$	$6.7{\cdot}10^{-9}$
OAFlux+SRB	$9.6{\cdot}10^{-9}$	$9.1{\cdot}10^{-9}$	$8.6{\cdot}10^{-9}$	$9.3{\cdot}10^{-9}$	$9.3{\cdot}10^{-9}$	$8.7{\cdot}10^{-9}$
ERA-Interim	$5.7{\cdot}10^{-9}$	$5.1{\cdot}10^{-9}$	$4.8{\cdot}10^{-9}$	$5.4{\cdot}10^{-9}$	$5.3{\cdot}10^{-9}$	$5.0{\cdot}10^{-9}$
MERRA	$1.1{\cdot}10^{-8}$	$1.0{\cdot}10^{-8}$	$1.0{\cdot}10^{-8}$	$1.1{\cdot}10^{-8}$	$1.1{\cdot}10^{-8}$	$1.0{\cdot}10^{-8}$
ECCO2	$6.4{\cdot}10^{-9}$	$5.8{\cdot}10^{-9}$	$5.4{\cdot}10^{-9}$	$6.1{\cdot}10^{-9}$	$6.1{\cdot}10^{-9}$	$5.5{\cdot}10^{-9}$
NOCS v.2	$7.9{\cdot}10^{-9}$	$7.3{\cdot}10^{-9}$	$7.2{\cdot}10^{-9}$	$7.6{\cdot}10^{-9}$	$7.5{\cdot}10^{-9}$	$7.4{\cdot}10^{-9}$
J-OFURO2	$9.0{\cdot}10^{-9}$	$8.4{\cdot}10^{-9}$	$8.3{\cdot}10^{-9}$	$8.7{\cdot}10^{-9}$	$8.7{\cdot}10^{-9}$	$7.9{\cdot}10^{-9}$

Table A.33: Comparison of estimated spice variance dissipation χ_τ ($(kg/m^3)^2/s$) using 10° latitude bands of different time-means of Q_{net} and E-P-R products

Q_{net} \ E-P-R	Schanze	MERRA	ECCO2	CORE2	NCEP2	HOAPS
OAFlux+ISCCP	$6.5{\cdot}10^{-9}$	$6.0{\cdot}10^{-9}$	$6.3{\cdot}10^{-9}$	$6.1{\cdot}10^{-9}$	$6.1{\cdot}10^{-9}$	$5.6{\cdot}10^{-9}$
OAFlux+CERES	$6.4{\cdot}10^{-9}$	$5.9{\cdot}10^{-9}$	$6.1{\cdot}10^{-9}$	$5.9{\cdot}10^{-9}$	$6.0{\cdot}10^{-9}$	$5.5{\cdot}10^{-9}$
OAFlux+SRB	$7.7{\cdot}10^{-9}$	$7.2{\cdot}10^{-9}$	$7.4{\cdot}10^{-9}$	$7.2{\cdot}10^{-9}$	$7.3{\cdot}10^{-9}$	$6.8{\cdot}10^{-9}$
ERA-Interim	$4.7{\cdot}10^{-9}$	$4.2{\cdot}10^{-9}$	$4.6{\cdot}10^{-9}$	$4.3{\cdot}10^{-9}$	$4.3{\cdot}10^{-9}$	$4.0{\cdot}10^{-9}$
MERRA	$8.1{\cdot}10^{-9}$	$7.6{\cdot}10^{-9}$	$8.0{\cdot}10^{-9}$	$7.7{\cdot}10^{-9}$	$7.7{\cdot}10^{-9}$	$7.4{\cdot}10^{-9}$
ECCO2	$4.9{\cdot}10^{-9}$	$4.4{\cdot}10^{-9}$	$4.7{\cdot}10^{-9}$	$4.5{\cdot}10^{-9}$	$4.6{\cdot}10^{-9}$	$4.1{\cdot}10^{-9}$
NOCS v.2	$6.1{\cdot}10^{-9}$	$5.6{\cdot}10^{-9}$	$6.1{\cdot}10^{-9}$	$5.7{\cdot}10^{-9}$	$5.7{\cdot}10^{-9}$	$5.5{\cdot}10^{-9}$
J-OFURO2	$8.0{\cdot}10^{-9}$	$7.5{\cdot}10^{-9}$	$8.0{\cdot}10^{-9}$	$7.5{\cdot}10^{-9}$	$7.6{\cdot}10^{-9}$	$6.9{\cdot}10^{-9}$

Table A.34: Comparison of estimated spice variance dissipation χ_τ ($(kg/m^3)^2/s$) using monthly fields of different time-means of Q_{net} and E-P-R products. The use of monthly fields includes effects of the seasonal cycle and inter-annual variability in the estimate.

Q_{net} \ E-P-R	Schanze	MERRA	ECCO2	CORE2	NCEP2	HOAPS
OAFlux+ISCCP	$7.7{\cdot}10^{-9}$	$7.2{\cdot}10^{-9}$	$6.8{\cdot}10^{-9}$	$7.4{\cdot}10^{-9}$	$7.4{\cdot}10^{-9}$	$6.9{\cdot}10^{-9}$
OAFlux+CERES	$8.2{\cdot}10^{-9}$	$7.6{\cdot}10^{-9}$	$7.2{\cdot}10^{-9}$	$7.8{\cdot}10^{-9}$	$7.9{\cdot}10^{-9}$	$7.3{\cdot}10^{-9}$
OAFlux+SRB	$9.5{\cdot}10^{-9}$	$8.9{\cdot}10^{-9}$	$8.5{\cdot}10^{-9}$	$9.1{\cdot}10^{-9}$	$9.2{\cdot}10^{-9}$	$8.6{\cdot}10^{-9}$
ERA-Interim	$6.2{\cdot}10^{-9}$	$5.7{\cdot}10^{-9}$	$5.4{\cdot}10^{-9}$	$5.9{\cdot}10^{-9}$	$5.9{\cdot}10^{-9}$	$5.5{\cdot}10^{-9}$
MERRA	$9.7{\cdot}10^{-9}$	$9.2{\cdot}10^{-9}$	$8.9{\cdot}10^{-9}$	$9.4{\cdot}10^{-9}$	$9.4{\cdot}10^{-9}$	$9.0{\cdot}10^{-9}$
ECCO2	$6.8{\cdot}10^{-9}$	$6.3{\cdot}10^{-9}$	$5.8{\cdot}10^{-9}$	$6.5{\cdot}10^{-9}$	$6.5{\cdot}10^{-9}$	$5.9{\cdot}10^{-9}$
NOCS v.2	$8.2{\cdot}10^{-9}$	$7.6{\cdot}10^{-9}$	$7.5{\cdot}10^{-9}$	$7.9{\cdot}10^{-9}$	$7.9{\cdot}10^{-9}$	$7.6{\cdot}10^{-9}$
J-OFURO2	$9.3{\cdot}10^{-9}$	$8.7{\cdot}10^{-9}$	$8.6{\cdot}10^{-9}$	$8.9{\cdot}10^{-9}$	$9.0{\cdot}10^{-9}$	$8.2{\cdot}10^{-9}$

Table A.35: Comparison of estimated spice variance dissipation χ_τ ($(kg/m^3)^2/s$) using monthly fields of different time-means of Q_{net} and E-P-R products. The use of monthly fields includes effects of the seasonal cycle and inter-annual variability in the estimate. Here, the annual mean is removed from the fields rather than balancing fields by removing a time-mean.

E-P-R / Q_{net}	Schanze	MERRA	ECCO2	CORE2	NCEP2	HOAPS
OAFlux+ISCCP	$9.0{\cdot}10^{-9}$	$8.3{\cdot}10^{-9}$	$8.6{\cdot}10^{-9}$	$8.6{\cdot}10^{-9}$	$8.5{\cdot}10^{-9}$	$8.2{\cdot}10^{-9}$
OAFlux+CERES	$9.4{\cdot}10^{-9}$	$8.7{\cdot}10^{-9}$	$9.6{\cdot}10^{-9}$	$9.1{\cdot}10^{-9}$	$8.9{\cdot}10^{-9}$	$8.5{\cdot}10^{-9}$
OAFlux+SRB	$1.1{\cdot}10^{-8}$	$1.1{\cdot}10^{-8}$	$1.1{\cdot}10^{-8}$	$1.1{\cdot}10^{-8}$	$1.1{\cdot}10^{-8}$	$1.0{\cdot}10^{-8}$
ERA-Interim	$6.2{\cdot}10^{-9}$	$5.7{\cdot}10^{-9}$	$5.4{\cdot}10^{-9}$	$5.9{\cdot}10^{-9}$	$5.9{\cdot}10^{-9}$	$5.5{\cdot}10^{-9}$
MERRA	$9.7{\cdot}10^{-9}$	$9.2{\cdot}10^{-9}$	$8.9{\cdot}10^{-9}$	$9.4{\cdot}10^{-9}$	$9.4{\cdot}10^{-9}$	$9.0{\cdot}10^{-9}$
ECCO2	$6.8{\cdot}10^{-9}$	$6.3{\cdot}10^{-9}$	$5.8{\cdot}10^{-9}$	$6.5{\cdot}10^{-9}$	$6.5{\cdot}10^{-9}$	$5.9{\cdot}10^{-9}$
NOCS v.2	$9.1{\cdot}10^{-9}$	$8.4{\cdot}10^{-9}$	$8.8{\cdot}10^{-9}$	$8.8{\cdot}10^{-9}$	$8.6{\cdot}10^{-9}$	$8.6{\cdot}10^{-9}$
J-OFURO2	$9.1{\cdot}10^{-9}$	$8.4{\cdot}10^{-9}$	$9.2{\cdot}10^{-9}$	$8.8{\cdot}10^{-9}$	$8.7{\cdot}10^{-9}$	$8.1{\cdot}10^{-9}$

Bibliography

Adler, R., G. Huffman, A. Chang, R. Ferraro, P. Xie, J. Janowiak, B. Rudolf, U. Schneider, S. Curtis, D. Bolvin, et al. (2003). The Version-2 Global Precipitation Climatology Project (GPCP) Monthly Precipitation Analysis (1979–Present). *J. Hydrometeorol. 4*, 1147–1167.

Amante, C., B. Eakins, and N. G. D. Center (2009). *ETOPO1 1 arc-minute global relief model: procedures, data sources and analysis.* US Department of Commerce, National Oceanic and Atmospheric Administration, National Environmental Satellite, Data, and Information Service, National Geophysical Data Center, Marine Geology and Geophysics Division.

Baumgartner, A. and E. Reichel (1975). *World Water Balance: Mean Annual Global, Continental and Maritime Precipitation, Evaporation and Runoff.* Elsevier Scientific Pub. Co Amsterdam.

Berry, D. and E. Kent (2009). A new air-sea interaction gridded dataset from ICOADS with uncertainty estimates. *Bull. Amer. Meteor. Soc 90*(5), 645–656.

Bosilovich, M., S. Schubert, G. Kim, R. Gelaro, M. Rienecker, M. Suarez, J. Bacmeister, R. Todling, and J. Chen (2006). NASA's Modern Era Retrospective-analysis for Research and Applications (MERRA). In *AGU Fall Meeting Abstracts*, Volume 1, pp. 3.

Box, J., D. Bromwich, B. Veenhuis, L. Bai, J. Stroeve, J. Rogers, K. Steffen, T. Haran, and S. Wang (2006). Greenland Ice Sheet Surface Mass Balance Variability (1988–2004) from CalibratedPolar MM5 Output. *J. Climate 19*, 2783–2800.

Brutsaert, W. (1982). *Evaporation into the Atmosphere.* Kluwer Academic Publishers.

Chou, S., R. Atlas, C. Shie, and J. Ardizzone (1995). Estimates of Surface Humidity and Latent Heat Fluxes over Oceans from SSM/I Data. *Mon. Wea. Rev. 123*, 2405–2425.

Chou, S., E. Nelkin, J. Ardizzone, R. Atlas, and C. Shie (2003). Surface Turbulent Heat and Momentum Fluxes over Global Oceans Based on the Goddard Satellite Retrievals, Version 2 (GSSTF2). *J. Climate 16*, 3256–3273.

Church, J. and N. White (2006). A 20th century acceleration in global sea–level rise. *Geophys. Res. Lett. 33*, L01602.

Church, J., N. White, L. Konikow, C. Domingues, J. Cogley, E. Rignot, J. Gregory, M. van den Broeke, A. Monaghan, and I. Velicogna (2011). Revisiting the Earth's sea-level and energy budgets from 1961 to 2008. *Geophys. Res. Lett. 38*(18), L18601.

Cresswell, G. and J. Peterson (1993). The Leeuwin Current south of Western Australia. *Aust. J. Mar. Fresh. Res. 44*, 285–285.

Curtis, S. (2008). The El Niño–Southern Oscillation and Global Precipitation. *Geography Compass 2/3*, 600–619.

Dai, A., T. Qian, K. E. Trenberth, and J. D. Milliman (2009). Changes in Continental Freshwater Discharge from 1948 to 2004. *J. Climate 22*, 2773–2792.

Dai, A. and K. Trenberth (2002). Estimates of Freshwater Discharge from Continents: Latitudinal and Seasonal Variations. *J. Hydrometeorol. 3*, 660–687.

Dai, A. and K. Trenberth (2003). New estimates of continental discharge and oceanic freshwater transport. In *Proc. Symp. on Observing and Understanding the Variability of Water in Weather and Climate.*

Davis, R. (1994). Diapycnal mixing in the ocean: Equations for large-scale budgets. *Journal of physical oceanography 24*(4), 777–800.

Divakarla, M., C. Barnet, M. Goldberg, L. McMillin, E. Maddy, W. Wolf, L. Zhou, and X. Liu (2006). Validation of Atmospheric Infrared Sounder temperature and water vapor retrievals with matched radiosonde measurements and forecasts. *J. Geophys. Res-Atmos. 111*, D09S15.

Domingues, C., J. Church, N. White, P. Gleckler, S. Wijffels, P. Barker, and J. Dunn (2008). Improved estimates of upper–ocean warming and multi–decadal sea–level rise. *Nature 453*, 1090–1093.

Durack, P. and S. Wijffels (2010). Fifty-Year Trends in Global Ocean Salinities and their relationship to Broad-Scale Warming. *J. Climate 23*, 4342–4362.

Fairall, C., E. Bradley, J. Hare, A. Grachev, and J. Edson (2003). Bulk Parameterization of Air–Sea Fluxes: Updates and Verification for the COARE Algorithm. *J. Climate 16*, 571–591.

Fairall, C., E. Bradley, D. Rogers, J. Edson, and G. Young (1996). The TOGA COARE bulk flux algorithm. *J. Geophys. Res. 101*, 3747–3764.

Fekete, B., C. Vörösmarty, J. Roads, and C. Willmott (2004). Uncertainties in Precipitation and Their Impacts on Runoff Estimates. *J. Climate 17*, 294–304.

Gille, S. (2004). How nonlinearities in the equation of state of seawater can confound estimates of steric sea level change. *J. Geophys. Res. 109*, C03005.

Goodberlet, M., C. Swift, and J. Wilkerson (1990). Ocean surface wind speed measurements of the Special SensorMicrowave/Imager (SSM/I). *IEEE Trans. Geosci. Remote Sens. 28*, 823–828.

Gordon, C., C. Cooper, C. Senior, H. Banks, J. Gregory, T. Johns, J. Mitchell, and R. Wood (2000). The simulation of SST, sea ice extents and ocean heat transports in a version of the Hadley Centre coupled model without flux adjustments. *Climate Dyn. 16*(2), 147–168.

Hansen, J., L. Nazarenko, R. Ruedy, M. Sato, J. Willis, A. Del Genio, D. Koch, A. Lacis, K. Lo, S. Menon, et al. (2005). Earth's Energy Imbalance: Confirmation and Implications. *Science 308*, 1431.

Hartmann, D. (1994). *Global Physical Climatology*, Volume 56 of *International Geophysics*. Academic Press.

Huang, R. (2011). Defining the spicity. *J. Mar. Res. 69*(4–6), 545–559.

Huang, R. and R. Schmitt (1993). The Goldsbrough–Stommel Circulation of the World Oceans. *J. Phys. Oceanogr. 23*, 1277–1284.

Ingleby, B. and M. Huddleston (2007). Quality control of ocean temperature and salinity profiles–Historical and real-time data. *J. Mar. Sys. 65*(1-4), 158–175.

IOC, SCOR, and IAPSO (2011). *The international thermodynamic equation of seawater Ű 2010: Calculation and use of thermodynamic properties.*

Iudicone, D., G. Madec, and T. McDougall (2008). Water-mass transformations in a neutral density framework and the key role of light penetration. *J. Phys. Oceanogr. 38*(7), 1357–1376.

Jackett, D., T. McDougall, R. Feistel, D. Wright, and S. Griffies (2006). Algorithms for Density, Potential Temperature, Conservative Temperature, and the Freezing Temperature of Seawater. *J. Atmos. Oceanic Technol. 23*, 1709–1728.

Josey, S. (2001). A Comparison of ECMWF, NCEP–NCAR, and SOC Surface Heat Fluxes with Moored Buoy Measurements in the Subduction Region of the Northeast Atlantic. *J. Climate 14*, 1780–1789.

Josey, S., E. Kent, and P. Taylor (1998). The Southampton Oceanography Centre (SOC) ocean–atmosphere heat, momentum and freshwater flux atlas. Technical report, National Oceanography Centre, Southampton, UK.

Joyce, T. (1980). On Production and Dissipation of Thermal Variance in the Oceans. *J. Phys. Oceanogr. 10*, 460–463.

Joyce, T. (2012). New perspectives on eighteen-degree water formation in the north atlantic. *Journal of oceanography 68*(1), 45–52.

Kadko, D., J. Baross, and J. Alt (1995). *The magnitude and global implications of hydrothermal flux.* Number 91 in Geophys. Monogr. Ser.: Seafloor Hydrothermal Systems: Physical, Chemical, Biological, and Geological Interactions. AGU, Washington D.C.

Kanamitsu, M., W. Ebisuzaki, J. Woollen, S. Yang, J. Hnilo, M. Fiorino, and G. Potter (2002). Ncep-doe amip-ii reanalysis (r-2). *Bull. Amer. Meteor. Soc. 83*, 1631–1643.

Karsten, R. and J. Marshall (2002). Constructing the residual circulation of the ACC from observations. *J. Phys. Oceanogr. 32*, 3315–3327.

Kistler, R., E. Kalnay, W. Collins, S. Saha, G. White, J. Woollen, M. Chelliah, W. Ebisuzaki, M. Kanamitsu, V. Kousky, et al. (2001). The NCEP–NCAR 50–Year Reanalysis: Monthly Means CD–ROM and Documentation. *Bull. Amer. Meteor. Soc. 82*, 247–267.

Klocker, A. and T. McDougall (2010). Influence of the nonlinear equation of state on global estimates of dianeutral advection and diffusion. *Journal of Physical Oceanography 40*(8), 1690–1709.

Kubota, M., N. Iwasaka, S. Kizu, M. Konda, and K. Kutsuwada (2002). Japanese ocean flux data sets with use of remote sensing observations (J-OFURO). *Journal of oceanography 58*(1), 213–225.

Kuhlbrodt, T., A. Griesel, M. Montoya, A. Levermann, M. Hofmann, and S. Rahmstorf (2007). On the driving processes of the Atlantic meridional overturning circulation. *Rev. Geophys. 45*, RG2001.

Large, W. and S. Yeager (2009). The global climatology of an interannually varying air–sea flux data set. *Climate Dyn. 33*, 341–364.

Ledwell, J., A. Watson, and C. Law (1998). Mixing of a tracer in the pycnocline. *J. Geophys. Res. 103*(C10), 21499–21.

Levenspiel, O. and N. de Nevers (1974). The Osmotic Pump. *Science 183*(4121), 157–160.

McDougall, T. (1986). Thermobaricity, cabbeling, and water–mass conversion. *J. Geophys. Res–Oceans 92*, 5448Ű–5464.

McDougall, T. (1987). Neutral surfaces. *J. Phys. Oceanogr. 17*, 1950–1964.

McDougall, T. (2003). Potential enthalpy: A conservative oceanic variable for evaluating heat content and heat fluxes. *Journal of Physical Oceanography 33*(5), 945–963.

McDougall, T. (2011). *Getting started with TEOS-10 and the Gibbs Seawater (GSW) Oceanographic Toolbox.* SCOR/IAPSO WG127, ISBN 978-0-646-55621-5.

McDougall, T. and C. Garrett (1992). Scalar conservation equations in a turbulent ocean. *Deep–Sea Res. 39*, 1953–1966.

Menemenlis, D., J. Campin, P. Heimbach, C. Hill, T. Lee, A. Nguyen, M. Schodlock, and H. Zhang (2008). ECCO2: High resolution global ocean and sea ice data synthesis. *Mercator Ocean Q. Newsl 31*, 13–21.

Midttun, L. (1985). Formation of dense bottom water in the Barents Sea. *Deep Sea Research Part A. Oceanographic Research Papers 32*(10), 1233–1241.

Monaghan, A., D. Bromwich, and S. Wang (2006). Recent trends in Antarctic snow accumulation from Polar MM5 simulations. *Philos. T. Roy. Soc. A 364*, 1683.

Munk, W. (1981). Internal waves and small–scale processes. In C. Wunsch and B. Warren (Eds.), *Evolution of physical oceanography*, pp. 264Ű291. Massachusetts Institute of Technology.

Nash, J. and J. Moum (1999). Estimating salinity variance dissipation rate from conductivity microstructure measurements. *J. Atmos. Oceanic Technol. 16*(2), 263–274.

NCAR (2010). U.S. National Center for Atmospheric Research [Climate and Global Dynamics Division], U.S. Geophysical Fluid Dynamics Laboratory [NOMADS], U.K. Hadley Centre for Climate Prediction and Research, and U.S. National Centers for Environmental Prediction, updated half-yearly: CORE.2 Global Air-Sea Flux Dataset Dataset ds260.2 published by the CISL Data Support Section at the National Center for Atmospheric Research, Boulder, CO, available online at http://dss.ucar.edu/datasets/ds260.2/.

New, M., M. Todd, M. Hulme, and P. Jones (2001). Precipitation measurements and trends in the twentieth century. *Int. J. Climatol. 21*, 1899–1922.

Polzin, K., J. Toole, J. Ledwell, and R. Schmitt (1997). Spatial variability of turbulent mixing in the abyssal ocean. *Science 276*(5309), 93–96.

Quartly, G., E. Kyte, M. Srokosz, and M. Tsimplis (2007). An intercomparison of global oceanic precipitation climatologies. *J. Geophys. Res–Atmos. 112*, D10121.

Radko, T. (2007). Mechanics of merging events for a series of layers in a stratified turbulent fluid. *J. Fluid Mech. 577*, 251.

Radko, T. (2008). The double-diffusive modon. *J. Fluid Mech. 609*, 59–86.

Robinson, I. (2004). *Measuring the Oceans from Space: The Principles and Methods of Satellite Oceanography.* Springer.

Roderick, M. and G. Farquhar (2002). The Cause of Decreased Pan Evaporation over the Past 50 Years. *Science 298*, 1410–1411.

Sapiano, M. and P. Arkin (2009). An Intercomparison and Validation of High-Resolution Satellite Precipitation Estimates with 3-Hourly Gauge Data. *J. Hydrometeorol. 10*, 149–166.

Schanze, J., R. Schmitt, and L. Yu (2010). The global oceanic freshwater cycle: A state-of-the-art quantification. *J. Mar. Res. 3*(4), 569–595.

Schmitt, R. (1979). The growth rate of super-critical salt fingers. *Deep Sea Research Part A. Oceanographic Research Papers 26*(1), 23–40.

Schmitt, R. (1994). Double Diffusion in Oceanography. *Annu. Rev. Fluid Mech. 26*, 255–285.

Schmitt, R. (1995). The ocean component of the global water cycle. *Rev. Geophys. 33*, 1395–1410.

Schmitt, R. (1999). Spice and the Demon. *Science 283*, 498–499.

Schmitt, R., P. Bogden, and C. Dorman (1989). Evaporation minus precipitation and density fluxes for the North Atlantic. *J. Phys. Oceanogr. 19*, 1208–1221.

Schneider, E. and U. Bhatt (2000). A dissipation integral with application to ocean diffusivities and structure. *J. Phys. Oceanogr. 30*, 1158–1171.

Schulz, J., P. Schluessel, and H. Grassl (1993). Water vapour in the atmospheric boundary layer over oceans from SSM/I measurements. *Int. J. Remote Sens. 14*, 2773–2789.

Shepherd, A. and D. Wingham (2007). Recent Sea–Level Contributions of the Antarctic and Greenland Ice Sheets. *Science 315*, 1529.

Simmons, A., S. Uppala, D. Dee, and S. Kobayashi (2007). ERA-Interim: New ECMWF reanalysis products from 1989 onwards. *ECMWF Newsletter 110*, 25–35.

Smith, E., J. Vazquez, A. Tran, and R. Sumagaysay (1996). Satellite–derived sea surface temperature data available from the NOAA/NASA Pathfinder Program. *Eos, Transactions, American Geophysical Union 77*, 135.

Spencer, R., H. Goodman, and R. Hood (1989). Precipitation Retrieval over Land and Ocean with the SSM/I: Identification and Characteristics of the Scattering Signal. *J. Atmos. Oceanic Technol. 6*, 254Ű–273.

St. Laurent, L. and R. Schmitt (1999). The contribution of salt fingers to vertical mixing in the North Atlantic Tracer Release Experiment. *J. Phys. Oceanogr. 29*, 1404–1424.

Sterl, A. (2004). On the (In) Homogeneity of Reanalysis Products. *J. Climate 17*, 3866–3873.

Stern, M. (1969). Collective instability of salt fingers. *J. Fluid Mech. 35*, 209–218.

Stern, M. (1975). *Ocean Circulation Physics.* Academic Press.

Sturaro, G. (2003). A closer look at the climatological discontinuities present in the NCEP/NCAR reanalysis temperature due to the introduction of satellite data. *Climate Dyn. 21*, 309–316.

Talley, L. (2008). Freshwater transport estimates and the global overturning circulation: Shallow, deep and throughflow components. *Prog. Oceanogr. 78*, 257–303.

Thorpe, S. (2005). *The Turbulent Ocean.* Cambridge Univ Press.

Toggweiler, J. and B. Samuels (1995). Effect of Drake Passage on the global thermohaline circulation. *Deep–Sea Res. Pt. I 42*, 477–500.

Trenberth, K., J. Fasullo, and J. Kiehl (2009). Earth's Global Energy Budget. *Bull. Amer. Meteor. Soc. 90*, 311–323.

Trenberth, K., L. Smith, T. Qian, A. Dai, and J. Fasullo (2007). Estimates of the global water budget and its annual cycle using observational and model data. *J. Hydrometeorol. 8*, 758–769.

Turner, J. S. (1979). *Buoyancy Effects in Fluids.* Cambridge Monographs on Mechanics. Cambridge University Press.

Uppala, S., P. Kållberg, A. Simmons, U. Andrae, V. Da Costa Bechtold, M. Fiorino, J. Gibson, J. Haseler, A. Hernandez, G. Kelly, et al. (2005). The ERA–40 re–analysis. *Quart. J. Roy. Meteor. Soc. 131*, 2961–3012.

Vaughan, D., J. Bamber, M. Giovinetto, J. Russell, and A. Cooper (1999). Reassessment of Net Surface Mass Balance in Antarctica. *J. Climate 12*, 933–946.

Veronis, G. (1972). On properties of seawater defined by temperature, salinity and pressure. *J. Mar. Res. 30*, 227–255.

Warren, B. (2009). Note on the Vertical Velocity and Diffusive Salt Flux Induced by Evaporation and Precipitation. *J. Phys. Oceanogr. 39*, 2680–2682.

Weyl, P. (1968). The role of the oceans in climatic change: A theory of the ice ages. *Meteor. Mon. 8*, 37–62.

Wijffels, S., R. Schmitt, H. Bryden, and A. Stigebrandt (1992). Transport of freshwater by the oceans. *J. Phys. Oceanogr. 22*, 155–162.

Wolter, K. and M. Timlin (1993). Monitoring ENSO in COADS with a Seasonally Adjusted Principal Component Index. In *Proc. 17th Climate Diagnostics Workshop*, pp. 52–57.

Woodgate, R. and K. Aagaard (2005). Revising the Bering Strait freshwater flux into the Arctic Ocean. *Geophys. Res. Lett. 32*, L02602.

Woodruff, S., R. Slutz, R. Jenne, and P. Steurer (1987). A Comprehensive Ocean–Atmosphere Data Set. *Bull. Amer. Meteor. Soc. 68*, 1239–1250.

Wunsch, C. and R. Ferrari (2004). Vertical Mixing, Energy, and the General Circulation of the Oceans. *Annu. Rev. Fluid Mech. 36*, 281–314.

Wunsch, C. and P. Heimbach (2007). Practical global oceanic state estimation. *Physica D 230*, 197–208.

Xie, P. and P. Arkin (1997). Global precipitation: A 17-year monthly analysis based on gauge observations, satellite estimates, and numerical model outputs. *Bull. Amer. Meteor. Soc. 78*, 2539–2558.

Yin, X., A. Gruber, and P. Arkin (2004). Comparison of the GPCP and CMAP Merged Gauge: Satellite Monthly Precipitation Products for the Period 1979–2001. *J. Hydrometeorol. 5*, 1207–1222.

Yu, L., X. Jin, and R. A. Weller (2008). Multidecade Global Flux Datasets from the Objectively Analyzed Air–sea Fluxes (OAFlux) Project: Latent and Sensible Heat Fluxes, Ocean Evaporation, and Related Surface Meteorological Variables. Technical Report OAFlux Project Technical Report (OA2008–01), Woods Hole Oceanographic Institution.

Yu, L. and R. Weller (2007). Objectively Analyzed Air–Sea Heat Fluxes for the Global Ice–Free Oceans (1981–2005). *Bull. Amer. Meteor. Soc. 88*, 527–539.

Zahariev, K. and C. Garrett (1997). An apparent surface buoyancy flux associated with the nonlinearity of the equation of state. *J. Phys. Oceanogr. 27*(2), 362–368.

Zeng, L., P. Shi, W. Liu, and D. Wang (2009). Evaluation of a satellite-derived latent heat flux product in the South China Sea: A comparison with moored buoy data and various products. *Atmos. Res. 94*, 91–105.

Zhang, J. and R. Schmitt (2000). The Impact of Salt Fingering on the Thermohaline Circulation under Mixed Boundary Conditions. *J. Phys. Oceanogr. 30*(6), 1223–1231.

Zhang, Y., W. Rossow, A. Lacis, V. Oinas, and M. Mishchenko (2004). Calculation of radiative fluxes from the surface to top of atmosphere based on ISCCP and other global data sets: Refinements of the radiative transfer model and the input data. *J. Geophys. Res–Atmos. 109*, D19105.